IMPROVED LENS SYSTEMS FOR THE ELECTRON MICROSCOPE

A Thesis submitted for the Degree

of

DOCTOR OF PHILOSOPHY

at

The Department of Physics

The University of Aston in Birmingham

by

HISHAM HASHIM ELKAMALI

JULY 1981

بِسْمِ اللَّهِ الرَّحْمَٰنِ الرَّحِيمِ

لَا يُكَلِّفُ اللَّهُ نَفْسًا إِلَّا وُسْعَهَا ۚ لَهَا
مَا كَسَبَتْ وَعَلَيْهَا مَا اكْتَسَبَتْ ۚ رَبَّنَا لَا تُؤَاخِذْنَا إِن
نَّسِينَا أَوْ أَخْطَأْنَا ۚ رَبَّنَا وَلَا تَحْمِلْ عَلَيْنَا إِصْرًا كَمَا حَمَلْتَهُ
عَلَى الَّذِينَ مِن قَبْلِنَا ۚ رَبَّنَا وَلَا تُحَمِّلْنَا مَا لَا طَاقَةَ لَنَا بِهِ ۖ
وَاعْفُ عَنَّا وَاغْفِرْ لَنَا وَارْحَمْنَا ۚ أَنتَ مَوْلَانَا فَانصُرْنَا
عَلَى الْقَوْمِ الْكَافِرِينَ ﴿٢٨٦﴾

(سورة البقرة)

THE UNIVERSITY OF ASTON IN BIRMINGHAM

ABSTRACT

IMPROVED LENS SYSTEMS FOR THE ELECTRON MICROSCOPE

Hisham Hashim Elkamali, Ph.D., 1981

The general aim of the present investigation was to design and build an experimental electron microscope column based on miniature single-polepiece magnetic lenses, suitable for operation at an accelerating voltage of 1000 KV or more, but comparable in size to that of a 100 KV transmission electron microscope (TEM). An AEI EM6 100 KV TEM was modified for the purpose. In particular the standard viewing chamber was considerably shortened and all the original imaging lenses were replaced.

Special attention was paid to the projection system. A novel wide-angle projection system was devised with a projection semi-angle of 30° compared with the usual value of 8° in commercial electron microscopes.

The improved performance has been achieved by the simultaneous correction of spiral and radial distortion in a two-lens system. This consists of two single-polepiece lenses excited by currents of opposite sign. Use is made of the asymmetric nature of the axial field distribution of single-polepiece lenses. Thus the final projector lens produces an unusually low amount of distortion. The corrector lens, on the other hand, produces a considerable amount of distortion, which enables it to contribute appreciably (3X) to the total magnification whilst reducing the overall distortion of the final image to negligible proportions.

Such a correction system is especially suitable for reducing the size and weight of high voltage electron microscopes, as well as for providing greatly improved viewing facilities.

Key Words:

electron optics, electron microscopy, single-polepiece magnetic lenses, projection system, distortion correction.

A C K N O W L E D G E M E N T S

I am much indebted and grateful to my supervisor Professor THOMAS MULVEY for suggesting the project of research, helpful discussions and guidance throughout.

I should also like to acknowledge the technical assistance of Mr. R. Keen (TEM, Physics Department), the staff of the Physics Workshop for putting into practice the lens designs described in the thesis, and the staff of the University Communication Media for preparing slides for conferences.

My colleagues S. Al-Hilly, S. Christofides, H. Nasr and A. Alshwaikh to whom I am grateful and who with such good grace gave me their time and energy over consultations and opinions. May I again thank Al-Hilly for the assistance with Munro's programs.

I would particularly like to acknowledge the generosity of the University of Khartoum, SUDAN, in providing the financial support that enabled me to undertake this research.

JULY 1981

H.H. ELKAMALI

LIST OF SYMBOLS

A_c	rectangular cross-sectional area of a coil
A_s	surface area of a wire
A_{sc}	surface area of a coil
A_w	cross-sectional area of a wire
a	axial distance between the two points at which the magnetic field is reduced to one half of the peak value.
B	magnetic flux density
B_{AC}	stray A.C. magnetic field
B_z	axial magnetic flux density distribution
B_{zo}	axial magnetic flux density distribution along the axis (z-axis) of symmetry of a magnetic lens
C_s	coefficient of spherical aberration
D	coefficient of distortion for a projector lens of infinite conjugates
D^*	coefficient of distortion for a projector lens of finite conjugates
D_1	inner diameter of a coil
D_2	outer diameter of a coil
D_b	diameter of the bore of a lens
D_{case}	overall diameter of an iron cased lens
D_{core}	outside diameter of the iron core of a lens
D_{corr}	coefficient of distortion of the corrector lens
D_m	mean diameter of a coil

D_{rad}	coefficient of radial distortion for a lens of infinite conjugates.
D^*_{rad}	coefficient of radial distortion for a lens of finite conjugates
D_{sp}	coefficient of spiral distortion for a lens of infinite conjugates
D^*_{sp}	coefficient of spiral distortion for a lens of finite conjugates
D_{proj}	coefficient of distortion for a projector lens of infinite conjugates
D^*_{proj}	coefficient of distortion for a projector lens of finite conjugates
e/m	charge to mass ratio of the electron
F	force on an electron
F_{eff}	effective focal length of the projection system
f	focal length of a lens
f_1	focal length of the first thin (corrector) lens
f_2	focal length of the second thin (corrector) lens
f_{corr}	effective focal length of the corrector lens
f_p	focal length of the final projector lens
h	coefficient of heat transfer
I	electric current
I_{max}	maximum electric current
I_o	electric current required to produce maximum magnification
k	coefficient of astigmatism

k_1	coefficient of linear radial distortion
k_2	coefficient of linear spiral distortion
L	projection distance (camera constant)
L_{FC}	projection distance to the film camera
L_{FS}	projection distance to the focusing screen
L_{PC}	projection distance to the plate camera
L_S	projection distance to the final screen
ℓ	inter-lens spacing
ℓ_1	separation between the two thin lenses representing a strong corrector lens
ℓ_2	separation between the second thin(corrector) lens and the thin lens representing the final projector lens
ℓ_p	separation between the thin lens (representing the final projector) and the final screen
ℓ_w	length of a wire in a coil
M	magnification
M_1	overall magnification of the projection system at the final screen
M_2	magnification of the projection system, when the corrector lens is switched off, at the final screen
M_{corr}	magnification of the corrector lens at the final screen
M_o	maximum magnification
m	conjugate ratio
N	number of turns in a coil

NI	ampere-turns
$(NI)_{max}$	maximum ampere-turns
$NI/V_r^{\frac{1}{2}}$	excitation parameter
$NI/V_r^{\frac{1}{2}}(corr)$	exitation parameter of a corrector lens
$NI/V_r^{\frac{1}{2}}(proj)$	excitation parameter of a projector lens
n	scaling factor of a lens
P	power input
Q	quality factor of a lens; related to distortion
Q_{corr}	quality factor of a corrector lens of infinite conjugates
Q_{eff}	effective quality factor of the projection system
Q_{proj}	quality factor of a projector lens of infinite conjugates
Q^*_{proj}	quality factor of a projector lens of finite conjugates
Q_{rad}	radial quality factor of a lens
Q_{sp}	spiral quality factor of a lens
q	quantity of heat
R	resistance
R_{arc}	radius of curvature of an electron ray in a uniform A.C. magnetic field
R_b	radius of a lens bore
R_o	resistance at room temperature
R_T	resistance at temperature T
r	radial co-ordinate of the electron trajectory in the object plane

r_1	radial height of a ray at the first corrector thin lens
r_2	radial height of a ray at the second corrector thin lens
r_3	radial height of a ray at the projector thin lens
r_{corr}	radial height of an electron at the bore of the corrector lens
r_{proj}	radial height of an electron at the bore of the projector lens
S	gap width between the polepieces of a conventional double-polepiece lens
T	temperature
T_s	surface temperature of a coil
T_w	temperature of water
t	axial depth of a coil
t_{base}	thickness of the base of the iron structure of a lens
t_{case}	thickness of the outer walls of the iron structure of a lens
u	object distance
V	voltage
V_{max}	maximum voltage
V_r	electron accelerating voltage (relativistically corrected)
V_{r1}	electron accelerating voltage (relativistically corrected) to be scaled up by a factor n^2
V_{r2}	electron accelerating voltage (relativistically corrected) scaled by a factor n^2.

V_{vol}	volume
v	image distance
v_{vel}	velocity of an electron
X	first particular solution of the paraxial ray equation
Y	second particular solution of the paraxial ray equation
y	relative sensitivity (or image deflection) produced by stray A.C. magnetic fields
y_o	radial height of an object point
z	distance along the electron-optical axis of a rotationally symmetric lens

LIST OF GREEK SYMBOLS

α	temperature coefficient of resistance
α_{corr}	projection semi-angle at the corrector lens
α_i	angle of inclination of an incident ray
α_p	projection semi-angle at the final projector lens
$\alpha_{p(m=o)}$	projection semi-angle at the final projector lens for infinite conjugates
$(\alpha_p)_{FC}$	projection semi-angle to the film camera
$(\alpha_p)_{FS}$	projection semi-angle to the focusing screen
$(\alpha_p)_{PC}$	projection semi-angle to the plate camera
$(\alpha_p)_S$	projection semi-angle to the final fluorescent screen
$\Delta\rho$	deviation of an image point from the corresponding Gaussian image point

$(\Delta\rho)_{rad}$	radial deviation of an image point from the corresponding Gaussian image point
$(\Delta\rho)_{sp}$	circumferential deviation of an image point from the corresponding Gaussian image point
$\Delta\rho/\rho$	relative distortion in the image at the final viewing screen
$(\Delta\rho/\rho)_{corr}$	relative distortion in the image produced by the corrector lens at the final viewing screen
$(\Delta\rho/\rho)_{eff}$	effective distortion in the image produced by the projction system at the final viewing screen
$(\Delta\rho/\rho)_{proj}$	relative distortion in the image produced by the final projector lens at the final viewing screen
$(\Delta\rho/\rho)_{rad}$	relative radial distortion in the image at the final viewing screen
$(\Delta\rho/\rho)_{sp}$	relative spiral distortion in the image at the final viewing screen
ε	angle of refraction of a ray
θ	angle of rotation of an image plane with respect to the object plane due to the magnetic field of a lens
θ_o	angle of rotation of an image plane with respect to an object plane of paraxial rays due to the magnetic field of a lens

θ_r	angle of rotation of an image plane with respect to an object plane of marginal rays due to the magnetic field of a lens
λ	wavelength
μ_o	permeability of free space ($4\pi \times 10^{-7}$ Hm^{-1})
μ_r	relative permeability
ρ	radial height of a Gaussian image point at the final viewing screen
ρ_e	resistivity
ρ_p	radial height of a Gaussian image point at the final viewing screen when the corrector lens is switched off
ρ_t	radial height of a Gaussian image point at the final viewing screen when both lenses of the projection system are energised
σ	current density
σ_{max}	maximum current density

Note: The S.I. system of units is employed throughout the text unless otherwise stated.

C O N T E N T S

CHAPTER 1

INTRODUCTION

1.1 THE ELECTRON MICROSCOPE

The electron microscope is a powerful analytical instrument in the physical and biological sciences. Since the first electron microscope to surpass the resolution of the optical microscope was built by Ruska in 1933, a wide range of transmission (TEM), scanning (SEM) and scanning transmission (STEM) electron microscopes have been developed. Recent efforts to improve microscope performance have concentrated on the illuminating system, vacuum technique, the incorporation of minicomputers for image handling and processing, photographic recording of images, and most importantly the design of the objective lens. The resolution of the electron microscope is fundamentally limited by the wavelength λ of the electrons and the coefficient of spherical aberration C_s of the objective lens since the resolution

$$d = \text{constant} \times C_s^{1/4} \lambda^{3/4} \quad .$$

The resolving power can thus, in principle, be improved by employing high electron accelerating voltages V, typically higher than 600 KV.

However, the full operational advantages of high resolution microscopy cannot be realised in practice unless attention is also paid to the projection system, the viewing arrangements, and the recording of the image on the photographic plate or image intensifier. Before considering the design of a viewing system for high voltage microscopy it may be useful to look at the design

of a typical 100 KV high performance electron microscope, such as the Philips EM 200, whose column is shown in figure (1.1). This instrument has been selected as being of advanced design in its viewing arrangement since the viewing chamber incorporates two cameras and two fluorescent screens as well as provision for fitting an external energy loss spectrometer or an image intensifier. The design of the viewing system cannot be carried out in isolation from that of the rest of the instrument.

This instrument comprises a source of electrons (electron gun) and a double condenser system to control the illumination on the specimen. The imaging system consists of an objective lens followed by three projector lenses capable of projecting an image on either of the two cameras or on either of the two fluorescent screens according to the operational requirements.

The complete viewing system is shown in more detail in figure (1.2). The small high resolution phosphor screen of 2 cm. diameter is used for focusing the image with the help of a binocular viewer. It can be mechanically removed from the electron beam by means of an outside control. This focusing screen is placed nearer the final projector lens than is the final viewing screen so as to obtain the best compromise between screen intensity and resolution when using the binoculars. The distance L between the point at which the electrons cross the optical axis after the final projector lens and the screen is defined as the projection distance; in the Philips EM 200, for example, the projection distance L_{FS} of the focusing screen is 29.6 cm. The corresponding maximum projection semi-angle $(\alpha_p)_{FS}$ of the outer rays to the focusing screen with the optical axis is small,

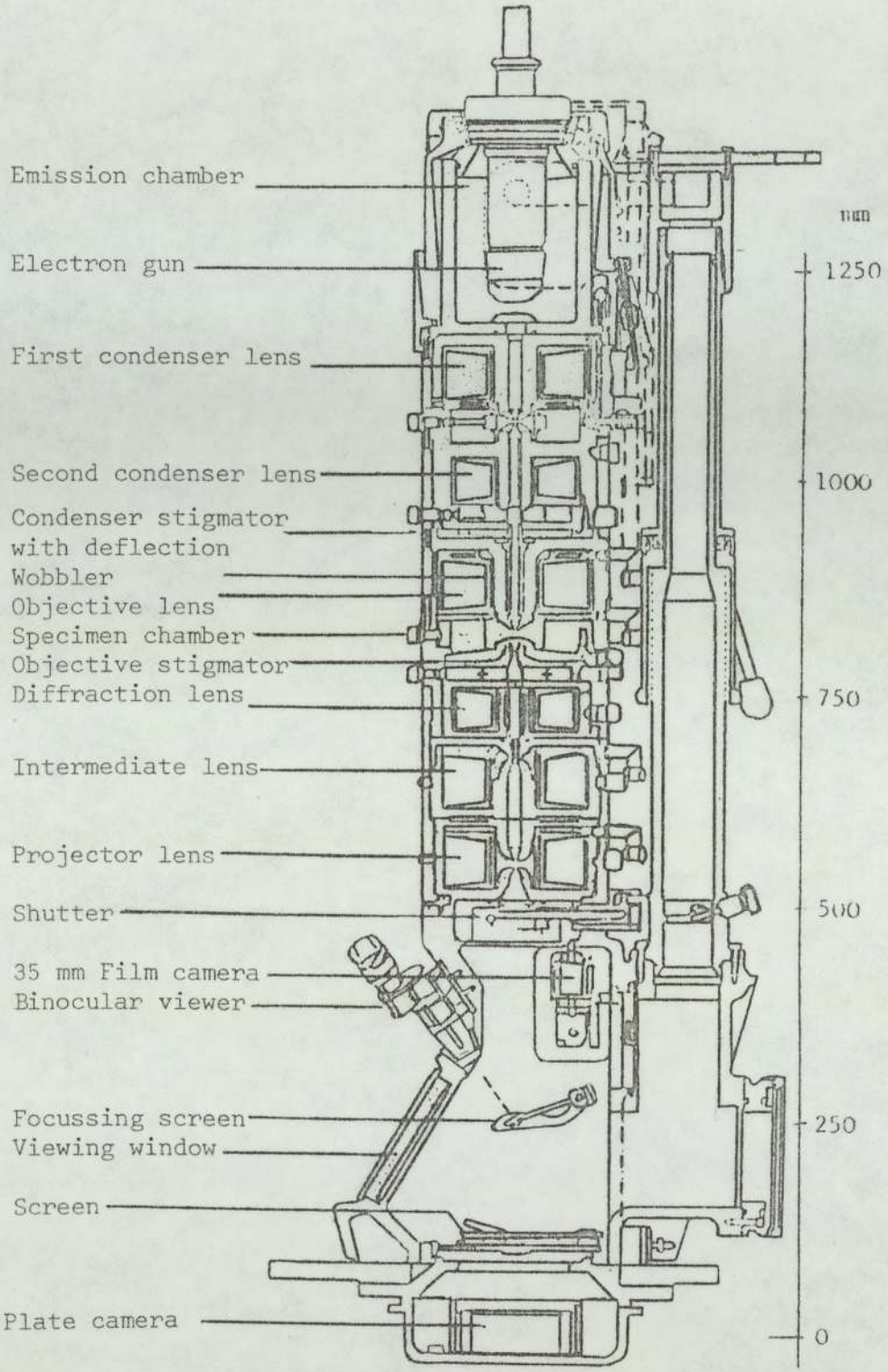

Figure (1.1) Schematic diagram of Philips EM 200 100 KV transmission electron microscope.

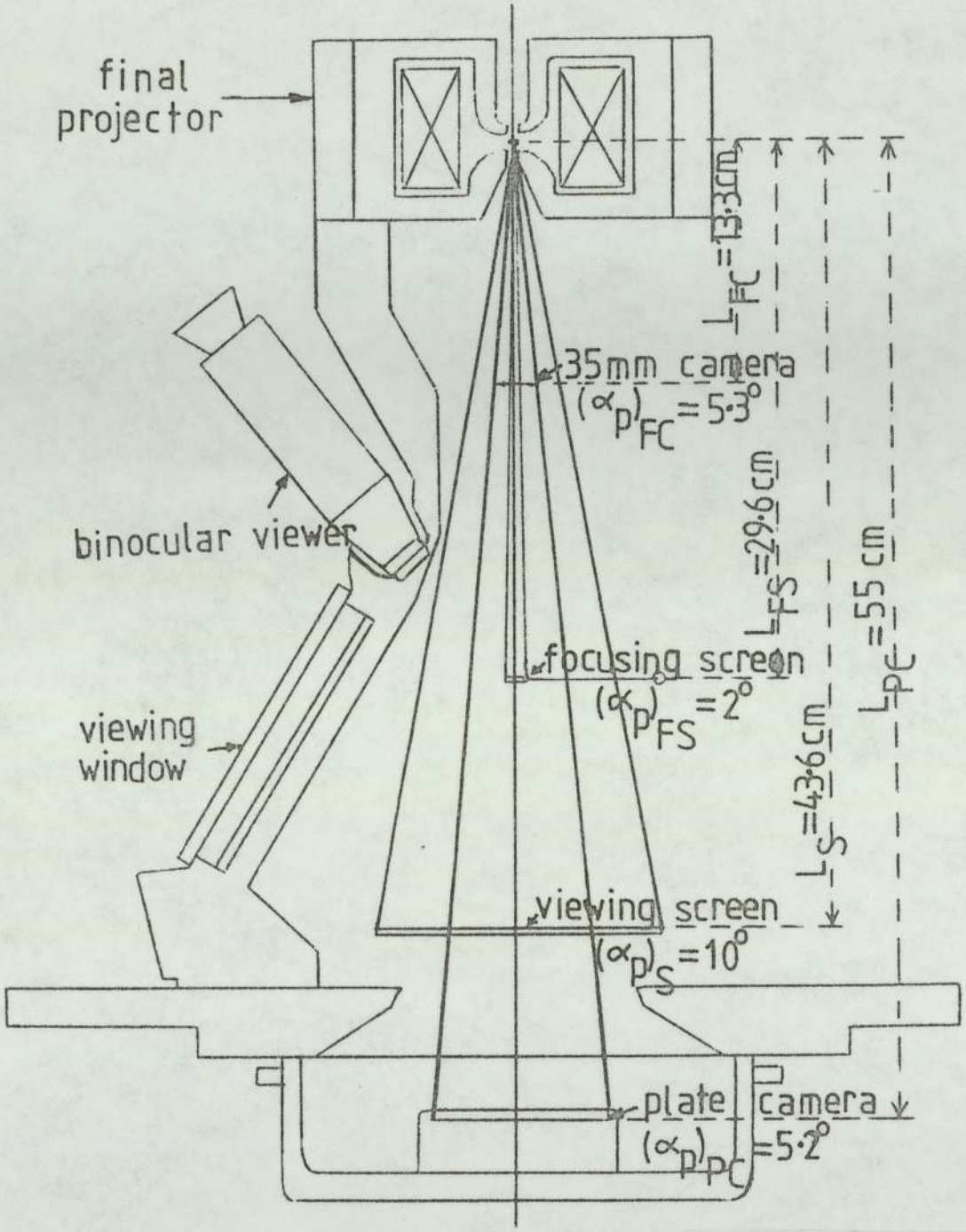

Figure (1.2) The viewing system of the Philips EM 200 100KV transmission electron microscope. Note the two viewing screens and two cameras. Essential parameters and nomenclure of the viewing system is also shown in the figure.

only 2°, as shown in figure (1.2). With such a small semi-angle the question of image distortion does not arise. The final fluorescent screen of the microscope, however, is 16 cm. in diameter at a projection distance L_S = 43.6 cm.; corresponding to a projection semi-angle $(\alpha_p)_S$ of 10°, a much larger angle, as shown in figure (1.2). With such a large projection semi-angle, spiral distortion amounting to 4.4% is clearly visible at the edge of the viewing screen. N.B. 2% of spiral distortion can just be detected by the eye. The plate camera is situated in the vacuum beneath the final fluorescent screen; the screen itself acting as a shutter. The plate is at a large projection distance L_{PC} = 55 cm. corresponding to a comparatively small projection semi-angle $(\alpha_p)_{PC}$ of 5.2°, as shown in figure (1.2). This gives rise to about 1% of spiral distortion. It should be noted that finer image details can be recorded on photographic plates than observed visually on the fluorescent screen because photographic plates have a better resolving power than that of the eye. For this reason the photographic plate should ideally be placed between the projector lens and the viewing screen. N.B. This, however, is not standard practice in most TEMs. The Philips EM 200 achieves this by fitting a second camera, namely a 35 mm camera above the focusing screen at a comparatively short projection distance L_{FC} = 13.3 cm. with a projection semi-angle $(\alpha_p)_{FC}$ = 5.3°, i.e., comparable with that of the plate camera. Although there is no loss of semi-angle with this camera, the effective width of the image is only 24.5 mm and this causes difficulty in avoiding graininess of the image. It would be a considerable advantage if

standard size photographic material could be employed in this position. Unfortunately image distortion at present makes this impossible. A further advantage of siting the camera in this position is that a spectrometer or an image intensifier can then be permanently attached to the instrument below the final fluorescent screen without interfering with photography.

This camera arrangement, with its shorter projection distance will also reduce the effect of stray alternating fields on the image, since it is difficult to screen the viewing chamber magnetically because of the presence of large viewing windows. This point is considered in more detail in the next section.

The present investigation is also relevant to TEMs fitted with a transmission fluorescent screen. A typical example is found in instruments with a short or inverted column like the JEOL Superscope 30 KV TEM, as shown in figure (1.3). This microscope is not arranged vertically with the electron gun at the top but its axis is inclined at an angle of 30° to the horizontal. It has only two lenses; an objective and a projector; no condenser lens is employed. The chief point of interest for this investigation lies in the viewing chamber; the image is projected onto a large transmission fluorescent screen. The projection distance is only 20 cm. which results in a convenient wide-angle projection system with a projection semi-angle of 14.6°. This is an excellent idea but the spiral distortion at the edge of the screen amounts to an intolerable 7%. A photographic film camera is fitted in the optimum position inside the column at a short projection distance of 7.3 cm. giving a projection semi-angle of 6.4° and an image spiral distortion of 1.25%

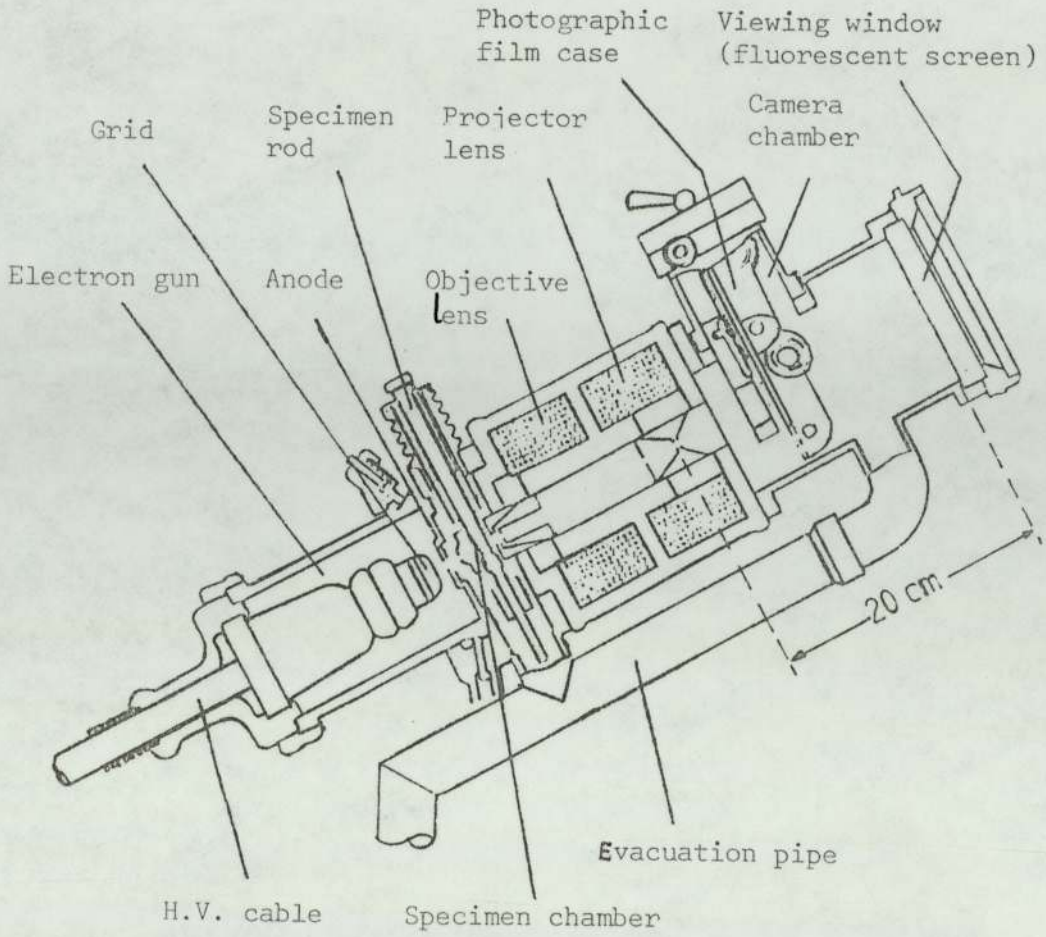

Figure (1.3) Schematic diagram of the JEOL Superscope 30 KV TEM

which is quite acceptable.

It would therefore seem that optimum viewing arrangements are not yet available in transmission electron microscopes. Where an attempt has been made to provide such facilities, it has not usually been successful mainly because the image distortion could not be reduced to acceptable levels. It is the purpose of this investigation to seek to remove these limitations.

1.1.1 HIGH VOLTAGE ELECTRON MICROSCOPES (HVEMs)

The above problems become more serious in high voltage

microscopes since there are additional factors to be considered in the design of the viewing chamber. Commercially available high voltage electron microscopes tend to be largely scaled up versions of 100 KV instruments. This has the practical merit of enabling existing designs of 100 KV instruments to be used with only minor modifications. However, this procedure results in an unwieldy and often inconvenient structure for the electron-optical column itself and certainly of the viewing chamber. This may be seen by considering the scaling laws for magnetic lenses. If a magnetic lens is scaled by a factor n and at the same time the ampere-turns are scaled by the same factor, the magnetic field strength at corresponding points of the original and scaled model will be the same. This is true even if magnetic saturation is present, provided that the B/H properties of the iron in the original and scaled model are the same. Hence for a given increase of voltage from V_{r1} to V_{r2} and for a given magnetic field strength at corresponding parts of the original and scaled lenses, $n = (V_{r2}/V_{r1})^{\frac{1}{2}}$. This follows since a given focal property depends essentially on the quantity $NI/V_r^{\frac{1}{2}}$, where V_r is the relativistically accelerating voltage and NI is the lens excitation. Thus the scaling factor n, for an increase of accelerating voltage from 100 KV (V_r = 110 KV) to 1 MV (V_r = 2000 KV), is $(2000/110)^{\frac{1}{2}} = 4.26$. The geometrical dimenstions, the ampere-turns of the magnetic lens and all focal properties will thus be scaled by a factor of 4.26. The volume of the lens will now be scaled by n^3 i.e. $(4.26)^3 = 77$ times. For a given excitation parameter $NI/V_r^{\frac{1}{2}}$, the focal length and aberration coefficients will be scaled up by 4.26. It should

be noted that in a projector lens such scaling operations alter the focal length f_p of the projector and hence the magnification but not the image distortion produced by the lens. This is discussed in section 1.2.1.3.

This scaling up procedure is especially inconvenient in the viewing system as a whole because in order to preserve the magnification of the final projector stage a scaling factor n must be applied to the length of the viewing chamber. Increasing the length of the viewing chamber is undesirable since it makes the instrument unduly sensitive to stray A.C. magnetic fields which cause unsharpness of the image. This unsharpness increases as the square of the projection length L [see Appendix (7)]. Thus a scaling factor of 4.26 would lead to an increase of stray field sensitivity of the same amount. In fact, in a viewing chamber scaled up in this way the sensitivity to stray A.C. magnetic fields would actually increase with increasing accelerating voltage. In practice, the viewing chamber is not scaled up exactly in this way; a compromise is actually adopted between the requirements of high magnification and convenience of manufacture. In some cases an extra intermediate projector lens is inserted in the column to produce the required total magnification. Both in theory and in practice, magnetic screening problems arise in high voltage microscopes. It is not uncommon for stray A.C. fields to limit the performance of high voltage microscopes. In order to illustrate the electron-optical system and viewing arrangements of a typical high voltage TEM, the electron-optical column of the AEI EM7 instrument is shown in figure (1.4). This instrument operates up to an accelerating voltage of 1.2 MV.

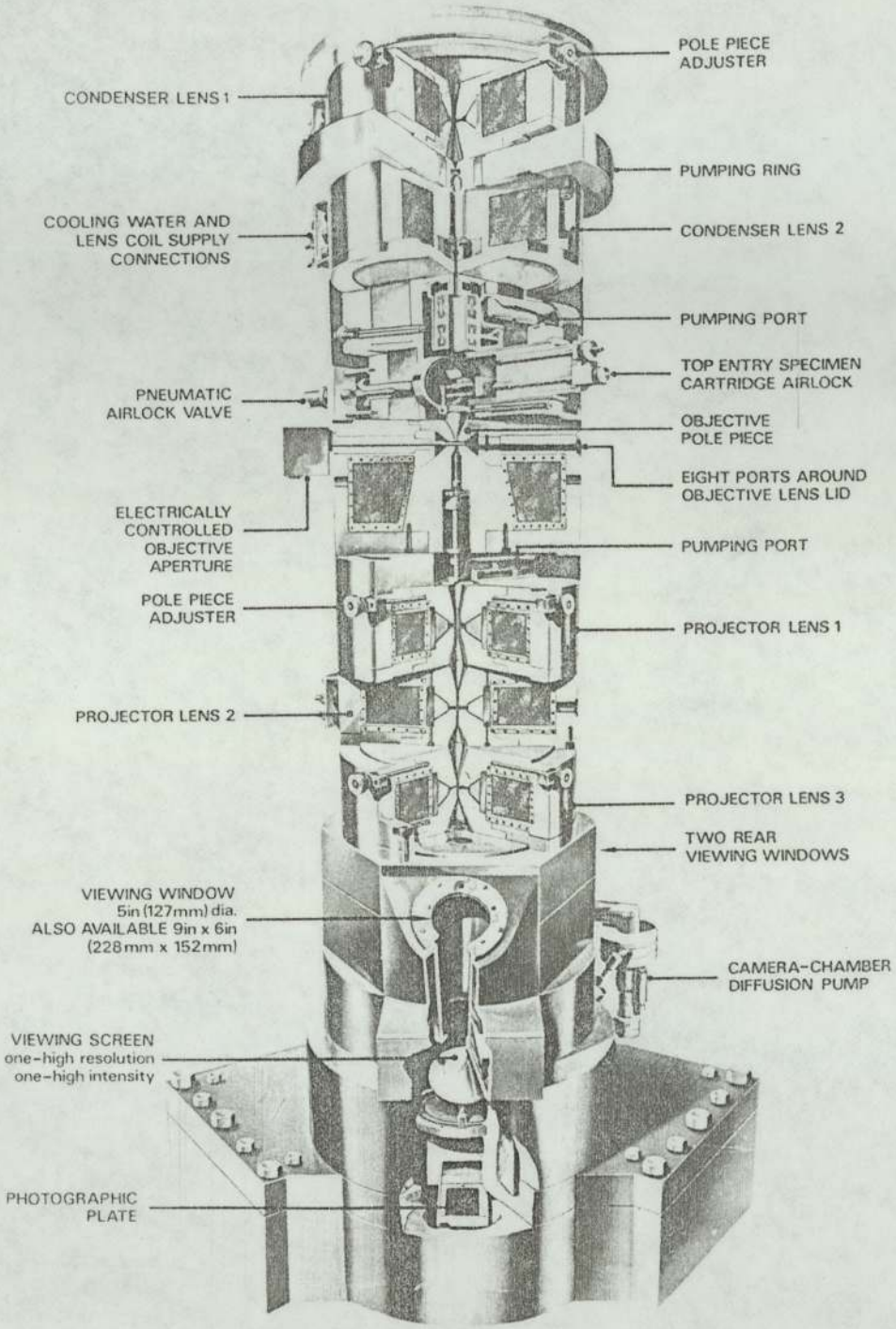

Figure (1.4) Photograph of the AE1 EM7 1MV TEM

The diameter of the magnetic lenses is 47 cm. The projection distances L_S and L_{PC} to the screen and camera plate are 61.5 cm. and 80 cm. respectively, corresponding to projection semi-angles $(\alpha_p)_S$ and $(\alpha_p)_{PC}$ to the screen and camera of 7.4° and 3.6° respectively. The diameters of the screen and the plate camera are 16 cm. and 10 cm. respectively. The distortion at the edge of the screen and of the photographic plate is 1.7% and 0.4% respectively. The weight of this instrument is about eight tons. The viewing chamber cannot therefore be reduced in height without serious increase in image distortion.

Another example of the HVEM is the Hitachi 3MV TEM (Ozasa et.al., 1970) installed at Osaka University in Japan. The column of this microscope, shown in figure (1.5), is 4 metres long and 1 metre in diameter and weighs 20 tons. The combined microscope and accelerator weighs 67 tons. The lead glass viewing window is 60 cm. thick i.e. about 100 times thicker than that of a 100 KV TEM. The projection distances to the screen L_S and to the camera plate L_{PC} are large, 80 cm. and 100 cm. respectively. The diameter of the screen is 12.5 cm. and that of the photographic plate is 10 cm. The corresponding projection semi-angles $(\alpha_p)_S$ and $(\alpha_p)_{PC}$ to the screen and camera are thus 4.5° and 2.9° respectively. The distortion at the edge of the screen and of the photographic plate is 0.6% and 0.27% respectively. Once again no reduction in size or weight are possible without serious increase in image distortion.
Table (1.1) summarises the scaled and actual projection distances for the viewing chambers of the three microscopes (100 KV, 1 MV and 3MV). It is clear from the table that the projection

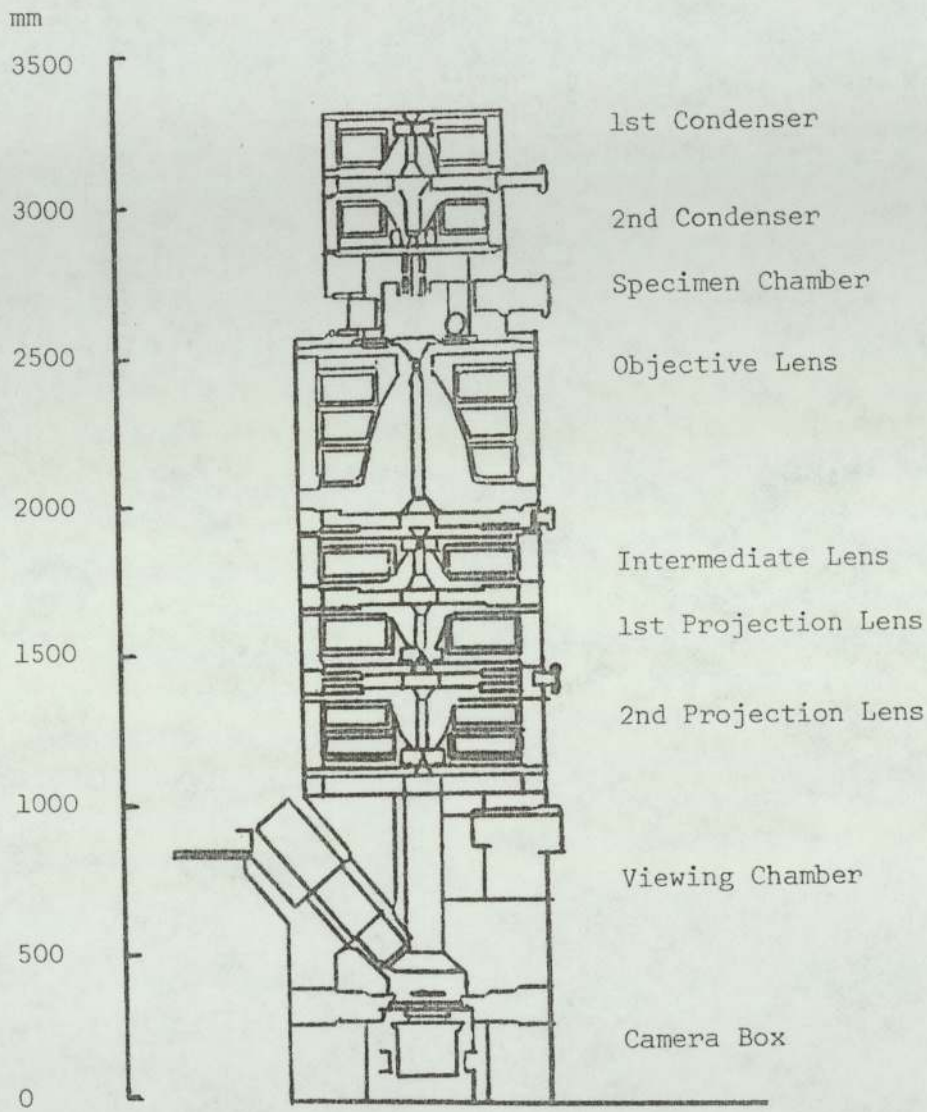

Figure (1.5) Schematic diagram of the Hitachi 3MV TEM column installed at Osaka University, Japan. (Ozasa et.al., 1970).

distances of the 1MV and 3MV viewing chambers are not in fact scaled up 4.26X and 10.44X respectively as they should have been to preserve projector magnification. Instead, they were only scaled up by the factors 1.46X and 1.82X respectively thus sacrificing image magnification by factors of 2.92X and 5.74X respectively. The reason for not employing the desirable scaling factor n to the heights of the viewing chamber is that their heights would have been 234 cm. for the 1MV and 574 cm. for the 3MV microscopes, inconveniently long from the constructional point of view. It was also clearly desirable to shorten the projection distance L so as to reduce the effects of stray A.C. magnetic fields.

It should be noted that for a typical stray A.C. field of 1μT (10 milli-Gauss) the image displacement is 135μm at 100 KV, which would impose severe limitations on the resolution of the recorded image. At 3000 KV this would be reduced to some 40μm which, although not negligible, is probably acceptable.

It is the purpose of the present investigation, therefore, to devise projection systems and associated viewing chambers for high voltage electron microscopes, preferably of a size that is not appreciably larger than that of a conventional 100 KV microscope without sacrificing in any way the viewing and recording facilities of a 100 KV instrument. This can in principle by achieved by employing miniature projector lenses one of which is a wide angle projector lens. The following advantages would be expected from such a system: a short viewing chamber and hence a reduction in the effect of stray A.C. magnetic fields on the image; a more rational arrangement of the viewing

Accelerating Voltage (KV)	100 (Philips)	1000 (EM7)	3000 (Hitachi 3MV)
Scaled projection distance for given projector magnification (m)	0.55	2.34	5.74
Actual projection distance (m)	0.55	0.80	1.00
Reduction of magnification in the projector	1X	2.9X	5.7X
Sensitivity to stray A.C. field ($y/B_{A.C.}$) of system scaled for given projector magnfication ($\mu m/\mu T$)	135	576	1409
Sensitivity to stray A.C. field ($y/B_{A.C.}$) of actual system ($\mu m/\mu T$)	135	67	43

Table (1.1) A table showing the projection distances scaled for a given magnification and the actual projection distances of commercial TEMs operating at 100, 1000 and 3000 KV respectively, together with the corresponding sensitivity to stray magnetic fields. The reduction of magnification incurred by the reduced projection distances is also shown.

screen and photographic plate. The magnification of the final projector lens would probably be smaller than usual in such an arrangement but this can be compensated by the addition of suitable intermediate lenses.

1.2 REQUIREMENTS OF THE PROJECTION AND VIEWING SYSTEM

The purpose of projection lenses is to magnify the image produced by the objective lens so that the finest image detail can be seen on the fluorescent screen and recorded on the photographic plate. In a projector lens the angular aperture of the ray pencils is much smaller than those in the objective and therefore aberrations such as spherical aberration do not occur. This means that the projection system cannot affect the sharpness of the image and so it cannot impair the resolution of the microscope. However, image distortion can be serious. Distortion, of course, refers to the deviation $\Delta\rho$ of an image point from the corresponding Gaussian image point of radius ρ, as shown in figure (1.6). Distortion is undesirable and inconvenient since it makes identification of shapes and sizes difficult. A convenient measure of distortion is the quantity $\Delta\rho/\rho$ or relative distortion. In general, one can tolerate only one or two percent of distortion in an electron microscope image.

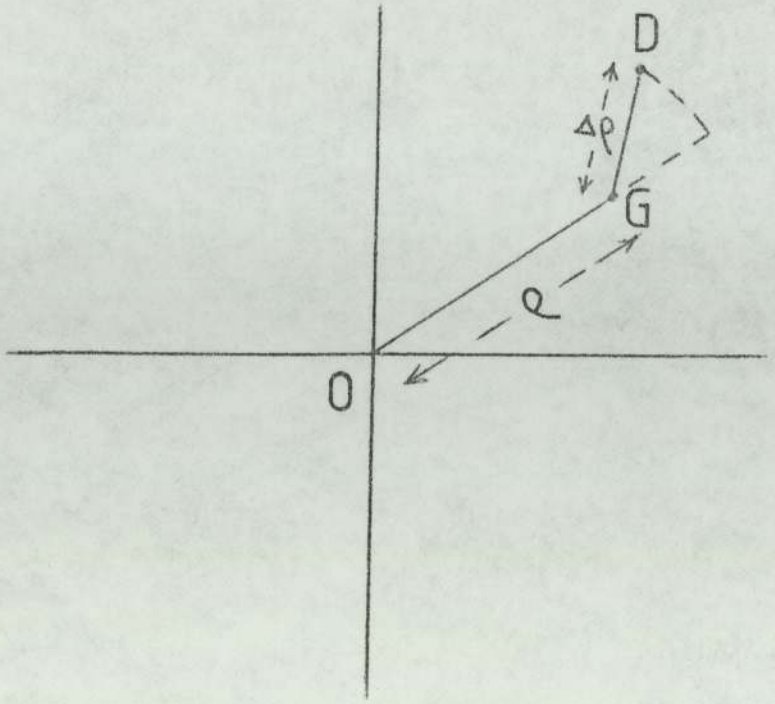

Figure (1.6) Displacement of a Gaussian image point G to point D by distortion. O is the centre of the image.

1.2.1 DISTORTION IN THE FINAL PROJECTOR LENS

Distortion is an aberration that changes the shape of the image. It may displace an image point in both radial (radial distortion) and circumferential (spiral distortion) directions from the corresponding Gaussian image point. Experience shows that the eye can generally tolerate about 1% of radial distortion and 2% of spiral distortion, without being disturbed by the presence of distortion in the image.

1.2.1.1 RADIAL DISTORTION

Radial (isotropic) distortion is the result of a change in the magnification of the image with radial height. It causes the Gaussian image points to be displaced either away from or

towards the centre of the image thus giving rise to pin-cushion or barrel distortion respectively, as shown in figure (1.7). In this figure O is the centre of the image in which the Gaussian image line AG is distorted into the curve BCD_1 in the case of pin-cushion distortion and the curve BCD_2 in the case of barrel

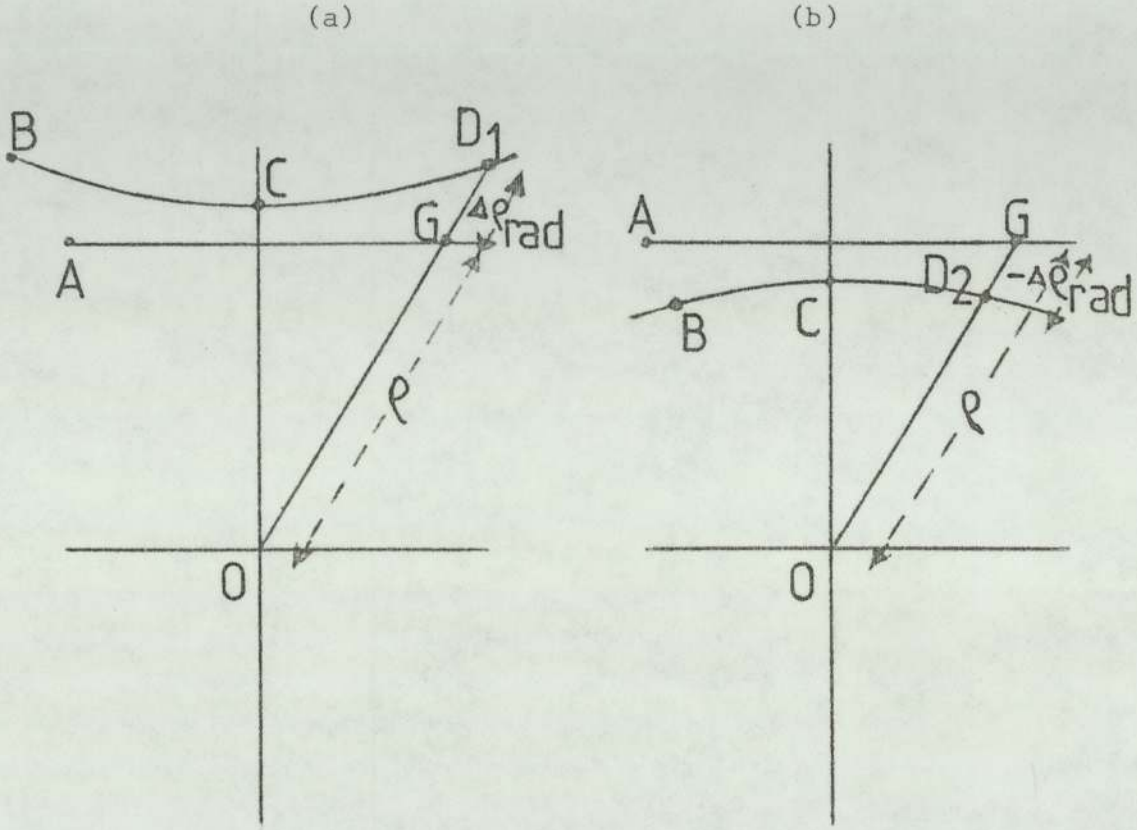

Figure (1.7) Distortion in the image (a) pin-cushion (b) barrel. The line AG is distorted in shape. G is a Gaussian image point; D_1 and D_2 are the corresponding displaced image points by pin-cushion and barrel distortion respectively. O is the centre of the image (optical axis).

distortion. If an electron beam is used to project the image of a rectangular grid, the general appearance of the projected image is shown in figure (1.8) for (a) pin-cushion and (b) barrel distortion.

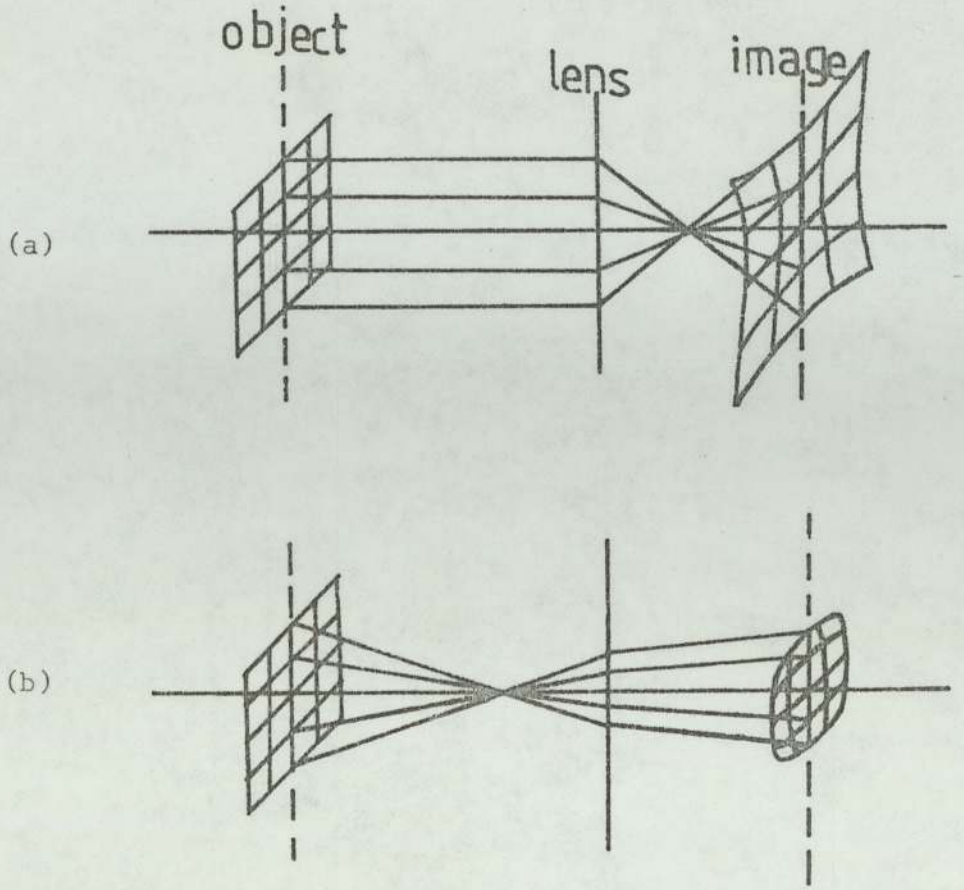

Figure (1.8) A distorted projection image of a perfect grid by (a) pin-cushion and (b) barrel distortion.

Distortion of this type is invariably present in the final projection image of all electron microscopes. Distortion is usually the only troublesome aberration in projector lenses, since these lenses have to project rays incident on the lens at relatively large distances from the axis. Correct choice of projector excitation $NI/V_r^{\frac{1}{2}}$ can, in fact, eliminate radial distortion (Liebmann, 1951) in a single projector lens. This situation occurs when the projector lens is operated near its minimum focal length, i.e. maximum image **magnification**. The radial displacement $\Delta\varrho_{rad}$ from the Gaussian image point is defined [see Klemperer

and Barnett (1971)] as

$$\Delta\rho_{rad} = MD_{rad}r^3 \quad \text{.....(1.1)}$$

where M is the projector magnification, D_{rad} is the coefficient of radial distortion, r is the radial co-ordinate of the electron trajectory in the object plane. Notice that D_{rad} has the dimensions of $[L^{-2}]$. The more convenient relative distortion $(\Delta\rho/\rho)_{rad}$ is given by

$$(\Delta\rho/\rho)_{rad} = D_{rad}r^2 \quad \text{.....(1.2)}$$

since $Mr = \rho$ where ρ is the radial height of the Gaussian image point.

1.2.1.2 SPIRAL DISTORTION

In a magnetic lens the axially symmetric magnetic field distribution of a projector lens causes the image to rotate through an angle θ_o relative to the object during its passage through the lens. θ_o , for paraxial rays, is given by

$$\theta_o = (e/8mV_r)^{\frac{1}{2}} \int_{z_1}^{z_n} B_{zo}\, dz \quad \text{.....(1.3)}$$

where e/m is the charge to mass ratio of the electron, V_r is the relativistically accelerating voltage, B_{zo} is the magnetic field distribution along the electron-optical axis (z-axis), and z_1 and z_n are the positions of the beginning and ending of the magnetic field distribution respectively. This integral taken over the entire field is given by $\mu_o NI$ where $\mu_o = 4\pi \times 10^{-7}$ H/m is the permeability of free space. Hence equation (1.3) becomes

$$\theta_o = 0.1863\ NI/V_r^{\frac{1}{2}} \quad \text{.....(1.4)}$$

where NI is the ampere-turns of the lens coil. But the magnetic field in the lens varies with radial height r. In general, therefore, we obtain different values of angle of rotation (θ_r) for electrons of different radial height. The associated angular difference $\delta\theta = (\theta_r - \theta_o) = (\Delta\rho/\rho)_{sp}$ is called spiral distortion, as illustrated in figure (1.9). We can therefore write

$$(\Delta\rho/\rho)_{sp} = D_{sp} r^2 \quad \ldots\ldots\ldots\ldots\ldots\ldots\ldots\ldots (1.5)$$

where D_{sp} is known as the coefficent of spiral distortion. For parallel illumination, r is the radial height of the incident electron trajectory at the lens.

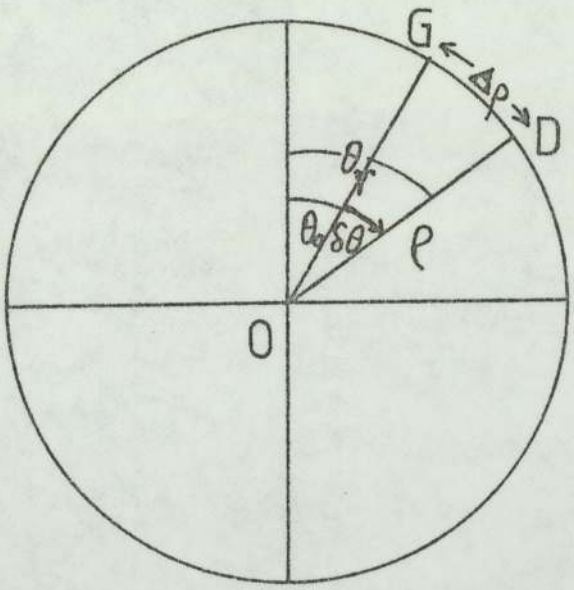

Figure (1.9) The **angular** difference $\delta\theta = \theta_r - \theta_o$ between the angles of rotation of the image relative to the object for radial heights r and zero. Note that $\delta\theta$ represents the spiral distortion $(\Delta\rho/\rho)_{sp}$ where the Gaussian image point is displaced to point D. O is the centre of the image.

The effect of spiral distortion on the image of an object such as a wire is shown in figure (1.10); the optical axis of the image is at O; in this figure the image rotation is anti-clockwise. The spiral distortion causes the Gaussian point G,

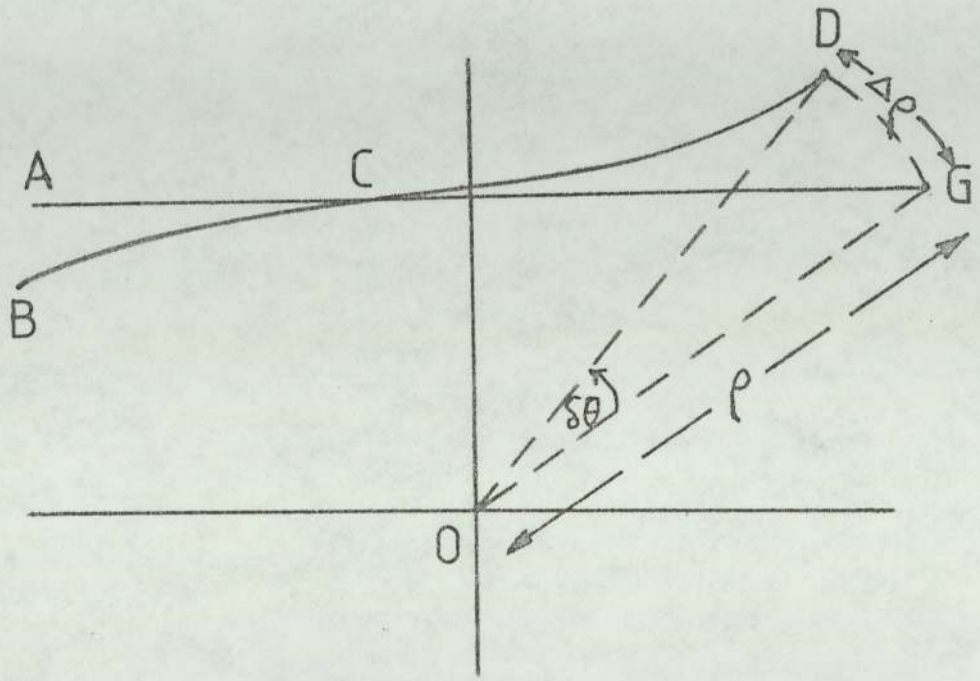

Figure (1.10) Gaussian image AG of a straight edge and the corresponding image (curve BCD) in the presence of spiral distortion. Note: G is the Gaussian image point which is moved to D by spiral distortion. The centre of the image (optical axis) is at O.

shown in figure (1.10), to be displaced to the point D, i.e. by an angle $\delta\theta$ subtended at the centre (O) of the image. Note: If the lens current is reversed, the image rotation changes sign and so does the spiral distortion.

It might be thought that spiral distortion could easily be corrected by arranging the current in a subsequent projector

lens to produce an image rotation and hence a spiral distortion in the opposite direction, so as to cancel the spiral distortion of the preceding lenses. This is, however, not an easy matter to arrange. Marai and Mulvey (1977) and Lambrakis et.al. (1977) have shown that spiral distortion is surprisingly difficult to correct in this way especially if conventional twin polepiece lenses are employed. Their work will be reviewed in section 1.2.4.

1.2.1.3 THE EFFECT OF LENS SCALING ON DISTORTION

The coefficient D_{sp} has dimensions $\left[L^{-2}\right]$. From this we can infer that if we scale up a projector lens by a factor n, D_{sp} becomes (D_{sp}/n^2). The radial height r will then be scaled linearly to (rn) in the scaled up lens. Thus the image distortion

$$(\Delta\rho/\rho)_{sp} = \left(\frac{D_{sp}}{n^2}\right)(rn)^2 = D_{sp}r^2$$

is not affected. The same applies to radial distortion. On the other hand the magnification, which is inversely proportional to the focal length, will be reduced by a factor n for a given projection distance L since the focal length scales linearly with n. In fact, the projection distance L by itself does not affect distortion since α_p remains the same when ρ and $\Delta\rho$ are scaled up to $(n\rho)$ and $(n\Delta\rho)$ respectively, as shown in figure (1.11). These scaling rules are useful in considering the design of high voltage systems.

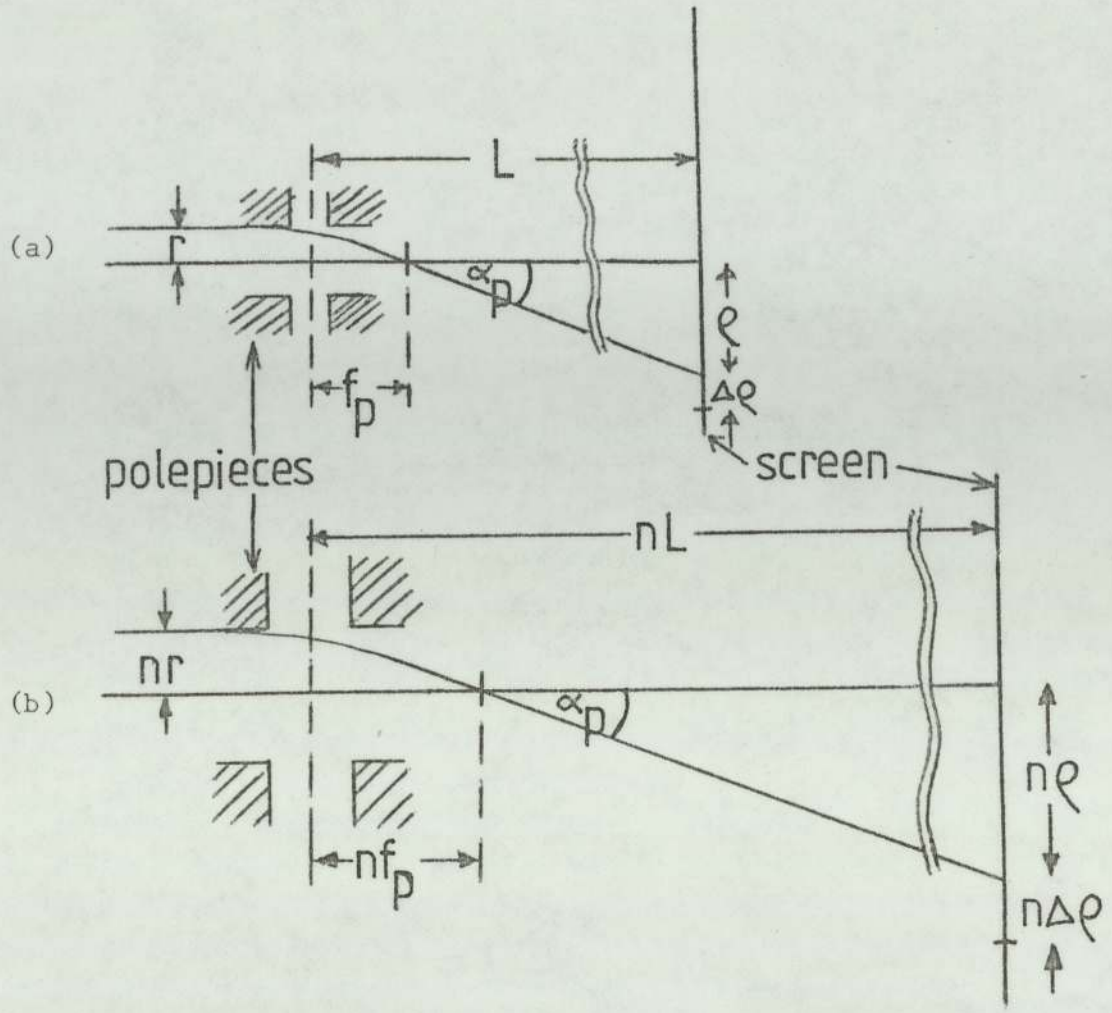

Figure (1.11) The scaling up of a projector lens by a factor n from (a) to (b) in which r, f_p, ρ and $\Delta\rho$ are scaled to (nr), (nf_p), ($n\rho$) and ($n\Delta\rho$) respectively. Note that (i) α_p does not change (ii) L does not affect the scaling procedure because ($\Delta\rho/\rho$) is unaltered.

1.2.1.4 THE QUALITY FACTOR (Q) OF A LENS

The distortion coefficients D_{rad} and D_{sp} are not, of themselves, a sufficient guide to the distortion that will actually occur in an image. For example, in a weak lens the spiral distortion in the image is large, in spite of the fact that D_{sp}

is negligibly small. Image distortion is, in fact, closely bound up with the refractive power of the lens. This is illustrated in figure (1.12). Here, an incident ray of height r, parallel to the optical axis, passes through a final projector lens and strikes the screen at an off axis distance ρ.

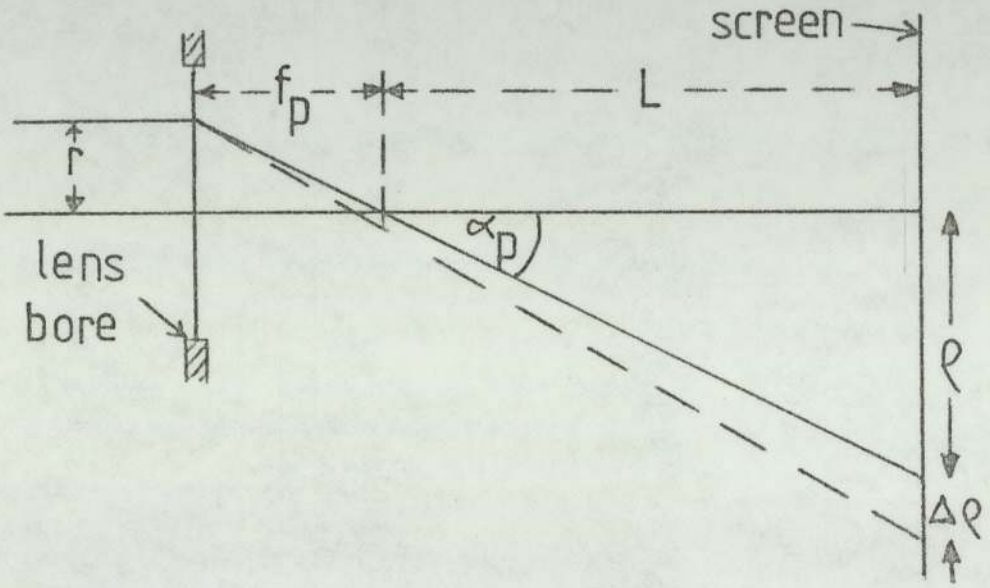

Figure (1.12) Electron trajectories through a final projector lens producing a distorted projected image on a viewing screen.

The radial distortion $(\Delta\rho/\rho)_{rad}$ is given by equation (1.2) as

$$(\Delta\rho/\rho)_{rad} = D_{rad} r^2$$

From figure (1.11)

$$r = \rho f_p / L \quad \ldots\ldots\ldots\ldots\ldots\ldots\ldots\ldots\ldots\ldots\ldots\ldots (1.6)$$

where ρ is the off-axis distance of the projected image on the screen, f_p is the focal length of the final projector lens and L is the projection distance. Hence the radial distortion becomes

$$(\Delta\rho/\rho)_{rad} = D_{rad}(\rho f_p/L)^2$$

$$= (D_{rad} f_p^2)(\rho/L)^2$$

$$= Q^2_{rad} \tan^2\alpha_p \quad \ldots\ldots\ldots\ldots\ldots\ldots (1.7)$$

where $Q_{rad} = D^{\frac{1}{2}}_{rad} f_p$ $\ldots\ldots\ldots\ldots\ldots\ldots\ldots\ldots (1.8)$

and α_p is the projection semi-angle.

Similarly, the spiral distortion can be written as

$$(\Delta\rho/\rho)_{sp} = Q^2_{sp} \tan^2\alpha_p \quad \ldots\ldots\ldots\ldots\ldots\ldots (1.9)$$

where $Q_{sp} = D^{\frac{1}{2}}_{sp} f_p$ $\ldots\ldots\ldots\ldots\ldots\ldots\ldots\ldots\ldots (1.10)$

Marai and Mulvey (1977) have proposed the use of the dimensionless 'quality factors' Q_{rad} and Q_{sp} of the lens as a measure of projector lens performance. The reason for the introduction of these dimensionless quantities Q_{rad} and Q_{sp} is that the image distortions $(\Delta\rho/\rho)_{rad}$ and $(\Delta\rho/\rho)_{sp}$ do not necessarily tend to zero when the coefficients D_{rad} and D_{sp} approach zero. For example, at a very low lens excitation D_{sp} tends to zero whereas f_p tends to infinity. This causes $(\Delta\rho/\rho)_{sp}$ and Q_{sp} to tend to infinity. This example explains the presence of very high radial and spiral distortion in electron micrographs taken at weak excitations. Mulvey (1980) has studied the quality factor Q_{sp} of various types of magnetic electron projector lenses and found that all conventional double-polepiece lenses have a minimum value of $Q_{sp} = 1.0$ whereas the best single-polepiece lens gives a

minimum value of 0.75. Smaller values of Q_{rad} and Q_{sp} indicate a better lens.

In a search for lens shapes giving minimum aberration, Alshwaikh and Mulvey (1977) have investigated the quality factors, Q_{rad} and Q_{sp}, for a hemispherical single-polepiece lens at different relative excitations NI/NI_o. Their results are shown in figure (1.13); here NI denotes lens excitation in ampere-turns and NI_o is the excitation when the lens is operated at its minimum focal length, i.e. at maximum magnification M_o.

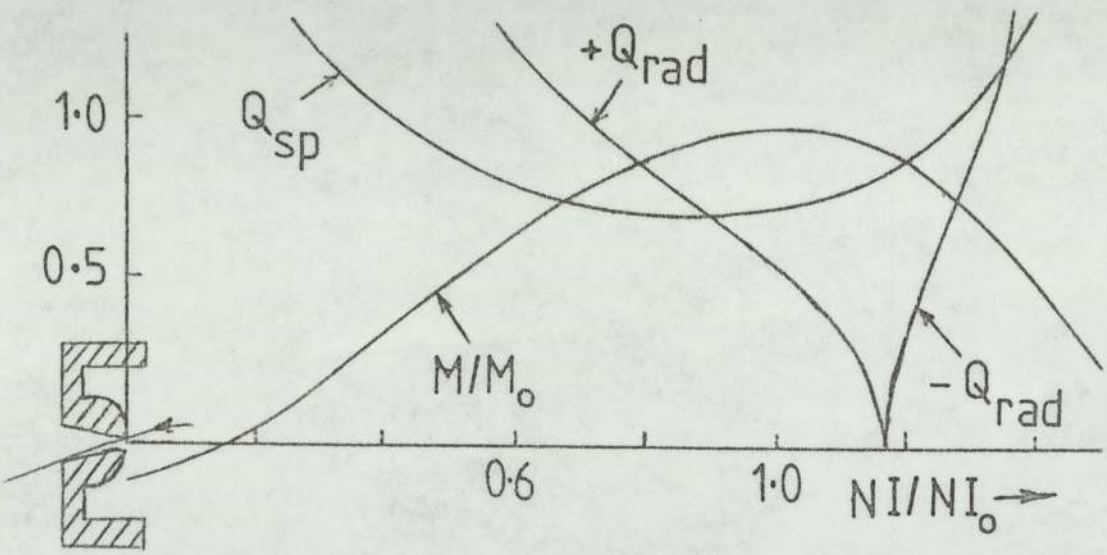

Figure (1.13) Quality factors Q_{rad} and Q_{sp} against the relative excitation NI/NI_o; the relative magnification M/M_o versus NI/NI_o for a hemispherical single-polepiece lens (Alshwaikh and Mulvey, 1977).

The figure also shows the relative magnification M/M_o against NI/NI_o where M is the magnification of the projector lens. The important conclusion from their computational work is that the hemispherical single-polepiece lens produces a lower spiral distortion than any other known lens (minimum $Q_{sp} \simeq 0.7$ when

electrons enter the lens with the snout facing the incoming beam). Since image distortion depends on Q_{sp}^2, it follows that such a single-polepiece lens will produce only half the distortion that would be produced by a conventional double-polepiece projector lens ($Q_{sp} = 1.0$) at the same projection angle. At the tolerable limit of spiral distortion (2%) the projection semi-angle for a conventional lens is 8^{o}. With a single-polepiece lens this can be increased to 11.4^{o}, a useful increase. It should also be noticed from figure (1.13) that in the excitation range NI/NI_o from 0.6 to 1.2 the Q_{sp} value changes only slowly with excitation whereas Q_{rad} changes rapidly. This characteristic of the single-polepiece lens has turned out to be of great significance in the production of distortion-free images at large semi-angles. The reason for this is that it is useful to be able to introduce large amounts of pin-cushion distortion into the image without substantially affecting the amount of spiral distortion. In this way any barrel distortion produced by the preceding corrector lens can be compensated, as discussed in more detail in Chapters (6) and (7).

This possibility of correcting the spiral and radial distortion independently forms the basis of the present method. The method thus differs considerably from methods previously proposed and exploits to the full the unusual electron-optical properties of single polepiece magnetic lenses.

1.2.2 THE MAGNETIC LENS

1.2.2.1 THE CONVENTIONAL DOUBLE-POLEPIECE LENS

It has already been mentioned that conventional double-polepiece lenses do not lend themselves for the correction of

image distortion, because their distortion coefficients do not vary significantly with lens geometry. In addition the restricted shape of the polepieces makes it difficult to accommodate wide angle beams ($\alpha_p > 10^\circ$) in a corrector system. Furthermore the large size of the exciting coil makes it difficult to fit a corrector lens close enough to the final projector. Figure (1.14) shows a typical conventional double-polepiece lens in which the iron core is bored to a diameter D_b to allow the electron beam to pass through the lens.

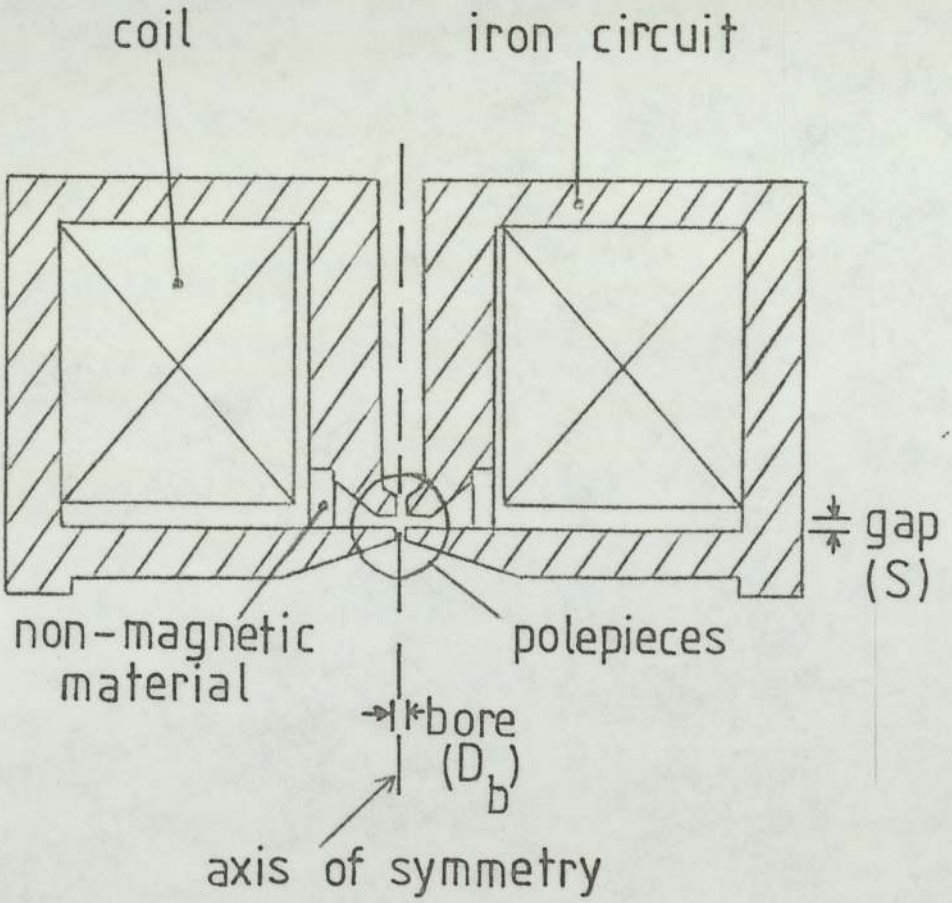

Figure (1.14) Schematic diagram of a typical conventional double-polepiece lens.

The two iron polepieces, separated by a gap S, concentrate the magnetic flux in this region thereby produce a high peak magnetic field and a narrow half-width; this creates a short focal length and low aberration coefficients.

The design of conventional lenses is well understood. Such lenses have probably reached technical perfection. The subject has been dealt with comprehensively by Mulvey (1953), Durandeau and Fert (1957), and Fert and Durandeau (1967). Lens design can be approached in two ways. Either the designer considers an initial lens design and calculates the optical characteristics directly changing the geometrical and electrical parameters if necessary in the light of the calculated results. Alternatively, one starts with a set of performance requirements and designs a lens, by successive approximations, to meet them.

1.2.2.2 THE MINIATURE LENS

Although conventional lenses are dominant in commercial electron microscopes, yet the large size of the high voltage microscope is a major disadvantage; among other things it usually necessitates the provision of a special building. The size of the polepieces, which are the important part of the lens, are small compared to that of the iron circuit as a whole. The magnetic field in the remainder of the iron should be reduced to a low value in order to reduce the unwanted magnetic fields in the axial region remote from the pole-gap. Consequently, large iron cross sections are used in conventional lenses. On the other hand, by operating the windings at an appreciably higher current density, the exciting coil can be made correspondingly smaller and most of the iron can be dispensed with.

For these reasons miniaturisation of the conventional lens is found to be highly desirable. Le Poole (1964) introduced the first iron-free miniature lens (a long thin solenoid) water-cooled and operated successfully at 8000 ampere-turns/cm.^{2}. Cooke and Duncumb (1968) have designed a miniature double-polepiece lens for the electron microscope microanalyser (EMMA). Mulvey and Newman (1972) built a miniature projector lens shown in figure (1.15). A current density of 6930 amps/cm.^{2} was obtained which evidently compares favourably with the 200 amps/cm.^{2} of the conventional lens.

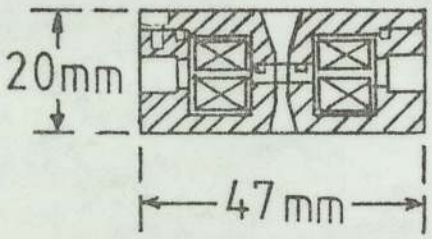

Figure (1.15) Miniature projector lens, designed by Mulvey and Newman (1972), for the 100 KV electron microscope. Minimum focal length 1.8 mm.; gap width 3 mm.; bore diameter 2 mm.; and excitation 4000 ampere-turns.

A disadvantage of a miniature lens is that the exciting coil consumes more electrical power than does the conventional lens, as shown in Appendix (4). Roughly speaking the power needed for a given excitation increases inversely with its axial length. However, an increase in the electrical power by a factor of 4 allows us to reduce the lens volume by about 50 times. The minimum permissible size of coil depends on the efficiency of the

cooling. Mulvey and his collaborators have investigated cooling of coils both by direct flowing water and by boiling. Juma and Mulvey (1975) have obtained a current density of 2000 amps/cm.^{2} using the flowing water cooling method; whilst Mahmoud, Muhammad and Mulvey (to be published) reached a current density of some 40 000 amps/cm.^{2} using the boiling water cooling method. Either method gives good results and comparable with those of superconducting lenses. Cooling by boiling is also briefly described in Appendix (4).

1.2.2.3 THE SINGLE-POLEPIECE LENS

Miniaturisation of the lens coils gives the designer greater freedom in positioning the lenses in the column. However, it is frequently necessary in a wide-angle corrector system to accommodate unusually wide beams. This is often not possible with double-polepiece lenses. Frequently a single-polepiece lens can be used to accommodate such beams without difficulty.

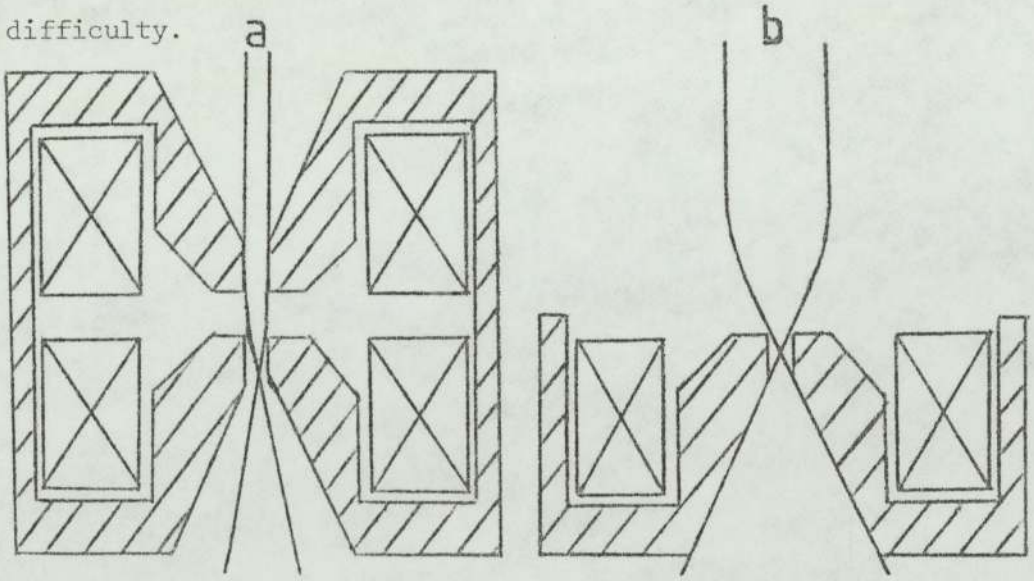

Figure (1.16) Cross-section of (a) a double-polepiece and (b) a single-polepiece lens. Notice the wide-beam accommodated by the single-polepiece lens.

Thus, if the double-polepiece lens of figure (1.16a) is cut in half we obtain two single-polepiece lenses (Mulvey, 1972) one of which is shown in figure (1.16b). A typical axial magnetic flux density distribution of a single-polepiece lens is shown in figure (1.16c).

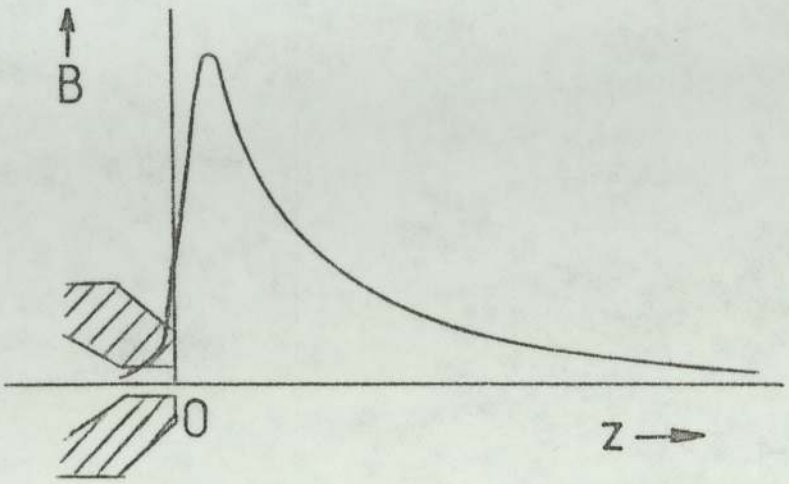

Figure (1.16c) The axial magnetic field B_z of a single-polepiece magnetic lens as a function of the axial distance z measured from the poleface.

The distribution is very assymetric and so its focal properties,including its aberrations, are sensitive to the direction of the incident electron beam. If the polepiece of the single-polepiece lens is designed carefully one can obtain a magnetic field distribution with a high peak value and small half-width, comparable in magnitude to those obtained with conventional double-polepiece lenses of small bore diameter and gap width. In a single-polepiece lens the diamter of the bore controls the degree of steepness of the rapidly rising part of the field distribution; the smaller the bore diameter, the more

steep this part of the field distribution will be (Juma and Mulvey, 1979). The axial height of the snout, or snorkel, may be chosen so as to allow the magnetic field distribution and hence its peak position to fall outside the lens structure. This is particularly important in an objective lens for specimen manipulation and collection of x-ray photons which are usually hindered in a conventional double-polepiece lens by the presence of the second polepiece.

The highly asymmetrical field distribution of the single-polepiece lens gives it two characteristic modes of operation. For a projector lens, if the polepiece faces the incoming electron beam (preferred direction) the image distortion will be lower than if the polepiece faces the screen (non-preferred direction) by a factor of about 2.5X. The projector focal length, however, does not depend on the direction of the beam. In the present investigation attention has been concentrated on the application of miniature single-polepiece lens to improved projector systems. The detailed design of such projector lenses are described in Chapters (4), (5) and (7).

1.2.3 PREVIOUS ATTEMPTS AT CORRECTING DISTORTION

All previous attempts to correct image distortion were mainly concerned with radial distortion only and for small projection semi-angles ($\leqslant 7^{\circ}$). To this end several authors have studied or devised two-lens projection systems aimed at correcting or at least minimising radial distortion in the image. Thus Hillier (1946) showed that it is possible to correct the radial distortion produced by the final projector lens by placing an additional lens of the same focal length in the back focal plane

of the projector, as shown in figure (1.17).

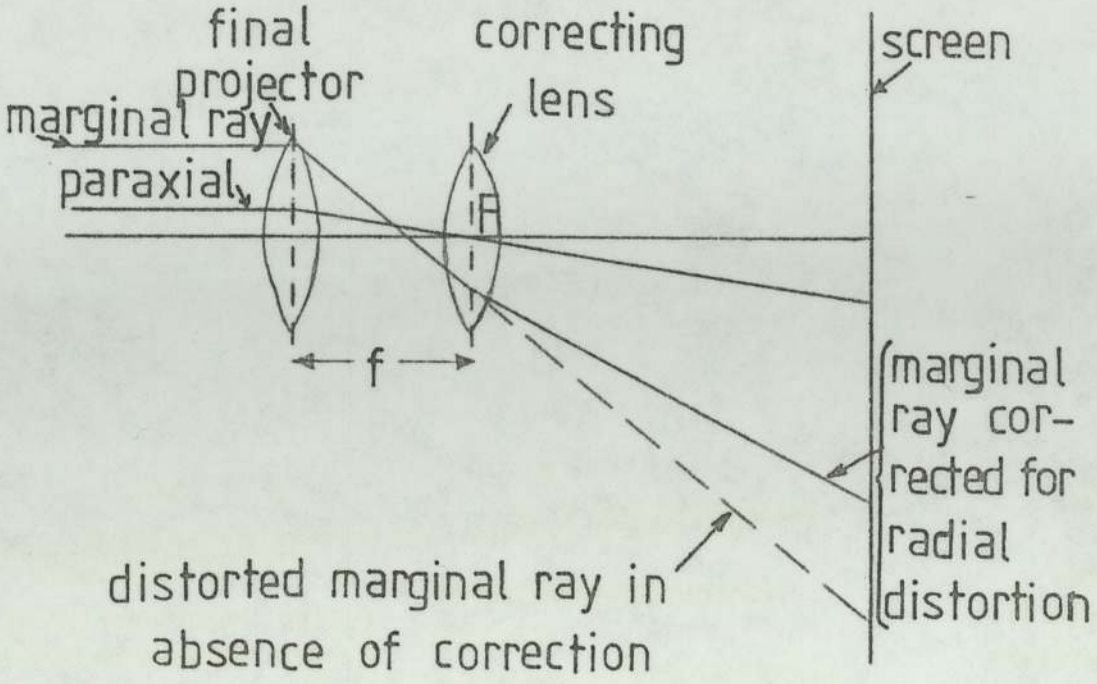

Figure (1.17) Schematic arrangement of Hillier's system for correcting radial distortion. A correcting lens of the same focal length as that of the projector is placed in the back focal plane (F) of the projector.

This correcting lens does not contribute to the refractive power of the projector system but serves to correct radial distortion. Unfortunately, in his practical realisation of this method Hillier employed a single coil to energise the two lens-gaps in series, so that the image rotation of each lens was in the same sense. This meant that the spiral distortion produced the lenses was additive. Thus in his arrangement, shown in figure (1.17), although radial distortion in the final image could be eliminated in this way spiral distortion was greatly increased.

No improvement in the projection semi-angle α_p was therefore possible since this was now restricted to some 6° by the effect of spiral distortion. This fact, combined with the other disadvantage, namely that the correcting lens contributed nothing to the total magnification prevented the method being used in practice.

In an alternative system proposed by Kynaston and Mulvey (1963) for correcting radial distortion at low magnification; pin-cushion distortion produced by the final projector lens is compensated by an appropriate amount of barrel distortion produced by an intermediate projector lens. This system cannot correct spiral distortion in practice since at low magnification the intermediate is essentially a weak lens. Thus no increase in projection semi-angle was possible. The experimental investigations were originally carried out on the two projector lenses of an AEI EM6 100 KV TEM. Electron trajectories through the intermediate lens are shown in figure (1.18a) and those through the two-lens system are shown in figure (1.18b). The maximum magnifications of the objective, intermediate and final projector lenses were 44, 14 and 200 times. Kynaston and Mulvey (1963) found that at a certain excitation of the intermediate lens the negative (barrel) distortion of the intermediate lens was always equal in magnitude to the positive (pin-cushion) distortion produced by the final projector lens whatever the excitation of the projector lens. This meant that no measurable radial distortion occurred over a wide range of projector excitation. In their experiments an overall magnification range of distortion-free magnification was obtained from 3000X down to 200X. However, at

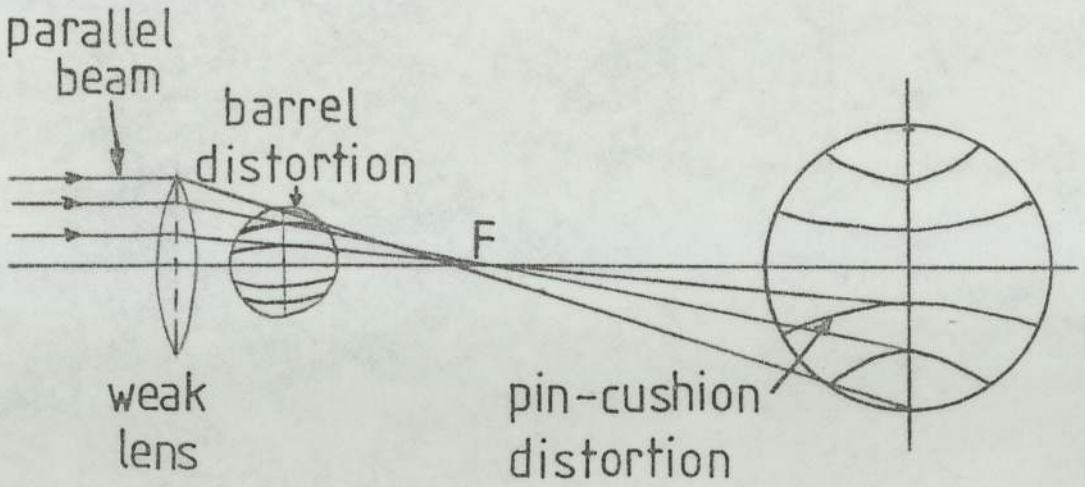

Figure (1.18a) Distortion produced by a weak intermediate lens; when image is formed before the focal plane F the distortion is barrel and when formed after F the distortion is pin-cushion.

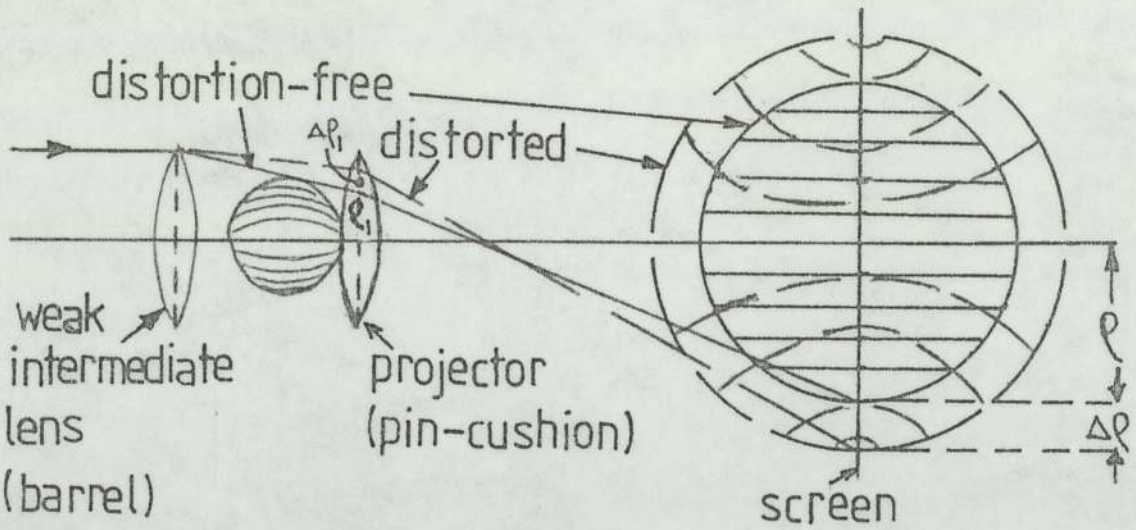

Figure (1.18b) Correction of radial distortion. Kynaston and Mulvey (1963) . Broken lines show the trajectories and pin-cushion distortion ($\Delta\rho / \rho$) of the final projector lens when the image from intermediate lens is distortion-free. Full lines show barrel distortion ($\Delta\rho_1 / \rho_1$) from intermediate lens as well as the corrected image on the screen.

magnifications less than about 900X, a limitation of the size of the image occurred on the fluorescent screen. In fact although no image distortion appeared at the lower magnifications the field of view of the specimen remained constant below a magnification of 900X. This was a consequence of the employment of a conventional projector lens in which it is difficult to maintain a projection semi-angle of 8^{o} at low magnification.

The important advantage of this method of correcting radial distortion is that it is not critically dependent on the focal lengths of intermediate lens and projector lens nor on their physical separation. Another useful feature is that the correction does not depend critically on the design of the final projector.

In order to adapt this sytem for the additional correction of spiral distortions, some way has to be found for replacing the weak intermediate lens by a strong intermediate lens which can then produce a large amount of spiral distortion for correction purposes, but at the same time allowing for the compensation of any radial distortion in the system.

The above attempts at correcting distortion by conventional double-polepiece lenses have therefore revealed some fundamental difficulties, namely, in correcting spiral distortion and in achieving large projection semi-angles. It is inherently easier with a single-polepiece lens, with its low Q_{sp} value, to obtain a larger semi-angle than with a double-polepiece lens since the absence of a polepiece on the entry side of the lens enables a wide beam to be employed, as previously shown in figure (1.16).

1.2.4 THE ROTATION-FREE PROJECTION SYSTEM

More recently, Juma and Mulvey (1974,1975 and 1978) improved the Hillier (1946) two-lens projection system by employing two miniature projector lenses in which each projector lens is energised separately with opposing currents so as to eliminate image rotation. This also results in the focal lengths being equal, regardless of lens current. From an operational point of view a rotation-free image is a great advantage to the operator especially when investigating specimens with strong crystallographic features. It is clearly inconvenient if the orientation of a selected area diffraction pattern cannot be readily correlated with the changing orientation of the image as the magnification is varied. Another advantage of the rotation-free system is that the image will always be free from chromatic change of rotation. A schematic diagram of Juma and Mulvey (1978) miniature rotation-free doublet is shown in figure (1.19). It consists of two identical lenses of conventional polepiece design. Each lens has a gap of S = 3 mm., and a bore D_b = 2 mm., a maximum excitation of 4000 ampere-turns, and with an inter-lens spacing L = 20 mm. The final projector lens of an AEI EM6 100 KV electron microscope was removed and replaced by the miniature rotation-free lens system. The standard lens in this instrument has a bore of 1.5 mm. and a gap of 3 mm. giving a minimum focal length of 1.8 mm. with an excitation of some 4000 ampere-turns. Thus if the lower lens of the rotation-free doublet alone were energised, the microscope would be expected to perform exactly in the same way as with a conventional lens. When operated as a rotation-free unit the minimum effective focal

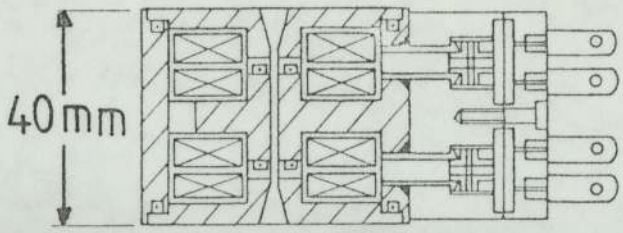

Figure (1.19) Schematic diagram of a 100 KV miniature rotation-free lens unit. [Juma and Mulvey (1978)] .

length would be reduced from 1.8 mm. to 0.18 mm.; a substantial gain in maximum magnification from 200X to 2000X. In this twin-lens system the contribution of each lens towards the final image distortion varies with lens excitation. At high magnification the off-axis distance of the ray in the first lens is relatively small and so this lens provides essentially distortion-free magnification. Any image distortion must therefore arise from the second lens and thus the image distortion has the same value as when this lens acts alone. This means, of course, that no correction of distortion is possible in this mode. In other words, at high magnification the unit behaves as a normal projector lens but with a much higher magnification. On the other hand, when the focal length of each lens is equal to the inter-lens spacing l radial distortion is completely corrected as in Hillier's system. Unfortunately, in this design α_p is restricted to 3^o; this is caused by the smallness of the lens bores (D_b = 2 mm.). This restricted image size, however, can be increased from approximately 4 cm. in diameter to the standard plate diameter 10 cm. by increasing the lens bore from 2mm. to

5 mm. at the expense of increasing the minimum focal length to 2.48 mm. and hence decreasing the maximum magnification from 2000X to 1060X which is still a relatively high magnification. Unfortunately, although correction of radial distortion at this low magnification (20X) is achieved, spiral distortion is not completely corrected even in the rotation-free mode (Marai and Mulvey, 1977) and would amount to about 3% at the edge of the image when $\alpha_p = 7^o$.

It seems therefore that rotation-free projection systems allow radial distortion to be eliminated at low magnifications whereas spiral distortion cannot in general be eliminated. It does seem possible to obtain a useful reduction of the spiral distortion of the Hillier correction system by operating in the rotation-free mode rather than the non-rotation-free mode used by Hillier. On the other hand, it seems that even in the rotation-free mode the image distortion is not significantly less than that of a well designed conventional projector lens and certainly not as good as a well designed single-polepiece projector lens.

1.2.5 THE CORRECTION OF SPIRAL DISTORTION

It seems, therefore, that the rotation-free mode is not very promising for the correction of spiral distortion. It therefore seemed more useful to investigate in more detail the non-rotation-free mode using two miniature single-polepiece lenses as suggested previously by Mulvey (1976) and experimentally investigated by Lambrakis, Marai and Mulvey (1977). Before discussing the principle of correcting spiral distortion we will mention some important parameters in a wide-angle correction

system. The aberrations of a projector lens change appreciably as the projector conjugates are varied. In addition the magnification M_{corr} of the intermediate (corrector) lens has an important influence on the amount of correction that it can contribute for the correction of the distortion produced by the projector itself.

In a two-lens system, the distortion coefficients of each lens depend on the position of the conjugate points of each lens. The distortion coefficients D_{rad} and D_{sp} are usually defined and calculated for electrons entering the projector lens parallel to the electron-optical axis; in this case the conjugate ratio

$$m = |v/u| \quad \ldots\ldots\ldots\ldots\ldots\ldots\ldots\ldots\ldots\ldots\ldots\ldots (1.11)$$

is zero, as shown in figure (1.20), where u and v are the object and image distances from the thin lens. In general the aberrations of a lens are smaller for zero conjugate ratio than for finite conjugates. Figure (1.20) illustrates the effect of finite conjugates for a thin lens.

Thus a parallel ray ($u = -\infty$) entering the lens passes through the back focal plane on its way to the screen gives rise to an image with a coefficient of spiral distortion D_{sp}. A ray entering the lens from a distance (-u) from the centre of the lens crosses the optical axis at a distance v give rise to an image of coefficent of spiral distortion D^{*}_{sp}. In general as u becomes smaller the aberrations of the lens, including the spiral distortion coefficient D_{sp} increase rapidly. For example, for equal conjugates (i.e. u = v) the distortion coefficient might

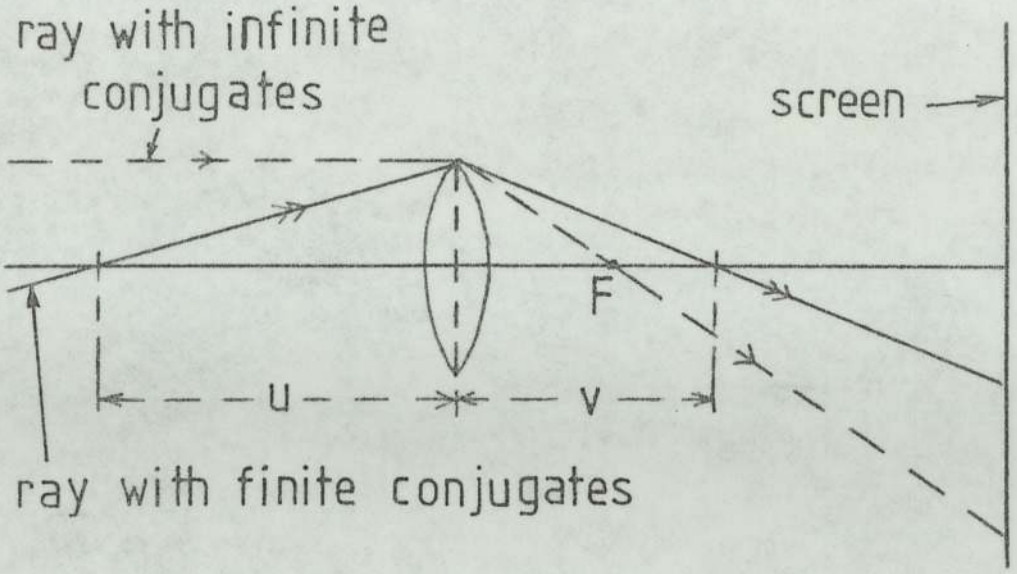

Figure (1.20) Ray with finite conjugate distances u and v through a thin lens shown in solid lines; and a ray with infinite conjugates.

well increase by a factor of two or three. This effect clearly complicates the design of a correcting system since in practice it is necessary to place the correcting lens close to the lens to be corrected. It is therefore desirable to operate the lens to be corrected at a value of m as small as possible from the point of view of minimising the aberration to be corrected. Alshwaikh (1979) has shown that the enhanced spiral distortion coefficient D^{*}_{sp} is related to the coefficient D_{sp} for infinite conjugates by the following approximate relation

$$D^{*}_{sp}/D_{sp} \simeq 1 + 1.37\ m + 1.28\ m^2 \quad \ldots\ldots\ldots\ldots (1.12)$$

which is further illustrated in figure (1.21). An analogous expression

$$D^{*}_{rad}/D_{rad} \simeq 1 + 1.37m + 1.28m^2 \quad \ldots\ldots\ldots\ldots\ldots\ldots (1.13)$$

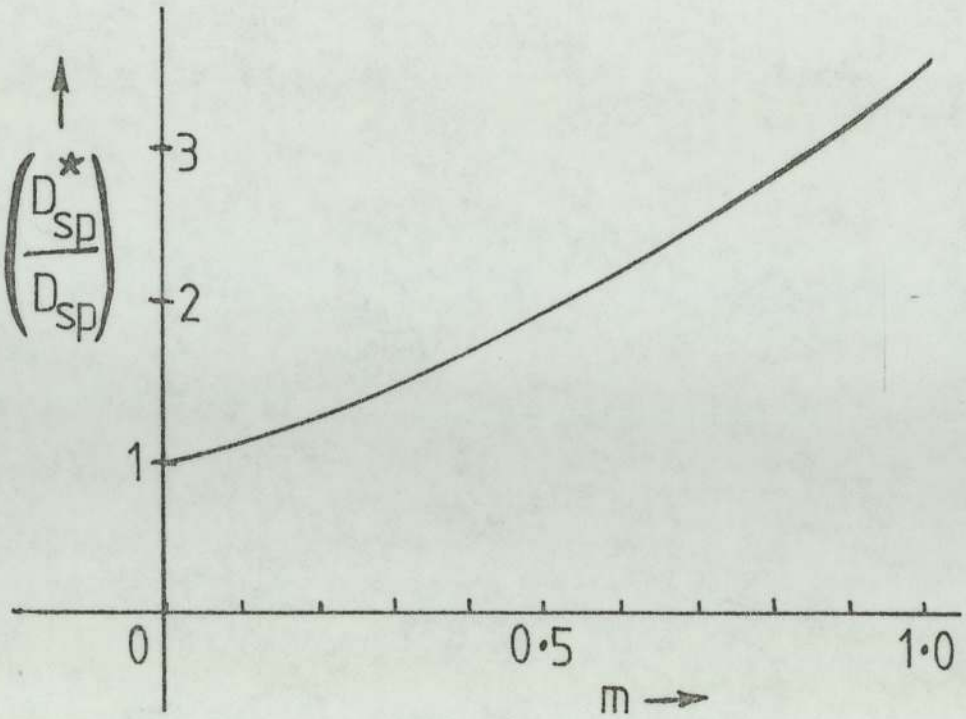

Figure (1.21) Ratio of the coefficients of spiral distortion (D^*_{sp}/D_{sp}) for finite and infinite conjugates as a function of the conjugate ratio ($m = |v/u|$).

holds for radial distortion.

The other important factor that influences the correction of spiral distortion is the magnification M_{corr} of the corrector lens which precedes the final projector lens. The spiral distortion produced by the corrector lens is, unfortunately, reduced at the viewing screen by a factor M^2_{corr} where M_{corr} is the effective magnification provided by the corrector lens. A convenient way of defining and measuring M_{corr} is to measure the magnification of the microscope at the final screen (a) with the corrector lens on (M_1) and (b) with the corrector lens off (M_2). M_{corr} is then given by

$$M_{corr} = M_1/M_2 = \frac{\rho_t}{\rho_p} \quad \ldots\ldots\ldots\ldots\ldots\ldots\ldots\ldots\ldots\ldots (1.14)$$

This is illustrated in figure (1.22) for thin lenses, where ρ_t and ρ_p denote the radial heights of the final image on the

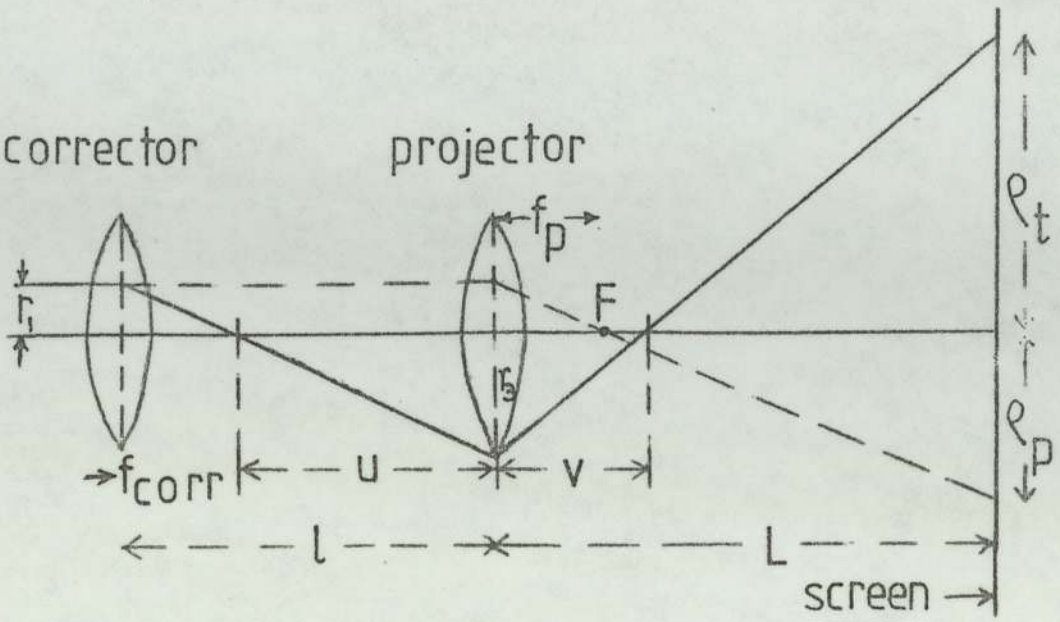

Figure (1.22) Ray trajectories through a thin lens optical system. Solid lines show the ray path for both lenses being energised; dashed lines represent the ray path with only the final projector lens excited.

fluorescent screen with and without the corrector lens being excited respectively; r_1 and r_3 are the radial heights of the ray in the corrector and final projector respectively; f_p and f_{corr} are the focal lengths of the final projector and corrector respectively; l is the lens separation; and L is the projection distance between the final projector lens and the screen.

In order to illustrate the relationship between the conjugate ratio m and the magnification M_{corr} of the corrector we need to calculate M_{corr} from figure (1.22). When the corrector lens is energised

$$M_1 = \frac{\rho_t}{r_1} = \frac{\rho_t}{r_3} \cdot \frac{r_3}{r_1} = \left(\frac{L-v}{v}\right)\left(\frac{u}{f}\right) \quad \text{.....(1.15)}$$

and when the projector lens is energised **alone**

$$M_2 = \frac{\rho_p}{r_1} = \frac{L - f_p}{f_p} \quad \text{.....(1.16)}$$

and hence

$$M_{corr} = \left(\frac{L-v}{v}\right)\left(\frac{u}{f_{corr}}\right)\left(\frac{f_p}{L-f_p}\right) \quad \text{.....(1.17)}$$

Since $L \gg f_p$, $m = |v/u|$, $v = \frac{uf_p}{u+f_p}$ and $u = l - f_{corr}$

$$M_{corr} \simeq \frac{1}{m}\left(\frac{f_p}{f_{corr}}\right)\left[1 - \frac{f_p(l-f_{corr})}{L(l-f_{corr}+f_p)}\right] \quad \text{.....(1.18)}$$

Equation (1.18) can usually be written in the simplified form

$$M_{corr} \propto \frac{1}{m}\left(\frac{f_p}{f_{corr}}\right) \quad \text{.....(1.19)}$$

if $l \gg f_{corr}$ and $l \gg f_p$.

From the point of view of minimising the distortion of the final projector lens to be corrected it is desirable to keep m as small as possible. At the same time, although it would be desirable for M_{corr} to be large so that the correcting lens can make a contribution to the magnification, an upper limit is set to M_{corr} to avoid the need to generate excessive spiral distortion in the corrector lens. The two requirements of small m and not too large M_{corr} are conflicting. Hence from equation (1.19) it therefore seems desirable to make the ratio (f_p/f_{corr}) as small as

possible so as to make m small and M_{corr} to the required value suitable for correction of sprial distortion. Thus the corrector focal length should be as large as possible consistent with obtaining a large amount of spiral distortion. In practice a value of M_{corr} of about 3X seems feasible with a single polepiece corrector lens. Higher values of M_{corr} will lead to excessive excitations being required for correcting the spiral distortion of the projector.

The correction of spiral distortion on these lines was first investigated by Lambrakis et.al. (1977) in an experimental arrangement making use of a 30 KV 'Intercol' electron-optical bench. The investigation was concerned with the simultaneous correction of radial and spiral distortion. To achieve the correction of radial distortion it was decided to operate each lens at an excitation where radial distortion was negligible, i.e. near the point of minimum focal length in the first focal zone for the projector and in the first or second focal zone for the corrector. This condition, in fact,imposed severe restrictions on the design. For example, the final projector and the preceding (correcting) lens were restricted to equal and opposite excitation parameters $NI/V_r^{\frac{1}{2}} = 15.5$ for which $Q_{rad} = 0$, as shown in figure (1.23). Unfortunately, the distortion produced by the correction lens at this excitation is just less than three times that produced by the projector. This in turn means that M_{corr} cannot be less than $\sqrt{3}$, so that according to equation (1. 19) $m = 1/\sqrt{3} = 0.58$. This will increaæ the spiral distortion in the projector lens by a factor of 2.2X, so that a revised value for M_{corr} would be about unity, a situation similar

to that of Hillier's (1946) system. Hence the method cannot work with the corrector in the first focal zone.

If the corrector is operated at the point of zero radial distortion in the second focal zone ($NI/V_r^{\frac{1}{2}} \simeq 34$), see figure (5.7), these difficulties can be overcome. At this higher excitation the corrector can produce a much higher amount of spiral distortion , in fact about twenty times as much as that produced by the projector for the same projection semi-angle. This means that M_{corr} can be in the region of three or four times. At the same time a more favourable value of $m \simeq 0.3$ can be achieved. In addition, because of the larger value of M_{corr} the distance between the corrector and projector can be increased and so problems of field cancellation* become less serious. However it should be noted that the system is no longer rotation-free.

The essential part of this experimental correcting system is shown in figure (1.23). The system consists of two miniature single-polepiece lenses arranged with their polepieces facing each other in such a way that the electrons enter the corrector lens from the non-preferred direction to yield high distortion, and enter the final projector lens from the preferred direction to keep the projector distortion to a minimum as pointed out in section 1.2.2.3.

---

* Note: The axial magnetic fields produced by the corrector and projector polepiece of opposite polarity will tend to cancel if the polepieces are too close to each other.

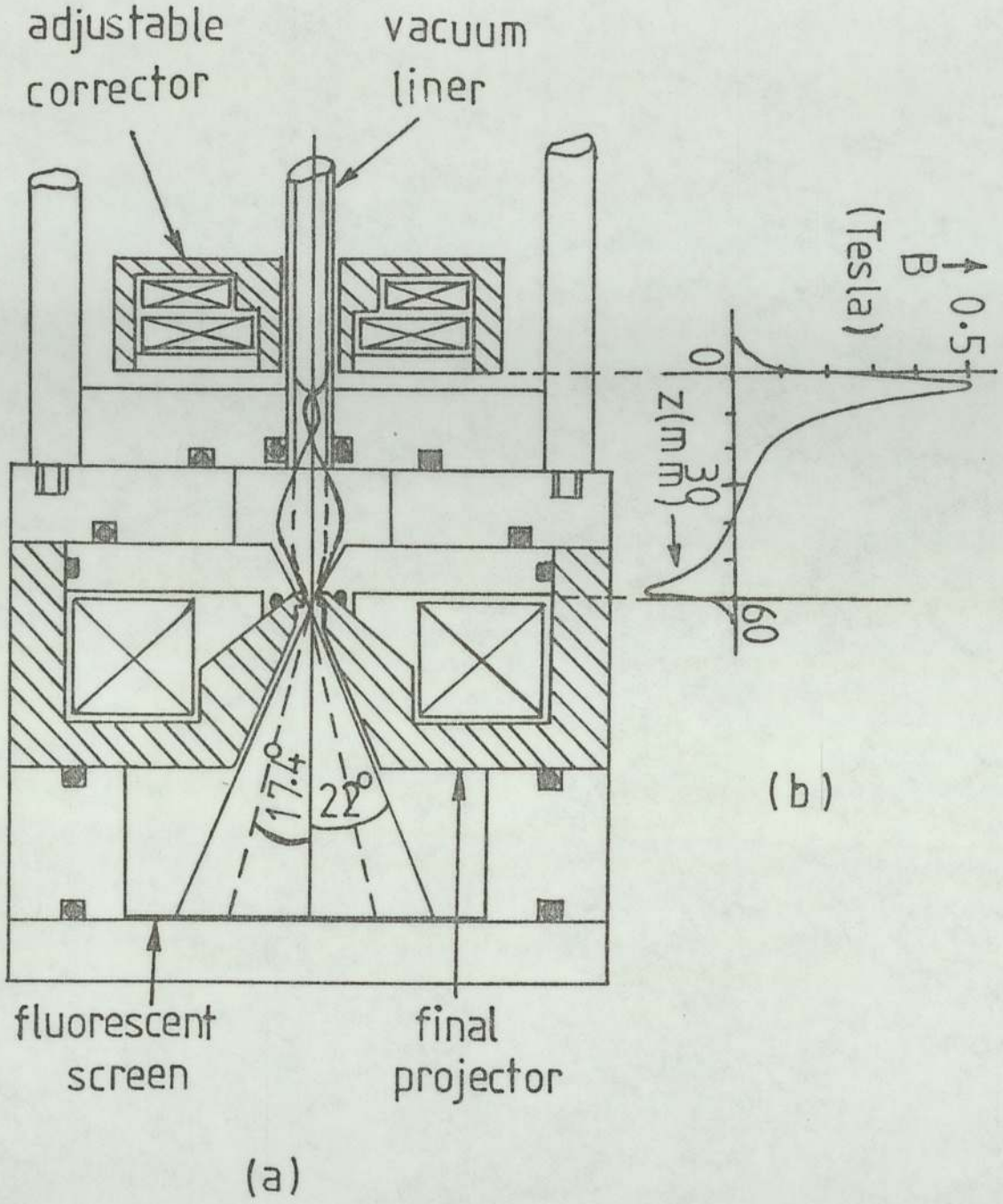

Figure (1.23) (a) Experimental arrangement of the two single-polepiece projection system for the correction of spiral distortion. [Lambrakis, Marai and Mulvey (1977)]. Also shown are the electron trajectories through the system. (b) The combined axial magnetic field distribution of the system for a projector excitation $NI/V_r^{\frac{1}{2}} = 15.5$ and corrector excitation $NI/V_r^{\frac{1}{2}} = 34$.

Since the lens excitations are determined in advance by the necessity not to produce radial distortion, and at the same time a specific value of M_{corr} must be provided, taking into account the effect of the finite conjugates of the projector lens, it is difficult to predict the correct separation of the opposing polepieces. This is made especially difficult since field cancellation effects will alter the axial field distribution of the lens combination as the lens separation is varied. For these reasons it was necessary to provide a means of altering the lens separation under vacuum. A vacuum liner tube of inside diameter 5 mm. was therefore inserted through the 8 mm. bore of the corrector; this allowed the corrector to slide up and down the tube so as to enable the polepiece separation to be changed under vacuum. The single-polepiece projector lens had a bore diameter of 2 mm. and was capable of projecting a wide-angle image ($\alpha_p = 22^\circ$) onto the transmission fluorescent screen. The corresponding projection distance L was 56 mm., and the image could be photographed by external photography.

The coils of the two single-polepiece lenses were excited with opposing but unequal ampere-turns typically +2725 and -6000 A-T as shown in the combined axial magnetic field distribution of figure (1.23b). Even at the comparatively large snout separation of 60 mm., about 25% the ampere-turns applied were lost by field cancellation. Actual experiment confirmed that when the corrector lens was operated in the second focal zone at $NI/V_r^{\frac{1}{2}} = 34$, (equivalent to $NI/V_r^{\frac{1}{2}} = 31$ when field cancellation is taken into account), radial distortion was negligible. Adjustment of the

position of the corrector lens showed that a magnification $M_{corr} \simeq 3.4$ could be achieved. The projector lens was operated at an excitation $NI/V_r^{\frac{1}{2}} = 15.5$ at which its radial distortion was also negligible and its spiral distortion was at a minimum. The overall magnification of the two lens system was 15X. In a standard EM6 TEM of projection distance 36 cm. this would be about 100X. The focal lengths of the projector and corrector lenses at the excitation parameters quoted above were about 10 mm. each.

As this was a fairly crude experimental arrangement, the quality of the external photographs was not of the standard obtainable with internal photography but useful conclusions can nevertheless be drawn. Thus figure (1.24) shows two projected images obtained with this system. In figure (1.24a) the corrector lens was switched off. Because of the presence of the vacuum liner tube the projection semi-angle is restricted to $\alpha_p = 17.4^\circ$. The spiral distortion at the edge of the image is about 7%. At a projection semi-angle of 22° this corresponds to a spiral distortion of 12%. There is no radial distortion. Figure (1.24b) shows the image with the corrector lens energised and the lens separation correctly adjusted. There is no radial distortion and spiral distortion is only just visible at the edge of the image ($\alpha_p = 22^\circ$). Because of the lack of sharpness of the image and the low amount of distortion it is difficult to measure accurately but it is estimated as being less than 3%. Such a lens-system fitted in a standard TEM (L = 36 cm.) would produce an image 29 cm. in diameter.

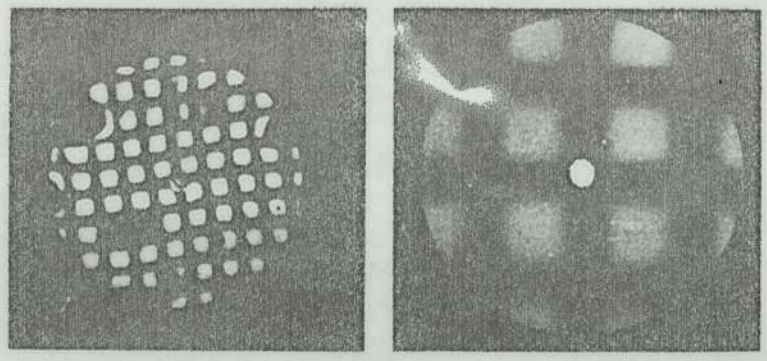

(a) (b)

Figure (1.24) (a) Corrector lens switched off. Spiral distortion with restricted field of view ($\alpha_p = 17.4^o$) 7% (Corresponds to 12% at full field of view). (b) Corrected image with corrector lens in the second focal zone. M_{corr} = 3.4X. Spiral distortion at full field of view ($\alpha_p = 22^o$) less than 3%.

The experimental results of Lambrakis et. al. (1977) have thus shown that it is not possible to obtain satisfactory correction of spiral distortion with the correcting lens operating in the rotation-free mode even with a single-polepiece correcting lens. They were, however, able to correct the spiral distortion when the correcting lens is operated in its second focal zone. However, the design has many practical disadvantages, especially the need to be able to adjust the separation of the lenses under vacuum and the severe interaction between the two lens fields. In adjusting the system there are three variables

mutually influencing each other, namely, the excitation of each lens and the lens separation. It would be desirable to eliminate one of these if possible. Furthermore it is, of course, very desirable to adapt the system for use in a commercial electron microscope.

In the present investigation we are therefore concerned with the design of a distortion-free projection system suitable eventually for high voltage electron microscopes. An AEI EM6 100 KV TEM was modified for this purpose using miniature single-polepiece lenses. The design and characteristics of the corrector lens are described in Chapter (5). The projector lens was originally designed by Newman (1976) but we found it necessary to modify the polepiece design considerably as indicated in Chapter (6). A later development was to increase the projection semi-angle α_p still further from 22° to 30°. The correction of spiral distortion with the new system is described in Chapters (6) and (7).

The improved corrector lens, in fact, operates in the first focal zone, at the high excitation end of this zone. This necessitates an independent correction of radial distortion. The system finally developed has been found to be insensitive to lens separation and can operate successfully with projection semi-angles of up to 30°. The design of the corrector lens and indeed the complete lens-system is greatly facilitated by the use of a computer as described in the next section.

1.3 COMPUTATION OF THE PROPERTIES OF ELECTRON LENSES AND ELECTRON LENS SYSTEMS

Electron-optical computations for magnetic lenses or lens-systems are valuable for two reasons. Firstly, the lens or lens-system can be optimized before the manufacturing process begins, thus saving time and cost. Secondly, a computation of the magnetic and optical properties of the lens or lens system provides a means of checking the correct working of the experimental system. Useful properties to be calculated include the magnetic flux density distributions, electron trajectories, focal properties and aberration coefficients. Finally, image simulation can be carried out in the computer, which can be helpful in interpreting the observed images.

1.3.1 THE AXIAL MAGNETIC FLUX DENSITY DISTRIBUTION

The axial magnetic flux density distribution is the starting point for most calculations of the electron-optical properties of a lens. The vector potential distribution and the magnetic flux density distribution throughout the magnetic circuit and coil windings of both saturated and unsaturated rotationally symmetric magnetic lenses can be calculated using readily available computer programs such as that written by Munro (1975). The computation makes use of the finite element method and establishes equations relating the potentials at adjacent mesh points. The resulting matrix is then inverted, yielding the vector potential at all mesh points inside the chosen boundary.

In order to prepare the data, an accurate diagram of the

lens cross-section is made and a mesh distribution in both the z and r directions is imposed, taking into consideration the position of the iron circuit and the exciting coil. It should be mentioned that the results are strongly influenced by the choice of the boundary of the computed mesh system where the vector potential A must be set to zero.

Other important data are the current density in the coil and the relative permeability of the iron.

If iron saturation occurs, the permeability of the iron circuit is no longer high and constant but depends rather upon the magnetic flux density distribution B at each point of the iron circuit. In the "saturation" program (M13 program) this is allowed for; the corresponding B-H curve (Table 1.2) is then supplied as data and the flux density in the iron is established by an iterative method. This program was found particularly useful for the determination of the field distribution of combined corrector and projector lenses.

B (Tesla)	H (A/m)	B (Tesla)	H (A/m)	B (Tesla)	H (A/m)	B (Tesla)	H (A/m)
1.300	270	1.560	1000	1.840	10000	2.025	30000
1.400	320	1.600	1500	1.905	15000	2.045	35000
1.450	400	1.630	2000	1.960	20000	2.055	40000
1.520	700	1.730	5000	2.000	25000		

Table (1.2) B-H values for soft iron

1.3.2 THE FOCAL PROPERTIES AND DISTORTION COEFFICIENTS OF MAGNETIC LENSES

Once the axial flux density distribtion of a lens is known its focal properties can be calculated. At the start of this investigation only one program was available for calculating the properties of magnetic projector lenses (Marai 1977). This program was called D-DISTORTION. This program calculated the electron trajectory, projector focal length and the distortion coefficients D_{rad} and D_{sp} for a single lens as a function of the lens excitation parameter $NI/V_r^{\frac{1}{2}}$. It was not possible, for example, to calculate the focal properties of a double lens system satisfactorily with this program. There were also a number of additonal shortcomings, the ill-effects of which had to be guarded against. This program divided the magnetic field distribution into a series of square-topped elements; the electron trajectory was determined and the Scherzer distortion coefficients D_{rad} and D_{sp} evaluated in the standard way. The square-topped field method, although crude, was however quite accurate enough for the present purpose and had the advantage that the axial extent of the square-topped elements can be readily chosen to suit particular requirments.

In evaluating the performance of projector lenses, it is useful to compute the quality factors Q_{rad} and Q_{sp} for radial and spiral distortion respectively.

During the initial design stages the trajectory program was found particularly useful since in a corrector-projector doublet it is quite difficult to arrange the polepieces in such a way that they produce the desired axial flux density distribution and yet

do not obstruct the wide-angle trajectories.

1.3.3 COMPUTED IMAGE SIMULATION

It is often useful to be able to visualize the appearance of an image of radial extent ρ at a projection distance L, in the presence of radial distortion (Q_{rad}) and spiral distortion (Q_{sp}) or a combination of both. A computer program DGPH (distortion graphics) was written for this purpose and is described in detail in Appendix (6). In this program we have formulated an expression that calculates the co-ordinates of displaced points. The object was assumed to be a perfect square grid. The DGPH program computes these coordinates and the plotter connects the points using a cubic spline fit. Examples of the computed results are shown in figures (1.25), (1.26) and (1.27).

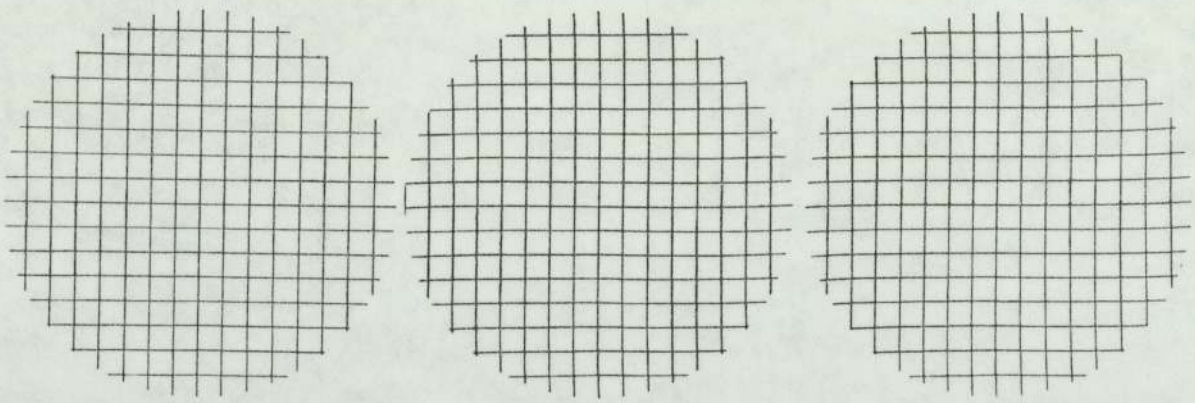

(a) (b) (c)

Figure (1.25) Simulated images taken at a projection semi-angle $\alpha_p = 32^\circ$ showing the maximum tolerable distortion (a) $Q_{rad} = 0.16$, $(\Delta\rho/\rho)_{rad} = 1\%$ (b) $Q_{sp} = 0.226$, $(\Delta\rho/\rho)_{sp} = 2\%$ (c) $(\Delta\rho/\rho)_{rad} = 1\%$, $(\Delta\rho/\rho)_{sp} = 2\%$.

The simulated images of figure (1.25) show that radial and spiral distortion of up to 1 and 2% respectively do not degrade the shape of the image even at the wide projection semi-angle of $\alpha_p = 32^\circ$. The high distortion produced by the projector lens is shown in figure (1.26). Here the radial (pin-cushion and barrel alternatively) and spiral distortion of the lens are considered both separately and jointly at 39% each for $\alpha_p = 32^\circ$. The severe distortion expected to be produced by the corrector lens is shown in figure (1.27) for pure spiral distortion and the combined effect of spiral and barrel distortion.

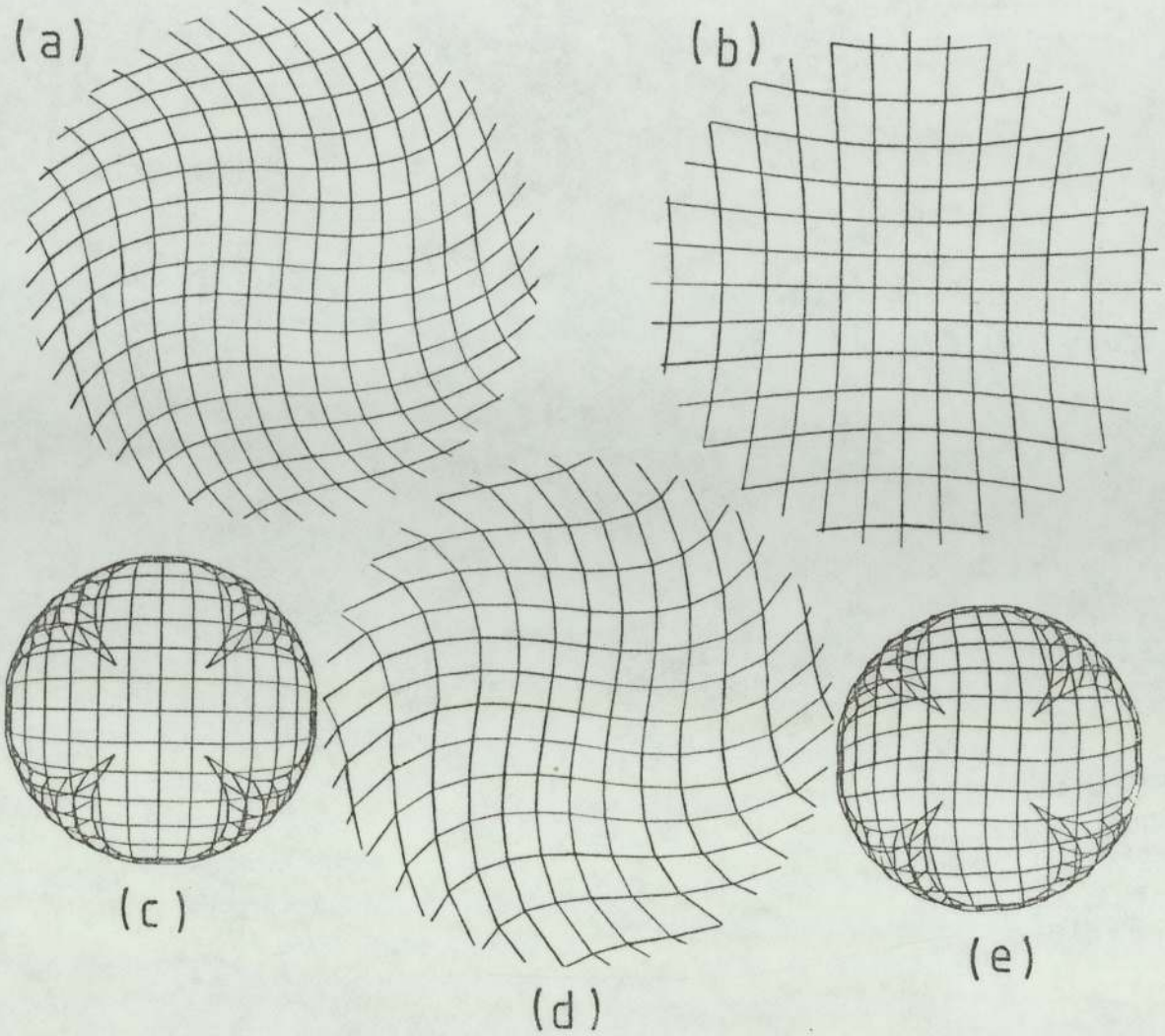

Figure (1.26) Simulated images in a single-polepiece projector lens at a large projection semi-angle $\alpha_p = 32^\circ$.

(a) pure spiral distortion $Q_{sp} = 1$, $(\Delta\rho/\rho)_{sp} = 39\%$.

(b) pure pin-cushion distortion $Q_{rad} = 1$, $(\Delta\rho/\rho)_{rad} = 39\%$.

(c) pure barrel distortion $Q_{rad} = -1$, $(\Delta\rho/\rho)_{rad} = -39\%$.

(d) radial (pin-cushion) and spiral distortion $Q_{rad} = 1$, $(\Delta\rho/\rho)_{rad} = 39\%$, $Q_{sp} = 1$, $(\Delta\rho/\rho)_{sp} = 39\%$.

(e) radial (barrel) and spiral distortion $Q_{rad} = -1$, $(\Delta\rho/\rho)_{rad} = -39\%$, $Q_{sp} = 1$, $(\Delta\rho/\rho)_{sp} = 39\%$.

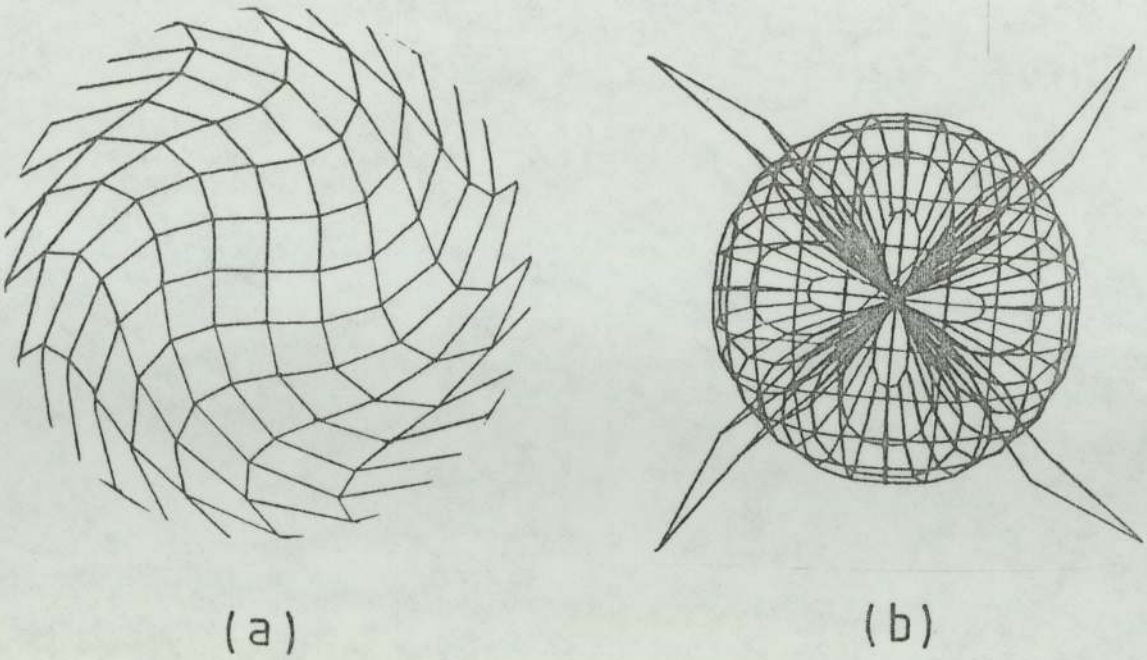

Figure (1.27) Simulated images in a single-polepiece corrector lens (a) pure spiral distortion: $\alpha_p = 22^\circ$, $Q_{sp} = 2.5$, $(\Delta\rho/\rho)_{sp} = 102\%$; (b) $\alpha_p = 16.5^\circ$, $Q_{rad} = -3$, $(\Delta\rho/\rho)_{rad} = -79\%$, $Q_{sp} = 2.4$, $(\Delta\rho/\rho)_{sp} = 50.5\%$.

CHAPTER 2

ELECTRON OPTICS OF THE PROJECTION SYSTEM

This chapter deals with some important focal properties and distortion characteristics that influence the design of a two-lens wide-angle projection system. This includes experimental and computer-based methods of obtaining the necessary design data. The detailed design of a correcting system usually requires a knowledge of the electron trajectories especially the trajectories of marginal rays. This is necessary in the design of the lens polepieces. In the present investigation a program to calculate the general ray was not available. Instead, the corresponding Gaussian rays were calculated, from which the required polepiece shapes could be deduced to a first approximation. In the final design of the polepieces an allowance was made for the effects of the lens aberrations.

2.1 THE ELECTRON-OPTICAL PROPERTIES OF THE PROJECTION SYSTEM

Before describing the detailed design concepts of the electron-optical correcting system it may be helpful to represent the system by a suitable combination of thin optical lenses. The optical properties of such a thin lens can be characterised by the positions of the principal and focal planes and the focal length f, as illustrated in figure (2.1). In a thin lens these quantities are related by the following expression.

$$1/u + 1/v = 1/f \quad \ldots\ldots\ldots\ldots\ldots\ldots\ldots\ldots\ldots\ldots (2.1)$$

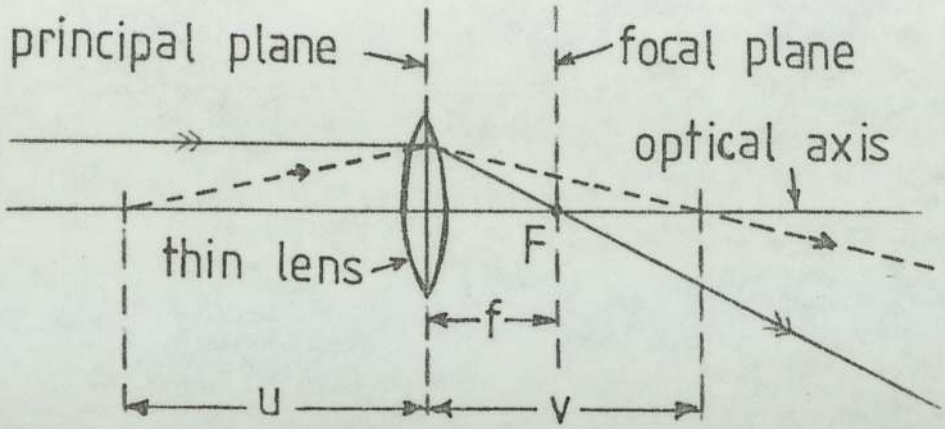

Figure (2.1) The object and image distances u and v for a thin lens of focal length f.

where u and v are the object and image distances respectively measured from the lens centre.

The wide-angle projection system that finally emerged from the present investigation is shown to scale in figure (2.2). It consists essentially of two single-polepiece magnetic lenses. Unlike the design of Lambrakis et.al. (1977), the corrector lens is larger than the projector lens so as to accommodate the larger number of ampere-turns required. In order to reduce the field cancellation effects, this lens was also provided with an iron face plate as shown in figure (2.2). This plate was fixed to the lens by means of a brass spacer in such a way that its axial position could be varied in the preliminary investigations. In addition, during the course of the testing of the corrector, the face plate was bored out to different diameters so as to determine the optimum magnetic design. At the same time, calculations were carried out as a guide to finding the optimum position. The detailed calculations and experimental tests are

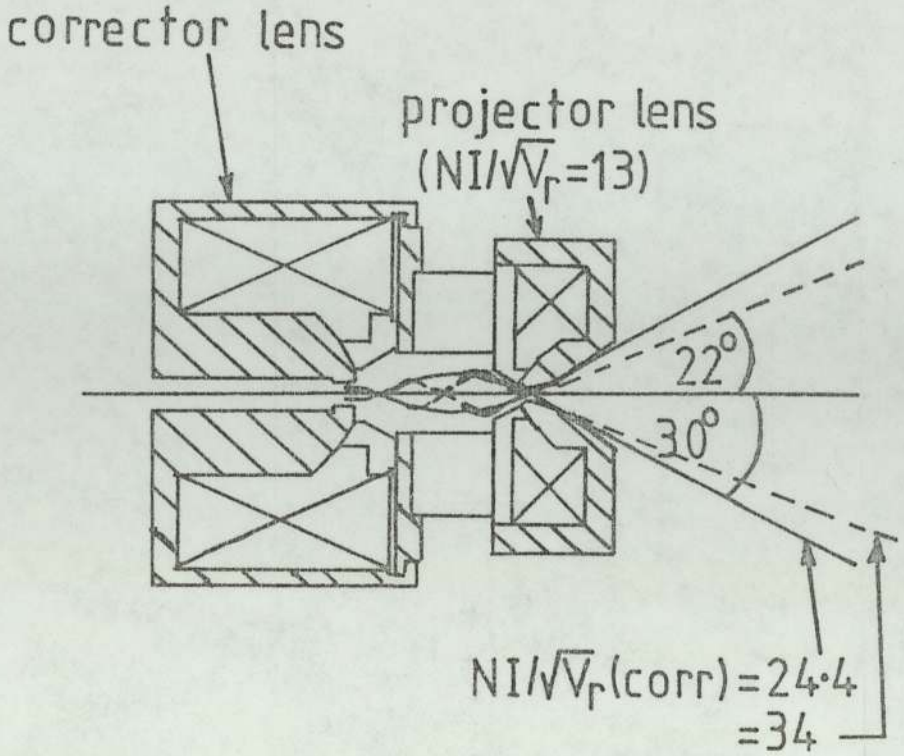

Figure (2.2) Scale drawing of a wide-angle projection system showing a typical calculated Gaussian trajectories through the present projection system (solid lines), and the corresponding trajectories through the Lambrakis et.al. projection system (dashed lines).

described in Chapter (7).

The final projector lens is normally operated at an excitation slightly below its minimum focal length so as to produce the least possible spiral distortion and a predetermined amount of pin-cushion distortion. The corrector lens produces a virtual intermediate image; although the excitation ratio

NI/NI_o = 1.44, the corrector is nevertheless still operating in the first focal zone. In the system previously described by Lambrakis et.al. (1977) the corresponding excitation ratio NI/NI_o = 2.13 is at the point of minimum corrector focal length in the second focal zone. The essential difference between the electron-optical trajectories, figure (2.2), is that in the previous approach the rays inside the corrector lens cross the optical axis twice (second focal zone). However, they cross the axis only once in the present method since the corrector is operated in its first focal zone. This is an important point because it means that the corrector now produces a virtual image, so that the conjugate points of the projector lens and the corresponding value of the conjugate ratios $m = |v/u|$ are much improved. A typical value is $m \simeq 0.1$ compared with the value of m = 0.3 in the system of Lambrakis et.al.(1977).

In order to illustrate the formation of the virtual image in a simple manner, the optics of the new arrangement can be conveniently represented by an analogous light-optical system consisting of three thin glass lenses as shown in figure (2.3). Here, the corrector lens is represented by two thin lenses separated by a short distance l_1. The projector lens is represented by a single thin lens of focal length f_p, situated at a distance l_2 from the nearest face of the corrector lens. The projection distance of the final projector is denoted by l_p. In this arrangement a ray of height r_1 passes through the lens system and strikes the screen at an off-axis distance ϱ_t.

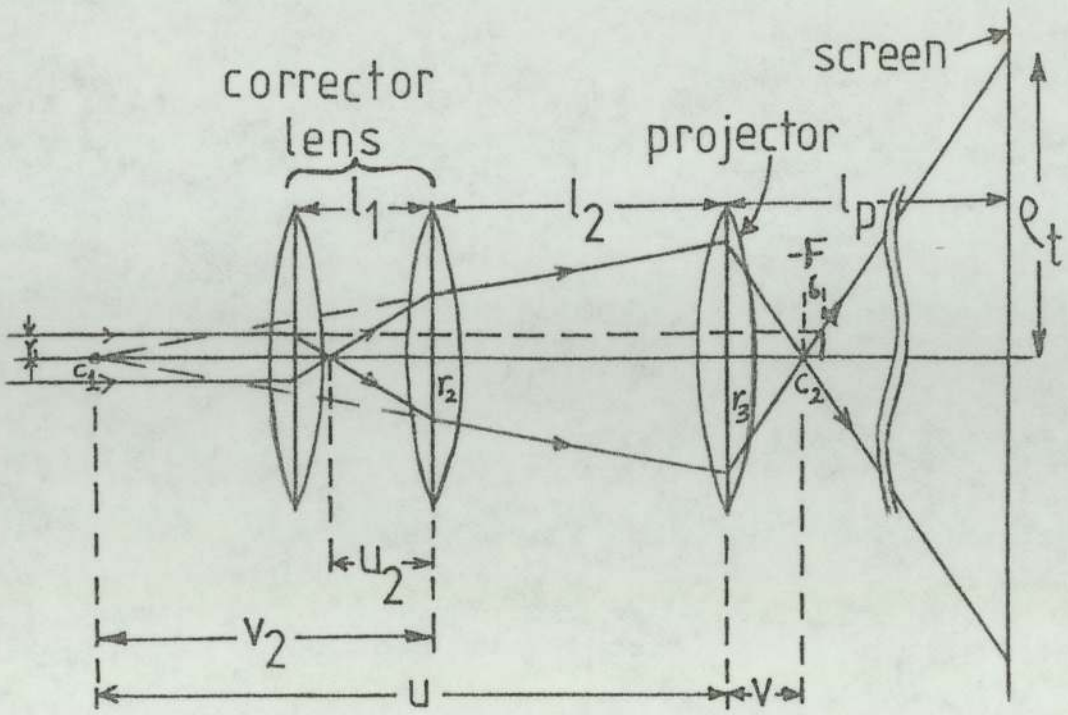

C_1 and C_2 are conjugate points of projector

Figure (2.3) Ray trajectories through a three-thin-lens system forming an image of radius ρ_t on the screen. Thin lens equivalent of the corrector system showing the formation of a virtual intermediate image at C_1 by the corrector and the wide-angle projection capability of the projector. Note the favourable conjugate points C_1 and C_2 of the final projector lens in this arrangement.

The overall magnification M_1 of the system, shown in figure (2.3), is given by

$$M_1 = \frac{\rho_t}{r_1} = \frac{\rho_t}{r_3} \cdot \frac{r_3}{r_1} = \left(\frac{u}{f_{corr}}\right)\left(\frac{l_p - v}{v}\right) \quad \text{.....(2.2)}$$

where r_1, r_3 and ρ are the ray heights at the first and third

lenses and the final screen respectively; u and v are the object and image distances of the projector (third) lens; l_p is the projection distance between the third lens and the screen; and f_{corr} is the effective focal length of the corrector lens, represented by the first two lenses of focal lengths f_1 and f_2 respectively; they are separated by a distance l_1. The effective focal length f_{corr} of the corrector lens is given by

$$1/f_{corr} = 1/f_1 + 1/f_2 - l_1/f_1 f_2 \quad \ldots\ldots\ldots\ldots\ldots\ldots\ldots (2.3)$$

We can therefore rewrite equation (2.2) in the simpler form.

$$M_1 = -\frac{1}{m}\left(\frac{l_p - v}{f_{corr}}\right) \quad \ldots\ldots\ldots\ldots\ldots\ldots\ldots\ldots\ldots (2.4)$$

since the ratio of the conjugates m = v/u. Equation (2.4) shows that the maximum magnification M_1 of the system depends, as would be expected, directly on the refractive power of the corrector lens. It also depends inversely on the conjugate ratio m. As mentioned previously it is desirable to make m as small as possible. However, this requirement conflicts with the need to keep the magnification M_{corr} of the corrector lens sufficiently small so that its corrective aberrations can be transferred to the final image.

Recalling that $M_{corr} = M_1/M_2$ where M_2 is the magnification with the corrector lens switched off, equation (1.14), we can write

$$M_{corr} = \frac{M_1}{M_2} = -\frac{1}{m}\left(\frac{l_p - v}{f_{corr}}\right) \Big/ \left(\frac{l_p - f_p}{f_p}\right) \quad \ldots\ldots\ldots (2.5)$$

After re-arranging we find that

$$M_{corr} = -\frac{1}{m}\left(\frac{f_p}{f_{corr}}\right)\left(\frac{\ell_p - v}{\ell_p - f_p}\right) \quad \text{.....(2.6)}$$

Since $\ell_p \gg v$ and $\ell_p \gg f_p$ we may write

$$M_{corr} \simeq -\frac{1}{m}\left(\frac{f_p}{f_{corr}}\right) \quad \text{.....(2.7)}$$

It is perhaps more convenient to express the magnifications M_1 and M_{corr} in terms of the lens separation ℓ_1, ℓ_2 the projection distance ℓ_p and the focal lengths f_1, f_2, f_{corr} and f_p rather than in terms of the object and image distances u and v. The derivations of these formulae are dealt with in Appendix (5) and the result is the following

$$M_1 = -\left(\frac{\ell_p - f_p}{f_p}\right)\left(\frac{\ell_2}{f_{corr}} + \frac{\ell_1}{f_1} - 1\right) + \frac{\ell_p}{f_{corr}} \quad \text{.....(2.8)}$$

and

$$M_{corr} = -\left(\frac{\ell_2}{f_{corr}} + \frac{\ell_1}{f_1} - 1\right) + \frac{\ell_p f_p}{f_{corr}(\ell_p - f_p)} \quad \text{.....(2.9)}$$

Equations (2.8) and (2.9) can now be applied to the present correcting system as well as that of Lambrakis et.al. (1977). For example, if we wish to compare the performance of these two systems under comparable conditions we can select the following data, namely, ℓ_1 = 17 mm., ℓ_2 = 30 mm., ℓ_p = 400 mm., f_p = 10 mm. and the initial ray height r_1 = 1 mm. In this comparison the magnification M_{corr} of the corrector lens and the total magnification M_1 are the same in both systems. In order to satisfy these conditions, specific values of f_1, f_2 and f_{corr} were chosen for each system, as shown in Table (2.1) and figure (2.4).

Parameter	Present System	Lambrakis et.al. (1977)
f_1(mm)	4.9	6.8
f_2(mm)	14	4
f_{corr}(mm)	36.1	-4.4
m(=v/u)	0.09	0.75
M_1	-117	117
M_2	39	39
M_{corr}	-3	3
α_p^o	16.7	17
D*/D(proj)	1.13	2.75

Table (2.1) Focal properties of a thin-lens equivalent of the present correcting system compared with that of Lambrakis et.al. (1977). l_1 = 17 mm., l_2 = 30 mm., l_p = 400mm., f_p = 10 mm. and r_1 = 1 mm. N.B. M_{corr} and M_1 have the same value and α_p is approximately the same in each system.

The results shown in table (2.1) and illustrated in figure (2.4) show that if the corrector forms a virtual image it is possible for a given value of M_{corr} to obtain a much smaller value of the conjugate ratio m than is possible with the Lambrakis system. In practical terms, according to equation (1.12), the finite conjugate ratio $m \simeq 0.1$ of the present system will increase the coefficient of distortion D_{sp} of the projector by about 15% over that for infinite conjugates (m = o). In the Lambrakis system, however, the corresponding increase is about 175% (m = 0.75); in the actual experiment the lens separation is larger giving m = 0.3 i.e. an increase in D_{sp} of 53%. Such a large increase in the distortion coefficient of the projector largely cancels the initial benefit of employing a single-polepiece lens.

This can also be explained qualitatively by the ray paths through the projector lens as shown in figure (2.4). In the Lambrakis system the ray height is 5.3 mm. compared with 3.3 mm. in the present system. Since image distortion is roughly proportional to the square of the ray height in the lens ($\Delta\rho/\rho_{sp} = D_{sp}r^2$), the corresponding increase in image distortion produced by the projector in the two systems respectively is $(5.3/3.3)^2 = 2.6$. This confirms that the present system of forming a virtual image, and hence of reducing the conjugate ratio m, greatly reduces the amount of distortion to be corrected.

In the thin lens equivalent of the present system $\alpha_p = 16.7^o$ for $r_1 = 1$ mm. Higher values of α_p may be obtained by increasing r_1.

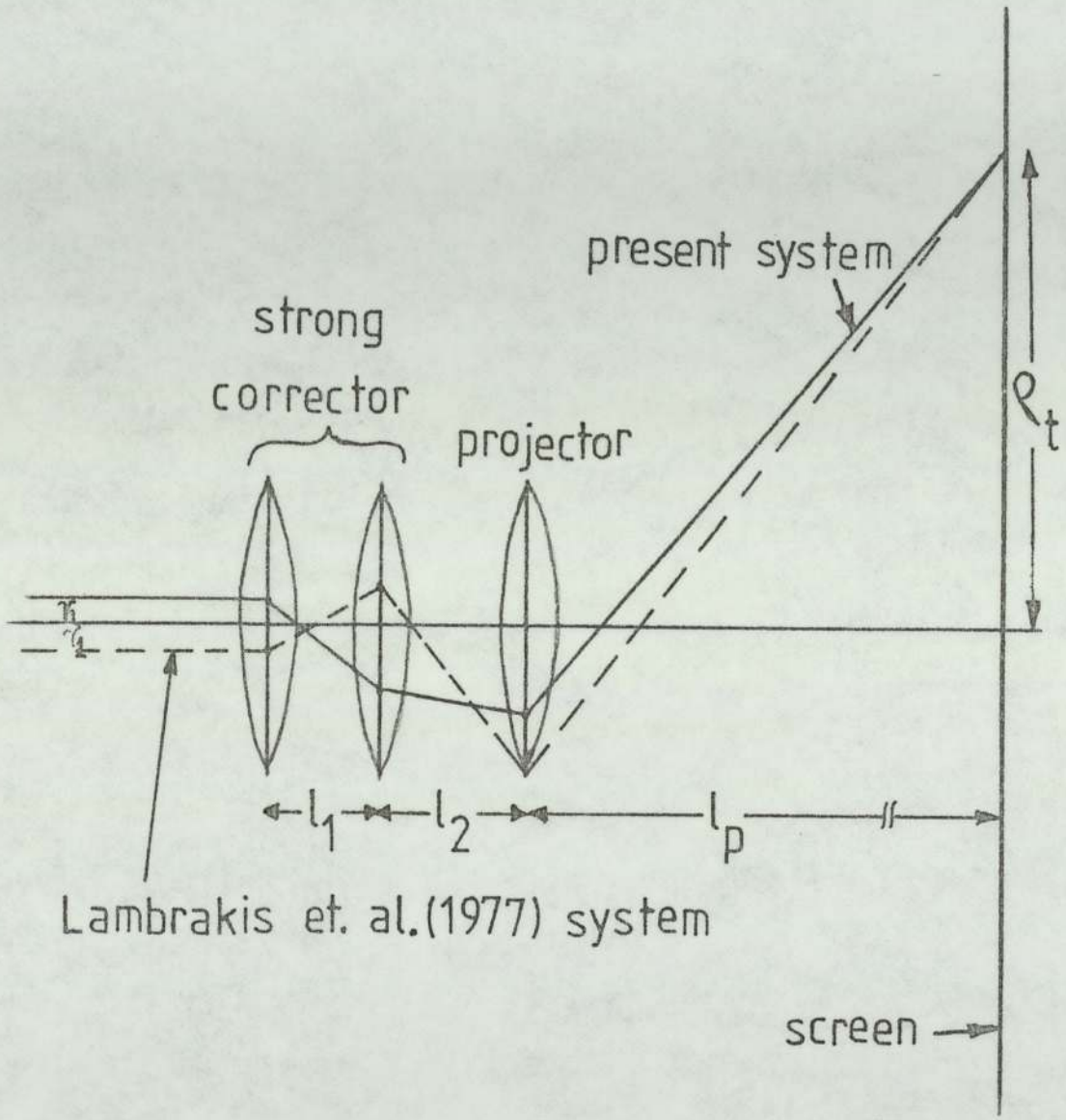

Figure (2.4) Schematic diagram showing the ray trajectories through the thin lens equivalent of the present correcting system and that of Lambrakis et.al.(1977) for equal magnitudes of M_1 and M_{corr} in each system.

It is of interest to know the effective focal length F_{eff}, or more usefully, the effective refracting power of the combined corrector-projector system. This may be calculated from figure (2.3), as shown in Appendix (5), and given as follows:

$$\frac{1}{F_{eff}} = \frac{1}{f_p} + \frac{1}{f_{corr}} - \frac{1}{f_p}\left[\frac{l_2}{f_{corr}} + \frac{l_1}{f_1}\right] \quad \ldots\ldots\ldots\ldots (2.10)$$

Thus according to the data of table (2.1) and figure (2.4) the effective focal lengths of both systems are essentially the same (F_{eff}=3.27 mm. in the real focus system and F_{eff}=-3.31mm. in the virtual focus system).

2.1.1 Thin-Lens Theory of Distortion

A useful approximation to the distortion in a two-lens system may be obtained from the thin lens model. In a thin lens the refractive power depends mainly on the ray height r in the lens and not on the angle of inclination α_i of the incident beam. In other words, the refracted angle ε is the same for all incident rays entering the lens at height r, as shown in figure (2.5a), where ε is very small for a thin lens so that

$$\tan \varepsilon = \varepsilon = \alpha_{p(m=o)} = \alpha_i + \alpha_p \quad \ldots\ldots\ldots\ldots\ldots\ldots (2.11)$$

where $\alpha_{p(m=o)}$ is the projection semi-angle for infinite conjugates and α_p is the projection semi-angle for finite conjugates. Hence, it follows from figure (2.5a) and equation (2.11) that

$$\varepsilon = \frac{r}{f} = \frac{r}{u} + \frac{r}{v}$$

where f is the focal length of the lens.

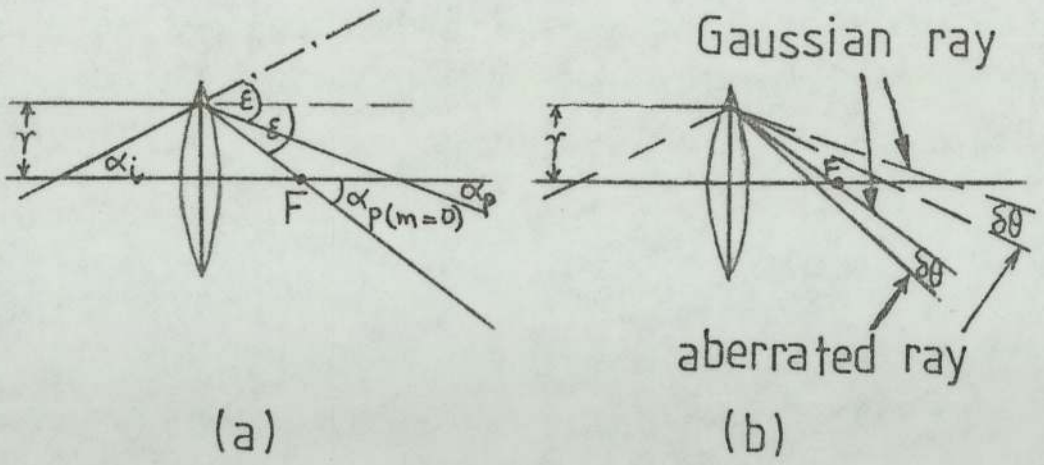

Figure (2.5) Schematic diagrams of thin lenses receiving incident rays of the same ray height r but different angle of inlcination α_i showing (a) equal angles of refraction ε and (b) equal deviation of rays $\delta\theta$ between the aberrated and the Gaussian rays.

Similarly, to a first approximation, the deviation $\delta\theta$ of the aberrated rays from the Gaussian value does not depend on the angle of inclination α_i.

In a two-lens system as shown in figure (2.6), a parallel beam of rays is incident on the corrector lens and hence distortion $(\Delta\rho/\rho)_{corr}$ produced by the corrector on a distant screen in front of the projector lens is given by

$$\begin{aligned}(\Delta\rho/\rho)_{corr} &= \pm\ D_{corr}\, r^2_{corr} \\ &= \pm\ Q^2_{corr}\, r^2_{corr}/f^2_{corr} \\ &= \pm\ Q^2_{corr} \tan^2\alpha_{corr} \qquad .....(2.12)\end{aligned}$$

where α_{corr} is the semi-angle of projection as shown in figure (2.6)

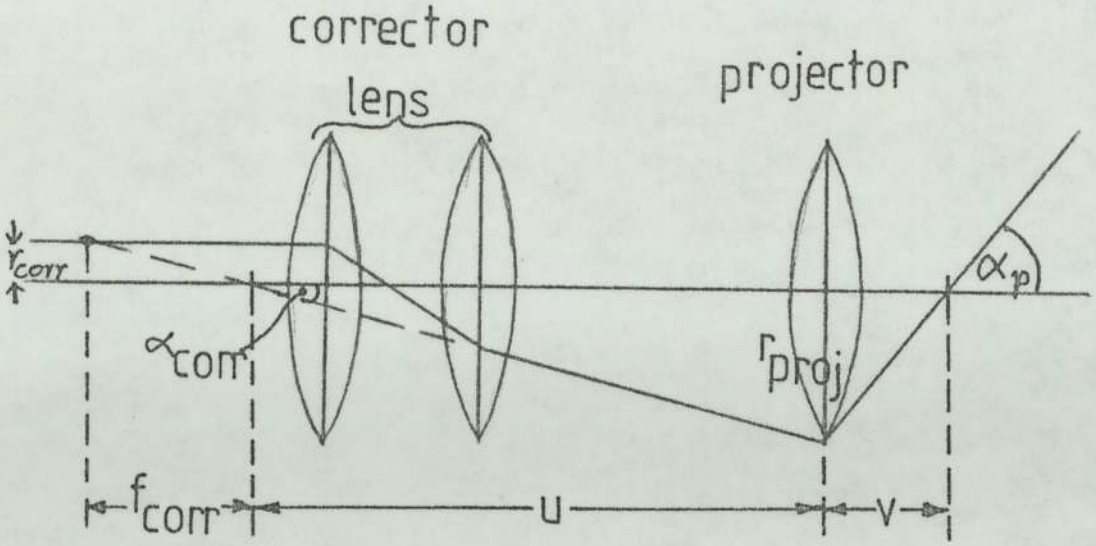

Figure (2.6) An incident ray trajectory of radial height r_{corr} passing through a thin-lens system to a distant screen showing the projection semi-angles α_{corr} and α_p.

After passing through the projector lens the projection semi-angle becomes α_p, and further distortion is introduced into the image. For thin lenses the angles α_p and α_{corr} are related as follows. From figure (2.6)

$$\tan \alpha_p = \frac{r_{proj}}{v}$$

Since $1/u + 1/v = 1/f_p$ and $m = v/u$

Thus

$$\tan \alpha_p = \frac{r_{proj}}{f_p(1+m)}$$

Also from figure (5.6)

$$\tan \alpha_{corr} = \frac{r_{corr}}{f_{corr}}$$

Thus $\tan \alpha_{corr} = \dfrac{r_{corr}\, f_p (1+m)}{r_{proj}\, f_{corr}} \tan \alpha_p$

The magnification M_{corr} of the corrector lens at the final screen is given by figure (1.22) and equation (1.14) as

$$M_{corr} = \frac{\rho_t}{\rho_p} = \frac{r_{proj}}{r_{corr}} \cdot \frac{\rho_t}{r_{proj}} \cdot \frac{r_{corr}}{\rho_p}$$

$$= \frac{r_{proj}}{r_{corr}} \cdot \frac{\ell_p - v}{v} \cdot \frac{f_p}{\ell_p - f_p}$$

since $v = f_p(1 + m)$

hence $$M_{corr} = \frac{r_{proj}}{r_{corr}} \cdot \frac{\ell_p - f_p(1 + m)}{f_p(1 + m)} \cdot \frac{f_p}{\ell_p - f_p}$$

and since $\ell_p \gg f_p$ and $0 \leqslant m \leqslant 1$

thus $M_{corr} \simeq \frac{r_{proj}}{r_{corr}(1+m)}$, so that

$$\tan \alpha_{corr} = \frac{f_p}{f_{corr} M_{corr}} \tan \alpha_p \quad \text{.....(2.13)}$$

Alternatively, we can write, from figure (2.6)

$$\tan \alpha_{corr} = \frac{r_{proj}}{u} \quad \text{and} \quad \tan \alpha_p = \frac{r_{proj}}{v}$$

Thus $$\tan \alpha_{corr} = \frac{v}{u} \tan \alpha_p = m \tan \alpha_p \quad \text{.....(2.14)}$$

Either formula can be used to evaluate the corrector distortion $(\Delta\rho/\rho)_{corr}$ at the final screen. Hence equation (2.12) becomes

$$(\Delta\rho/\rho)_{corr} = \pm Q^2_{corr} \left(\frac{f_p}{f_{corr} M_{corr}}\right)^2 \tan^2 \alpha_p \quad (2.15)$$

or

$$(\Delta\rho/\rho)_{corr} = \pm Q^2_{corr}\ m^2 \tan^2 \alpha_p \quad \ldots\ldots\ldots\ldots (2.16)$$

Equations (2.15) and (2.16) are also equivalent within the thin lens approximations involved in equation (2.7), page 72.

An apparent difficulty may occur if telescopic rays are used in the corrector lens, ie if electrons enter and leave the corrector lens as a parallel beam. This arrangement does not appear to have any advantages in practice. In any case care would have to be taken in evaluating equations (2.15) and (2.16) correctly, since m in these circumstances tends to zero, while f_{corr} and Q_{corr} tend to infinity.

We can conclude this part of the discussion by noting that the contribution of the corrector lens to the distortion at the final viewing screen varies greatly with the conjugate ratio m which in turn depends on f_p, f_{corr} and M_{corr}.

If the rays from the corrector lens entered the projector as a parallel beam (m = o) the distortion $(\Delta\rho/\rho)_{proj}$ produced by the projector lens at the final screen would be

$$(\Delta\rho/\rho)_{proj} = Q^2_{proj} \tan^2 \alpha_{p\ (m=o)} \quad \ldots\ldots\ldots\ldots (2.17)$$

where $\alpha_{p(m=o)}$ is the projection semi-angle for infinite conjugates.

Hence $\tan \alpha_{p(m=o)} = r_{proj}/f_p$ $\ldots\ldots\ldots\ldots (2.18)$

However, if the projector lens has conjugates u and v as shown in figure (2.6), then

$$\tan \alpha_p = \frac{r_{proj}}{v}$$

Since $1/u + 1/v = 1/f_p$ and $m = v/u$

Thus $$\tan\alpha_p = \frac{r_{proj}}{v} = \frac{r_{proj}}{f_p(1+m)} \quad \text{.....(2.19)}$$

Therefore, combining equations (2.18) and (2.19) we get

$$\tan\alpha_{p(m=o)} = (1 + m)\tan\alpha_p \quad \text{.....(2.20)}$$

This means that for a given refractive power, the projection semi-angle is reduced by a factor $(1 + m)$ when the conjugate ratio m is changed from $m = o$ to $m > o$. Although the displacement $\Delta\rho$ remains approxmately the same, the image height ρ is reduced by a factor $(1 + m)$. Hence equation (2.17) now becomes

$$(\Delta\rho/\rho)_{proj} = Q^2_{proj}\,(1 + m)^2 \tan^2\alpha_p \quad \text{.....(2.21)}$$

Equation (2.21) shows that, if $m = 0.1$, for example, the distortion produced by the projector lens is increased by about 21% due to the effect of the finite conjugates.

The effective distortion $(\Delta\rho/\rho)_{eff}$ in the two-lens system is obtained by adding equations (2.15) and (2.21),

i.e. $$(\Delta\rho/\rho)_{eff} = Q^2_{eff}\tan^2\alpha_p$$

$$= Q^2_{proj}\,(1 + m)^2\tan^2\alpha_p$$

$$\pm\, Q^2_{corr}\left(\frac{f_p}{f_{corr}M_{corr}}\right)^2\tan^2\alpha_p \quad \text{...(2.22)}$$

where Q_{eff} is called the effective quality factor of the two-lens system. It can be deduced from equation (2.22)

i.e. $$Q^2_{eff} = (1 + m)^2\,Q^2_{proj}$$

$$\pm\left(\frac{f_p}{f_{corr}M_{corr}}\right)^2 Q^2_{corr} \quad \text{.....(2.23)}$$

2.2 IMAGE DISTORTION IN A PROJECTOR LENS

Image distortion is usually insignificant in objective lenses since the field of view of the objective lens is usually small. Distortion is important in intermediate and projector lenses since the ray height in the lens is usually large in order to produce as large an image on the viewing screen as possible. In a projector lens the entire axial magnetic field contributes to the imaging process. The distortion coefficients D_{rad} and D_{sp}, previously mentioned, may be calculated if the axial magnetic field distribution is known, for example from experimental measurements or numerical calculations. The distortion coefficients D_{rad} and D_{sp} may be calculated from the equations of Scherzer (1936). These equations require a knowledge of two independent paraxial rays through the field distribution.

In this investigation we made use of an existing program by Marai (1977) for computing these coefficients. His program calculates D_{rad} and D_{sp} from Scherzer's (1936) expressions of radial and spiral distortion. These expressions may be written as follows:

$$D_{rad} = (3/8f_p^2) + (e/16mV_r)\int_{z_1}^{z_n}\left[(B_z')^2 + (3/8)(e/mV_r)\,B_z^4 - B_z^2 \cdot (Y')^2/Y^2\right] Y^3X \; dz \quad \ldots\ldots(2.24)$$

and

$$D_{sp} = (1/16V_r)(2e/mV_r)^{\frac{1}{2}}\int_{z_1}^{z_n} B_z\left[(3/8)(e/m)\,B_z^2 + (V_r/2)\left\{(Y'/Y)^2 + Y'X'/YX\right\}\right] Y^2 \; dz \quad \ldots\ldots(2.25)$$

where D_{rad} and D_{sp} are the coefficients of radial and spiral distortion respectively, e/m is the charge to mass ratio of the

electron, V_r is the relativistically corrected accelerating voltage, B_z is the axial magnetic flux density at an axial point z, X and Y are two particular solutions of the paraxial ray equation [illustrated in figure (2.7)], z_1 and z_n are the axial points where the magnetic field starts and terminates respectively, and f_p is the focal length of the projector lens.

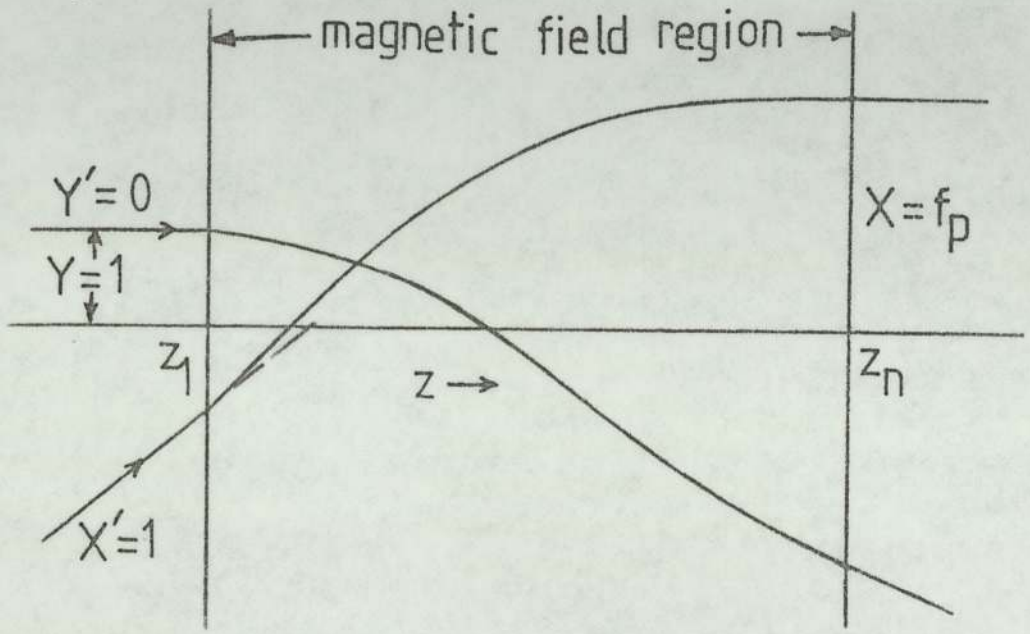

Figure (2.7) Schematic representation of the electron trajectories X and Y through the magnetic field of a single-polepiece lens.

Unfortunately, this program, like many other existing programs, applies only to the special case of a parallel incident beam of electrons, as illustrated in figure (2.7). Once the distortion coefficients D_{rad} and D_{sp} have been computed for various lens excitations $NI/V_r^{\frac{1}{2}}$ using equations (2.24) and (2.25), the distortion $\Delta\rho/\rho$ in the image can be calculated from equations (1.2), (1.5), (1.8), and (1.9), i.e. from

$$(\Delta\rho/\rho)_{rad} = D_{rad} r^2 = Q^2_{rad} \tan^2 \alpha_p$$

and

$$(\Delta\rho/\rho)_{sp} = D_{sp} r^2 = Q^2_{sp} \tan^2 \alpha_p$$

To facilitate this calculation the program was extended to calculate the Q values directly. At the same time some approximations made in the original Marai program were removed. These, however, did not significantly influence the results.

If the rays do not enter the projector lens parallel to the electron-optical axis then a correction for the effect of the finite conjugates has to be made. This can be made to a sufficient accuracy by means of the formulae (1.12) and (1.13).

Recently, developed projector programs now enable this calculation to be carried out for the combined field distribution of both corrector and projector lenses. Unfortunately, time did not permit the author to develop such programs during the early design stages of this project.

2.3 CORRECTION OF DISTORTION

It has been established in Chapter (1) that it should be possible to correct the distortion produced by the final projector lens by introducing a compensating distortion from a preceding correcting lens. Since the distortion introduced into the final image by such a correcting lens is reduced by the square of its magnification M_{corr}, the correcting lens should therefore produce a distortion $\Delta\rho/\rho$ some M^2_{corr} times greater than that to be corrected in the final projector lens. Unlike

the Lambrakis et.al. (1977) system, f_{proj} and f_{corr} are not approximately equal. In fact, in the present system f_{corr} is about 3 times greater than f_p at the excitations needed for correcting distortion. In general, one can now say that the distortion $(\Delta\rho/\rho)_{corr}$ produced by the corrector lens, in a two-lens projection system, is reduced at the final screen by the factor

$$\left(\frac{f_{corr}\, M_{corr}}{f_p}\right)^2$$

rather than by the factor M^2_{corr} alone.

If a single-polepiece lens is used, operated in the unfavourable direction of the electron beam, the spiral distortion $(\Delta\rho/\rho)_{sp}$ produced by the corrector lens is 2.6 times greater than that of the same lens operating in the favourable direction. In practice, a compromise has to be found between this desirable electron-optical property of the single-polepiece lens and the need to avoid field cancellation between the corrector and projector. This can be best achieved by using an asymmetrical double-polepiece corrector lens, as shown in figure (2.2). Here, the iron face plate of the corrector lens reduces the ampere-turn cancellation from 38% in the absence of the face plate to 20% with it in position. These figures refer to a snout separation of 50 mm. to 60 mm. as illustrated and computed in Chapters (5) and (6). The iron face plate has a comparatively large inside diameter of 25 mm. and hence the magnetic field distribution of the corrector lens retains the desirable electron-optical properties of an asymmetrical field-shape. The important effect

of the iron face plate is to strengthen the peak value of the magnetic field of the wide bore corrector. More importantly, the magnetic field screening effect of the face plate preserves the desirable shape of the magnetic field distribution of the projector lens which thereby retains its very low spiral distortion. It is of course essential to shape the polepiece of the corrector lens so as not to limit the field of view on the final viewing screen.

The final design of the corrector system was aimed at overcoming the difficulties encountered by previous workers in simultaneously correcting radial and spiral distortion. In particular it was desirable to remove the restriction of fixed lens excitations for both corrector and projector set by the need to eliminate radial distortion in each lens separately. Since it is desirable to make the conjugate ratio m of the final corrector lens as small as possible, for a given value of M_{corr} ($\simeq 3X$), the focal length f_{corr} of the corrector lens must be as large as possible [see equation (2.7)]. The condition of small m and large f_{corr} can in fact be fulfilled if the corrector lens is operated at the high excitation end of the first focal zone but below the excitation $NI/V_r^{\frac{1}{2}} \simeq 27$ corresponding to the telescopic ray path. In practice, an excitation $NI/V_r^{\frac{1}{2}} = 24.4$ proved convenient, as shown in figures (2.8) and (2.9). The high spiral distortion at this excitation (2700%) is reduced at the fluorescent screen to a value of 29.3%, as shown in figure (2.8), the value required to cancel the spiral distortion produced by the projector lens since the rotation of the two lenses is of opposite sign. At this excitation, namely $NI/V_r^{\frac{1}{2}} = 24.4$, the spiral

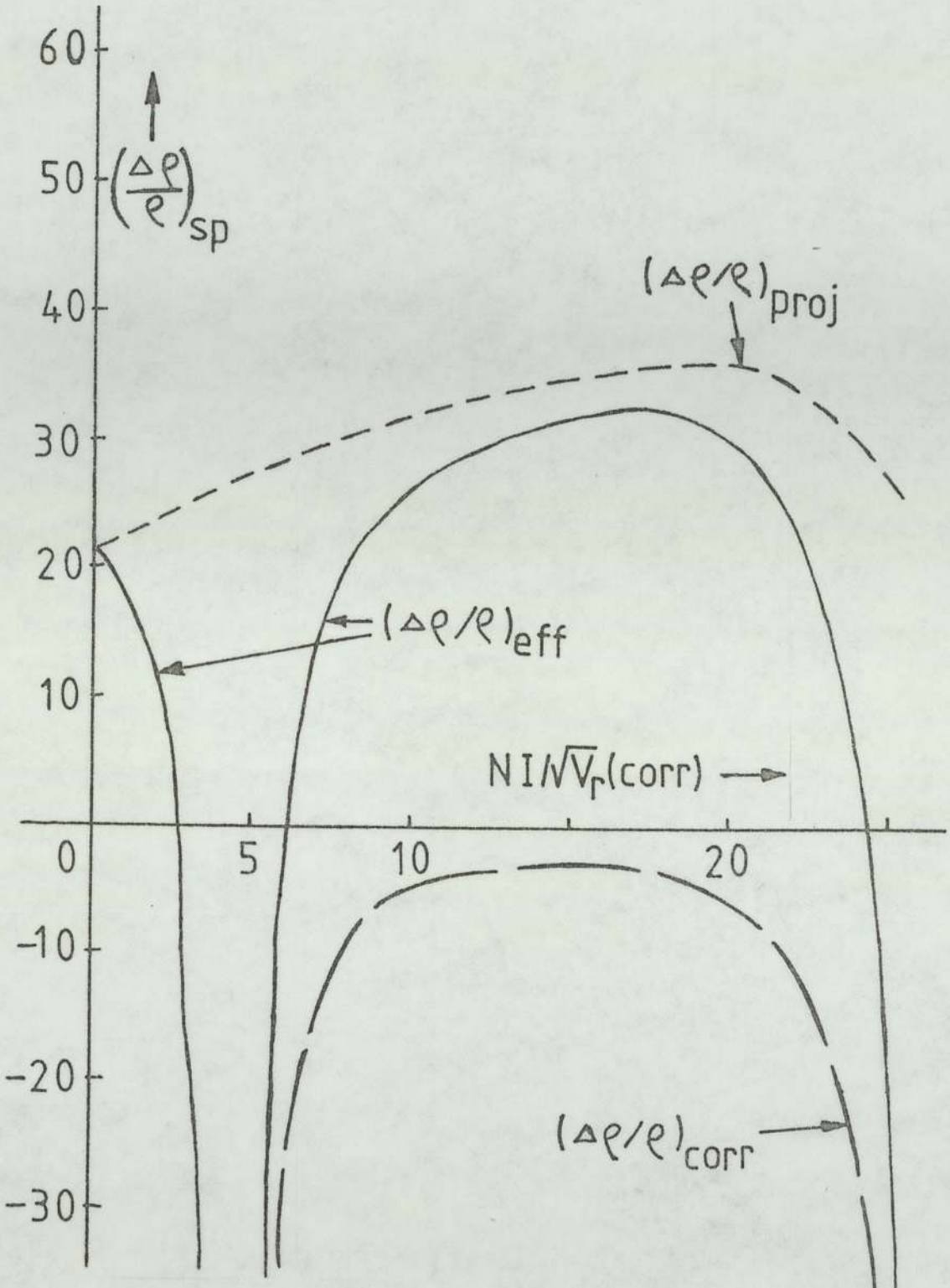

Figure (2.8) The spiral distortion $(\Delta\rho/\rho)_{proj}$ of the projector lens, $(\Delta\rho/\rho)_{corr}$ of the corrector lens, and $(\Delta\rho/\rho)_{eff}$ of the two-lens system at the final viewing screen as a function of the corrector excitation $NI/V^{\frac{1}{2}}_{r(corr)}$. $NI/V^{\frac{1}{2}}_{r(proj)} = 13$; $\alpha_p = 30^\circ$; $\alpha_{corr} = 5^\circ$. Negative distortion is due to opposing currents in lenses.

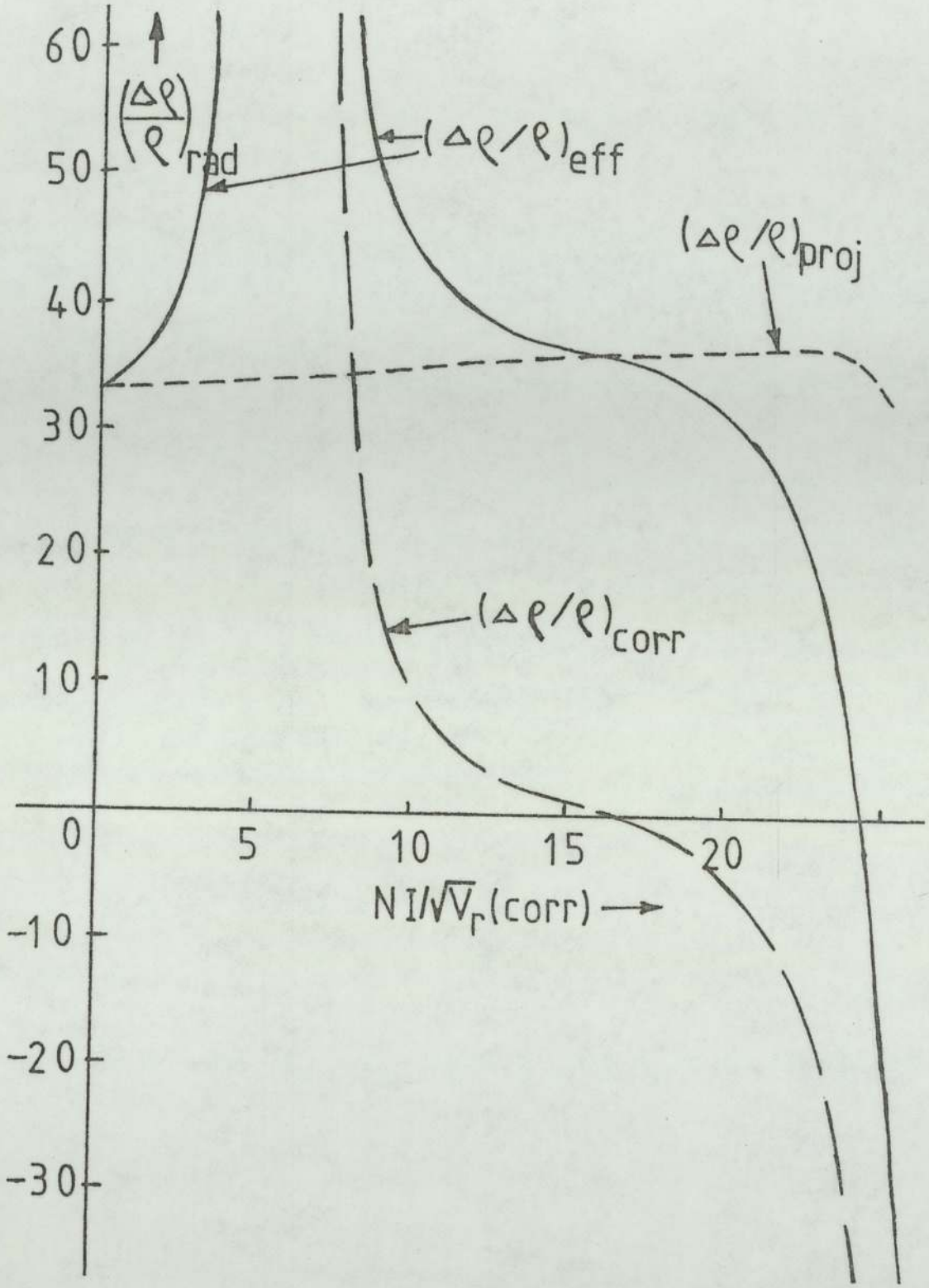

Figure (2.9) The radial distortion $(\Delta\rho/\rho)_{proj}$ of the projector lens, $(\Delta\rho/\rho)_{corr}$ of the corrector lens, and $(\Delta\rho/\rho)_{eff}$ of the two-lens system at the final screen as a function of the corrector exhibition $NI/V^{\frac{1}{2}}_{r(corr)}$. $NI/V^{\frac{1}{2}}_{r(proj)} = 13; \alpha_p = 30^\circ; \alpha_{corr} = 5^\circ$. Positive distortion denotes pin-cushion and negative distortion represents barrel distortion.

distortion of the corrector is accompanied by 3200% of barrel distortion. This is reduced at the screen to a value of 34.7%, as shown in figure (2.9), which can be readily compensated by reducing the excitation of the projector lens by approximately 23.5%. This will introduce 34.7% of pin-cushion distortion, as shown in figure (2.9). This reduction of projector excitation does not affect the correction of spiral distortion appreciably since the spiral distortion quality factor Q_{sp} of the projector varies only slowly over the excitation parameter range $NI/V_r^{\frac{1}{2}}$ 9 to 17, as shown in figure (7.20).

It is this property of a single-polepiece projector lens that enables the correction of radial distortion to be carried out relatively independently of the correction of spiral distortion. The process of correction therefore converges smoothly if the following procedure is carried out.

(1) With the corrector lens switched off, the projector is set to its minimum focal length (maximum magnification). Under these conditions the projector will produce a small amount of pin-cushion distortion ($Q_{rad} = 0.5$), as shown in figure (4.8), but an appreciable amount of spiral distortion ($Q_{sp} = 0.8$). The corrector lens is then switched on at an excitation $NI/V_r^{\frac{1}{2}}$ of about 25 in order to make an initial compensation of the spiral distortion produced by the corrector lens. For a projection semi-angle $\alpha_p = 30^\circ$, magnification $M_{corr} \simeq 3$, $f_p = 10$ mm. and $f_{corr} = 35$ mm. some -2800% of correcting spiral distortion is needed to compensate the distortion of 30% produced by the projector lens.

(2) The corrector will of course now introduce a considerable

amount of barrel distortion, as previously explained. This is now corrected by introducing an appropriate amount of pin-cushion distortion by reducing the excitation of the projector lens. This will increase the pin-cushion distortion from 5.5% to about 35%, see figure (2.9), in order to compensate the barrel distortion produced by the corrector lens.

(3) A further small improvement can now be made, if necessary, by a readjustment of the corrector and projector excitations. This is easy to carry out since the spiral distortion of the projector lens varies only slowly with lens excitation, so that the correcting procedure converges rapidly.

2.3.1 Production of Distortion in the Corrector Lens

In order to illustrate the production of the large amounts of distortion in the corrector lens, use can be made of the thin-lens model described earlier in this chapter, in which a strong lens was represented by two thin lenses separated by a distance l_1, as shown in figure (2.10). The production of barrel distortion from a strongly excited corrector lens in this way is shown schematically in this figure. Both thin lenses of the pair suffer from spherical aberration. The first lens itself would produce pin-cushion distortion on a distant screen [see figure (2.10)]. However, if the separation $l_1 < (f_1 + f_2)$ then the combination of the two lenses will produce barrel distortion, as shown in the same figure.

The compensation of the corrector barrel distortion by the projector lens is illustrated schematically in figure (2.11). Here the projector lens is operated at an excitation in which appreciable pin-cushion distortion is produced.

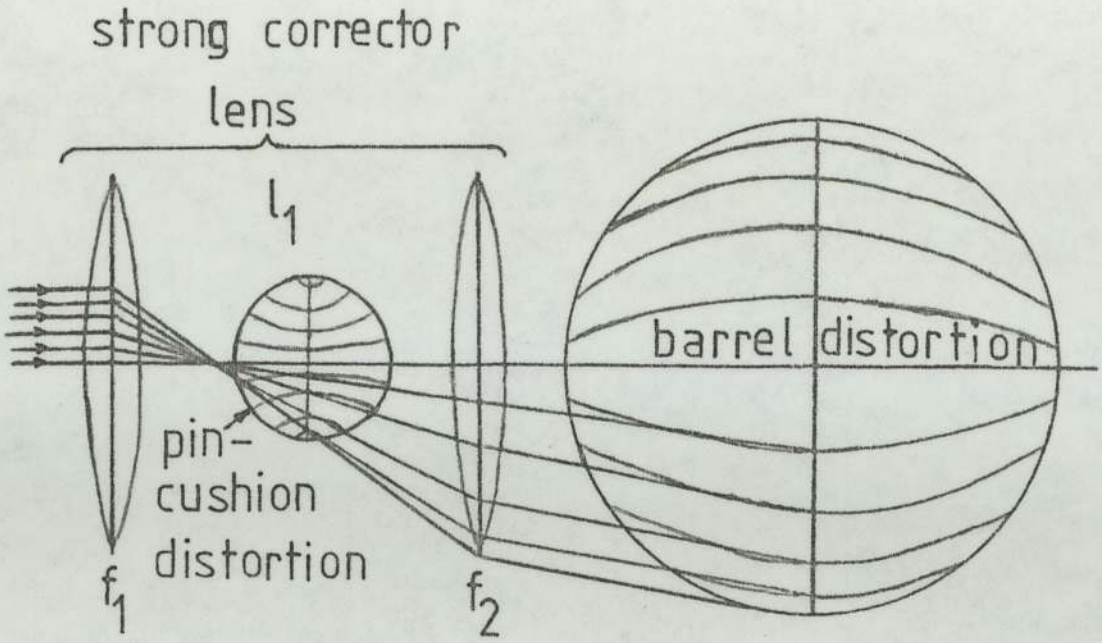

Figure (2.10) Illustration of barrel distortion produced by a strong corrector lens. The lens is represented by two thin glass lenses $[l_1 < (f_1 + f_2)]$.

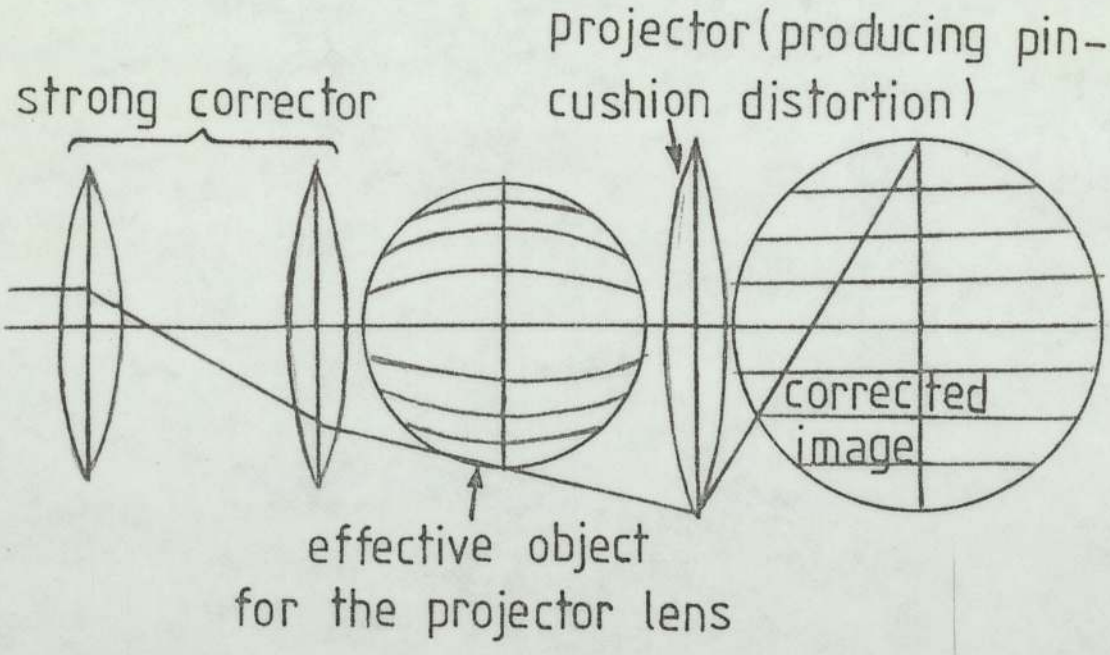

Figure (2.11) Compensation of barrel distortion from the corrector lens by an equivalent amount of pin-cushion distortion from the final projector lens.

2.3.3 The Complete Wide-Angle Projection System

The correction system that was finally devised is shown in figure (2.12). In order to correlate the electron trajectories with those of the thin lens model, the calculated trajectories are shown in relation to the calculated magnetic field distribution in the corrector lens and the projector lens at the appropriate excitation settings for zero distortion in the final image, namely $NI/V_r^{\frac{1}{2}} = 24.4$ in the corrector lens and $NI/V_r^{\frac{1}{2}} = 13$ in the projector. Figure (2.12) shows a parallel beam of electrons entering the corrector lens. This condition is satisfied to a good approximation in an electron microscope since the distance between the objective and the corrector is large compared with the focal length of the corrector. It should also be noticed that in this particular correcting system, the beam of electrons entering the magnetic field of the projector contribution is also approximately parallel. This simplifies the calculation procedure, since the projector properties may be calculated assuming a parallel incoming beam and subsequently making a small correction for the finite conjugate ratio m involved, as explained in Chapter (1). In figure (2.12), for example, $m \simeq 0.1$ and so from equations (1.12) and (1.13)

$$(D^*/D)_{proj} \simeq 1 + 1.37m + 1.28m^2 = 1.15$$

This means that, in this case, the correction of the parameter D_{proj} for finite conjugates amounts to only 15% so that the error involved in using the approximate equations (1.12) and (1.13) is not significant.

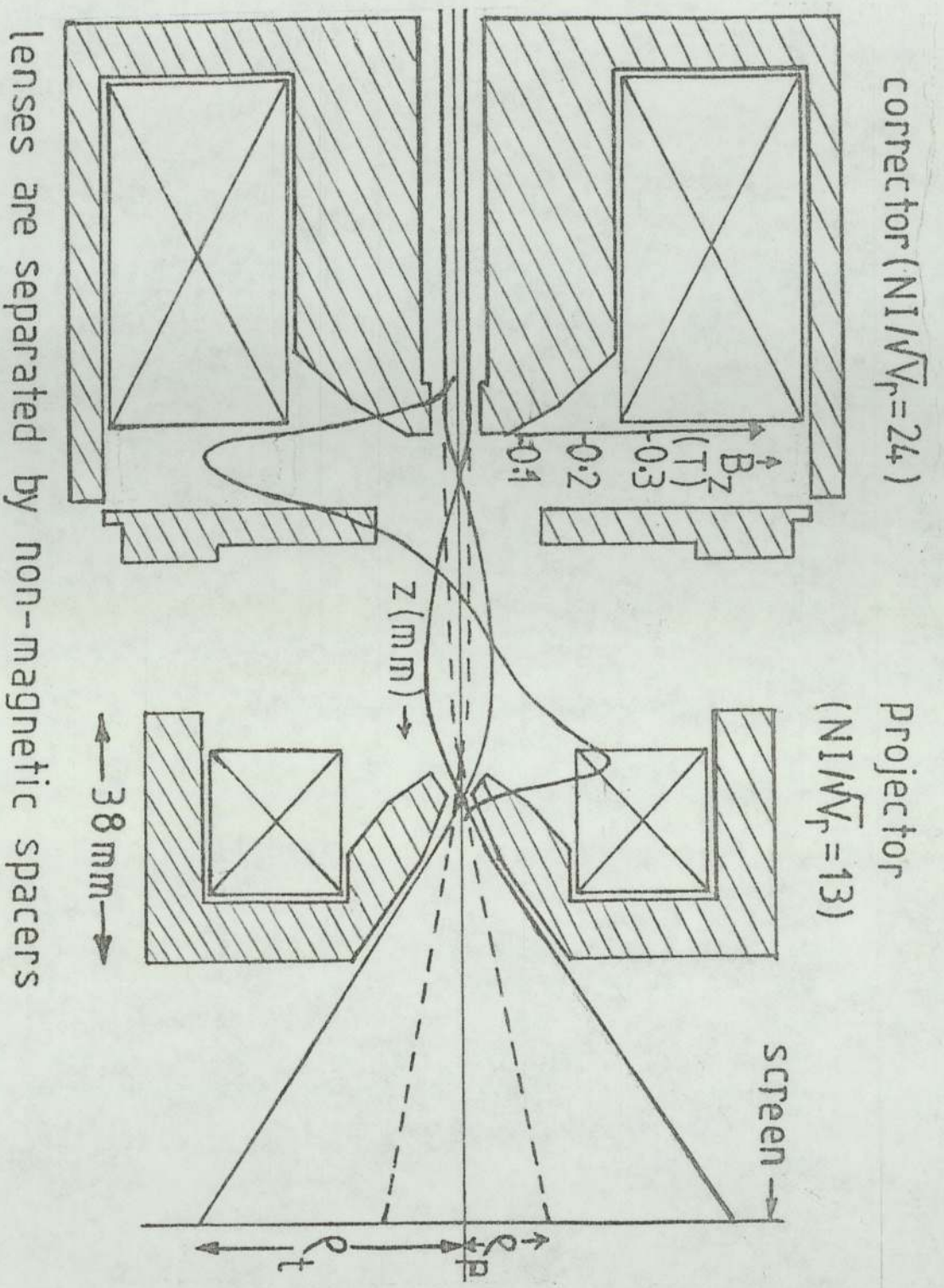

Figure (2.12) The final version of the two-lens projection system showing the axial magnetic field distribution and the off-axis trajectories for a parallel electron beam entering the corrector lens. Lens excitations are set for correction of distortion.

The **magnification** M_{corr} produced by the corrector lens can also be found from these electron trajectories. Thus in figure (2.12) the dashed lines indicate the trajectories when the projector lens alone is energised (image radius ρ_p). The full lines indicate the trajectories when both lenses are energised (image radius ρ_t). The ratio $\rho_t / \rho_p = M_{corr}$. In this example of figure (2.12) $M_{corr} = 3X$.

The distortion $(\Delta\rho/\rho)_{corr}$, radial or spiral, produced by the corrector lens is expressed in equation(2.12)as

$$(\Delta\rho/\rho)_{corr} = \pm\ Q^2_{corr} \tan^2\alpha_{corr}$$

The projection semi-angle α_{corr} may, for convenience, be expressed in terms of the projection semi-angle α_p of the two-lens system, as shown in equation (2.15).

Hence

$$(\Delta\rho/\rho)_{corr} = \pm\ Q^2_{corr} \left(\frac{f_p}{f_{corr} M_{corr}}\right)^2 \tan^2\alpha_p \quad \ldots(2.26)$$

The projector distortion $(\Delta\rho/\rho)_{proj}$, radial or spiral is usually influenced by the conjugates effect so that either of two approximate expressions may be used. The first is that of equation (2.21) and the second is derived from equations (1.7) and (1.12) where D and Q are replaced by D* and Q* respectively because of the projector finite conjugates.

Thus

$$(\Delta\rho/\rho)_{proj} = (Q^*_{proj})^2 \tan^2\alpha_p \quad \ldots\ldots\ldots(2.27)$$

where Q^*_{proj} is the quality factor of the projector lens for

finite conjugates and is related to Q_{proj} of the infinite conjugates by

$$(Q^*_{proj})^2 \simeq Q^2_{proj} \ (1 + 1.37m + 1.28m^2) \quad \ldots\ldots\ldots\ldots (2.28)$$

The effect of the projector conjugate ratio m on the final image radius ρ, the displacement $\Delta\rho$, and the distortion $(\Delta\rho/\rho)_{proj}$ is illustrated in figure (2.13). The resulting relationships in the figure are based on the following data

$D_{proj} = 5791.87\ m^{-2}$; $f_p = 10$ mm.; $NI/V^{\frac{1}{2}}_{r(proj)} = 13$; $r_{corr} =$ 2.25 mm. and $M_{corr} = 3X$. The figure shows two curves for $(\Delta\rho/\rho)_{proj}$; an approximate curve based on a constant $\Delta\rho$, and a reasonably accurate curve [so far as the approximate equation (1.12) permits]. At m = 0.1 the difference in $(\Delta\rho/\rho)_{proj}$ in the two curves of figure (2.13) is about 2% whereas in the Lambrakis et.al system ($m \simeq 0.3$) this difference is about 6%. It is therefore possible to assume that $\Delta\rho$ does not change appreciably with m.

The effective distortion $(\Delta\rho/\rho)_{eff}$ can now be obtained by adding equations (2.26) and (2.27).

i.e. $$(\Delta\rho/\rho)_{eff} = Q^2_{eff} \tan^2\alpha_p$$

$$= (Q^*_{proj})^2 \tan^2\alpha_p \pm Q^2_{corr} \left(\frac{f_p}{f_{corr} M_{corr}}\right)^2 \tan^2\alpha_p \quad \ldots\ldots\ldots (2.29)$$

where Q_{eff} is the effective quality factor of the two-lens projection system and is given by

$$Q^2_{eff} = (Q^*_{proj})^2 \pm Q^2_{corr} \left(\frac{f_p}{f_{corr} M_{corr}}\right)^2 \quad \ldots\ldots\ldots (2.30)$$

To correct radial and spiral distortion in the system, the magnetic fields produced by each of the two lenses must oppose each other. That is to say, the second term in equation (2.30) should be negative. It is also important that if $\alpha_p = 30^\circ$, Q_{eff} must not exceed 0.173 and 0.245 for the radial and spiral distortion respectively.

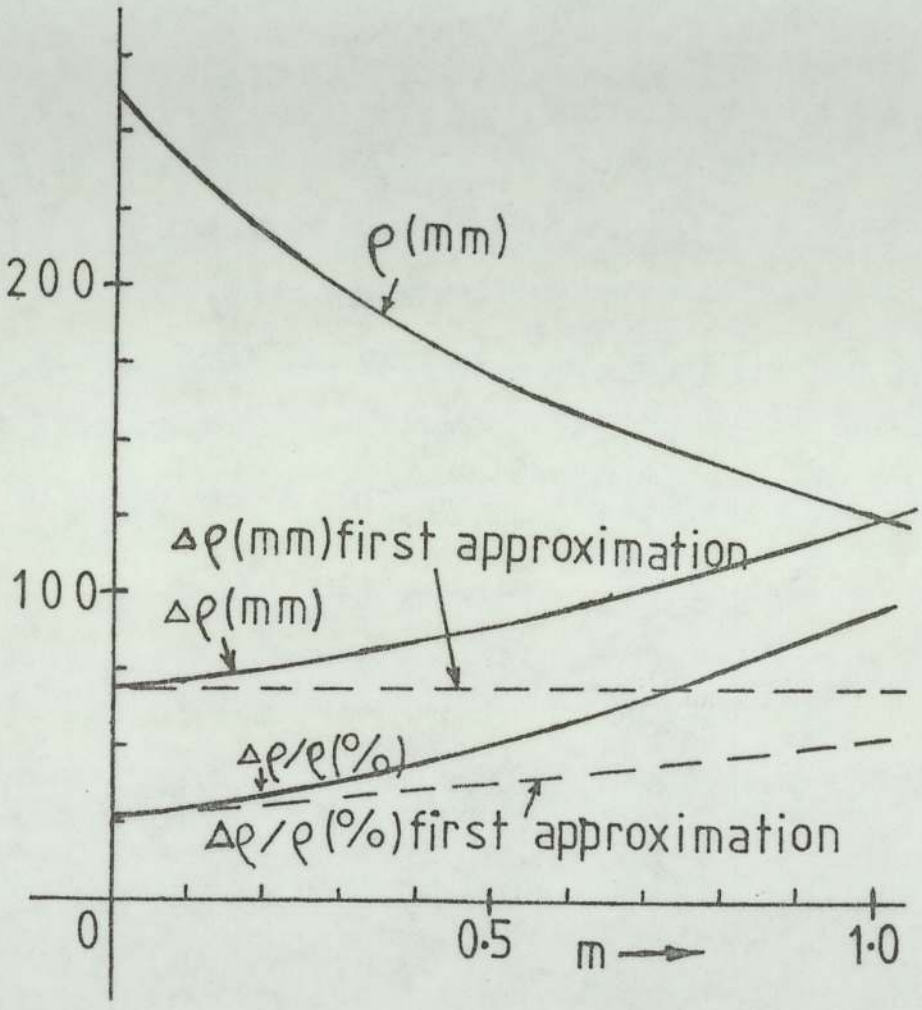

Figure (2.13) The effect of the projector conjugate ratio m on the radius of the image ρ, the displacement of $\Delta\rho$ and the projector distortion $(\Delta\rho/\rho)_{proj}$ at the final screen. $NI/V_r^{\frac{1}{2}}(proj) = 13$; $D = 5791.87\ m^{-2}$; $f_p = 10$ mm; $r_{corr} = 2.25$ mm. and $M_{corr} = 3X$.

CHAPTER 3

PRACTICAL METHODS FOR MEASURING DISTORTION

Distortion in the image can be measured conveniently by choosing appropriate specimens such as grids, cross-wires and straight edges. The effect of distortion on such elements can easily be calculated and measured. In Chapter (1) we defined distortion as $\Delta\rho / \rho = Dr^2$, in which r, the radial co-ordinate of the electron trajectory, is measured from the optical axis. In the image plane the radial height is represented by ρ and the optical axis by a single point, O, called the centre of the image. Point O will only coincide with the centre of the photographic plate, C, if the electron microscope is perfectly aligned. Figure (3.1) gives an illustrated example where O and C do not coincide. It is therefore necessary to devise a method for the location of the position of the centre of the image O.

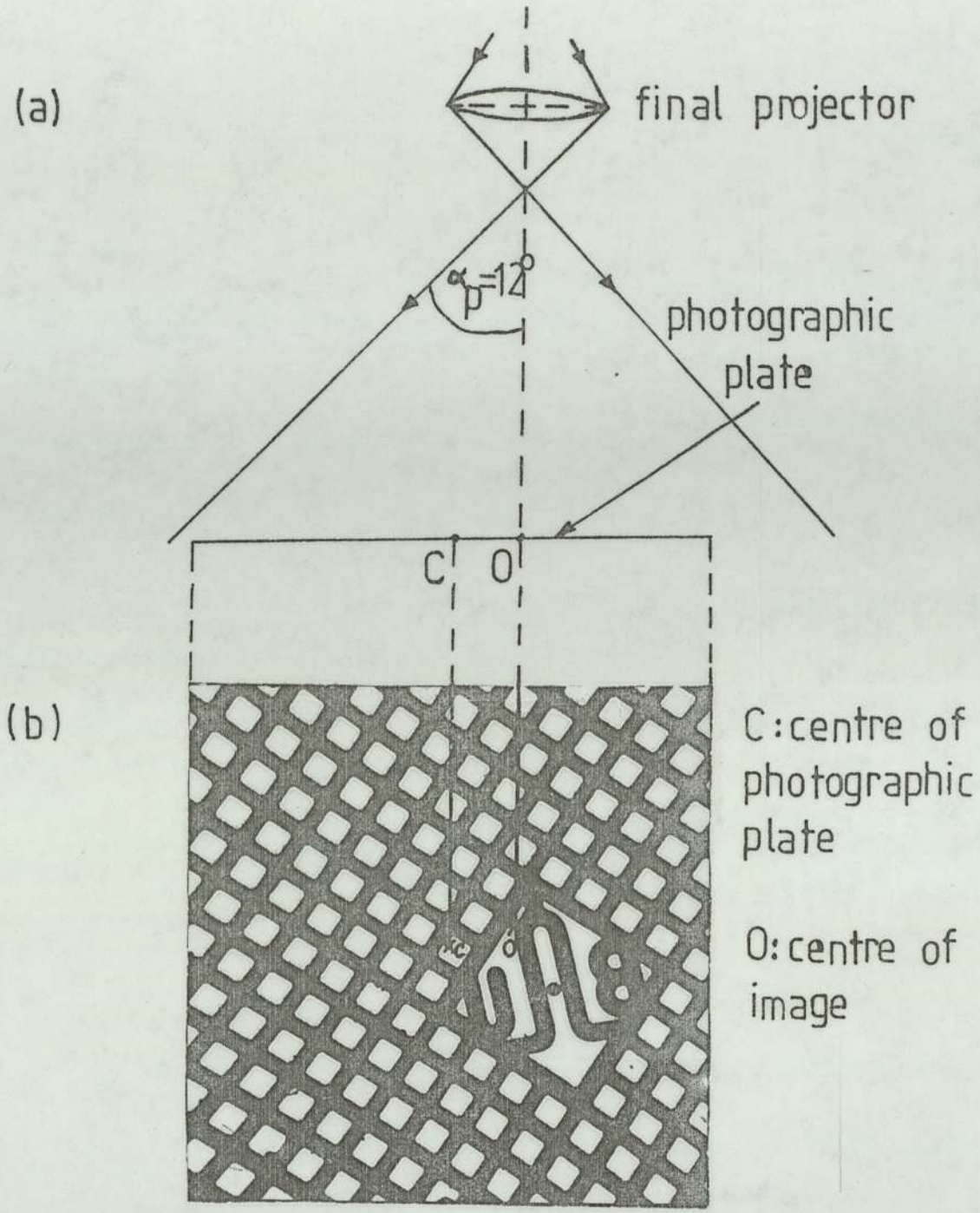

Figure (3.1) (a) Schematic diagram showing electron trajectories through the final projector lens to the photographic plate. O is the centre of the image and C is the centre of the photographic plate. (b) an image micrograph as recorded by the photographic plate showing the positions of O and C. $NI/V_r^{\frac{1}{2}}$(projector) 16.8; radial distortion 1%; spiral distortion 4%; $\alpha_p = 12^\circ$.

3.1 LOCATION OF THE CENTRE OF THE IMAGE

The centre of the image, O, is the only point that does not suffer any distortion because the radius of the image is zero. Now to locate the centre of the image, O, one has to choose a central area in the image where there is adequate geometrical symmetry and then select a point so that if the image or micrograph is mechanically rotated about this point the distortion at a given radius is constant. This can be carried out in practice by visual inspection.

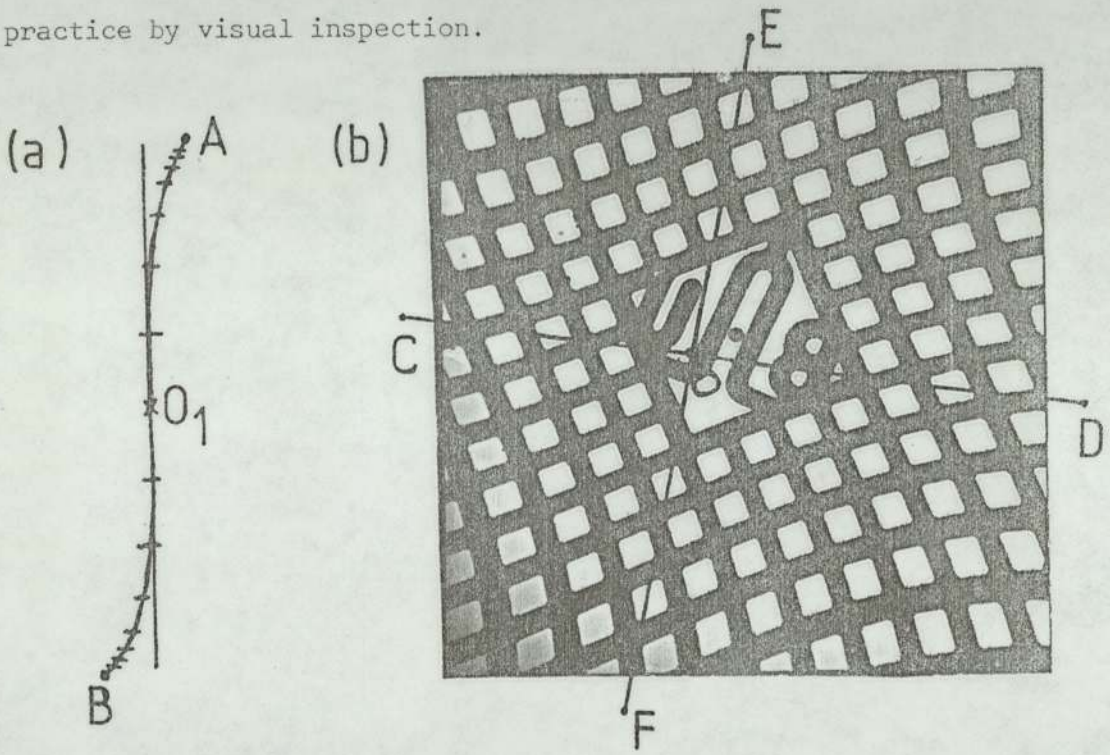

Figure (3.2) Location of a centre of the image of a (a) single distorted line (b) micrograph taken with a single-polepiece projector lens at $NI/V_r^{\frac{1}{2}} = 29$; radial distortion 20%; spiral distortion 15%; projection semi-angle α_p 12°.

Alternatively, we select a distorted line, e.g. the curved line AO_1B of figure (3.2a), and determine its centre O_1 in such a way that the curvature of this distorted line above and

below O_1 will be identical. We can then repeat this procedure for all the distorted lines from left to right in figure (3.2b) and join the resulting centres to obtain the straight line CD. Similarly, we can draw the straight line EF which join all centres of the distorted lines running from top to bottom in figure (3.2b). The intersection of lines CD and EF is the centre of the image, O.

3.2 MEASUREMENT OF RADIAL DISTORTION

In the following discussion we are mainly concerned with the pin-cushion form of radial distortion. However, the same principles hold true for barrel type radial distortion if the deviation, of the image point from its corresponding Gaussian image point, $\Delta\rho$ is replaced by $-\Delta\rho$. Consider the simulated image grid of figure (3.3). The full lines represent the distorted image suffering from pin-cusion distortion and the broken lines represent an undistorted, Gaussian, image. The points O, P_1, P_2, P_3, P_4 and P_5 of the Gaussian image are equally spaced where O is the centre of the image. Radial distortion does not affect point O but the other points quoted above, are displaced respectively to points P'_1, P'_2, P'_3, P'_4 and P'_5. The radial distortion $\Delta\rho/\rho_{rad}$ at point P_5 is therefore $\Delta\rho/\rho_{rad} = P_5P'_5/OP_5$.

However, it should be remembered that in an actual micrograph the points P_1 to P_5 do not exist and hence the only direct measurements we can make are of OP'_1, OP'_2, OP'_3, OP'_4 and OP'_5. If the specimen is a fine mesh grid, we can make the approximations $OP \simeq OP'_1$, and $OP_5 = 5OP_1 \simeq 5OP'_1$ so that

$$\Delta\rho/\rho_{rad} \simeq (OP'_5 - OP_5)/OP_5$$

$$= (OP'_5 - 5OP'_1)/(5\ OP'_1).$$

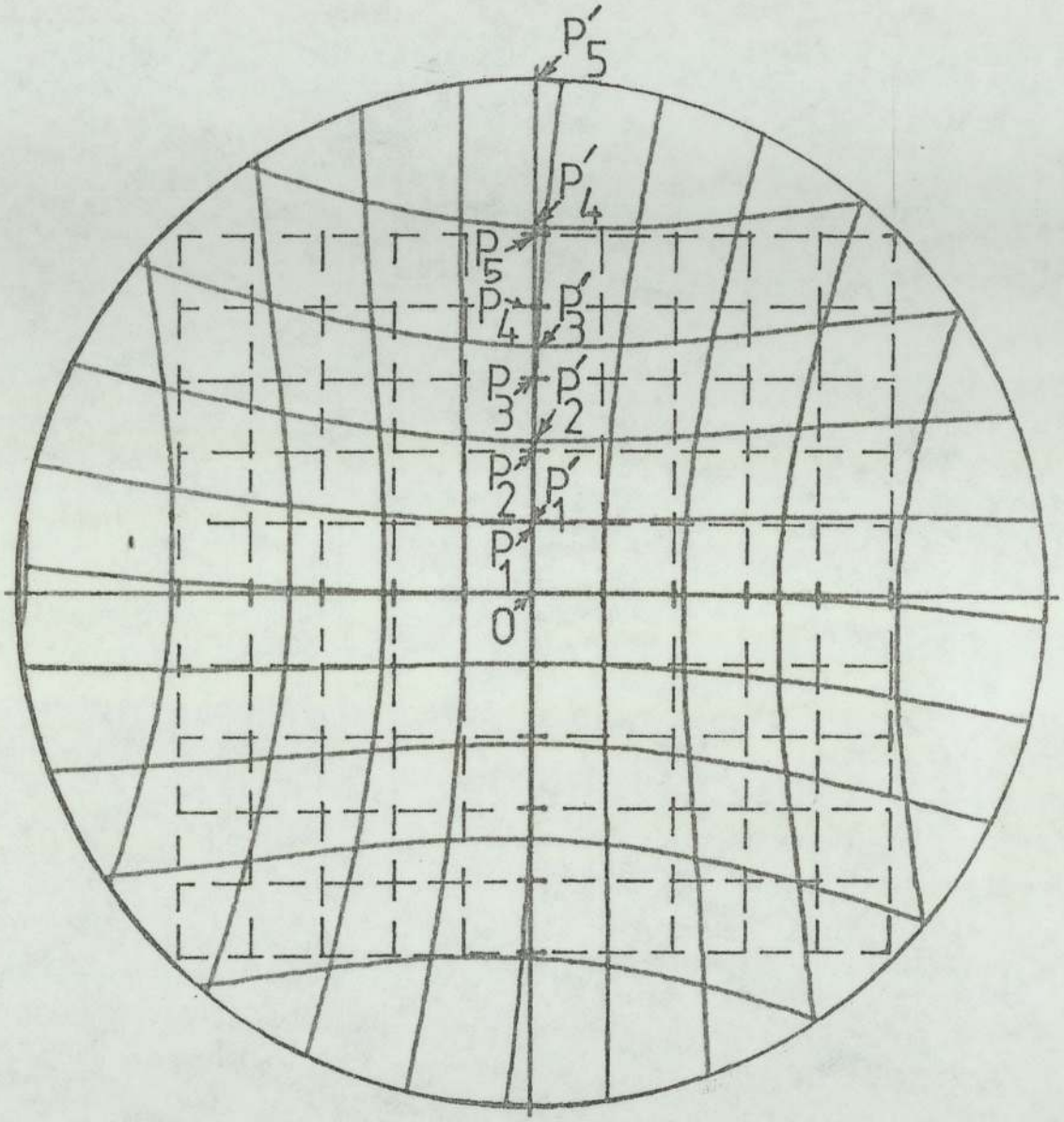

$$\rho = OP_5$$

$$\Delta\rho = P_5P'_5$$

Figure (3.3) Image simulation of an undistorted image (broken line) and a distorted image (full line) of a square grid. Pin-cushion distortion at the edge of the circle of radius OP_5 is 42.5%. Note the presence of 5.2% spiral distortion.

It is perhaps necessary to mention that in this example there are five grid lines from O to P_5 where P_5 is the point at which distortion is measured. The same method can of course be applied to any number of grids as convenient.

If the specimen is in the form of a long thin straight wire an alternative method can be adopted. Since the wire is assumed to be thin compared to its length, then the displacement or distortion near the centre will be ignored, as shown in figure (3.4). In other words, the shift of point P to P' is negligible. Hence

$$OP \simeq OP'.$$

The distortion at radius ρ may then be evaluated from figure (3.4) as

$$\Delta\rho/\rho = x/R$$

where R is the radius of the wire and $(x + R)$ is the radius of the distorted wire at the edge of the micrograph.

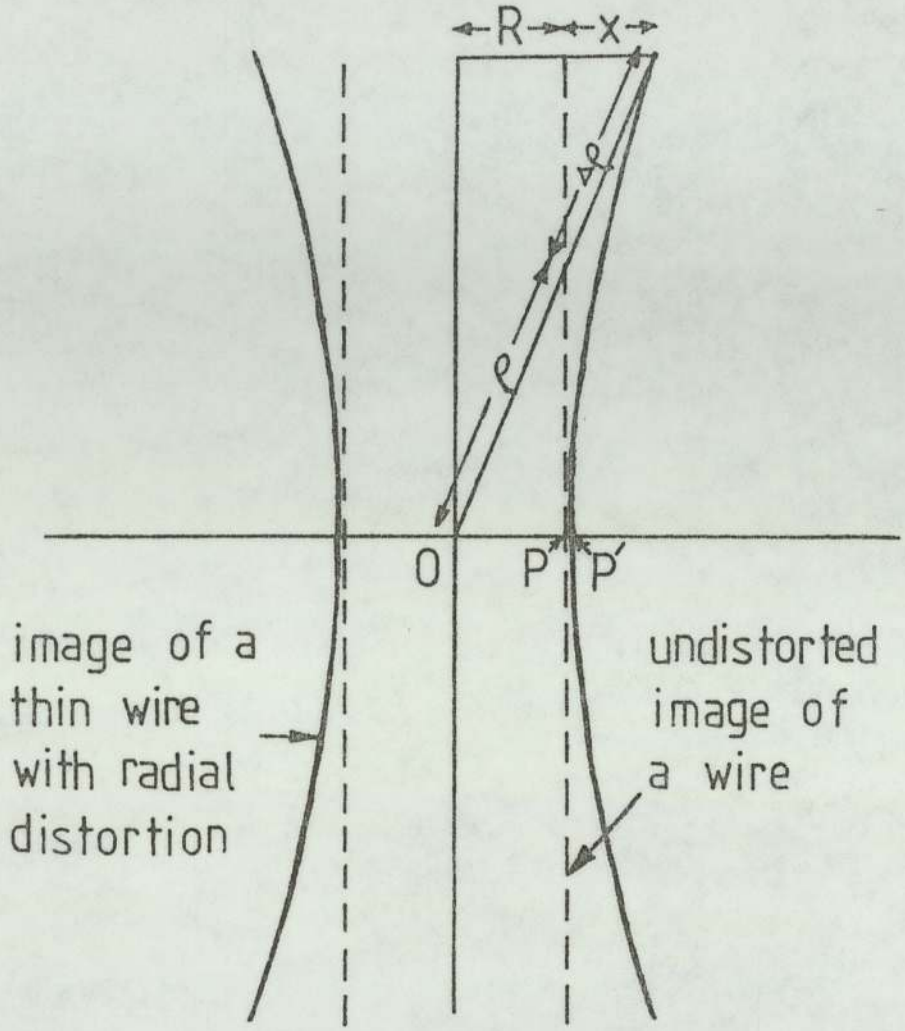

Figure (3.4) The radial distortion of a long thin straight wire.

R is the radius of the image of the undistorted wire.

3.3 MEASUREMENT OF SPIRAL DISTORTION

3.3.1 MEASUREMENT OF PURE SPIRAL DISTORTION

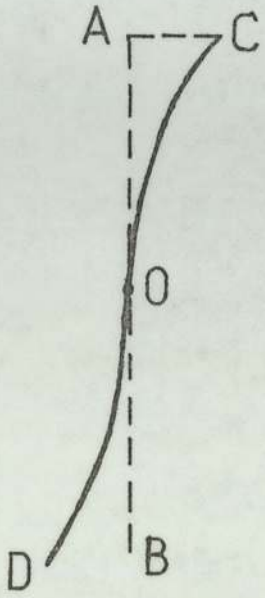

Figure (3.5) A distorted image of a thin wire CD of a grid caused by spiral distortion.

Since measurements of distortion are made from the centre of the image O, then we must carry them on the distorted line of the image of the grid that passes through O, figure (3.5).
We then draw a straight line AB passing through O so that the deviation from the displaced image COD is identical above and below O but keeping this deviation to a minimum and that the line AB and the displaced image COD should not cross in any point other than O.
The spiral distortion $\Delta\rho/\rho_{sp}$ at A is then given by

$$\Delta\rho/\rho_{sp} = AC/OA .$$

3.3.2 MEASUREMENT OF SPIRAL DISTORTION IN THE PRESENCE OF RADIAL DISTORTION

An accurate measurement of spiral distortion cannot be made unless subtraction of the simultaneously occuring radial distortion, if any,is dealt with. The radial distortion being affected by the stretch or contraction of image lengths, reveals the same influence on the rotation of the image points either by increasing the spiral distortion (when pin-cushion is present) or decreasing it (barrel presence). And hence the measured value of spiral distortion should thus be multiplied by the ratio

$$\left(\frac{\rho \mp \Delta\rho_{rad}}{\rho}\right)^2 .$$

Therefore, the actual spiral distortion becomes

$$\left(\frac{\Delta\rho}{\rho}\,sp\right)_{actual} = \left(\frac{\Delta\rho}{\rho}\,sp\right)_{measured} \left(\frac{\rho \mp \Delta\rho_{rad}}{\rho}\right)^2$$

The negative and positive signs refer to the alternatives of pin-cushion and barrel respectively.

3.4 COMPUTER SIMULATION OF THE FINAL IMAGE

Image simulation is the imitation of the image we see on the screen or photographic plate by a graphical representation. The simulation is carried out with the mathematically derived formulae, equations (A6.6) and (A8.7), of Appendix (6) for the determination of the coordinates of displaced image points due to radial and spiral distortion. The purpose of the simulation is to

replace the methods of measuring distortion described in the previous sections. Thus, adequate number of simulation charts should be made to cover all the practical possibilities of combining radial and spiral distortion.

A computer program is then written, Appendix (6), to solve equations (A6.6) and (A6.7) as well as to draw the graphical simulation of a square grid. The micrograph of figure (3.6) was taken with the single-polepiece corrector lens of Chapter 5. The computer simulation of this micrograph is superimposed on it in the same figure.

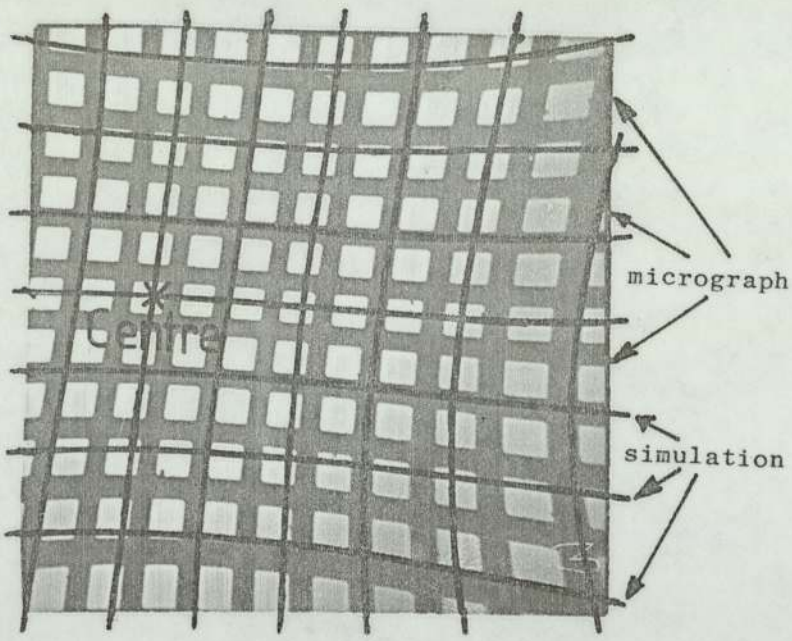

Figure (3.6) A computer image simulation superimposed upon a micrograph image taken with a single-polepiece lens at $NI/V_r^{\frac{1}{2}} = 10$. At an image radius of 50 mm. the radial distortion is 11%, the spiral distortion is 5% and α_p is 12°.

The image simulation can also be used to illustrate that spiral distortion does not change the area of the image. This is illustrated in figure (3.7) where the radial distortion is zero and the spiral distortion is 26% at screen diameter of 10 cm., shown by circle.

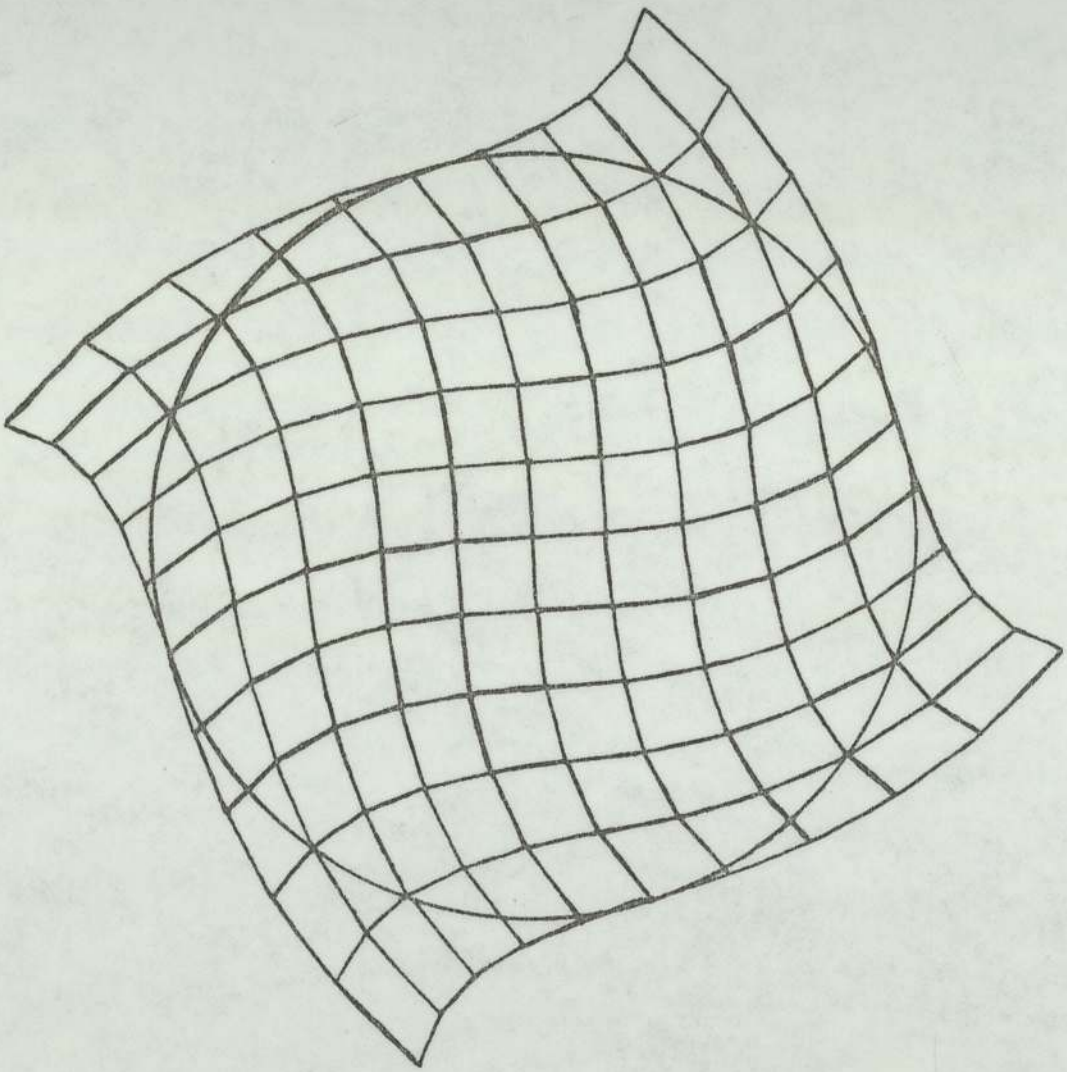

Figure (3.7) Image simulation of pure spiral distortion 26% at image radius ρ of 50 mm. shown by circle. (Note equal areas of grids in the absence of radial distortion).

3.4.1 EFFECT OF LENS ASTIGMATISM ON THE FINAL IMAGE

If the lens considered suffers from astigmatism due to lack of mechanical symmetry, the image simulation formulae for distortion, equations (A6.6) and (A6.7) of Appendix (6), should then be adapted accordingly. There, the image coordinates Mx and My of figure (A6.4) will then become $(Mx + \Delta x)$ and $(My + \Delta y)$ where

$$\Delta x = - Mky_o^2 \, r \cos\theta$$

and

$$\Delta y = + Mky_o^2 \, r \sin\theta$$

where M is the magnification; k is the astigmatism coefficient; y_o is the object point height from the axis $= M(x^2 + y^2)^{\frac{1}{2}}$; and r is the radial height of ray at the bore of the lens.

CHAPTER 4

THE SINGLE-POLEPIECE PROJECTOR LENS

4.1 DESIGN OF AN EXPERIMENTAL PROJECTION SYSTEM

In order to realise an experimental wide-angle projector lens-system of the type described in the previous chapters it was decided to modify the projection system and viewing chamber of an AEl EM6 100 KV electron microscope. This involved a considerable redesign and modification of the lower part of the instrument. In order to test the feasibility of the correcting system, existing components such as single-polepiece projector lenses from previous projects were pressed into service.

Figure (4.1) shows the drastically modified viewing chamber compared with that of the original standard EM6 electron microscope. The essential features of the redesigned projection

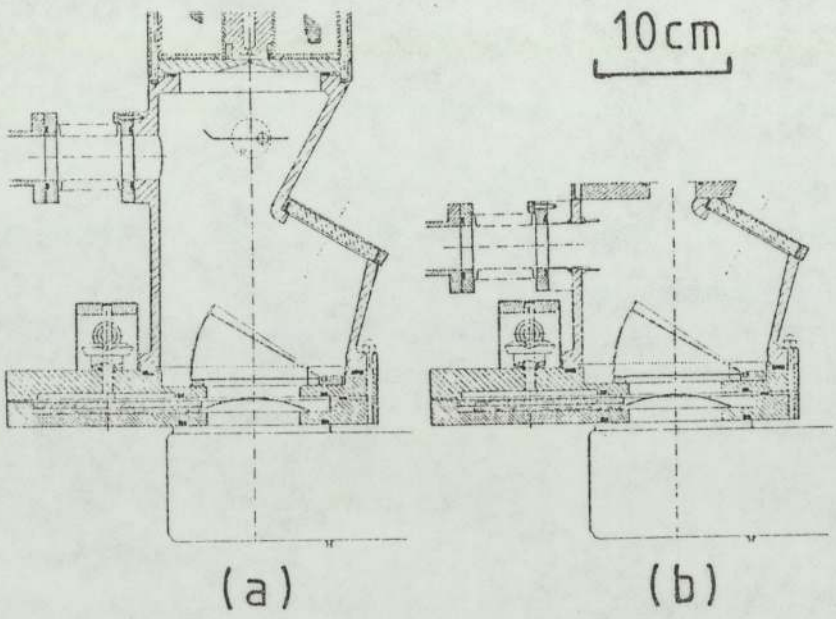

Figure (4.1) Cross-sectional drawings of (a) standard EM6 and (b) the heavily modified experimental viewing chamber.

system are compared with that of Lambrakis et.al.(1977) in figure (4.2). The present redesigned system consists basically of a shortened viewing chamber of height 14.9 cm. compared with 23.5 cm. in the EM6 TEM; an experimental 1MV single-polepiece projector lens of axial height 3.8 cm. and focal length 8 mm. This lens was originally designed by Newman (1976) and later employed by Marai (1977) and Lambrakis et.al.(1977). Marai, however, opened the back side of this lens into a smooth cone of projection semi-angle of up to $\alpha_p = 22^\circ$, as shown in figure (4.2). It was then found necessary to remachine the bore to a fine finish thus increasing its diameter from 2 mm. to 2.5 mm.

In addition, we employed a single-polepiece miniature 100 KV intermediate (correcting) lens built by Juma (1975). This had an axial depth of 2.9 cm. and was separated from the final projector lens by interchangeable duralumin spacers of maximum thickness 6.15 cm. in contrast to the narrow vacuum liner tube used by Lambrakis et.al.(1977). The spacer between the two lenses had a 2.6 cm. inside diameter which was wide enough so as to accept wider off axis electron trajectories needed for more area of specimen to be investigated and also to permit a larger field of view. The correcting lens was preferred to that employed by Lambrakis because of its wider bore, bore diamter 15 mm., so as not to restrict the field of view. This lens replaced the intermediate of the EM6 and acted as a spiral distortion compensator when its magnetic field opposed that of the projector. The projection distance L, from the focal point or more precisely from the crossover at the final projector lens to the photographic plate was thus reduced from 36 cm. to 24.5 cm. The large semi-angle , $\alpha_p =$

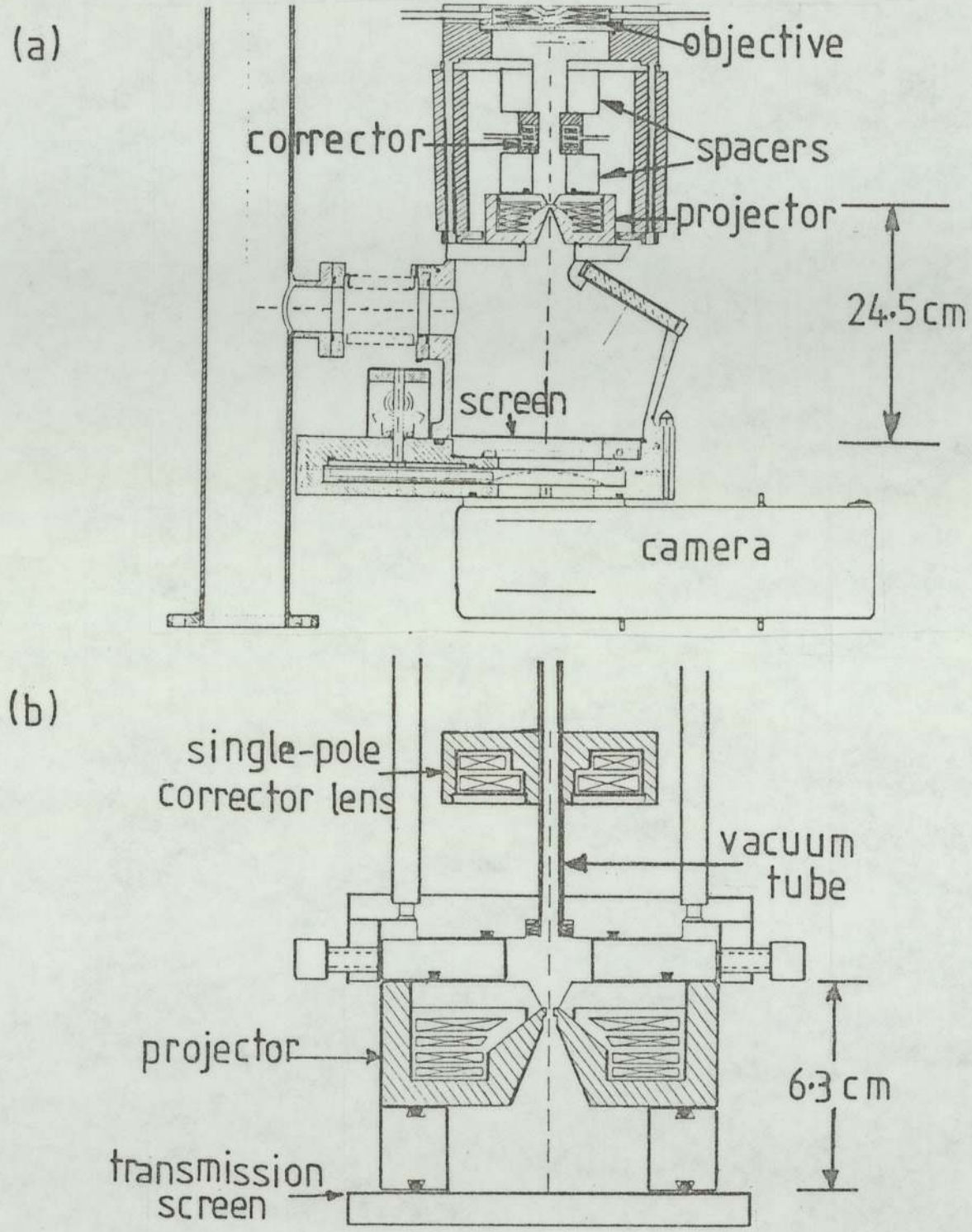

Figure (4.2) Comparison between the experimental projection system (a) for the present preliminary experiments using readily available projector and corrector lenses and (b) that of Lambrakis et.al.(1977).

22°, of the conical back bore of the projector permits an unusually large image angle at the projector lens thus contributing to a shorter L. This angle was adequate to fill the maximum diameter, 14 cm., of the enlarged viewing screen at such a short throw distance of 19.1 cm. from the crossover to the screen. The rest of the microscope column was the same as that of the EM6 TEM except for the objective lens. This was a miniature twin-polepiece objective lens, built into the instrument by Juma (1975). It was retained since it was convenient to make use of it, but it did not influence the investigation of the projector system. The cavity between the correcting lens and the objective could then be used to accommodate another intermediate lens or lenses for higher magnification when required.

In order to facilitate the alteration of the position of the corrector lens without dismantling the entire column, the objective and condenser lenses were supported on pillars, as shown in figure (4.3). These supports were designed in such a way that they could be used to jack-up the rest of the column so that the corrector lens and spacers could be altered when necessary. Figure (4.3) also exhibits the external mechanical alignment controls for centring the final projector.

Finally, the small viewing screen of the standard EM6, 8.3 x 8.4 sq.cm., was extended by surrounding it by a further fluorescent screen of 14 cm. outside diameter for visual observation of image distortion up to a projection semi-angle $\alpha_p = 22^{\circ}$. Clearly the existing camera, figure (4.2), could only accept an image with $\alpha_p = 12^{\circ}$. This was considered adequate for preliminary experiments. For photographing the image at $\alpha_p = 22^{\circ}$, it was

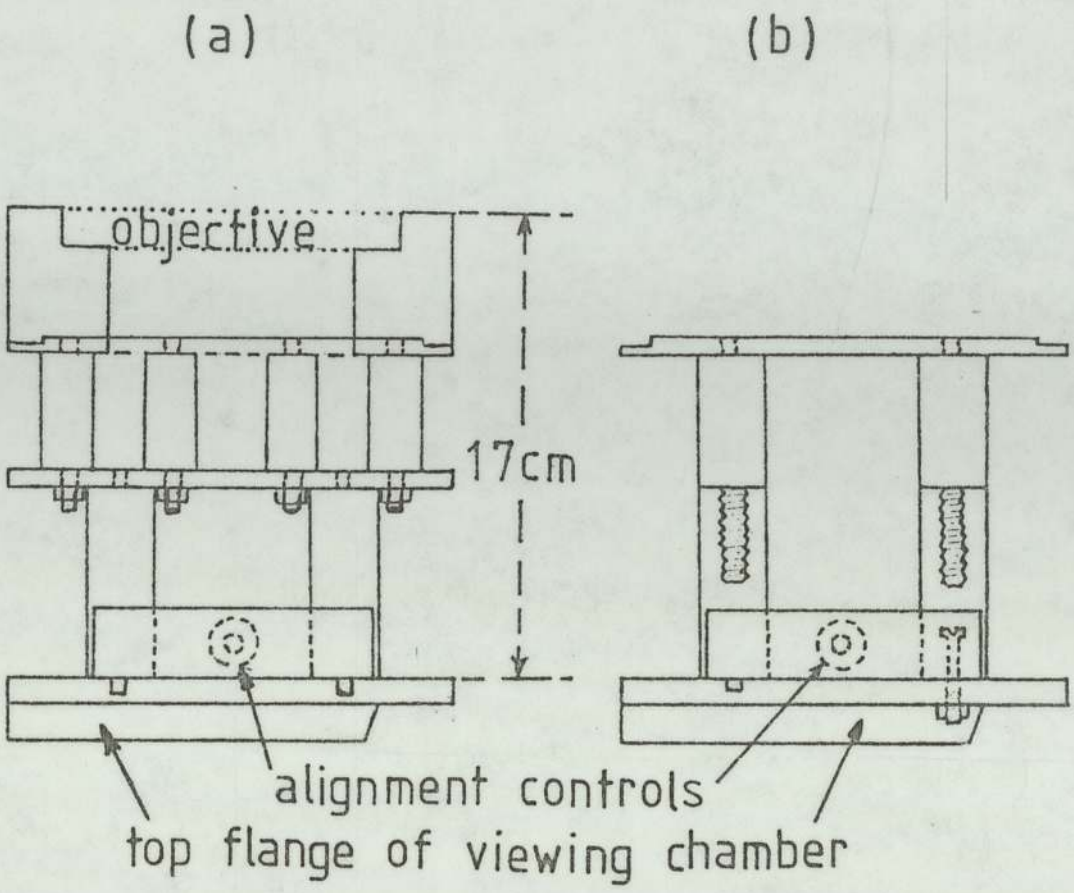

Figure (4.3) Column supports of microscope. The supports enclose the projection lenses. (a) front view (b) rear view. The alignment facilities for the final projector are also shown.

decided to adopt external photography, as later described in Chapters (6) and (7).

4.2 ELECTRON-OPTICAL PROPERTIES OF THE EXPERIMENTAL SINGLE-POLEPIECE PROJECTOR LENS

As the projector lens bore had been remachined, as explained in the previous section, it was necessary to redetermine its electron-optical properties. The field distribution of the lens was measured using a Hall probe and a Gaussmeter, figure (4.4). The measured field distribution was checked for accuracy by

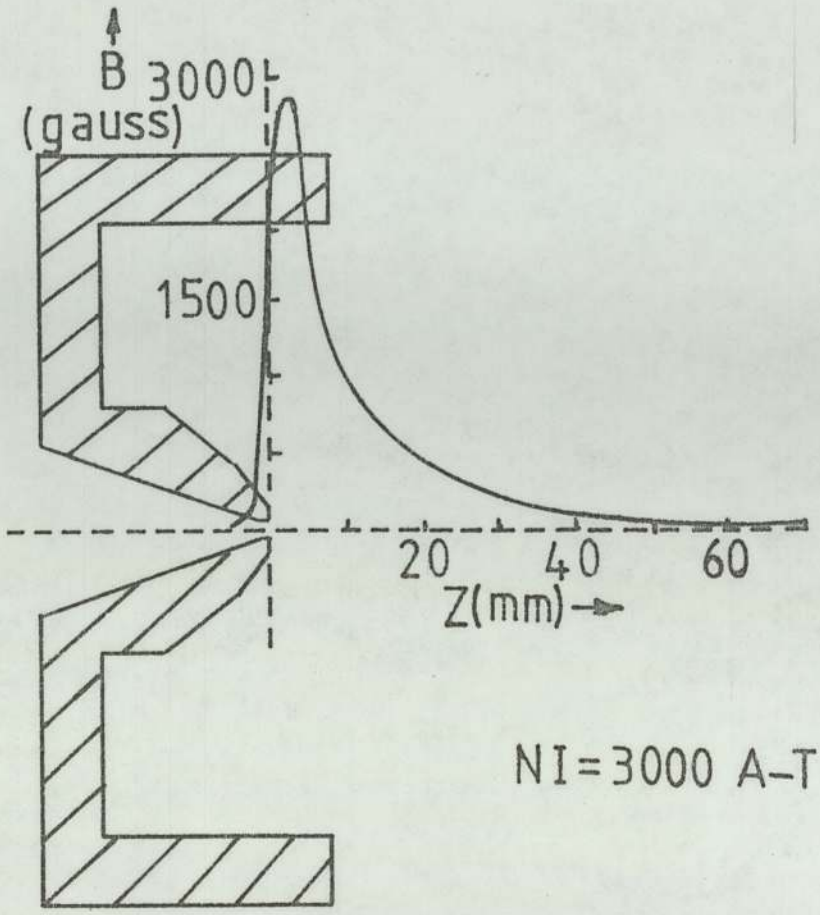

Figure (4.4) Cross-section of the remachined projector lens and its field distribution. Half-width a = 7.6 mm.

comparing the area under the field distribution with the known number of ampere-turns according to Ampere's law

$$\oint (B_z / \mu_r)\, dz = \mu_o NI \qquad \text{.....(4.1)}$$

The magnetic field B_z and the corresponding axial distance z from the lens snout was then fed into the computer for various calculations of focal properties and aberrations. Though single-polepiece projector lenses should be operated in their preferred direction, i.e. snout facing incoming electron beam, to yield the least possible

spiral distortion, the computation was, in fact, carried out for both orientations for completeness. The lens properties for the unfavourable directions gave useful information for the design of corrector lenses, where it is actually desirable to have large amounts of spiral distortion.

The field distribution of the remachined projector lens, shown in figure (4.4), has a half-width a = 7.6 mm. The half-width is usually a good guide to the magnitude of the minimum projector focal length f_p. This is shown in figures (4.4) and (4.5) in which the calculated focal properties are shown. The minimum projector focal length $f_p \simeq 8$ mm. is approximately equal to the half-width a = 7.6 mm.

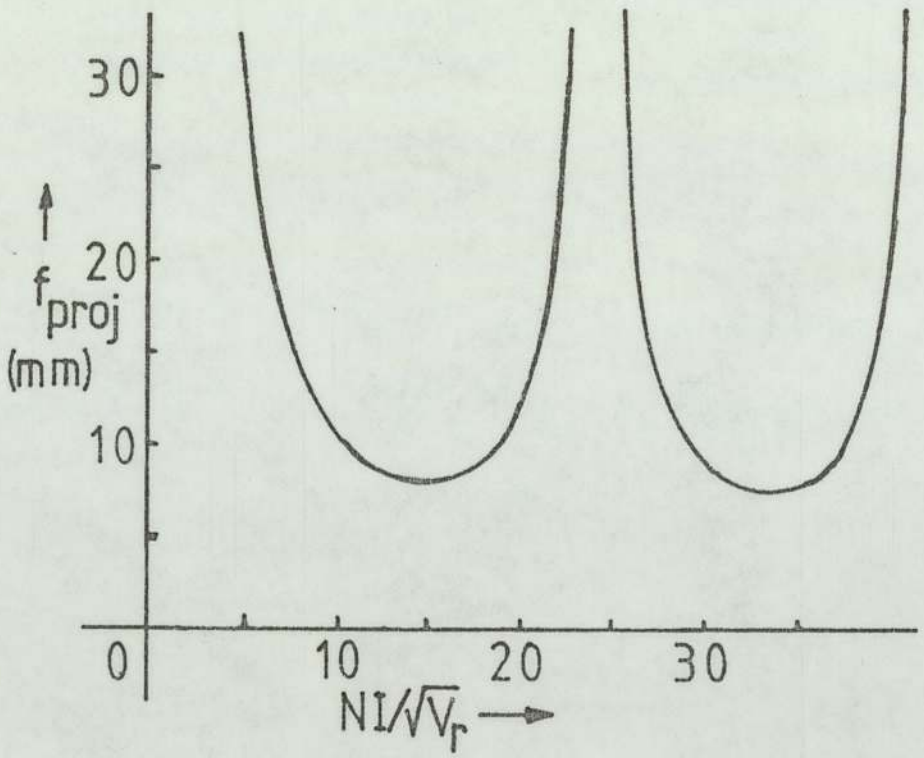

Figure (4.5) The focal length of the remachined projector lens as a function of the excitation parameter.

In wide-angle projector lens the exit cone of the pole-piece must not obstruct the electrons emerging at wide angles. The ray trajectories are illustrated in figure (4.6). This shows

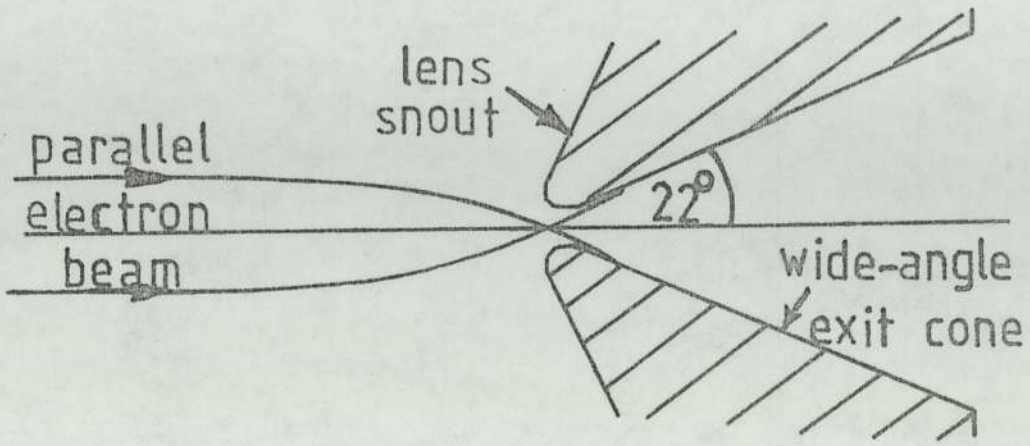

Figure (4.6) Critical wide-angle ray trajectories through the remachined projector lens.

that a single-polepiece lens can accept a wide bundle of rays and allow them to emerge from the lens in a wide angle in spite of the narrow bore in the polepiece itself. For projection semi-angles greater than $\alpha_p = 22^\circ$ extra special care has to be taken in the correct shaping of the polepiece, as shown in Chapter (7).

The calculated distortion coefficients D_{rad} and D_{sp} are shown in figure (4.7) against the excitation parameter $NI/V_r^{\frac{1}{2}}$. The solid lines refer to the distortion coefficients when the projector lens is oriented in its preferred direction whereas the dashed lines indicate the distortion coefficients for the non-preferred direction of the lens. The coefficient of spiral distortion

D_{sp} for the preferred direction increases gently from $D_{sp} = 0$ at $NI/V_r^{\frac{1}{2}} = 0$ to about $D_{sp} = 1 cm.^{-2}$ at $NI/V_r^{\frac{1}{2}} = 14$. The curve then maintains this value ($D_{sp} = 1\ cm.^{-2}$) up to the excitation of $NI/V_r^{\frac{1}{2}} = 22$. It is this characteristic of producting low distortion, particularly over such a wide range (plateau) from $NI/V_r^{\frac{1}{2}} = 14$ to $NI/V_r^{\frac{1}{2}} = 22$, that led to the choice of a single-polepiece projector lens. The coefficient of radial distortion D_{rad} D_{rad} is zero at $NI/V_r^{\frac{1}{2}} = 17.8$. It is therefore possible to operate the projector in such a way that it produces a predetermined amount of pin-cushion distortion by reducing its excitation (by up to 21%) without affecting the coefficient of spiral distortion D_{sp}. This unique property of the single-polepiece lens will be employed for the correction of radial and spiral distortion in Chapters (6) and (7). At excitations higher than $NI/V_r^{\frac{1}{2}} = 22$ the coefficient of spiral distortion D_{sp} rises rather rapidly relative to that part of the curve where $NI/V_r^{\frac{1}{2}} < 14$.

The corresponding quality factors Q_{rad} and Q_{sp}, for the two orientations of the projector lens relative to the electron gun, and their dependence on the excitation parameter $NI/V_r^{\frac{1}{2}}$ are shown in figures(4.8) and (4.9). It is thus clear from these figures that a zero distortion coefficient, D_{rad} or D_{sp}, does not imply that the image distortion will be zero. This is because the focal length under these conditions is very large and results in a very high distortion since $Q^2 = f_p^2 D$ where Q^2 is proportional to the distortion in the image. Here Q and D apply to both radial and spiral distortion.

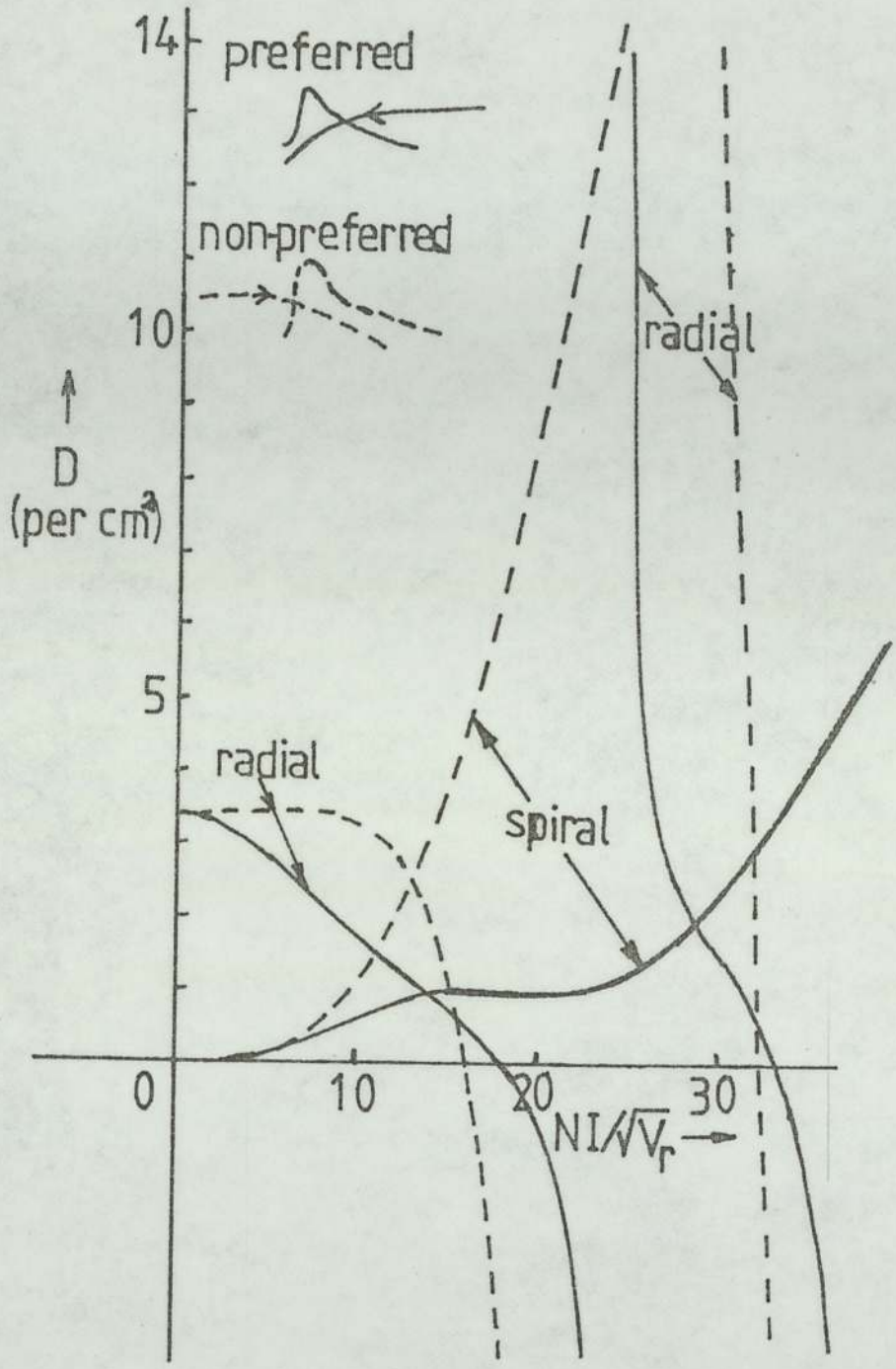

Figure (4.7) Distortion coefficients of the remachined projector lens for preferred and non-preferred orientations of the lens with respect to the incoming electron beam. Positive and negative radial distortion denote pin-cushion and barrel distortion respectively.

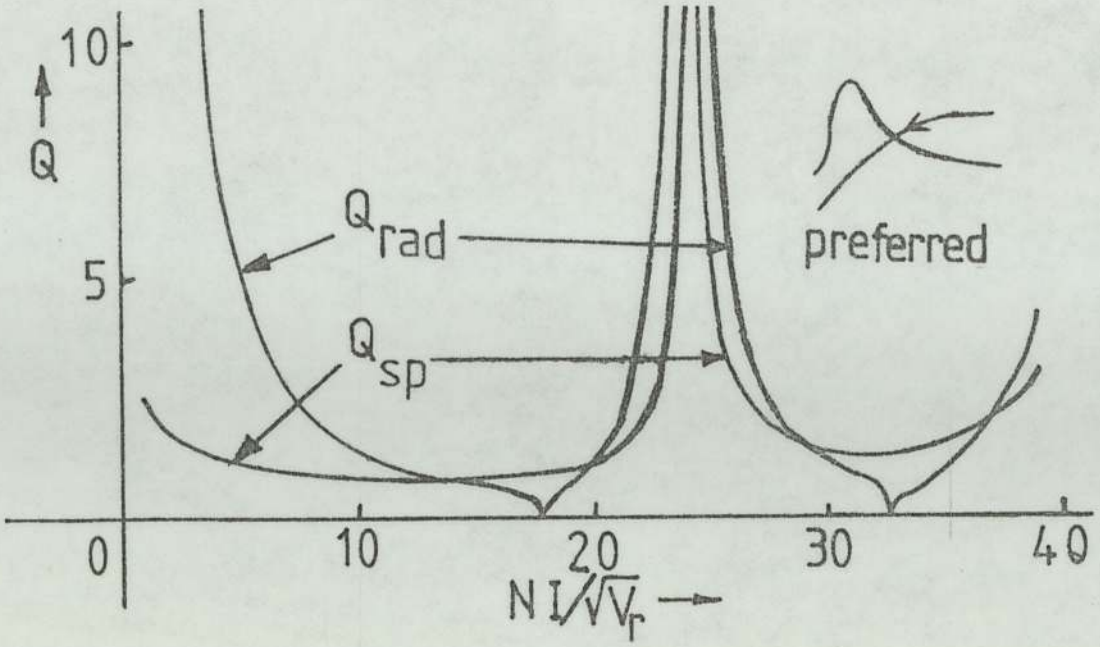

Figure (4.8) Quality factors Q_{rad} and Q_{sp} versus $NI/V_r^{\frac{1}{2}}$ for the preferred direction of the remachined projector lens.

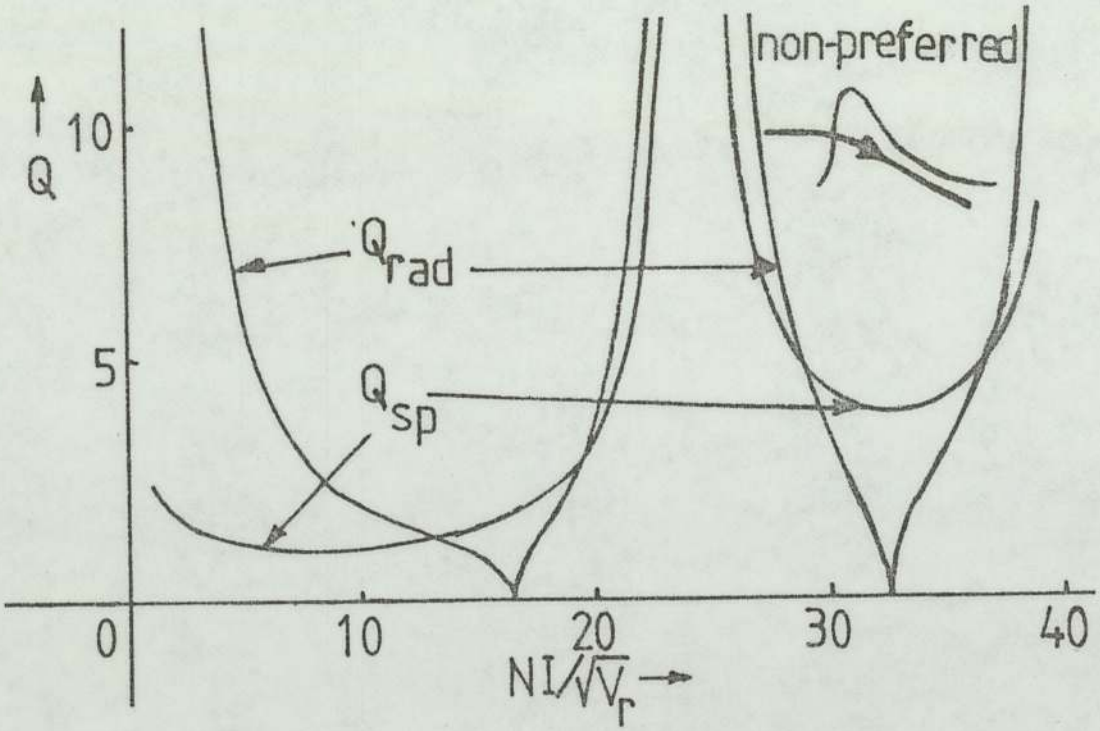

Figure (4.9) Quality factors Q_{rad} and Q_{sp} versus $NI/V_r^{\frac{1}{2}}$ for the non-preferred direction of the remachined projector lens.

4.3 PERFORMANCE OF THE EXPERIMENTAL PROJECTOR LENS

Images of low distortion are usually obtained when the projector is operated in the region of minimum focal length, i.e. at maximum magnification. Near maximum magnification radial distortion was measured and found to be essentially absent, while spiral distortion amounted to 2-3% . As mentioned previously spiral distortion below 2% is very difficult to detect. Since the projector lens was operated near its minimum focal length, the focal point was close to the apex of the back cone, as shown in figure (4.6); the lens structure does not restrict the field of view ($\alpha_p \simeq 22^\circ$). Even if the excitation of the projector lens is varied by $\pm$ 20% a projection semi-angle $\alpha_p \simeq 22^\circ$ can be obtained, as shown in figure (4.10).

As previously explained the maximum projection semi-angle of the modified EM6 camera was extended from 8° to 12°. However, visual estimates of distortion could be made on the extended fluorescent screen. These showed that in the region of maximum magnification the radial distortion was negligible for $\alpha_p = 22^\circ$. However, the spiral distortion was clearly visible and estimated at 10%, in agreement with calculation.

Images obtained at $\alpha_p = 12^\circ$ using the EM6 camera are shown in figure (4.11) and (4.12); the specimen is molybdenum trioxide mounted on a 400 mesh grid. These displayed the excellent performance of the projector lens in respect to distortion. A series of micrographs were taken at varying excitation parameters $NI/V_r^{\frac{1}{2}}$ and the corresponding radial and spiral distortion were evaluated. The result of these were in good agreement with the computed

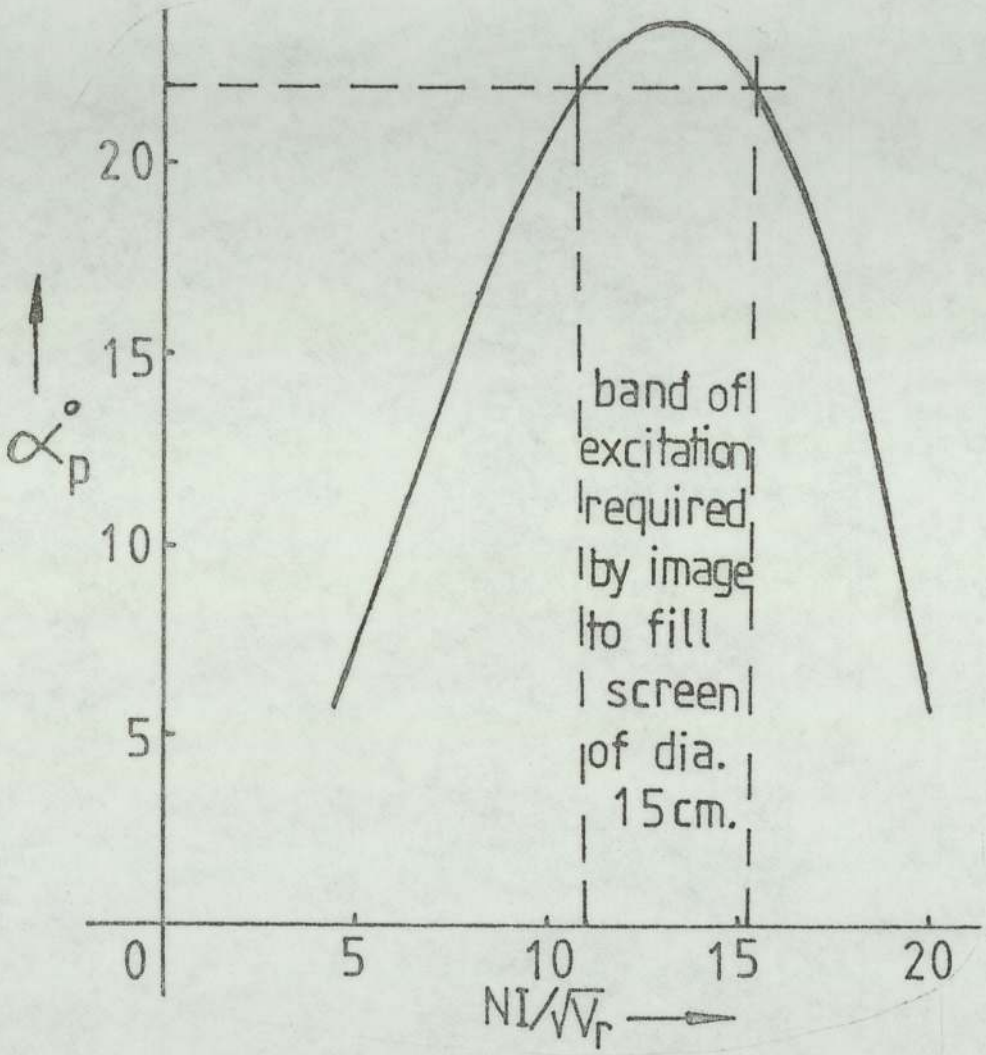

Figure (4.10) Projection semi-angle α_p of the remachined projector lens against the excitation parameter $NI/V_r^{\frac{1}{2}}$.

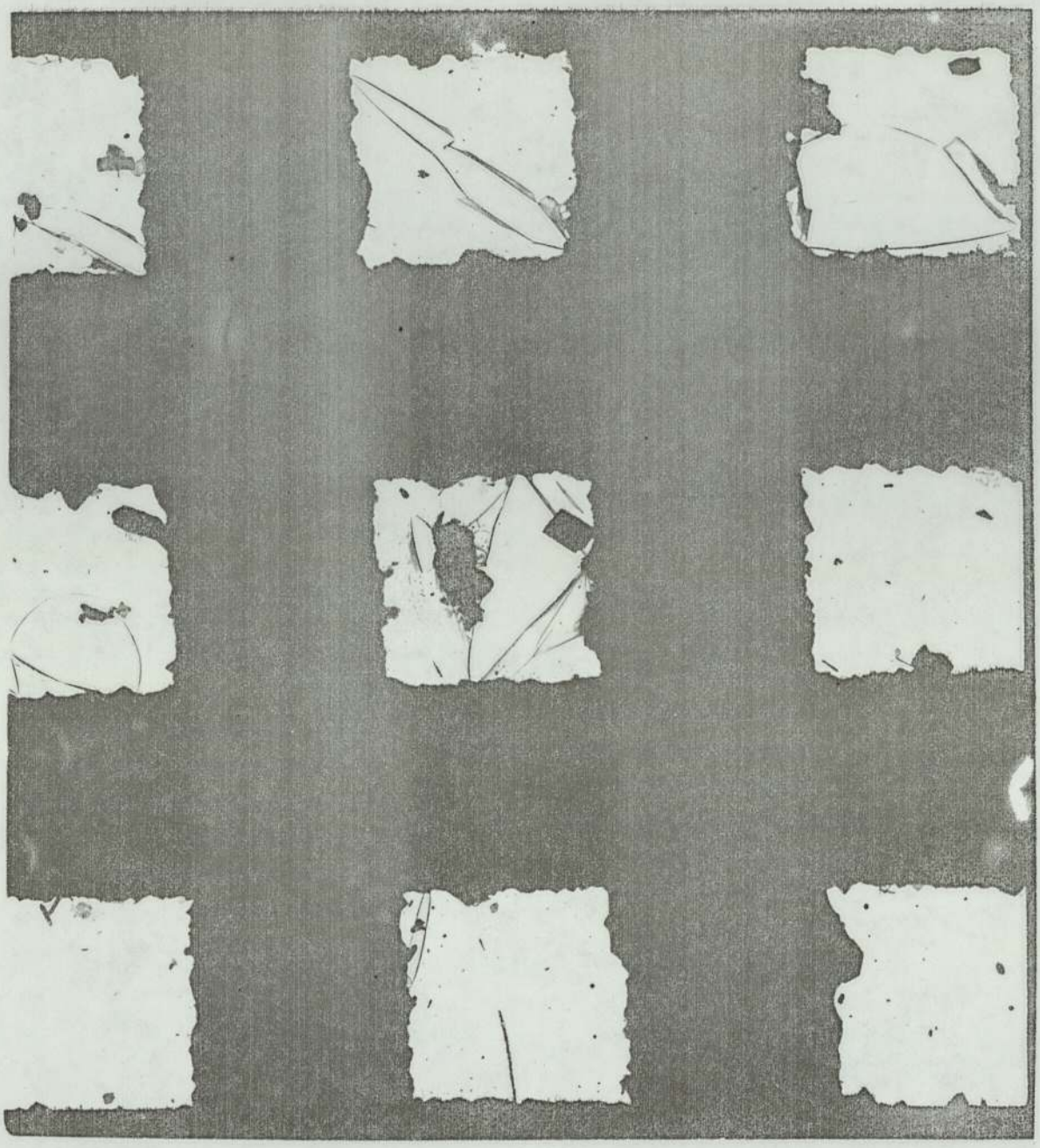

Figure (4.11) Electron micrograph of molybdenum trioxide mounted on a 400 mesh grid and taken with the remachined single-polepiece projector lens, adjusted for zero radial distortion ($NI/V_r^{\frac{1}{2}} = 15.5$). Maximum projection semi-angle $\alpha_p = 12^{\circ}$ (across the diagonal). Projector magnification 23.6X; objective magnification 20.3X; optical enlargement 2.1X. Spiral distortion barely visible (2-3%) at edge of the field.

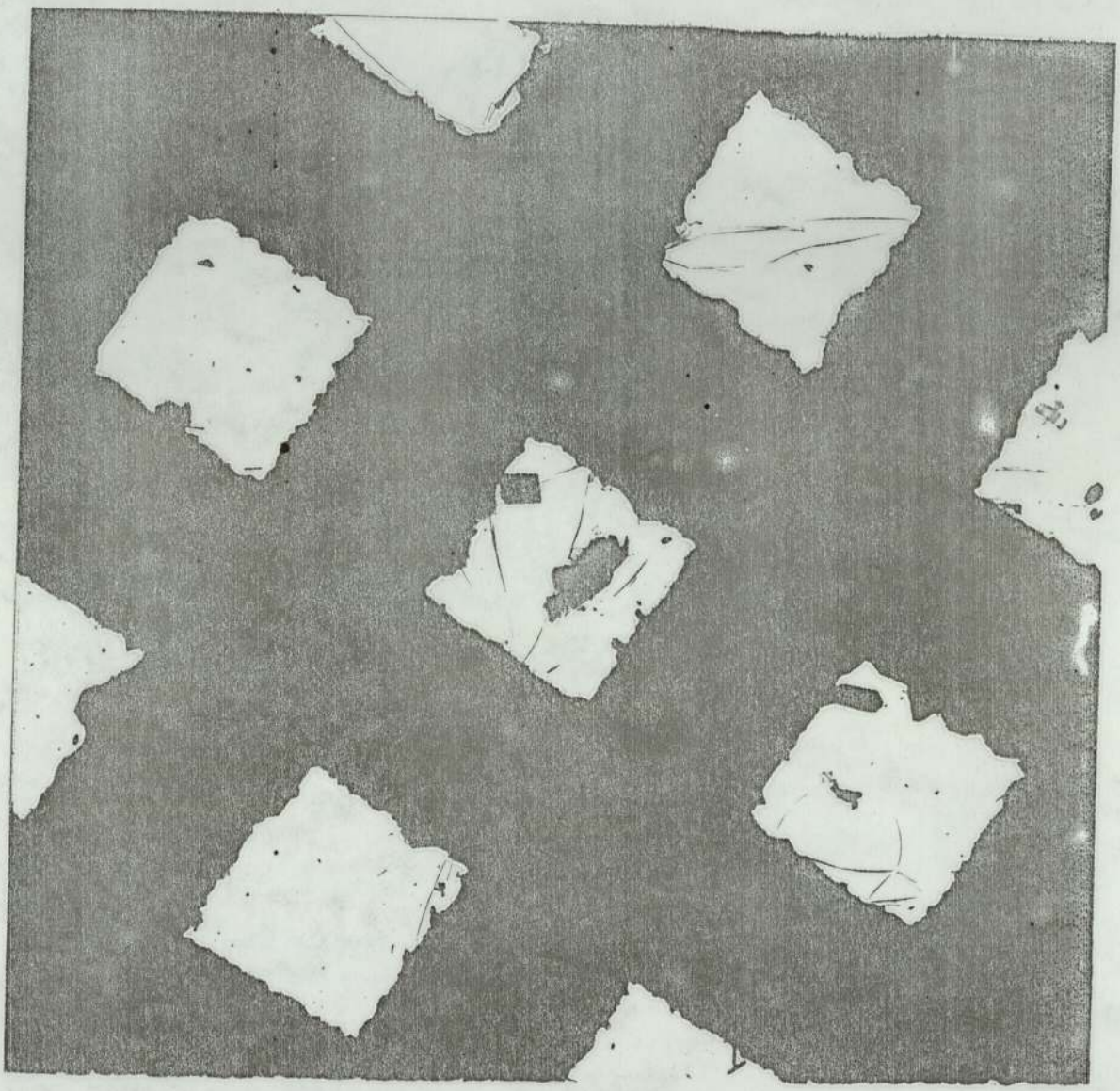

Figure (4.12) Electron micrograph of molybdenum trioxide mounted on a 400 mesh grid and taken with the remachined single-polepiece projector lens. Maximum projection semi-angle $\alpha_p = 12^\circ$ (across the diagonal). Projector magnification 22.6X; objective magnification 20.3X; optical enlargement 2.1X. Radial distortion about 2% at edge of the field. Spiral distortion barely visible (2-3%) at edge of the field.

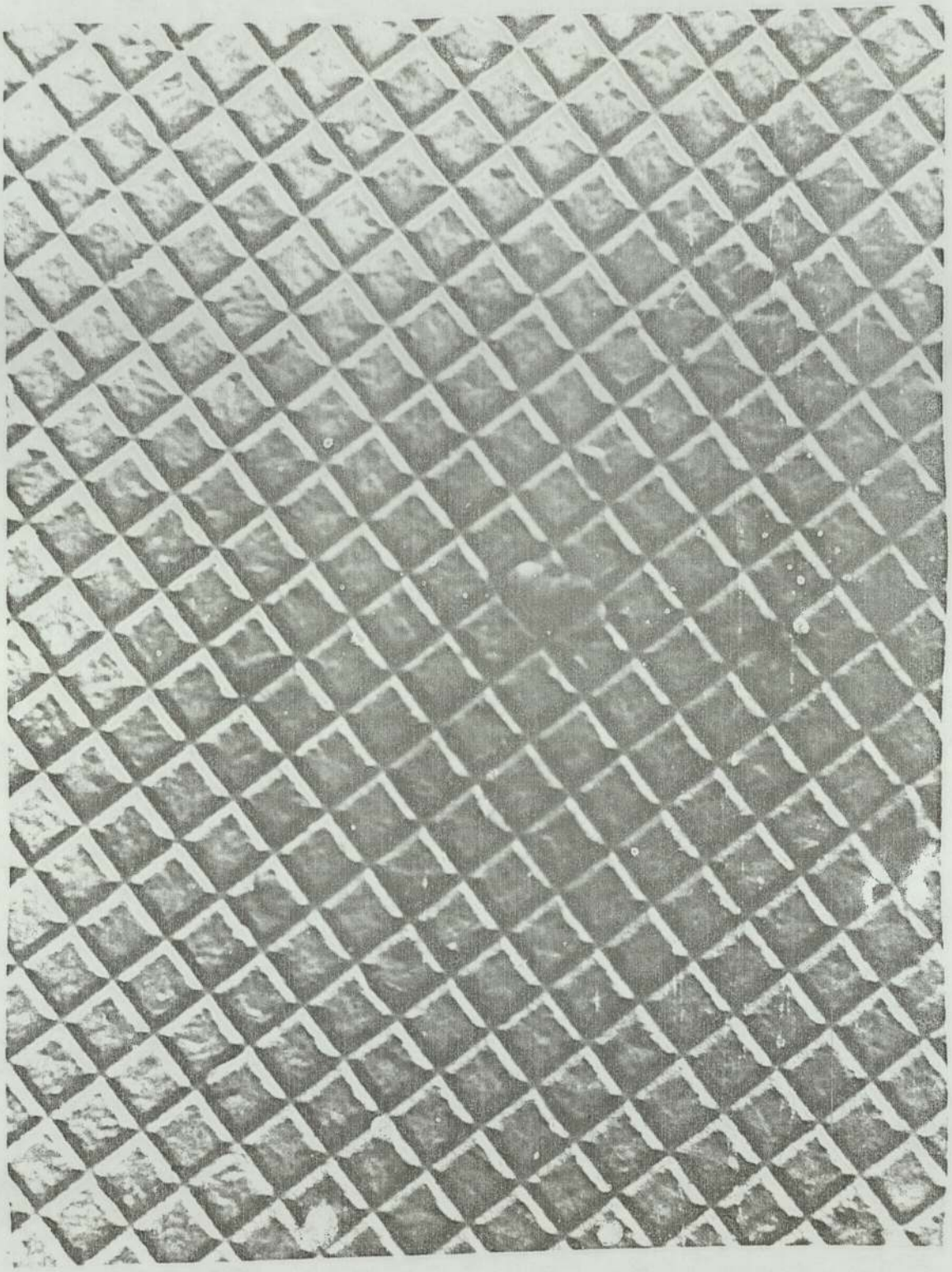

Figure (4.13) Electron micrograph taken on a Philips EM 200 TEM showing 2% at $\alpha_p = 5.3^{\circ}$ (across the diagonal).

theoretical calculations based on the experimental field distribution of the projector. It therefore became clear that even without correction such a lens is an appreciable improvement over a conventional projector lens. This may be seen by comparing the images of figures (4.11) and (4.12) with that of figure (4.13). The latter was taken favourably on a Philips EM 200 TEM in which $\alpha_p = 5.3^\circ$.

Even with this restricted angle one can measure 2% spiral distortion, compared with 2-3% at $\alpha_p = 12^\circ$ with the single-polepiece projector. This result is in good agreement with the previous calculation. The performance of the present projector is further described in Appendix (1) [Elkamali and Mulvey (1977)]. A critical comparison between single-polepiece and conventional double-polepiece projector lenses is shown in figure (4.14). This is a computer simulation of the spiral distortion for each type of lens at the point of zero radial distortion when the projection semi-angle is 22°. The inner circle, $\alpha_p = 8^\circ$, shows 2% of spiral distortion in the double-polepiece lens and 1.28% in the single polepiece lens. At the extreme edge of the image ($\alpha_p = 22^\circ$) the spiral distortion for the double-polepiece lens is 16.3% and only 10.4% for the single-polepiece lens.

A comparison can now be made between the experimental microscope with a wide-angle lens and a standard EM6 electron microscope. The relevant schematic diagrams of the viewing systems are shown in figure (4.15). The figure shows that the length of the viewing chamber had been reduced by 11.5 cm. thereby reducing the image sensitivity to stray A.C. magnetic fields by a useful factor of two. The spiral distortion at the photographic plate has

(a)

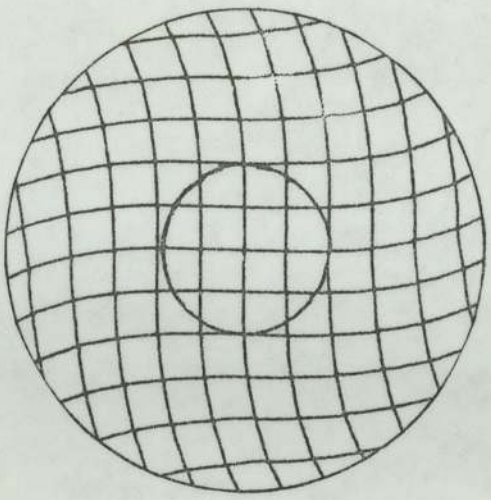

(b)

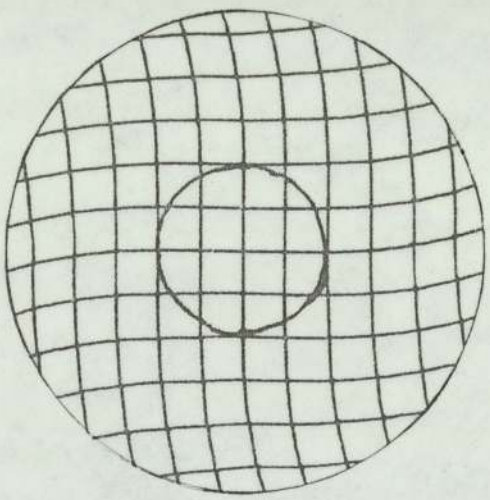

Figure (4.14) Computed image simulation (a) double-polepiece projector. 16.3% of spiral distortion at the edge of the image ($\alpha_p = 22^\circ$). Excitation set for zero radial distortion. Inner circle; $\alpha_p = 8^\circ$ (2% of spiral distortion). (b) single-polepiece projector. 10.4% of spiral distortion at the edge of the image ($\alpha_p = 22^\circ$). Excitation set for zero radial distortion. Inner circle; $\alpha_p = 8^\circ$ (1.28% of spiral distortion).

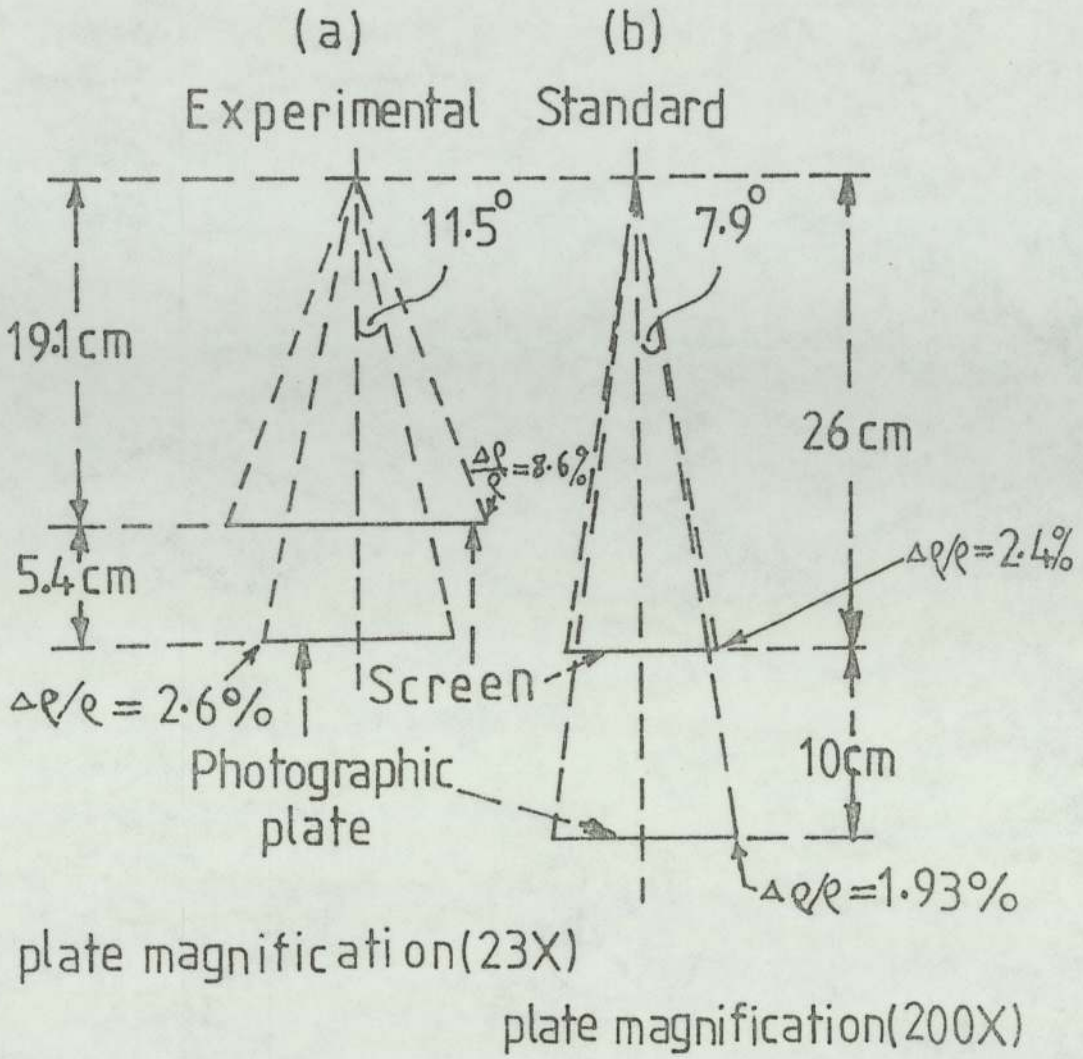

Figure (4.15) Schematic diagrams of the viewing arrangements in the (a) modified and (b) the standard EM6 microscopes showing arrangement of the viewing screen and photographic plate together with the spiral distortion at the edge of the relevant image.

increased from 1.9% in the standard instrument to 2.6% in the experimental instrument. This would mean that the spiral distortion in the image would exceed the allowed 2% at a diameter of 8.8 cm. rather than the standard 10 cm. The biggest advantage of the new system is that the diameter of the viewing screen is now 14 cm.

compared with 8.3 cm. of the standard instrument. Although spiral distortion at the edge of the screen amounts to 8.6%, this is not objectionable for visual search purposes. Since the single-polepiece projector lens has a longer focal length (10.7 mm) than that of the standard projector (1.8 mm) the plate magnification is reduced from 200X to about 23X. This means that the low magnification performance is improved but the top magnification is correspondingly reduced. However, it is a simple matter to add an extra intermediate projector lens to restore the original top magnification. These results show that a useful improvement in image performance can be obtained but further progress requires the actual correction of the spiral distortion. However, it was not possible to make use of the general purpose wide bore lens, designed by Juma (1975), as a compensator of spiral distortion because we could only operate it up to an excitation $NI/V_r^{\frac{1}{2}} = 16$.

4.4 THE FIRST EXPERIMENTAL CORRECTOR LENS

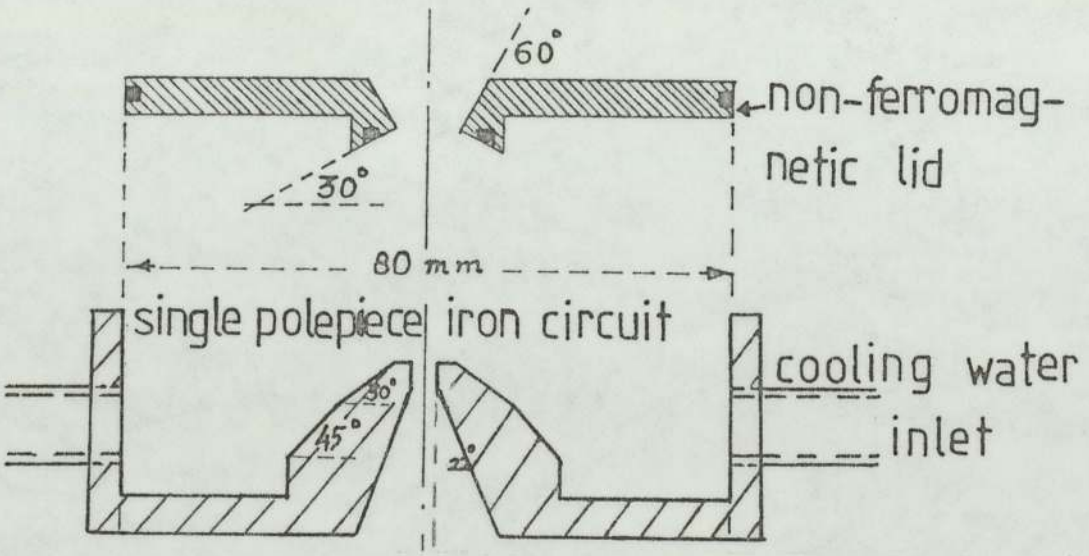

Figure(4.16) Early experimental single-polepiece corrector lens with asymmetrical field distribution and high excitation (11250 A-T).

Figure (4.16) shows the first design for a strong corrector lens, capable of operating in the second focal zone, and designed as a single-polepiece lens with a highly asymmetrical field distribution, as shown in figure (4.18). The lens body was made from Edgar Allen low carbon "O" quality steel; it was machined to a tolerance of $\pm$ 25μm. The lens has an overall diameter of 8.8 cm. and an axial depth of 2.9 cm. The winding consisted of a loosely wound wire coil of 450 turns of SWG 21 with cooling water circulating through the winding itself. The coil was initially wound on a solid former and then transferred to a specially designed Perspex box, as shown in figure (4.17), and then mounted inside the lens. This insulated box greatly reduces

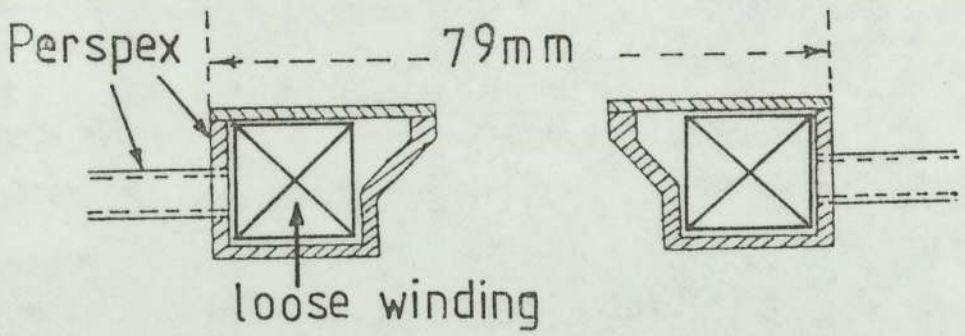

Figure (4.17) Perspex box for housing the loosely wound coil and for reducing possible electrolytic currents to the lens structure.

the possibility of electrolytic currents flowing from pinholes in the wire insulation to the adjacent iron structure. Such currents can eventually damage the windings. This compact water-cooled winding was capable of providing an excitation of 11250 A-T, sufficient

for operation in the second focal zone, up to accelerating voltages of 100 KV.

This lens was designed on similar principles to that of the projector lens but with a larger bore to allow passage of the electron beam in the non-preferred (high distortion) direction. The axial flux density distribution of the corrector lens was measured using a Hall probe and Gaussmeter as shown in figure (4.18). The resulting field distribution is shown in figure (4.19), which also shows the field distribution of the projector lens, both distributions being taken at the same excitation (3000 A-T).

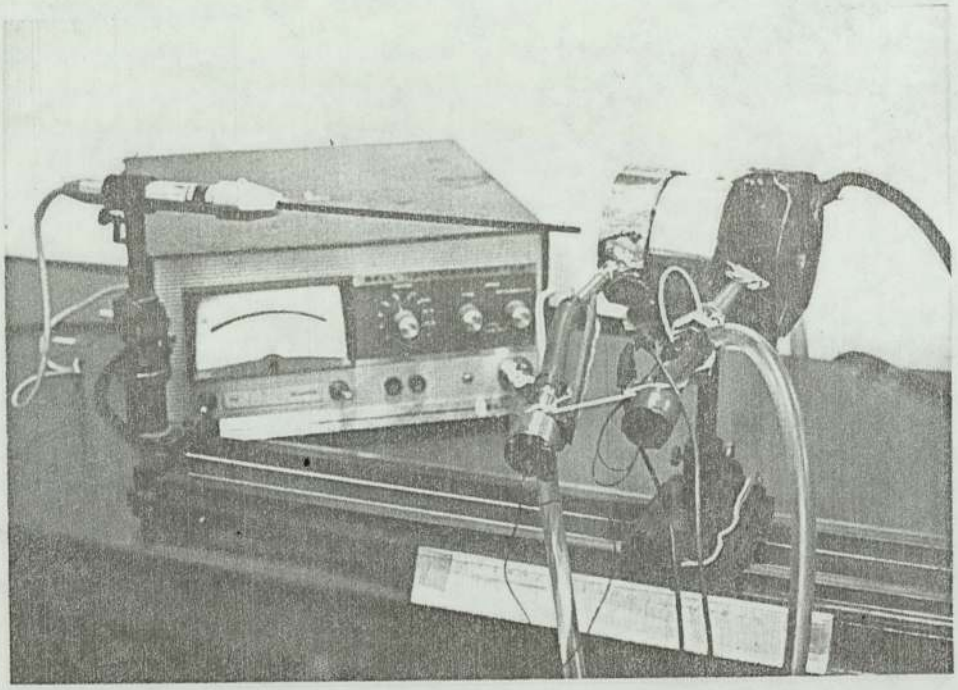

Figure (4.18) Photograph of the Gaussmeter arrangement for measuring the axial field distribution of the initial corrector lens.

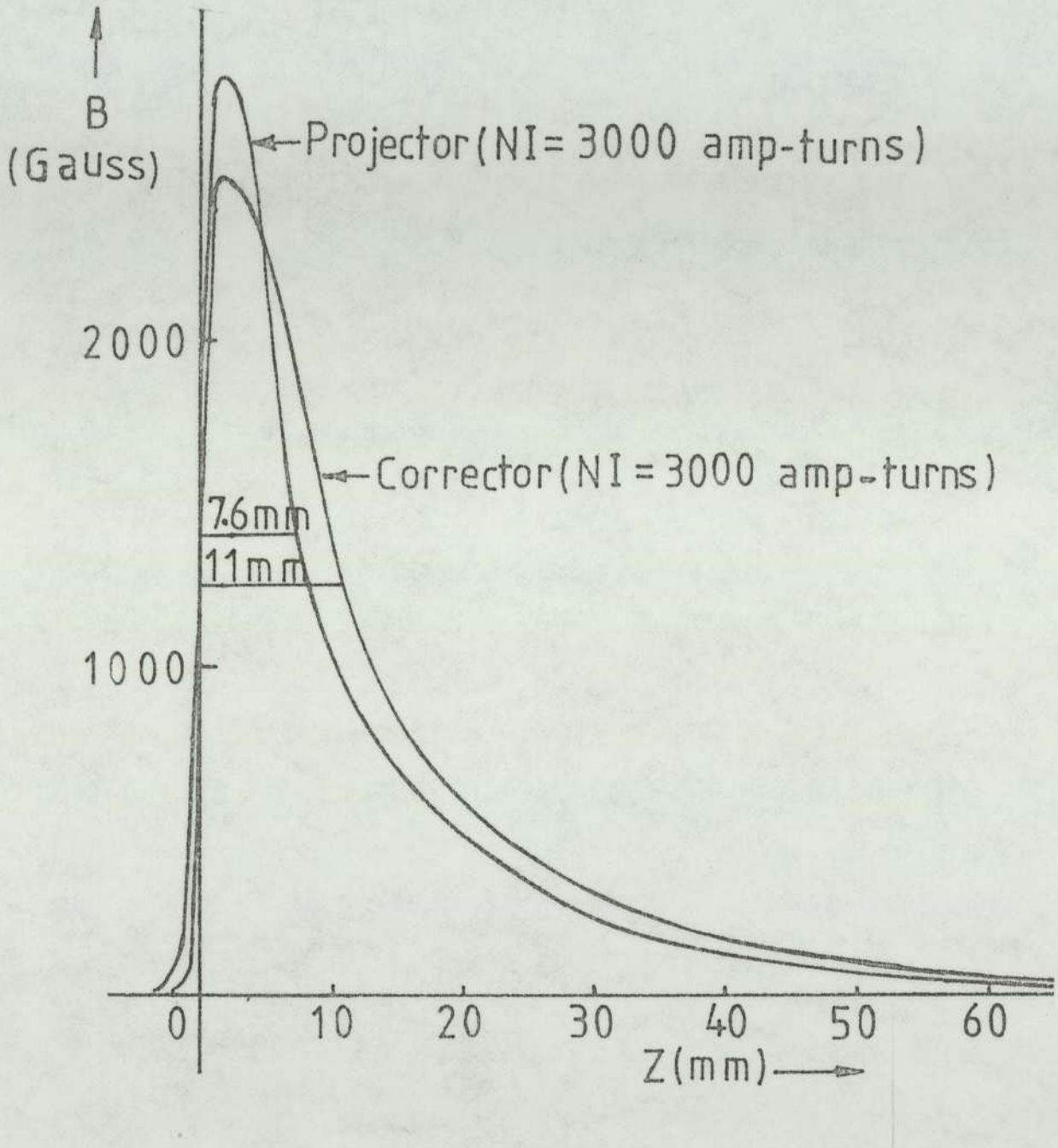

Figure (4.19) Experimental field distribution of the initial corrector lens (a = 11 mm.) together with that of the projector lens (a = 7.6 mm.) at the same excitation of 3000 A-T.

The focal properties, quality factors and distortion coefficients of the corrector lens are shown in figures (4.20), (4.21) and (4.22) respectively. These show that the corrector lens has a minimum focal length of 12 mm. in the first zone and 9 mm. in the second zone. These figures also show that the

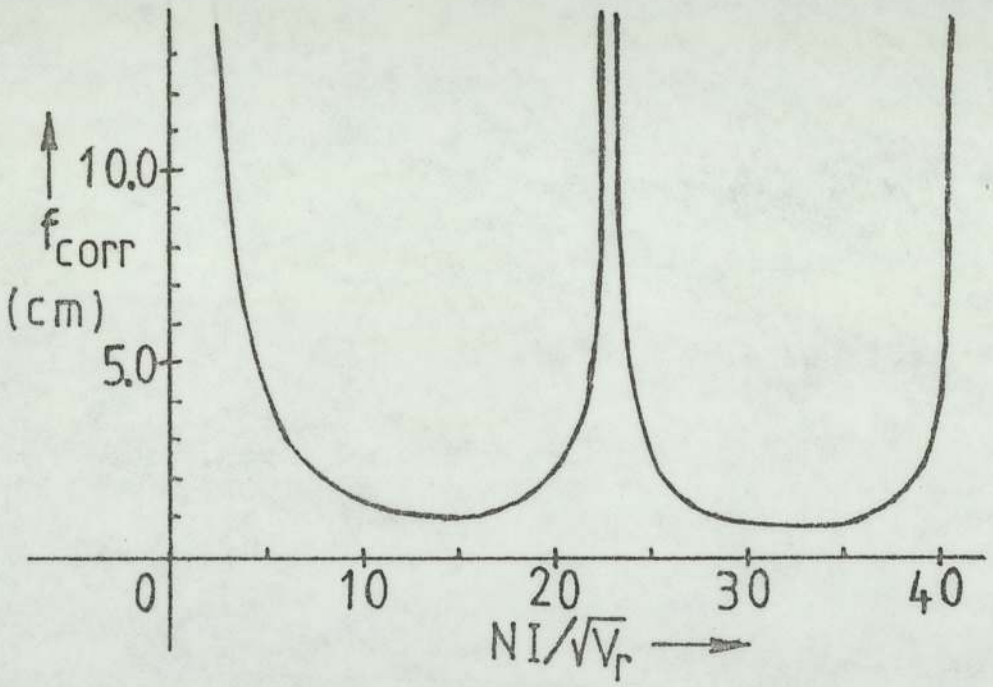

Figure (4.20) Focal length of the initial corrector lens as a function of the excitation parameter.

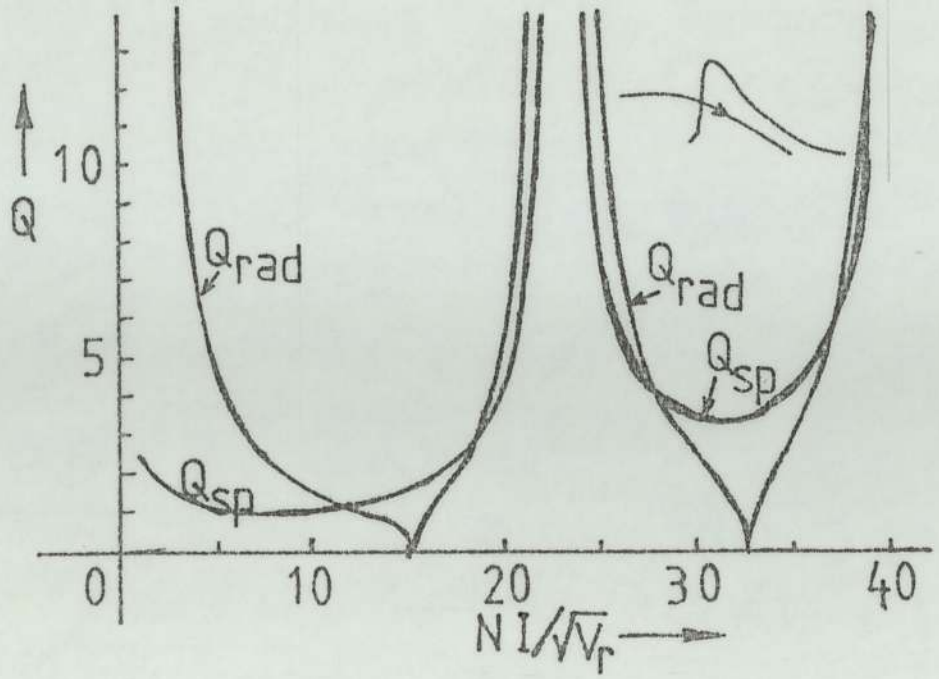

Figure (4.21) The quality factor Q_{rad} and Q_{sp} of the correcting lens for the non-preferred (high distortion) direction as a function of the excitation parameter $NI/V_r^{\frac{1}{2}}$.

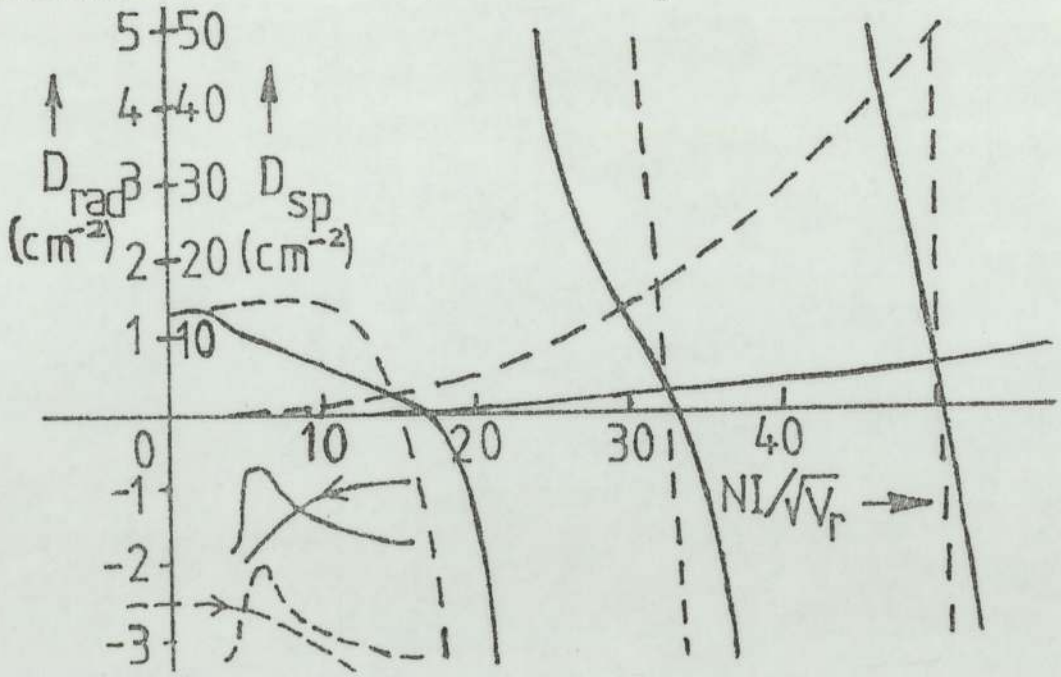

Figure (4.22) Distortion coefficients of the initial corrector lens as a function of the excitation parameter $NI/V_r^{\frac{1}{2}}$ for the two orientations of the lens.

increased distortion available with this lens appeared to satisfy the requirements for a viable correcting system. Thus at the minimum focal length in the second focal zone, the spiral quality factor Q_{sp} of the lens was 3.3, a remarkably high value. However, the experimental results obtained in the electron microscope revealed some difficulties. The close proximity of the two polepieces of opposite polarity led to a substantial cancellation of ampere-turns of the two lenses which substantially modified their field distributions and made adjustment difficult.

It was, therefore, necessary to devote some effort to this problem and find a design in which lens interaction and field cancellation could be minimised. Figure (4.23) shows the experimental arrangement adopted to study this question. It was soon found that at snout separations greater than 2.5 cm. the effect of the dummy snout and plate on the projector field distribution was almost negligible whereas serious magnetic interaction occurred at snout separations less than 2 cm., as shown in figure (4.24).

This result is in good agreement with the experiments of Lambrakis et.al. (1977) who adopted a separation of 60 mm. between the pole-tips of the corrector and projector. However, it was realised at this stage that a suitably designed iron screening plate between the two lenses might be the best practical solution. Before considering the insertion of such a plate, however, the corrector and projector lenses were placed with their snouts facing each other and the excitation of the corrector was set at twice that

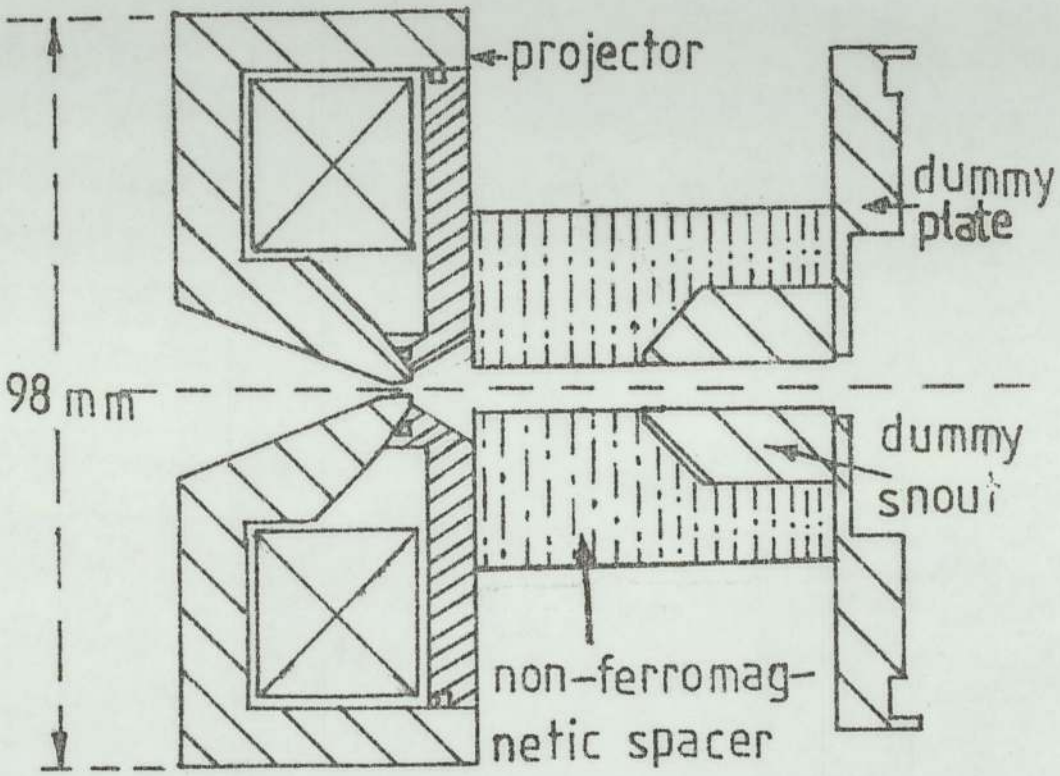

Figure (4.23) Dummy iron snout and plate to simulate the effect of the corrector lens on the field distribution of the projector lens as the two polepieces approach each other.

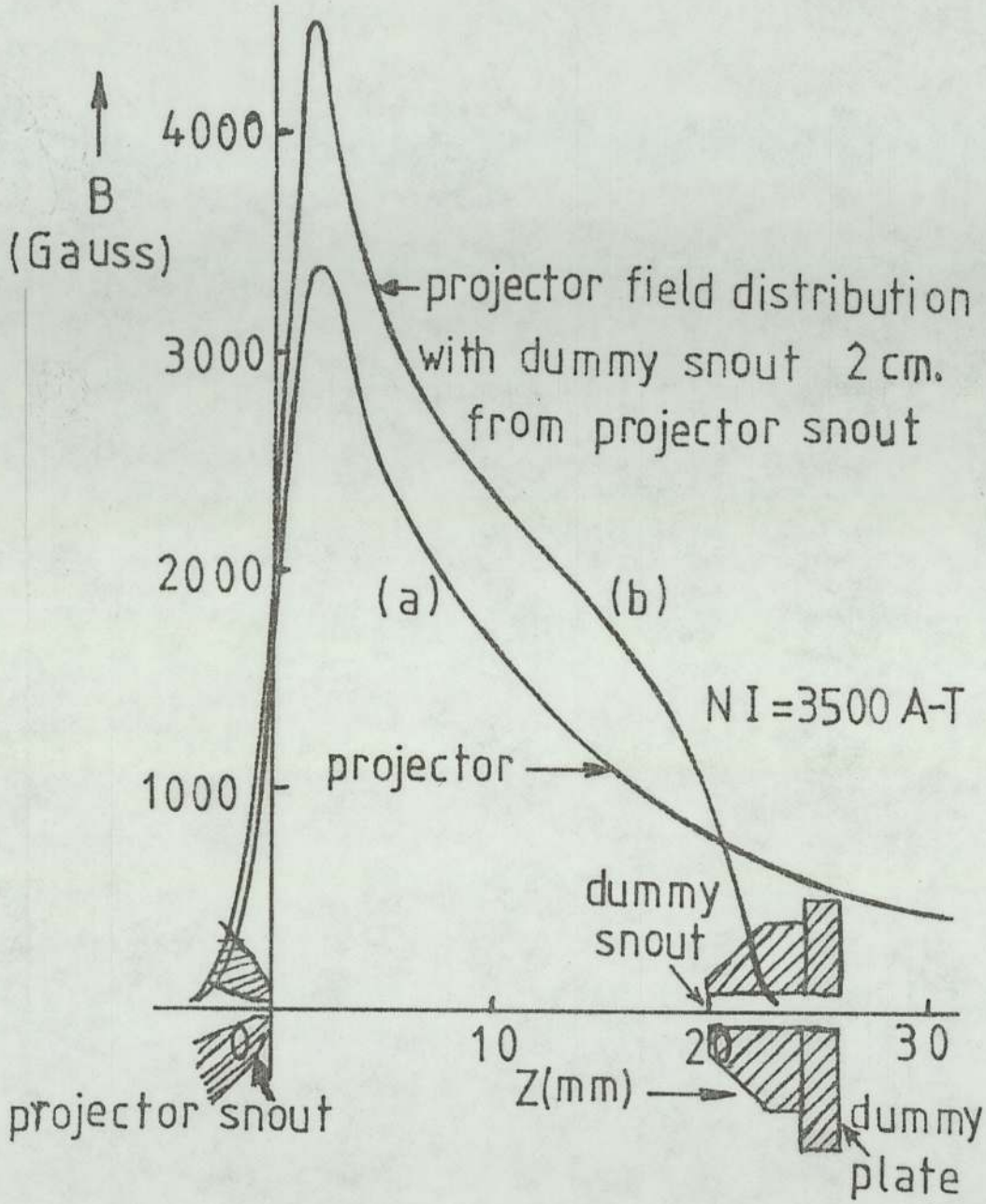

Figure (4.24) Projector field distribution with (a) dummy snout and plate removed and (b) with the tip of the dummy snout 2 cm. from the tip of the projector snout. Projector excitation constant at 3500 A-T.

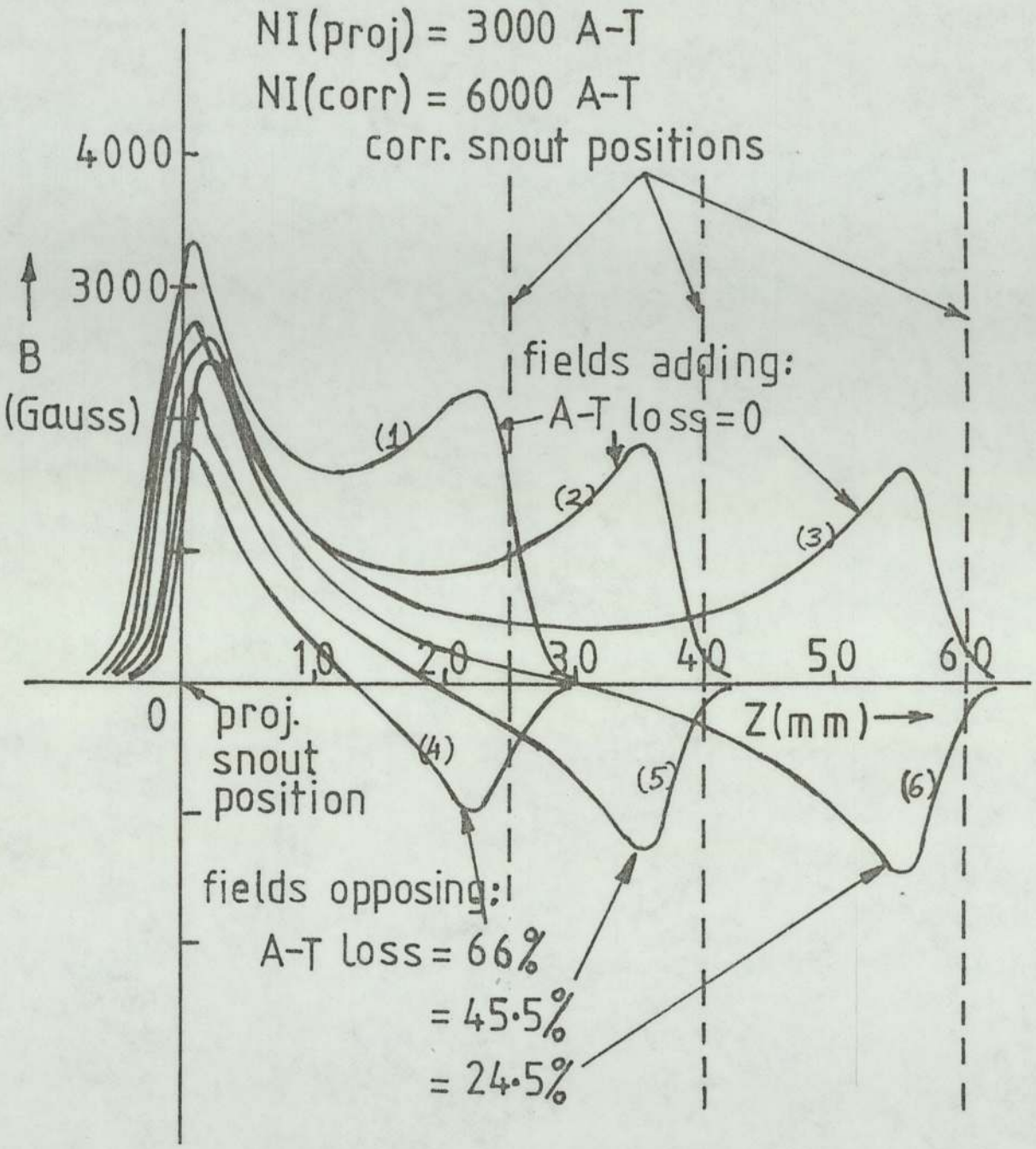

Figure (4.25) Experimentally measured axial field distribution of the combined corrector and projector single-polepiece lenses with snouts facing each other: (1), (2) and (3) lens excitations in same sense; (4), (5) and (6) lens excitations in opposite senses. The percentage loss of ampere-turns is indicated.

of the projector. The resulting field distributions were measured for snout separations 25, 40 and 60 mm. The axial field measurements were taken with the excitation of both lenses (a) in the same sense and (b) in opposite senses. This enables an estimate to be made of the loss of ampere-turns due to field cancellation when the excitations are in opposite senses. The resulting field distributions are shown in figure (4.25). The figure shows that the field cancellation is surprisingly high (25%) even at a separation of 60 mm. At this separation, the magnification of the corrector was too large for effective correction of spiral distortion. Thus it was decided to make a further reduction of the loss of ampere-turns by partially separating the fields using an iron screening plate between the two lenses. Furthermore, it was decided to increase the bore of the corrector lens to admit a larger field of view. At the same time it was decided to increase the size of the corrector lens so as to reduce the power needed to excite the energising coils.

CHAPTER 5

AN IMPROVED HIGH POWER SINGLE-POLEPIECE CORRECTOR LENS

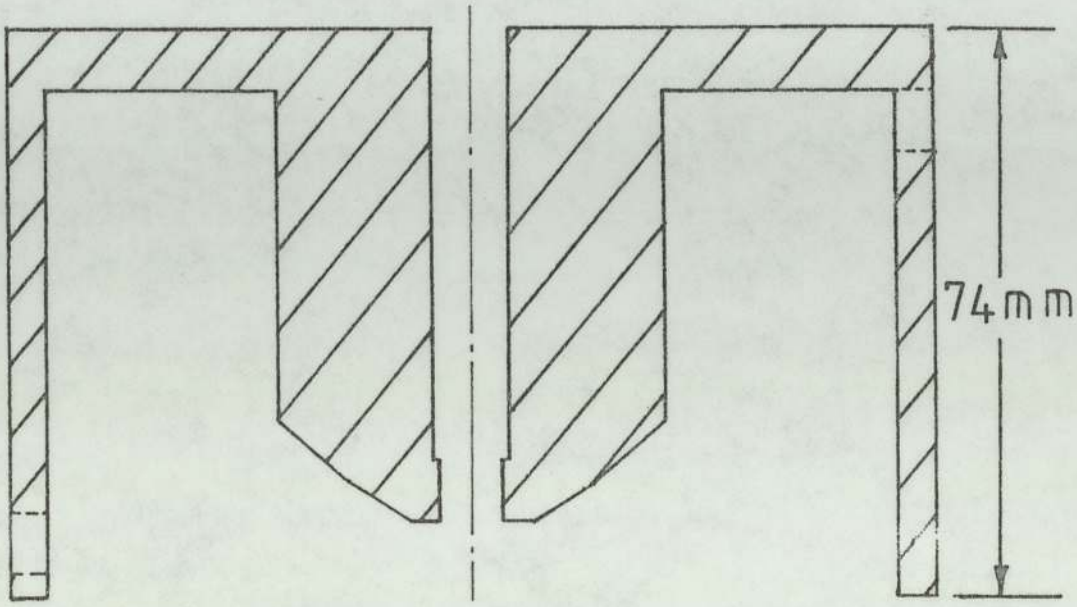

Figure (5.1) Magnetic iron circuit of the corrector lens.

The iron circuit of the new corrector lens is shown in figure (5.1). This design was made as close as possible to the requirements mentioned in Appendix (4) to overcome saturation of the iron and need for high power to excite the coil. The lens was made from "O" quality mild steel with an overall diameter of 12 cm., an axial depth of 7.4 cm., and a massive snout of 5 cm. diameter with a finely finished bore. As before, the coil was contained in a Perspex box made of two units, as shown in figure (5.2). The first unit acted as a former for the coil during the winding process. The second unit acted as the outer cylindrical cover of the

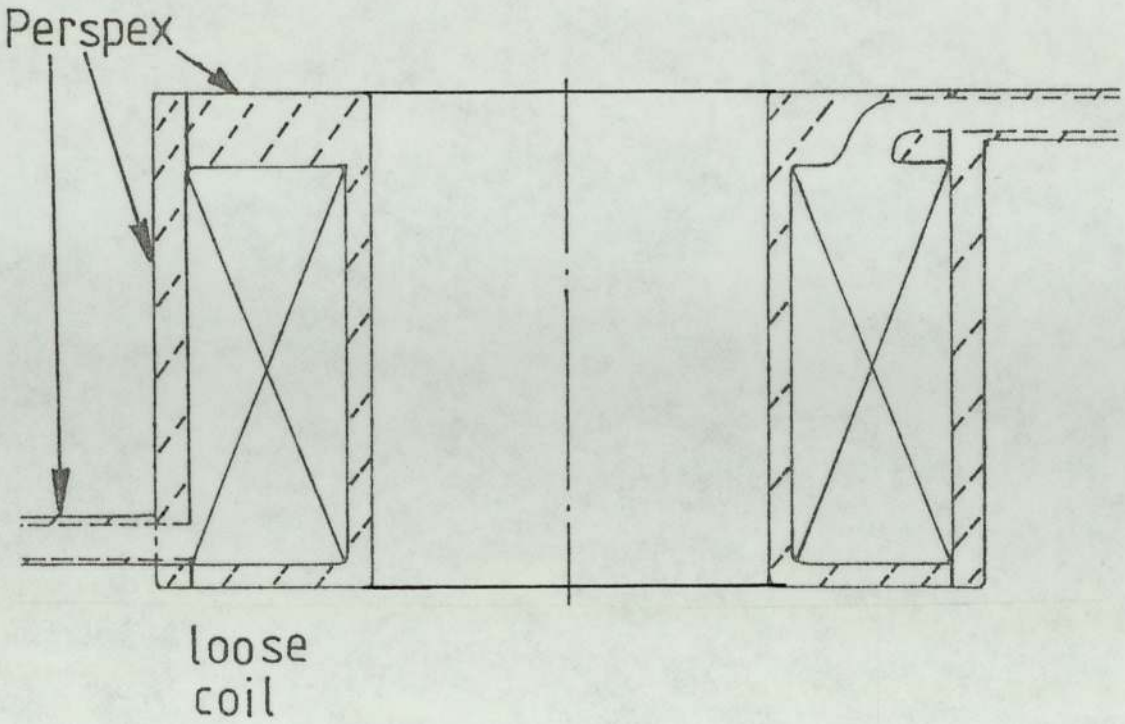

Figure (5.2) Two-piece Perspex box enclosing the coil of the corrector lens. Outside diameter of the coil 10.1 cm. Inside diameter of the coil 5.7 cm. Cross-sectional area of the coil 13.4 $cm.^2$ Length of wire 118 m. Resistance 1.71Ω .

coil. This was glued onto the former and the Perspex water connections during the final assembly of the coil. This ensured that the coil assembly was watertight and free from mechanical damage. The thick Perspex top lid was shaped so as to keep unwanted air bubbles away from the wire surface, as illustrated in figure (5.2). The coil was loosely wound and had 475 turns of SWG 18 enamelled copper wire, providing an excitation of 11875 ampere-turns. Below this excitation, the lens was free from saturation effects.

5.1 FOCAL PROPERTIES AND DISTORTION

The axial field distribution of the corrector lens, measured by means of a Hall probe, is shown in figure (5.3).

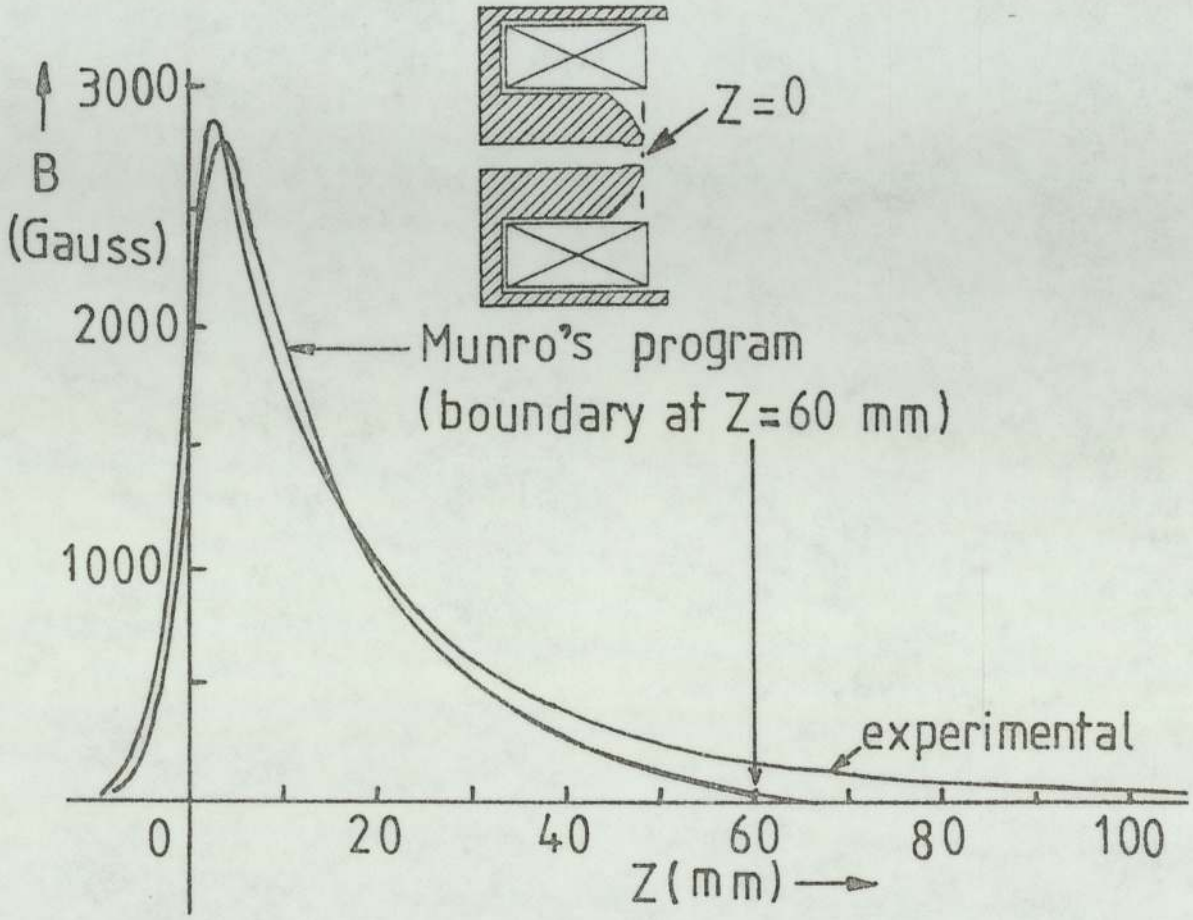

Figure (5.3) Measured and calculated axial field distribution of the improved corrector lens. z = o at the poleface.

The poleface is taken as the zero point on the z-axis. A computational analysis was carried out using the finite-element program due to Munro (1975); and the computed axial field distribution is also shown in figure (5.3). The agreement between

experiment and calculation is not perfect but is completely adequate for the present purpose.

The electron-optical properties were calculated at different excitation parameters $NI/V_r^{\frac{1}{2}}$ of the corrector lens employing the experimental field distribution. The focal length f_{corr} of the corrector lens is shown in figure (5.4) as a function

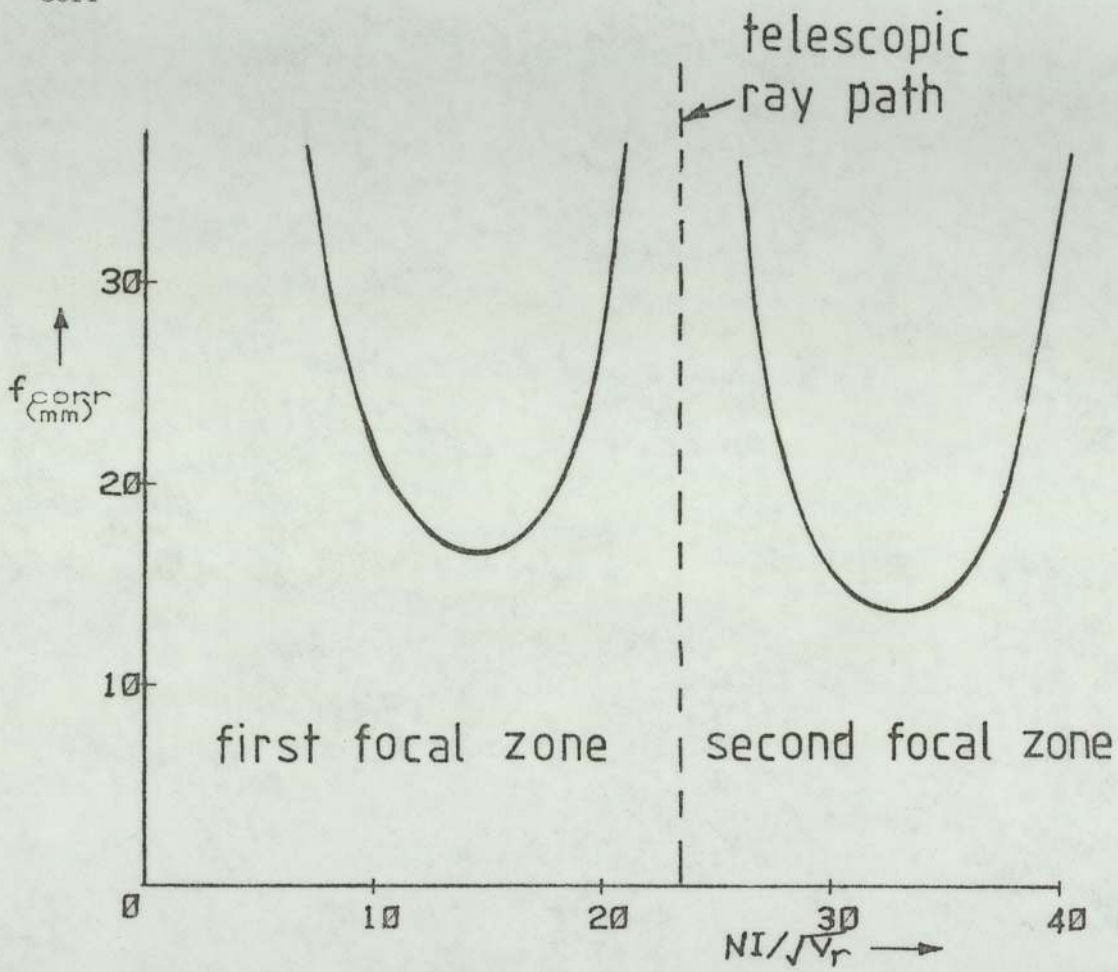

Figure (5.4) Focal length of the improved corrector lens as a function of the excitation parameter showing the first and second focal zones.

of $NI/V_r^{\frac{1}{2}}$. As the lens excitation parameter $NI/V_r^{\frac{1}{2}}$ was increased the focal length f_{corr} decreased, passing through a minimum of 16.63 mm. at $NI/V_r^{\frac{1}{2}} = 15.6$ and then started to rise to infinity at $NI/V_r^{\frac{1}{2}} \simeq 23$, the so called telescopic ray path which separates the first focal zone from the second focal zone, figure (5.4). The second focal zone occupied the excitation range $23 < NI/V_r^{\frac{1}{2}} < 42$ with a minimum focal length of 13.7 mm. at $NI/V_r^{\frac{1}{2}} = 33.1$. The focal length of projector lenses, including corrector lenses, does not of course depend on the direction of the electron beam.

The distortion coefficients D_{rad} and D_{sp} of the improved corrector lens are shown in figure (5.5). Notice that D_{rad} has a zero value in each focal zone, near the corresponding point of minimum focal length.

For the preferred direction of the lens $D_{rad} = 0$ when $NI/V_r^{\frac{1}{2}}$ is 16.5 or 33.8; and for the non-preferred direction $NI/V_r^{\frac{1}{2}}$ is 15.4 or 33.1. On the other hand D_{sp} does not follow a cyclic pattern but rather a continuous single curve starting from zero and rising indefinitely. Where D_{rad} vanished D_{sp} had the values 2615 m^{-2} at $NI/V_r^{\frac{1}{2}}$ 16.5 and 9745 m^{-2} at $NI/V_r^{\frac{1}{2}}$ 33.8 for the preferred direction. The numerical values for the non-preferred direction were 8900 m^{-2} and 70300 m^{-2} at excitation parameters of 15.4 and 33.1 respectively.

As previously explained, it is more useful to use the quality factor $Q = D^{\frac{1}{2}}f$ rather than the quantity D itself when assessing image distortion. The variation of Q_{rad} and Q_{sp} with $NI/V_r^{\frac{1}{2}}$ is shown in figure (5.6) for the non-preferred direction of the lens as essentially a projector or what we may call the optimum direction

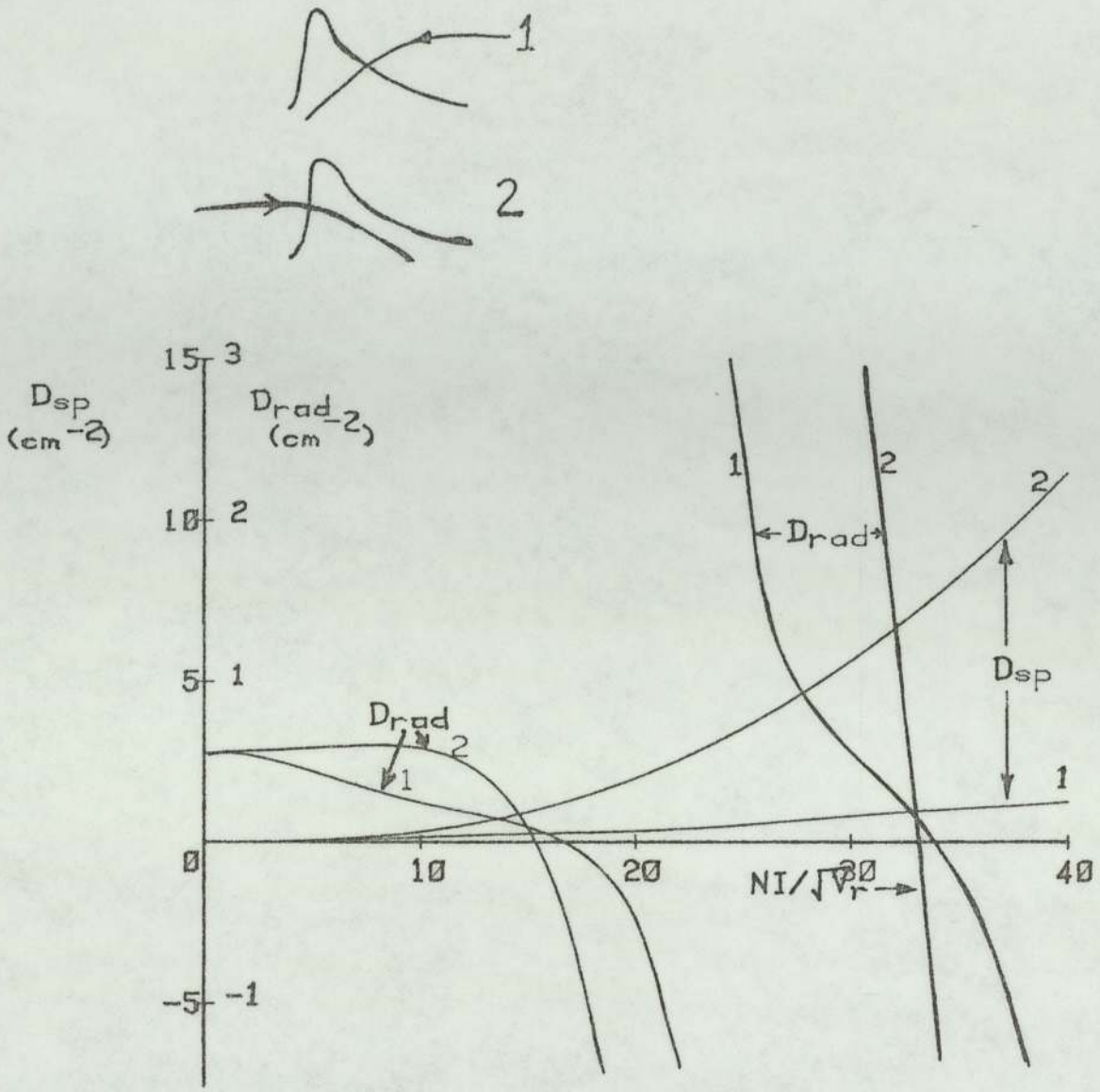

Figure (5.5) Distortion coefficients D_{rad} and D_{sp} of the improved corrector lens versus the excitation parameter $NI/V_r^{\frac{1}{2}}$.

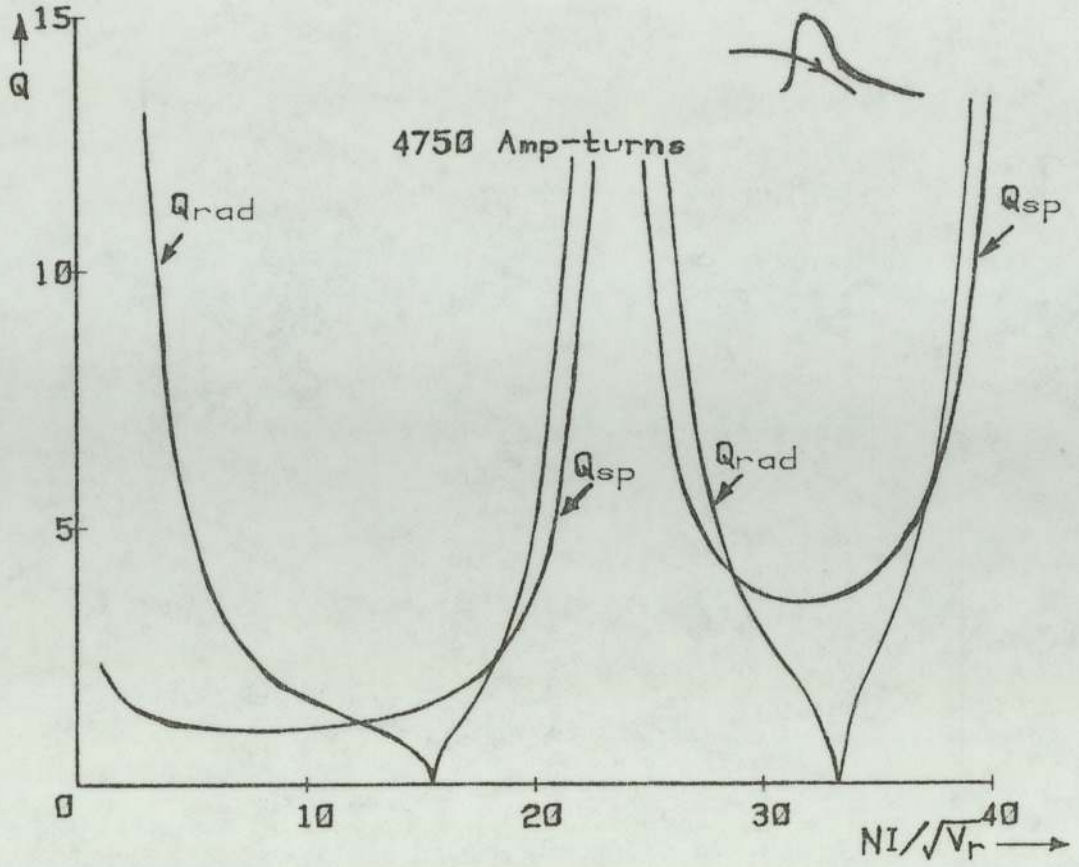

Figure (5.6) Quality factors Q_{rad} and Q_{sp} of the improved corrector lens versus excitation parameter for optimum direction for producing large amounts of distortion.

of the corrector for producing large amounts of distortion. The excitation parameters at which Q_{rad} vanish are of course the same as for which D_{rad} vanishes when the lens is operated near its minimum focal length. The values of Q_{sp}, at the focal length minima of the first and second focal zones, were 1.58 and 3.65 respectively. The high values of Q_{sp} in the region of excitaion $NI/V_r^{\frac{1}{2}}$ 18 to 34 made it possible to obtain high distortion with this improved corrector lens.

5.2 PERFORMANCE OF THE CORRECTOR LENS

The increased size of the new corrector lens made it necessary to redesign part of the column, as shown in figure (5.7). Here the projector lens has been removed and its place taken by a duralumin spacer of the same axial height. This enabled the electron-optical properties of the new corrector to be determined separately.

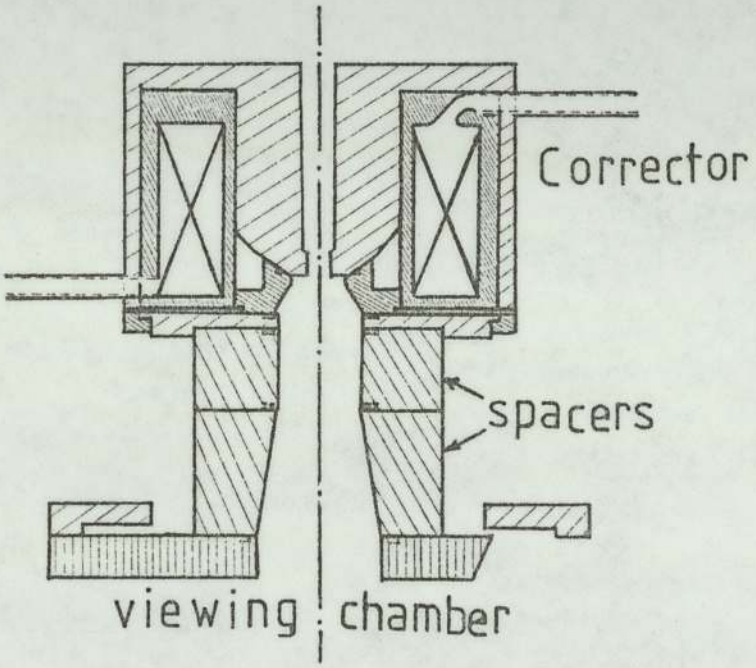

Figure (5.7) Cross-section of the corrector lens, duralumin spacers and the top flange of the viewing chamber.

The distance between the corrector lens snout and the photographic plate was 29.5 cm., giving a projection semi-angle $\alpha_{corr} = 10.6^{o}$ (plate diagonal 11 cm.)

Figures (5.8) and (5.9) show some typical projection

images produced by this lens. It can be seen that the distortion with the lens in the orientation shown in figure (5.7) is considerable and of the right order of magnitude for a corrector lens. These results showed,therefore, that we could have confidence in the previous calculations.

5.3 PROJECTOR-CORRECTOR FIELD INTERACTION

If two single-polepiece lenses are excited with opposite magnetic fields each lens will effectively lose some ampere-turns (field cancellation). Moreover,the lens half-widths will broaden. This increase in half-width leads to larger distortion coefficients.

Experimental investigations were carried out to study the effect of the iron structure of a lens on the field distribution of another lens at different lens separation between the corrector and projector; the projector lens was previously described in Chapter (4). These investigations catered for the presence and absence of the iron face plate. When the plate was present its near edge was 11.5 mm. from the snout of the corrector lens thus keeping the favourable projector field distribution, figure (5.10), as undisturbed as possible. This usually means that the corrector field distribution will not be of optimum shape. However, this is less important, electron-optically, than the necessity of keeping the distortion introduced by the projector lens as low as possible. Modification of the corrector field distribution due to presence and absence of the face plate as well as lens separation is shown in figure (5.11).

The effect of field cancellation occurs only when both lenses are simultaneously excited. This case is shown in figure (5.12) where the projector lens was operated near its

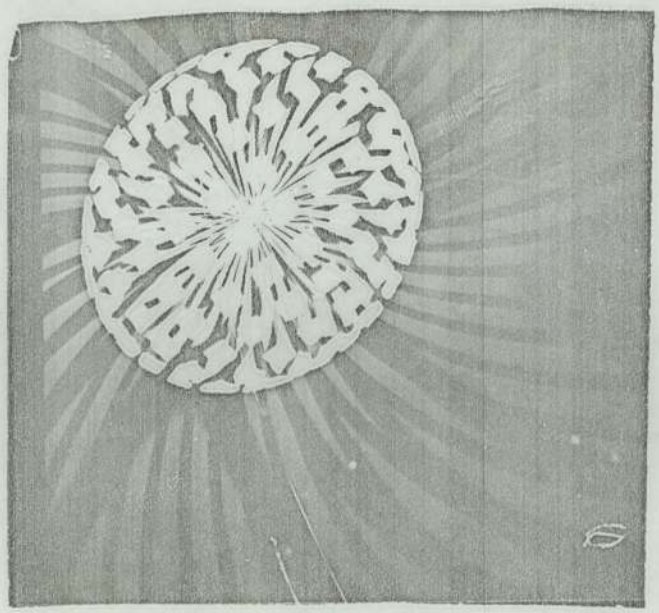

Figure (5.8) Distortion projection image with the single-polepiece corrector lens in the first focal zone. $NI/V_r^{\frac{1}{2}} = 18.4$; $\Delta\rho/\rho_{rad} = -84\%$ (negative sign indicates barrel distortion); $\Delta\rho/\rho_{sp} = 42.3\%$; $\alpha_{corr} = 10.6^{\circ}$.

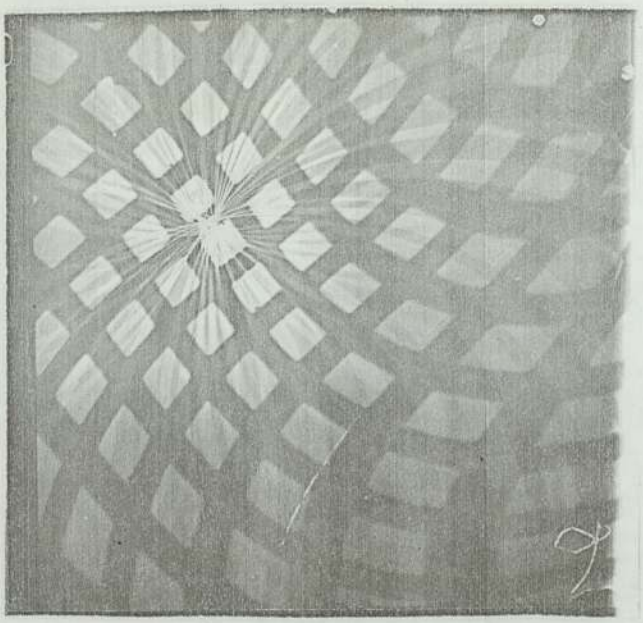

Figure (5.9) Distortion projection image with the single-polepiece corrector lens in the second focal zone. $NI/V_r^{\frac{1}{2}} = 27.4$; $\Delta\rho/\rho_{rad} = 55.7\%$; $\Delta\rho/\rho_{sp} = 52.4\%$; $\alpha_{corr} = 10.6^{\circ}$.

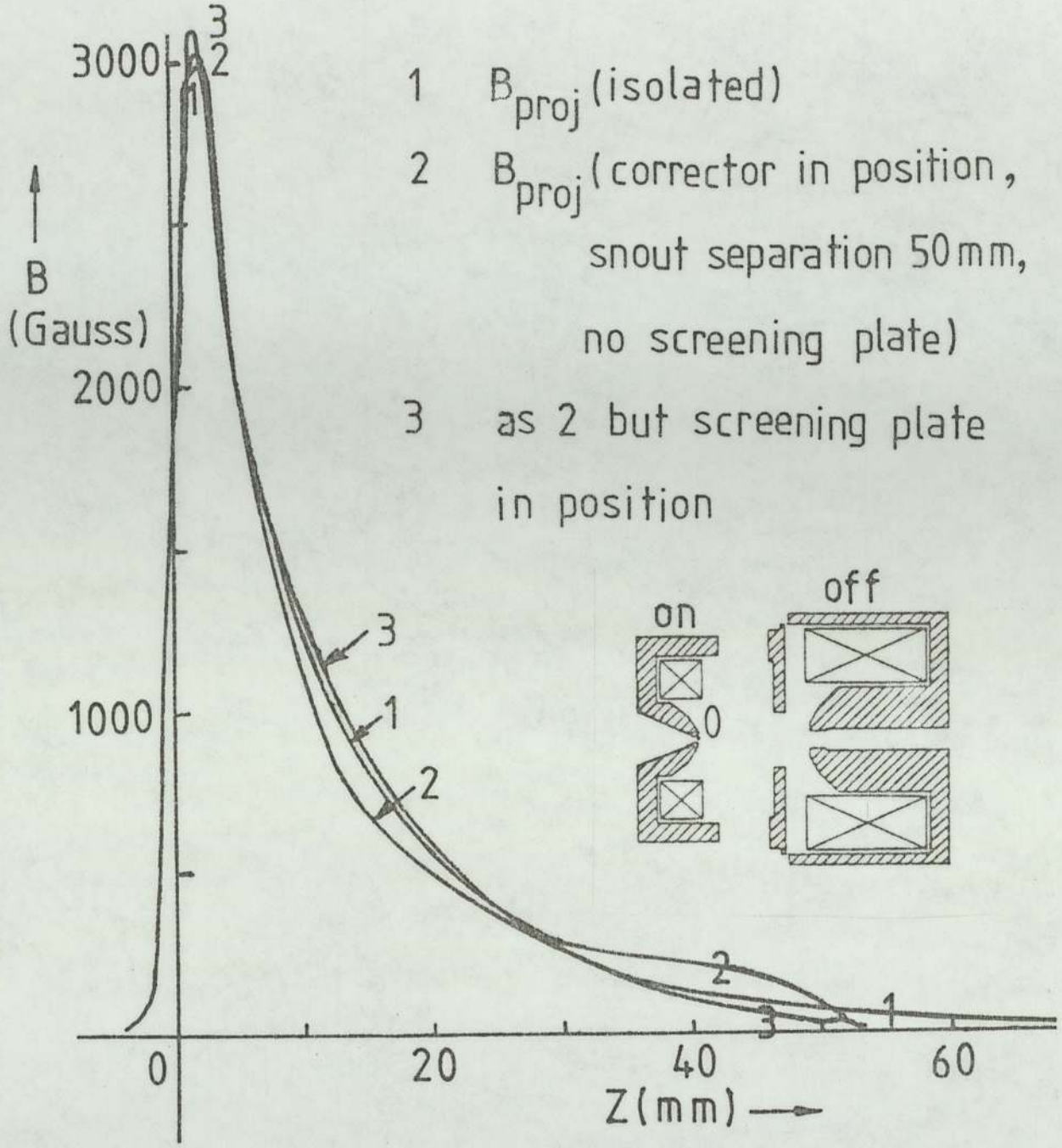

Figure (5.10a) Axial field distribution of the projector lens for:- 1. projector lens isolated from iron face plate and corrector lens. 2. projector lens in the presence of the corrector lens body (NI_{corr} = 0) but without the screening plate. 3. projector lens with screening plate and corrector lens in position, giving negligible change in projector field distribution from 1.

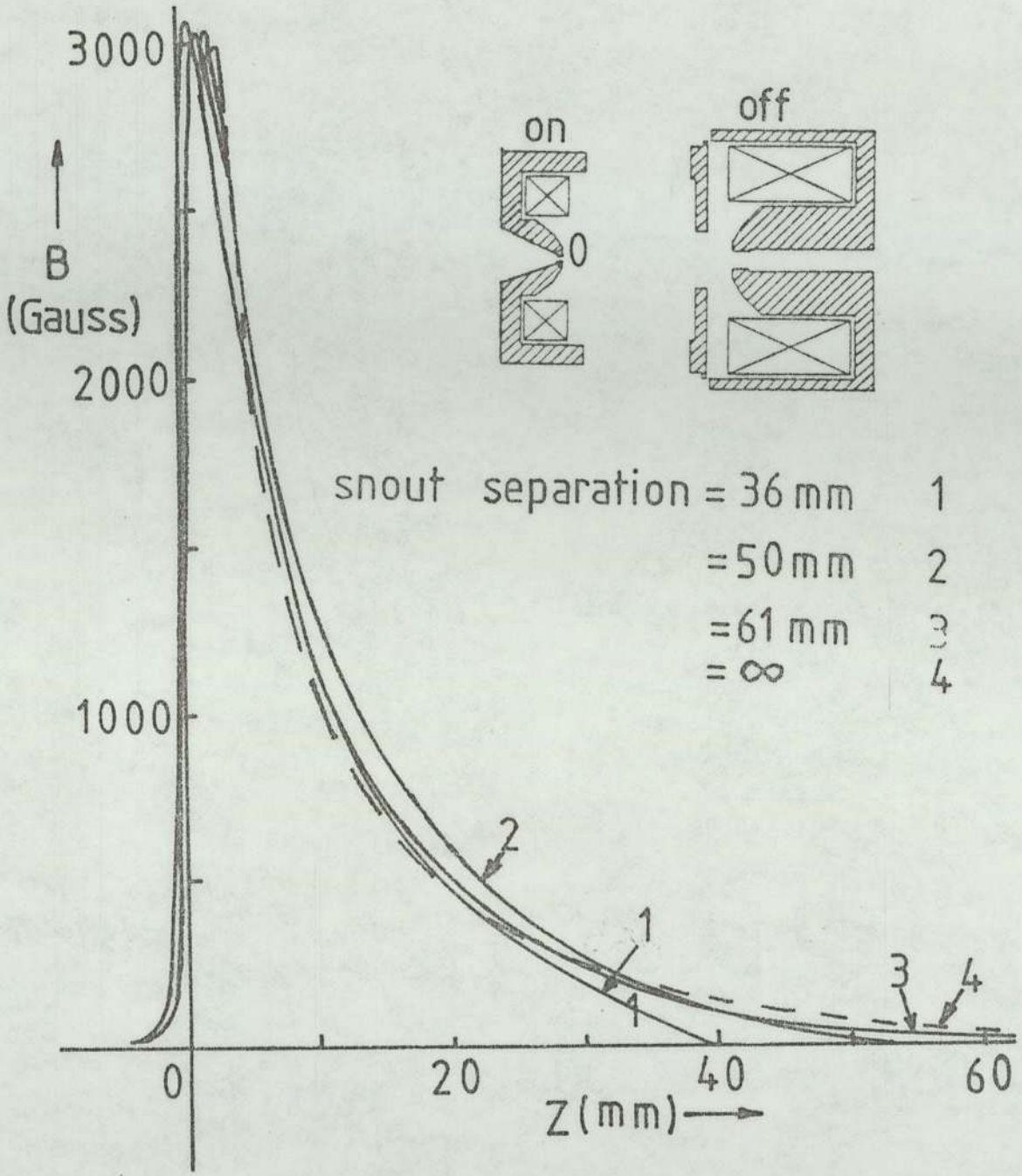

Figure (5.10b) Projector field distribution in the presence of the corrector lens body ($NI_{corr} = 0$) and screening (face) plate at different snout separation. The screening plate was permanently fixed to the corrector lens. Note: Position 2 adopted as good practical compromise.

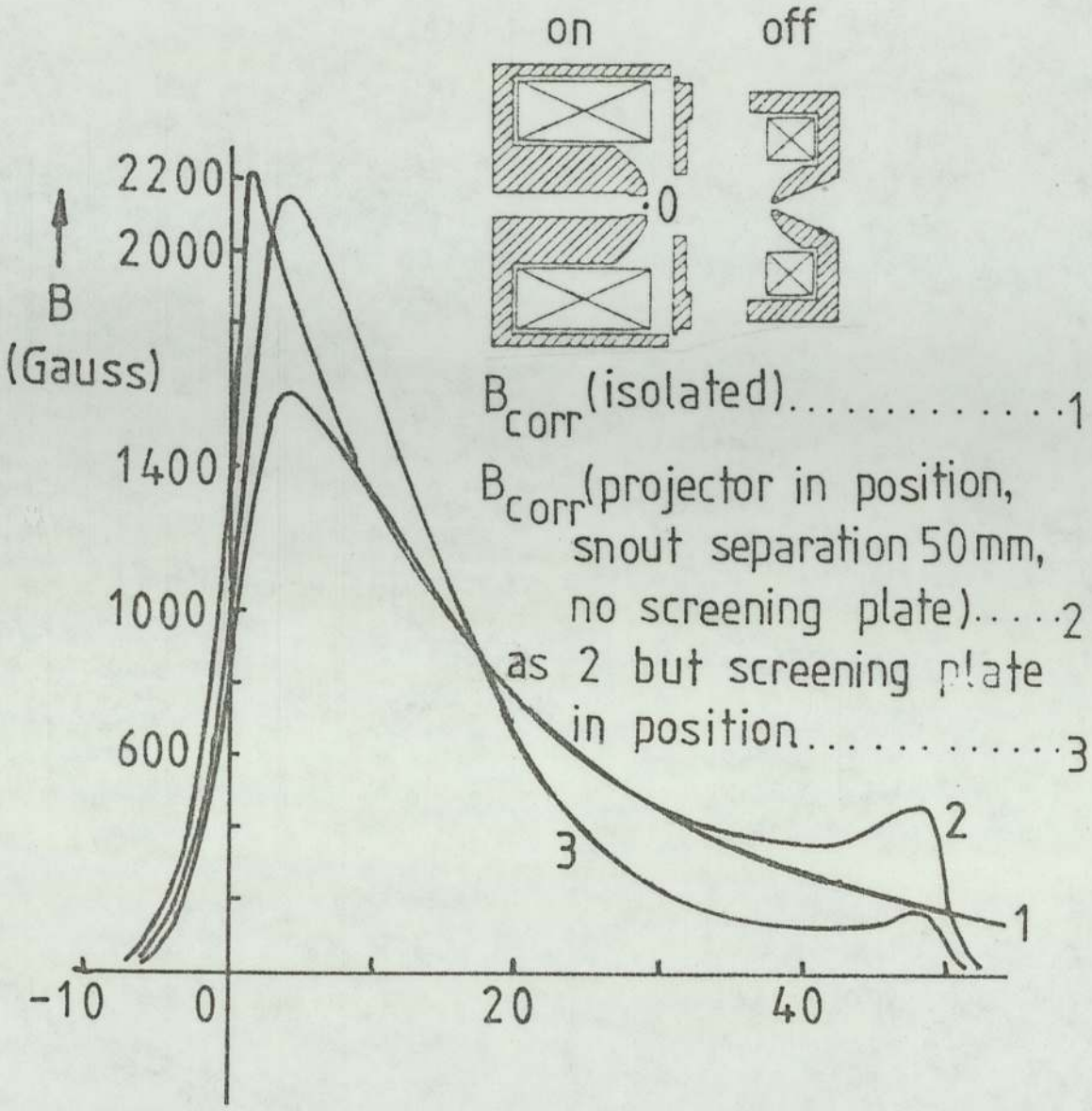

Figure (11a) Corrector lens field (B_{corr}) distribution: 1. isolated. 2. in the presence of the projector ($NI_{proj.} = 0$) but without the screening plate. 3. in the presence of the projector ($NI_{proj.} = 0$) and the screening plate. The plate is permanently fixed to the corrector lens. Note: Arrangement 3 chosen for practical convenience.

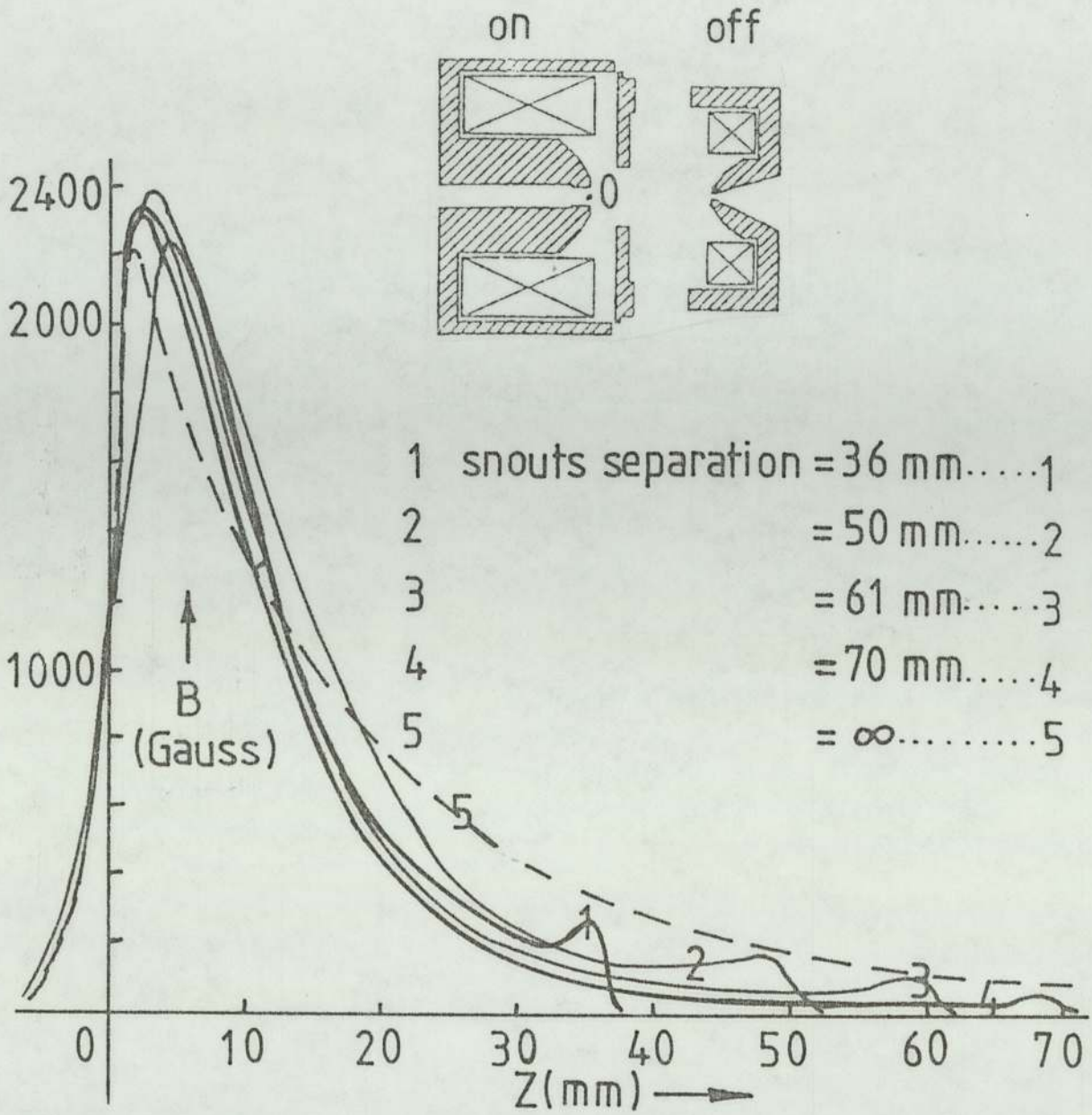

Figure (11b) Corrector field distribution in the presence of the projector lens body (NI_{proj} = 0) and screening plate at different snout separation. The screening plate was permanently fixed to the corrector lens.

minimum focal length of its first focal zone and the corrector lens was operated near its minimum focal length of its second focal zone. The curves in figure (5.12) include the overall axial field distribution (a) with the lenses opposing and (b) with the lenses assisting each other. The ampere-turn loss (fields opposing) was 20%, a reasonable value, and the shape of the field distribution in the critical region of the projector lens was hardly affected by the field due to the corrector.

5.4 THE INFLUENCE OF LENS FIELD INTERACTION ON THE ELECTRON-OPTICAL PROPERTIES OF THE PROJECTOR AND CORRECTOR

In this section we consider the focal properties of the projector and corrector lenses with snout separation of 50 mm. and compare them with those of the isolated individual lens fields. Here, only one lens is excited at a time. The focal lengths f_p and f_{corr} of the projector and corrector lenses respectively are drawn against their respective excitations in figures (5.13) and (5.14). The variation in the focal length f_{corr} of the corrector lens was great because the screening plate was only 11.5 mm. from the corrector lens snout which made it a highly asymmetrical double-polepiece lens. The corresponding change in the quality factors Q_{rad} and Q_{sp} for each lens are shown in figures (5.15) and (5.16). It was noticed that the minimum Q_{sp} of the corrector lens had improved from 3.55 to 3.25 due to the presence of the screening plate and the iron structure of the projector lens. This small improvement in Q_{sp} will not affect the correction of spiral distortion since the required value of Q_{sp} may be achieved by increasing or reducing the excitation.

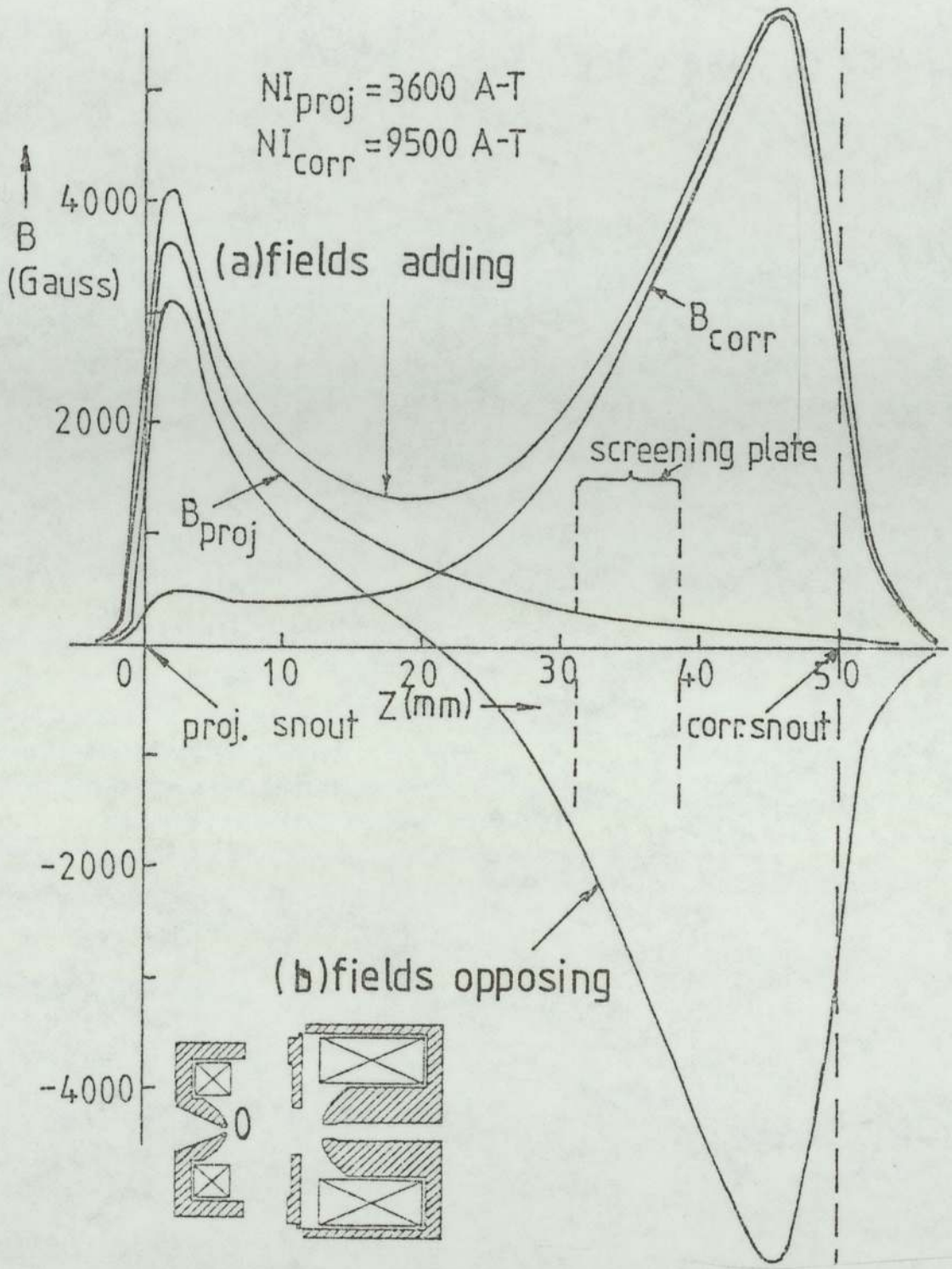

Figure (5.12) Combined field distribution of the corrector-projector system at snout separation of 50 mm. and the iron screening plate in position. For (a) fields adding (b) fields subtracting the associated loss of ampere-turns was 20%. Note the favourable field distribution maintained in the projector lens when the fields oppose each other.

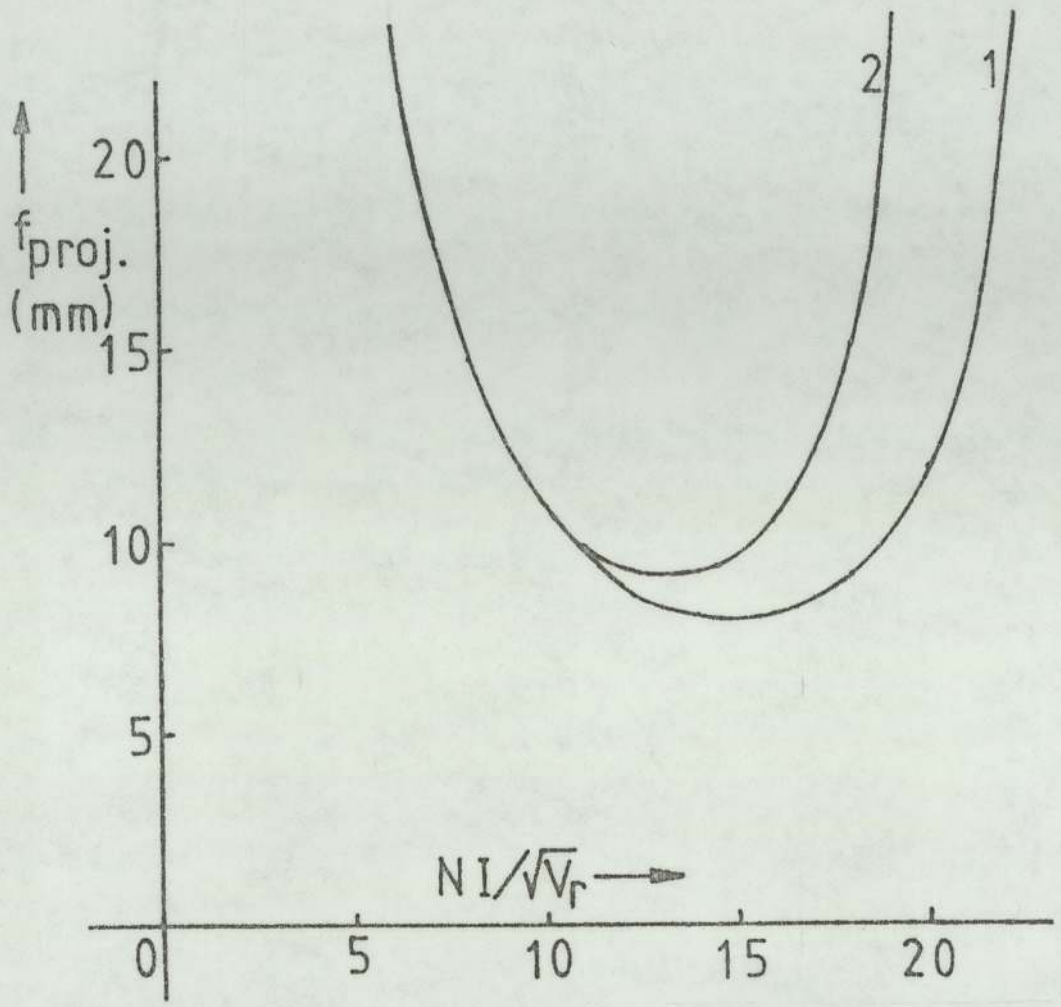

Figure (5.13) Focal length f_p of the projector lens against the excitation $NI/V_r^{\frac{1}{2}}$ (proj) (1) isolated projector (2) projector and corrector at snout separation of 50 mm. and screening plate in position, $NI/V_r^{\frac{1}{2}}$(corr) = 0.

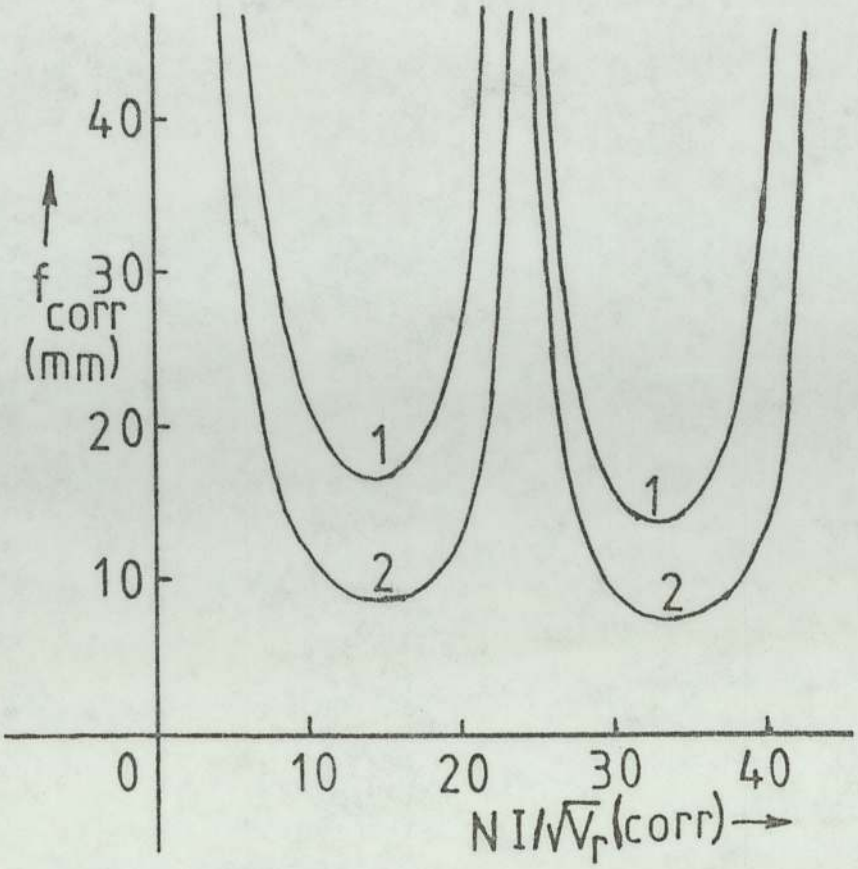

Figure (5.14) Focal length f_{corr} of the corrector lens against the excitation $NI/V_r^{\frac{1}{2}}(corr)$ (1) isolated corrector (2) projector and screening plate in position. Snout separation 50 mm. $NI/V_r^{\frac{1}{2}}(proj) = 0$.

The magnification M_{corr} produced by the corrector lens is drawn in figure (5.17) as a function of the excitation $NI/V_r^{\frac{1}{2}}(corr)$. The figure includes M_{corr} when the corrector was isolated and when the projector lens ($NI_{proj.} = 0$) and screening plate were placed in position. The screening plate,however, considerably modified f_{corr} and hence M_{corr}. This desired increase in M_{corr} will make it feasible to operate the corrector lens in an excitation

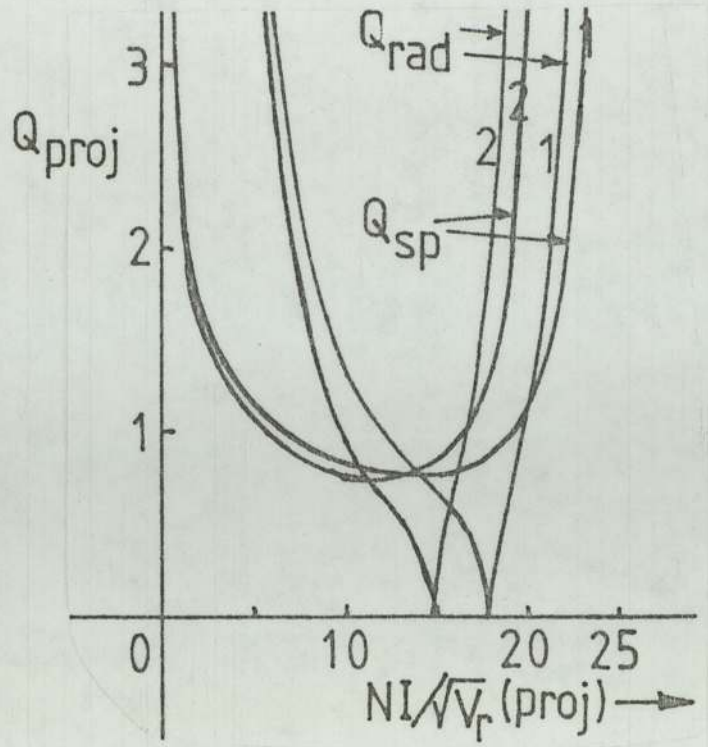

Figure (5.15) Quality factors Q_{rad} and Q_{sp} of the projector lens (1) isolated projector (2) projector with corrector and screening plate in position. $NI_{corr} = 0$.

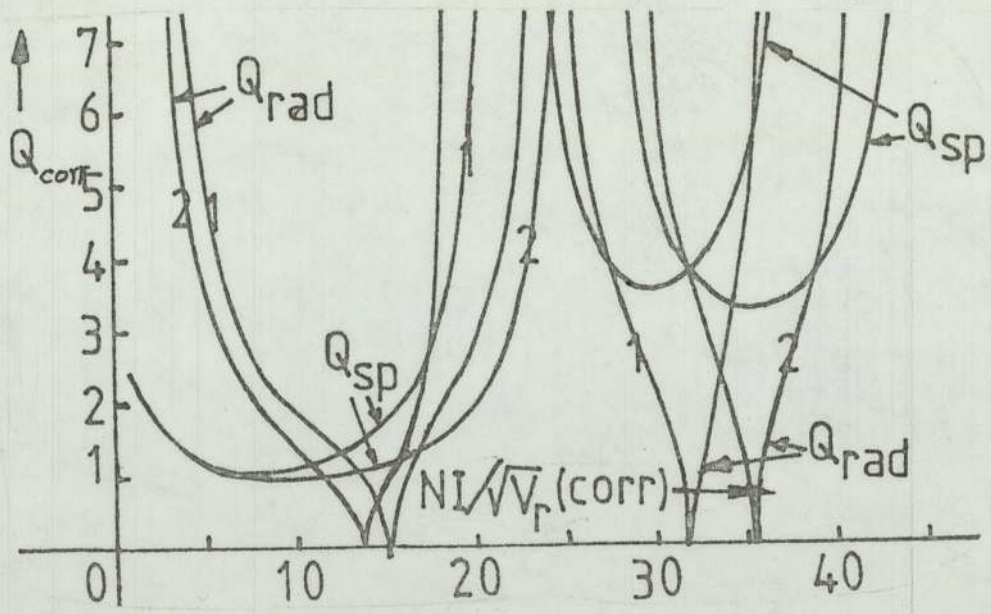

Figure (5.16) Quality factors Q_{rad} and Q_{sp} of the corrector lens (1) isolated corrector (2) corrector with iron screening plate and projector in position. $NI_{proj} = 0$.

range that gives $M_{corr} \simeq 3X$. It should be mentioned that when both the projector and corrector are excited simultaneously one should expect the M_{corr} curve to be modified again.

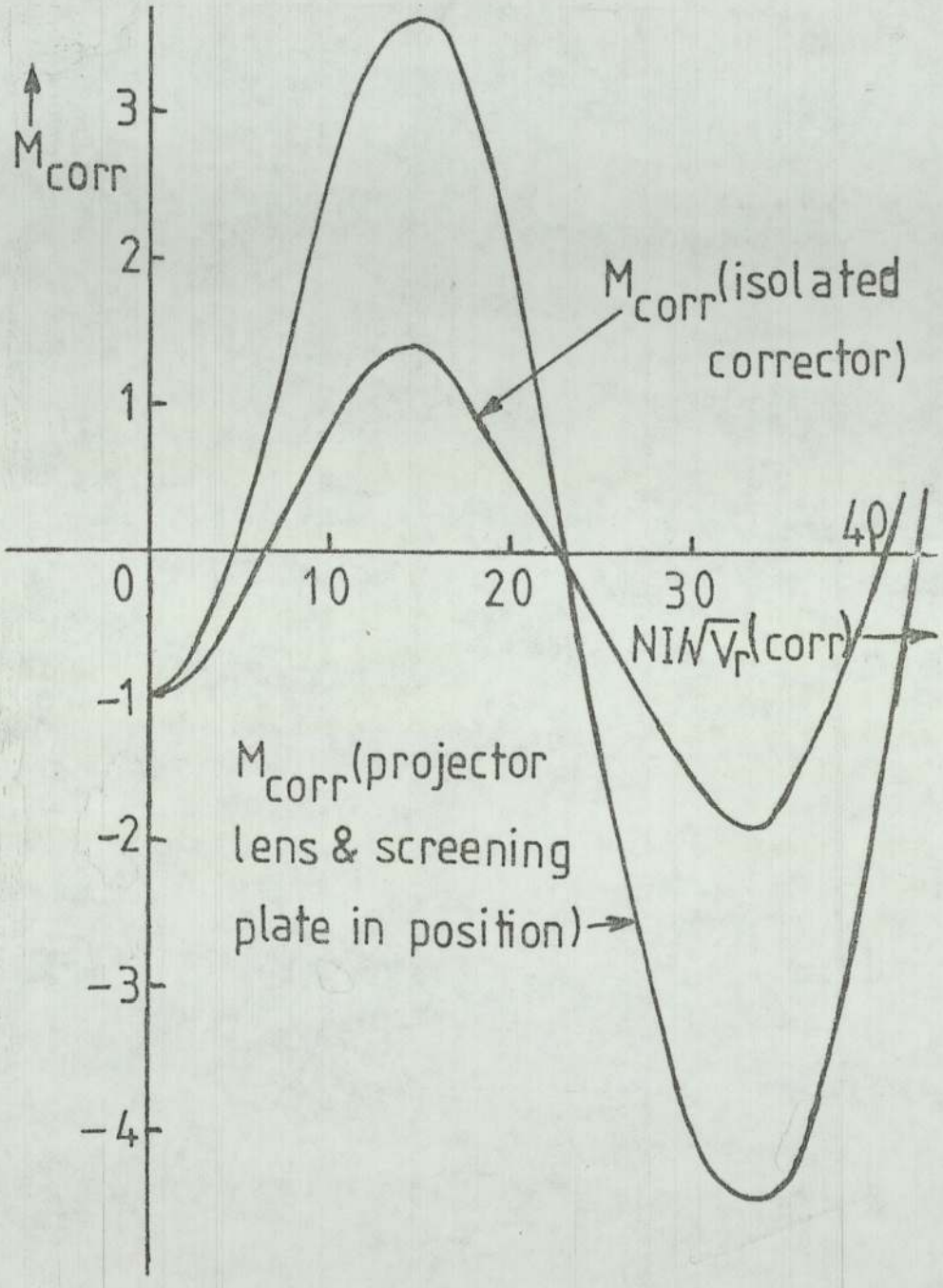

Figure (5.17) The magnification M_{corr} produced by the corrector lens (1) isolated corrector (2) corrector with iron screening plate and projector in position. $NI_{proj} = 0$.

CHAPTER 6

THE CORRECTOR-PROJECTOR LENS SYSTEM

6.1 COMPUTATION OF ELECTRON TRAJECTORIES AND MAGNIFICATION IN THE CORRECTOR-PROJECTOR SYSTEM FOR VARIOUS LENS SPACINGS

The experimental data of the interacting magnetic fields for the projector and corrector lenses at snout separations 36,50, 61 and 70 mm. of Chapter (5) was the basis of this analysis. Together with the relevant computer programs these data were used to evaluate the electron trajectories through the two-lens system and the range of magnification. The aim of the computation is to investigate polepiece separation and polepiece shape for corrector and projector lenses. Since the projector is usually operated at an excitation near that required for minimum focal length we may assume its excitation is constant at that particular value. On the other hand, the corrector excitation may vary over a wider range of excitation.

A knowledge of the electron trajectories through the two-lens system is important in the design of the polepieces themselves. Typical trajectories are shown in figures (6.1) to (6.4). The electron trajectories displayed in these figures assume that the projector is operated at its first minimum focal length $NI/V_r^{\frac{1}{2}}(proj) = 15.5$;the correcter lens is then operated at its first $[NI/V_r^{\frac{1}{2}}(corr) = 16]$ and second $[NI/V_r^{\frac{1}{2}}(corr) = 36]$ minimum focal lengths respectively. The electrons enter the system at parallel incidence. The system corresponds, therefore, to that of Lambrakis et.al.(1977). It can be seen that the design of the projector polepiece is very critical if large projection semi-angles

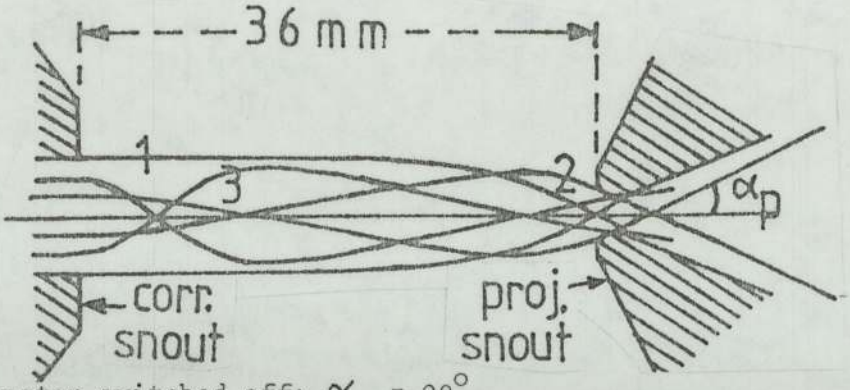

1. corrector switched off; $\alpha_p = 28^\circ$
2. corrector at first minimum focal length; $\alpha_p = 25^\circ$
3. corrector at second minimum focal length; $\alpha_p = 7^\circ$

Figure (6.1) Computer electron trajectories (parallel incidence) through the corrector/projector system. Poleface separation = 36 mm. Projector at first minimum focal length. Maximum possible semi-angle (α_p) is calculated for various excitations of the corrector lens.

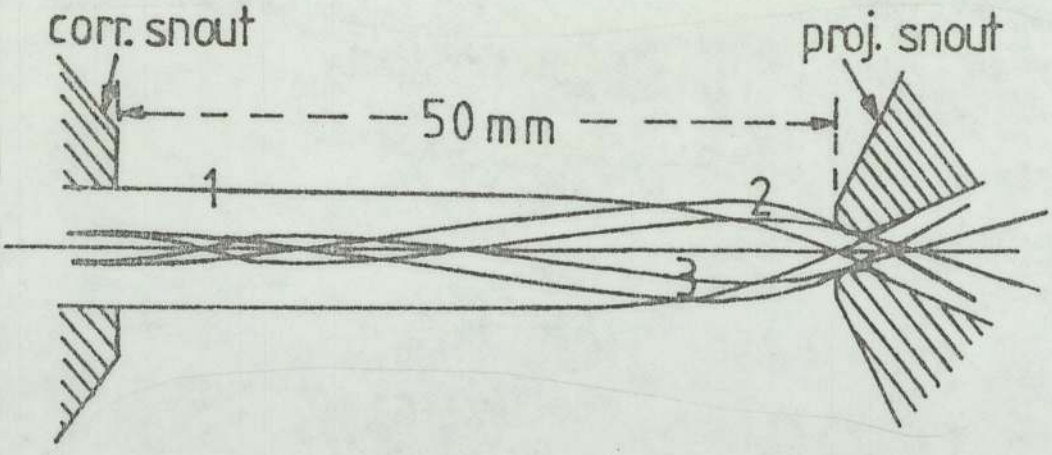

1. corrector switched off; $\alpha_p = 24^\circ$
2. corrector at first minimum focal length; $\alpha_p = 27^\circ$
3. corrector at second minimum focal length; $\alpha_p = 16^\circ$

Figure (6.2) Computer electron trajectories (parallel incidence) through the corrector/projector system. Poleface separation = 50 mm. Projector at its first minimum focal length. Maximum α_p calculated for various excitations of the corrector lens.

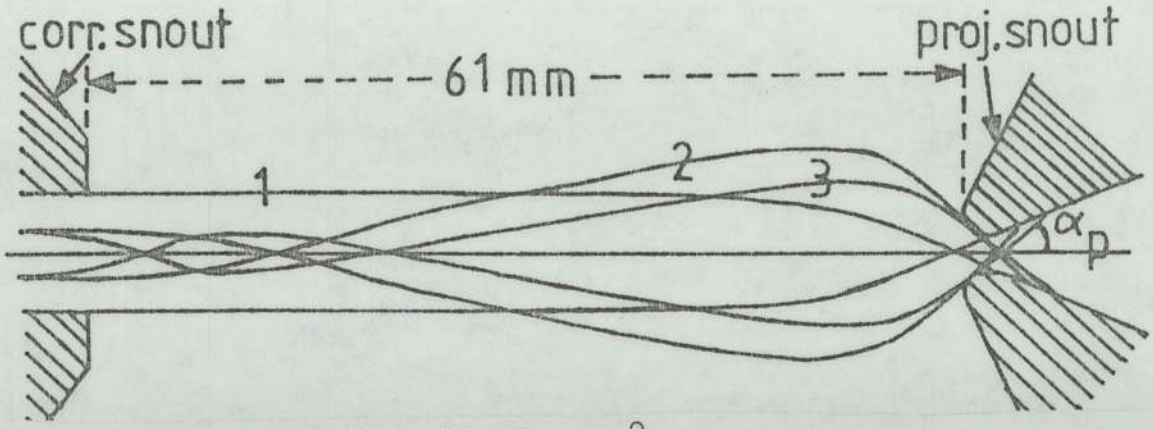

1. corrector switched off; $\alpha_p = 24^\circ$
2. corrector at first minimum focal length; $\alpha_p = 48^\circ$
3. corrector at second minimum focal length; $\alpha_p = 38^\circ$

Figure (6.3) Computer electron trajectories (parallel incidence) through the corrector/projector system. Poleface separation = 61 mm. Projector at first minimum focal length. Maximum α_p calculated for various excitation of the corrector lens.

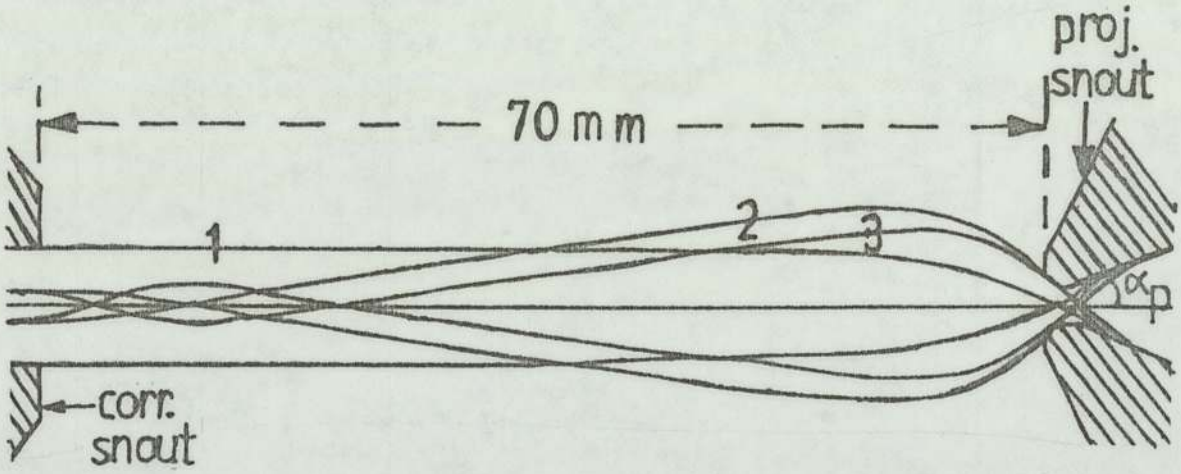

1. corrector switched off; $\alpha_p = 24^\circ$
2. corrector at first minimum focal length; $\alpha_p = 44^\circ$
3. corrector at second minimum focal length; $\alpha_p = 37^\circ$

Figure (6.4) Computer electron trajectories (parallel incidence) through the corrector/projector system. Poleface separation = 70 mm. Projector at first minimum focal length. Maximum α_p calculated for various excitations of the corrector lens.

of 22° or more are to pass through the narrow bore of the polepiece. Merely opening up the bore to allow the rays to pass is clearly not permitted since this would seriously disturb the required field distribution. It can also be seen from these figures that it is an advantage to choose the largest polepiece separation consistent with satisfying other requirements.

Similar remarks apply to the design of the corrector system developed in the present investigation, except that parameters such as lens separation are not so critical because there is more freedom in choosing the combination of lens separation and corrector excitation.

The magnification contributed by the corrector lens is also important since it determines the amount of distortion to be introduced by the corrector. The magnfication can be deduced from the ray trajectories. Figures (6.5) to (6.8) show the computed corrector magnification M_{corr} as a function of the excitation. These figures show that the corrector magnification in the second focal zone is smaller than that of the first focal zone at their minimum focal length; this is clear from the study of the trajectories. This is an advantage if spiral distortion is to be corrected with the corrector lens operated at its second focal zone. A magnification M_{corr} of about 3X is found to be convenient for correcting spiral distortion. However, even in the first focal zone, a value of M_{corr} = 3X can readily be obtained with snout separations in the region of 50 mm. as shown in figure (6.6) at an excitation $NI/V_r^{\frac{1}{2}}(corr)$ of about 25.

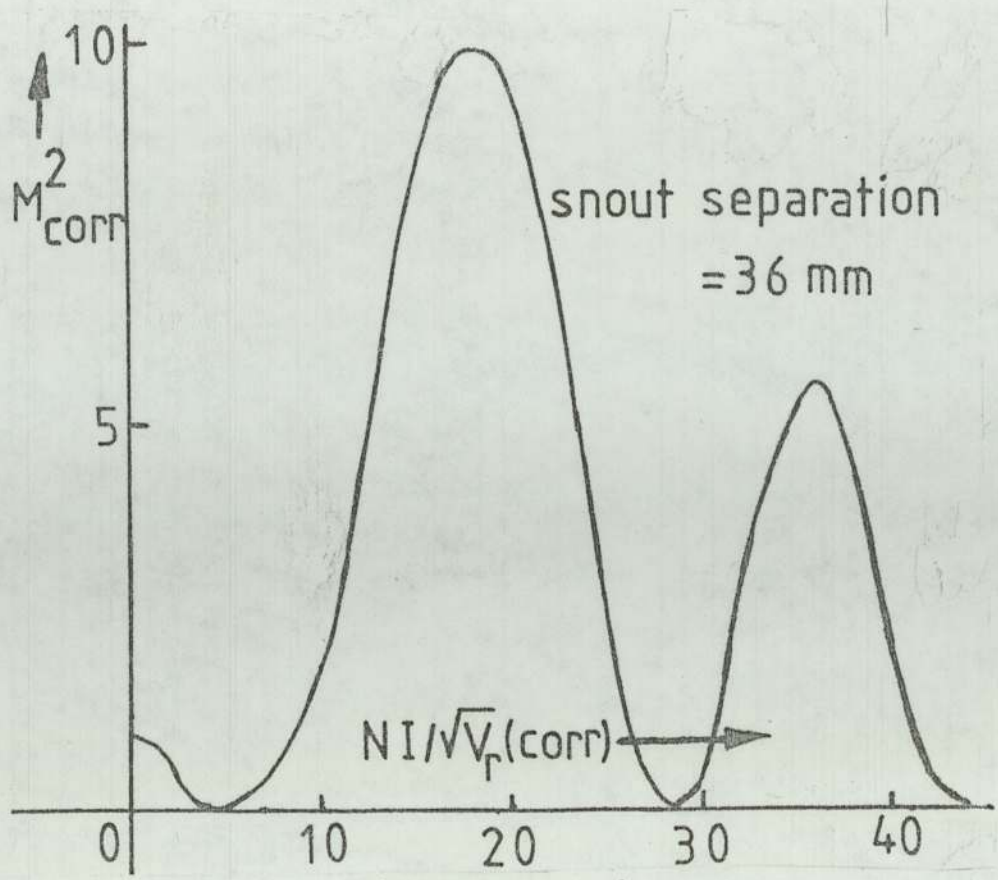

Figure (6.5) Variation of M^2_{corr} with $NI/V_r^{\frac{1}{2}}$(corr) at poleface separation 36 mm. Computed results.

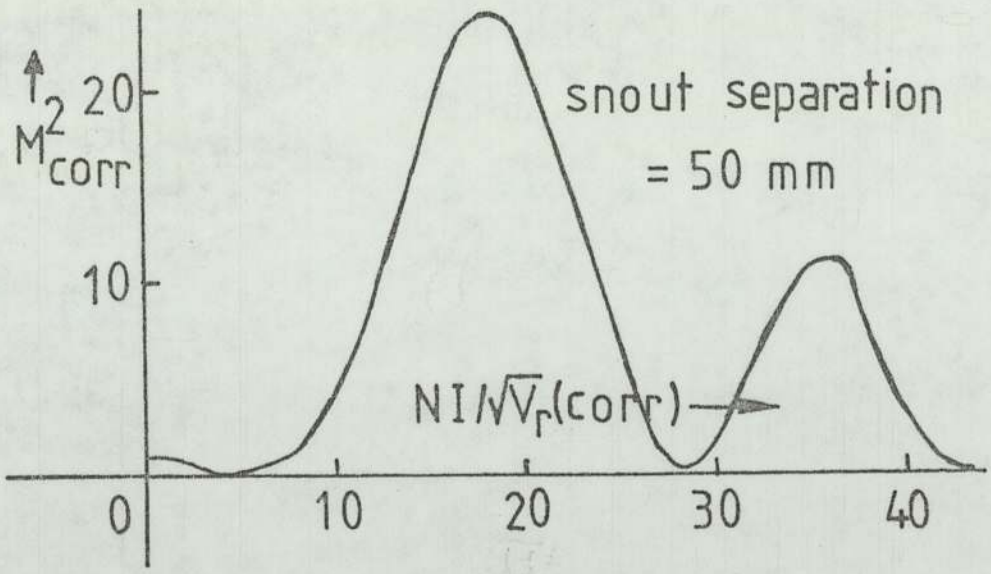

Figure (6.6) Variation of M^2_{corr} with $NI/V_r^{\frac{1}{2}}$(corr) at poleface separation 50 mm. Computed results.

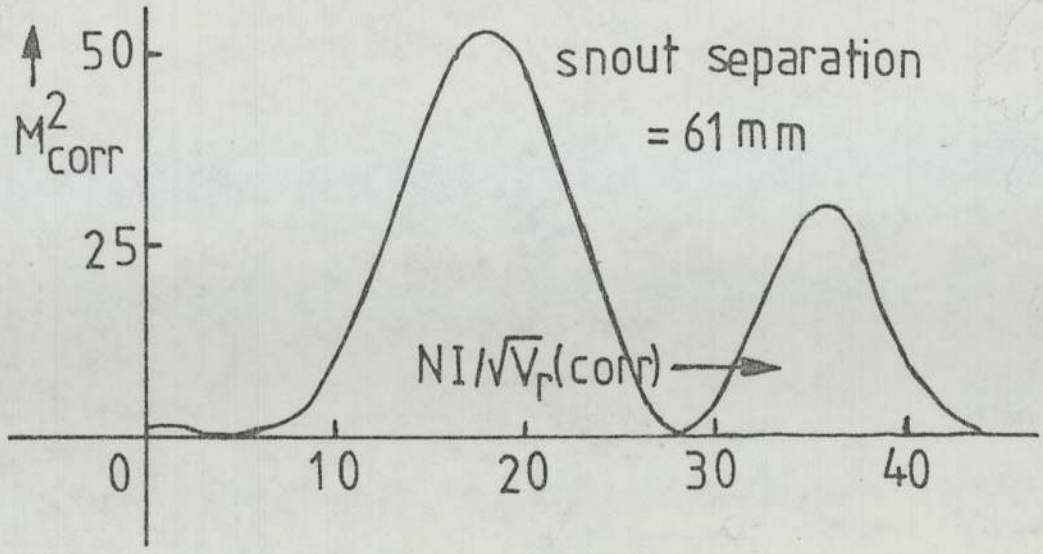

Figure (6.7) Variation of M^2_{corr} with $NI/V_r^{\frac{1}{2}}$(corr) at poleface separation 61 mm. Computed results.

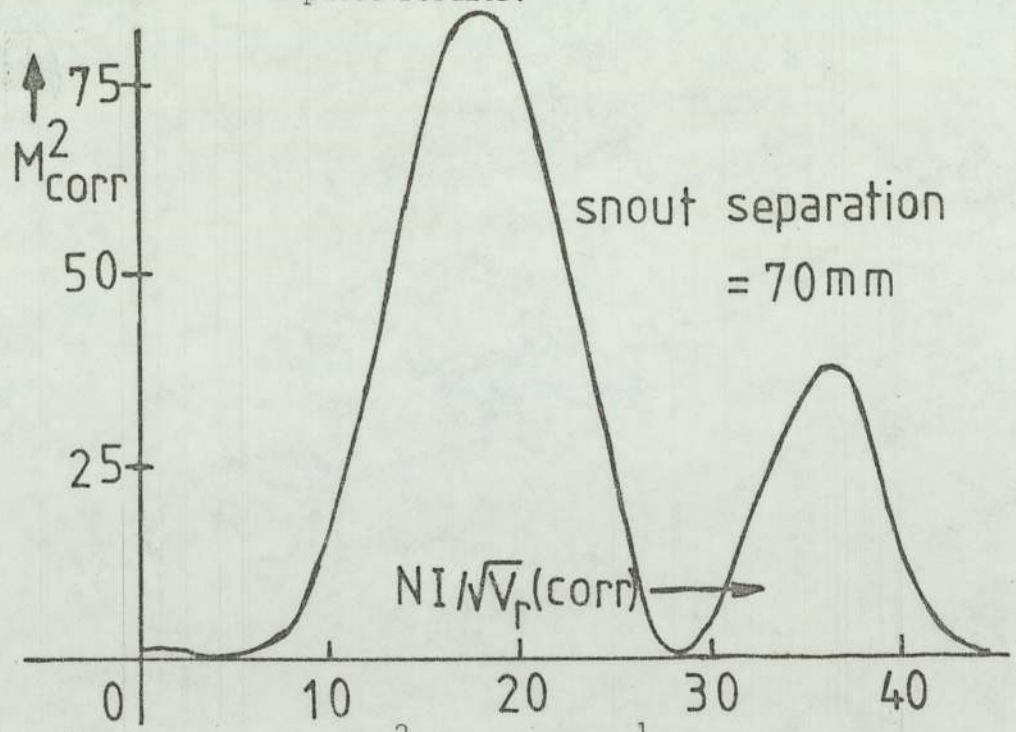

Figure (6.8) Variation of M^2_{corr} with $NI/V_r^{\frac{1}{2}}$(corr) at poleface separation 70 mm. Computed results.

6.1.1 IMAGE DISTORTION IN LAMBRAKIS et.al.(1977) SYSTEM

Finally the computed results enable one to assess the performance of the complete system. Figure (6.9) shows the effective distortion coefficient Q_{eff} of this corrector/projector system but operated in the mode proposed by Lambrakis et.al. (1977). Here only the spiral distortion contributes to the image

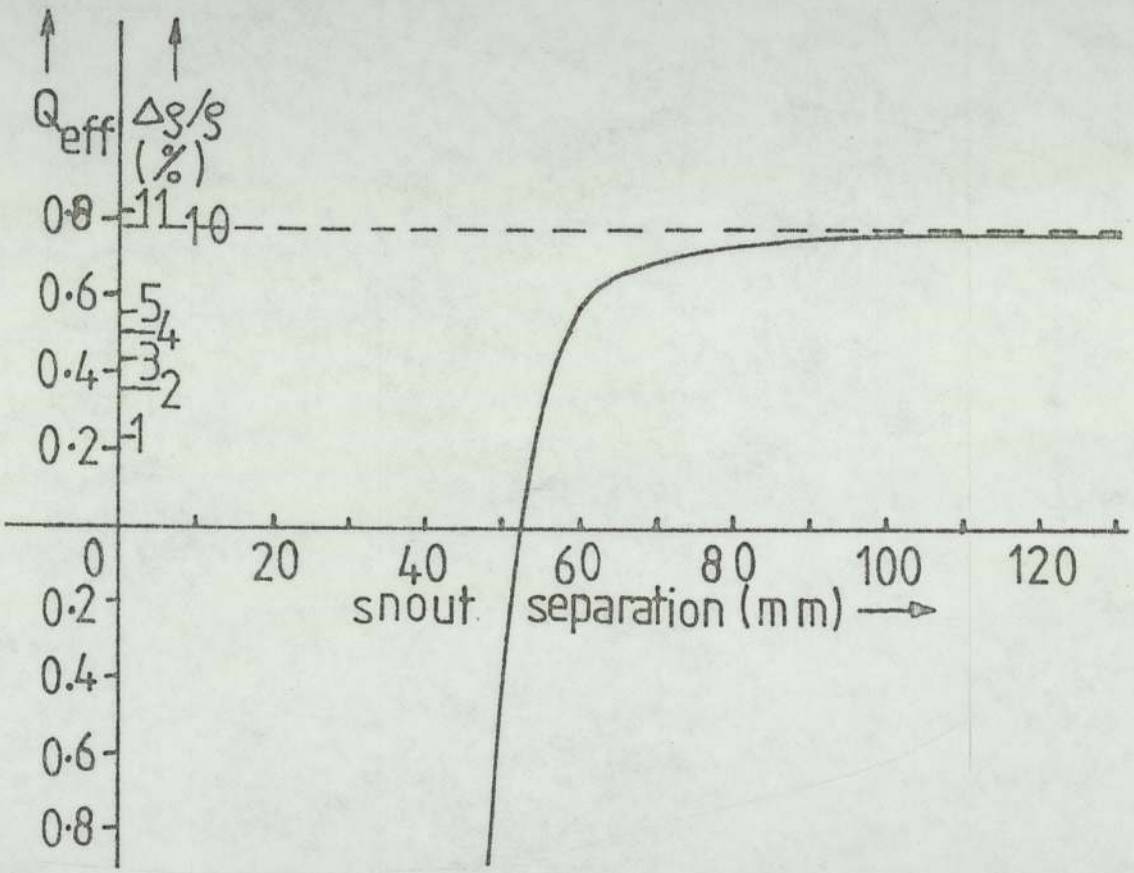

Figure (6.9) System quality factor Q_{eff} in the Lambrakis et.al. (1977) system as a function of the snout separation. The projector is operated at its first minimum focal length and the corrector at its second minimum focal length.

since radial distortion is eliminated in each lens by operating the lenses at minima focal lengths. Figure (6.9) shows that the spiral distortion vanishes at a snout separation of some 52 mm. However, the correct adjustment of the separation is clearly difficult since the slope of the distortion/separation curve is steep (a change in separation of $\pm$ 2 mm. changes the distortion by about 1%). In practice this is not a severe difficulty. However, it is very difficult to predict the correct separation itself and thus some form of mechanical adjustment must be provided which complicates the design.

6.2 EXPERIMENTAL SET-UP FOR 22° PROJECTION SEMI-ANGLE

Figure (6.10) show the experimental arrangement for projecting an image at a projection semi-angle of 22°. At this angle the normal fluorescent screen and photographic plate are far too small to record the complete image. It was therefore necessary to fit a transmission fluorescent screen just below the projector lens, as shown in figure (6.10). The image on this screen was photographed by external photography through a window placed on the base of the normal camera chamber.

Figure (6.11) shows, in schematic form, the electron-optical system corresponding to the cross-sectional diagram of figure (6.10). The polepiece separation between the corrector and projector was set at 50 mm. for the reasons given in the previous section.

6.3 EXPERIMENTAL RESULTS

In these experiments the corrector lens was operated at the high end of the first focal zone and the projector was

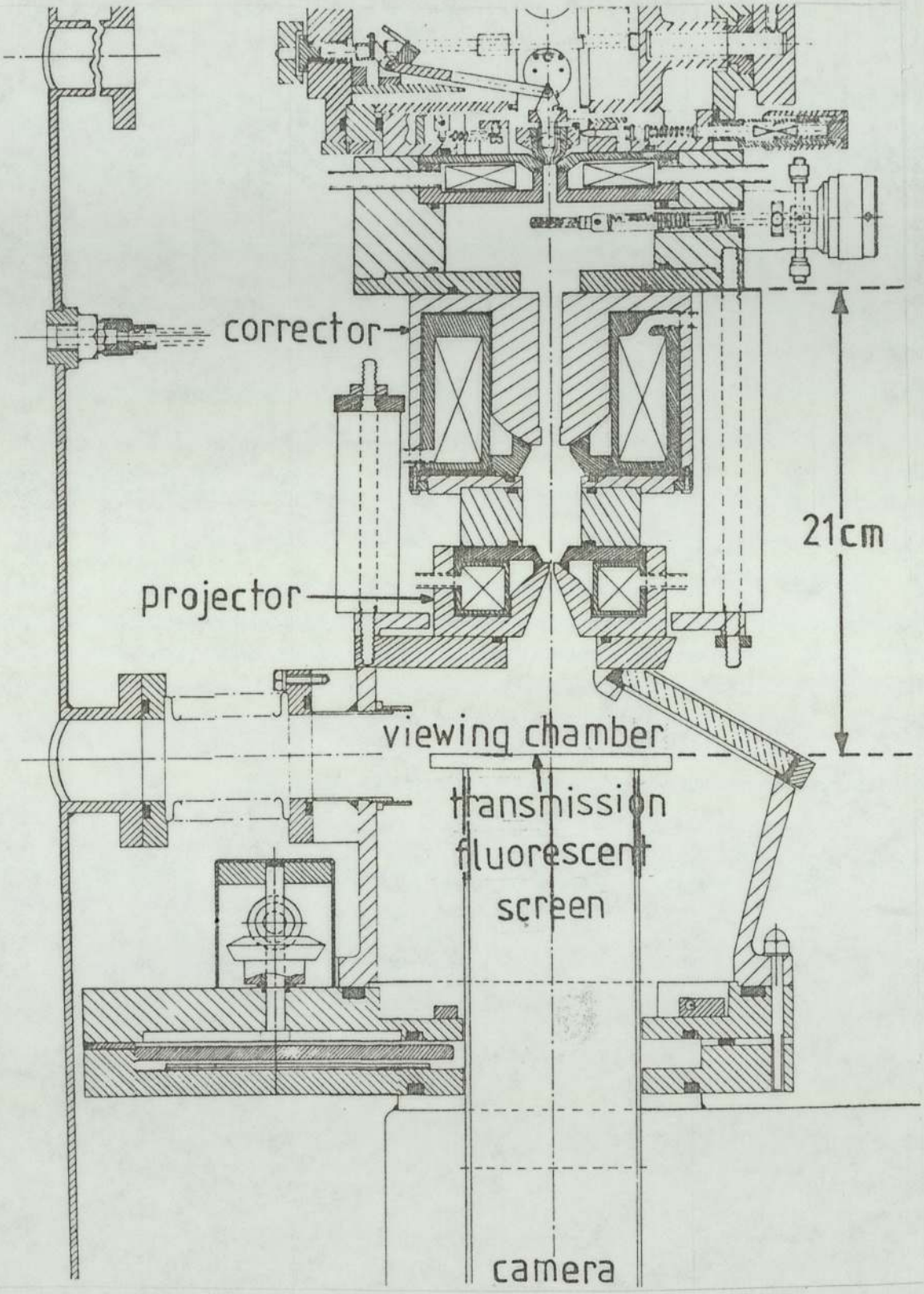

Figure (6.10) Viewing arrangement and projection system of the experimental TEM.

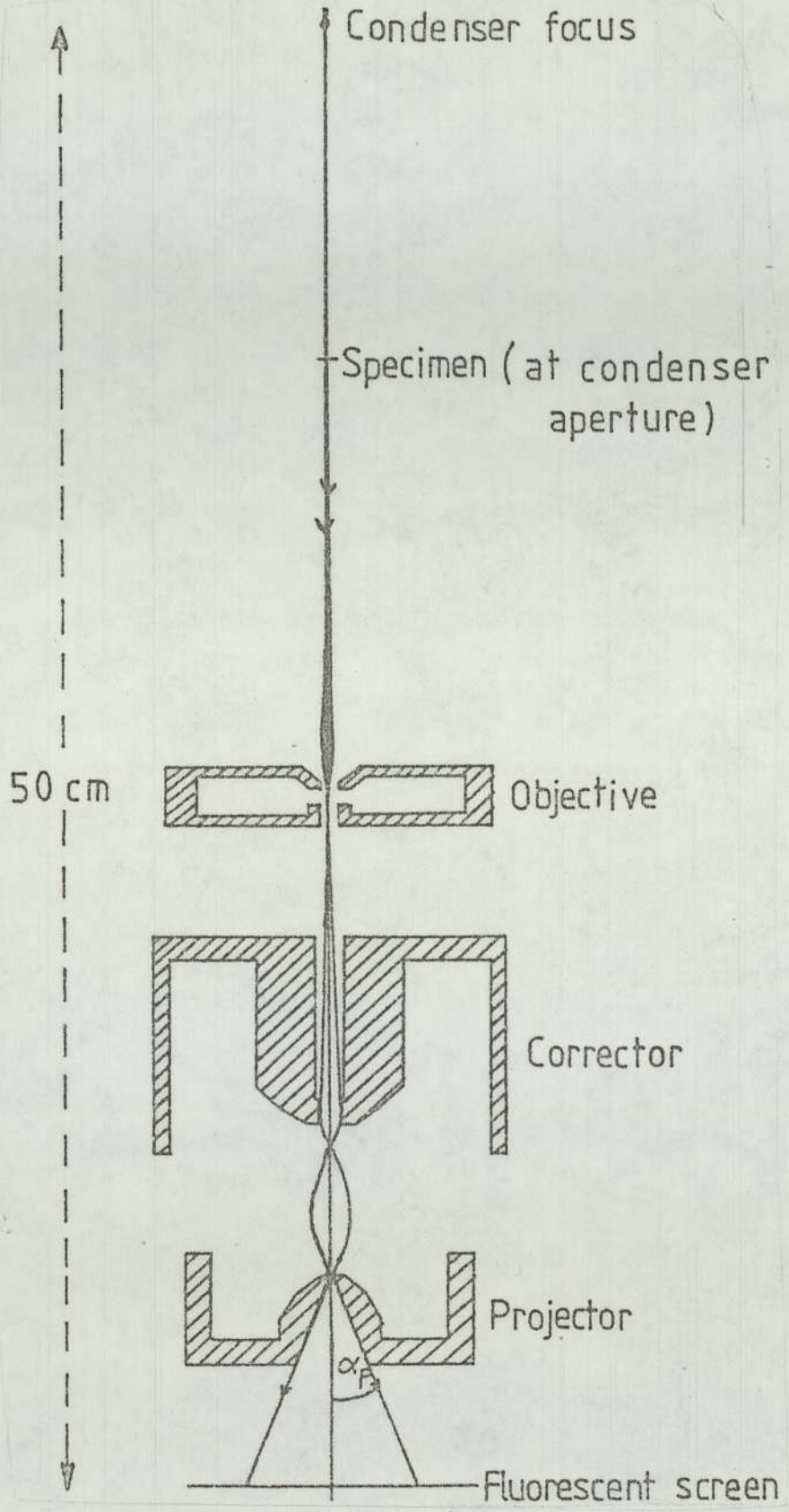

Figure (6.11) Schematic diagram of the electron-optical column of the experimental TEM with a wide angle projection system ($\alpha_p = 22^\circ$), $NI/V_r^{\frac{1}{2}}(corr) = 24$, $NI/V_r^{\frac{1}{2}}(proj) = 13$.

operated just below the point of minimum focal length so as to introduce a compensating pin-cushion distortion to remove the barrel distortion produced by the corrector.

Figure (6.12) shows some typical projection images obtained with this system. Figure (6.12a) shows a projection image obtained with the corrector lens switched off. The projection semi-angle is restricted to 11.5° where the spiral distortion is 2.7%. This is equivalent to 10.6% as shown by the dotted line in the figure. Figure (12.6b) shows a projected image with the projector and corrector lenses switched on. The projection semi-angle has increased to $\alpha_p = 22^{\circ}$ and the corresponding spiral distortion at the edge of the image is less than the permitted 2%.

Thus the principle has been verified that correction of distortion is possible with the corrector lens operating at the high excitation end of the first focal zone. The results of the correction of distortion in this system have already been published [(Elkamali and Mulvey 1980), cf. Apendix(2)].

The combined field distribution of this system for the condition of no distortion is shown in figure (6.13) for a projector excitation $NI/V_r^{\frac{1}{2}} = 13$ and a corrector excitation $NI/V_r^{\frac{1}{2}} = 24$ as determined experimentally. In this figure the positive part of the field distribution is that of the projector whereas the negative part is that of the corrector. The calculated distortion of this field distribution gave [see equations (2.26) and (2.27)] the following results:

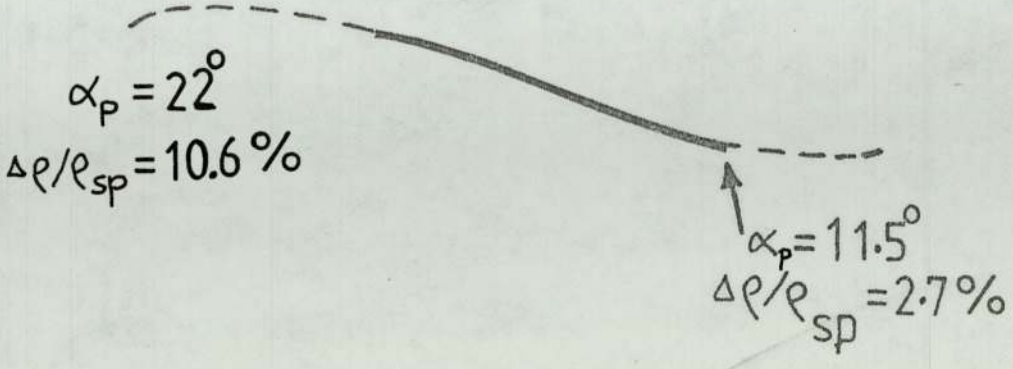

Figure (6.12a) An electron micrograph image taken with the single-polepiece projector lens. $NI/V_r^{\frac{1}{2}}(proj) = 13$; $\alpha_p = 11.5^\circ$; $\Delta\rho/\rho_{sp} = 2.7\%$.

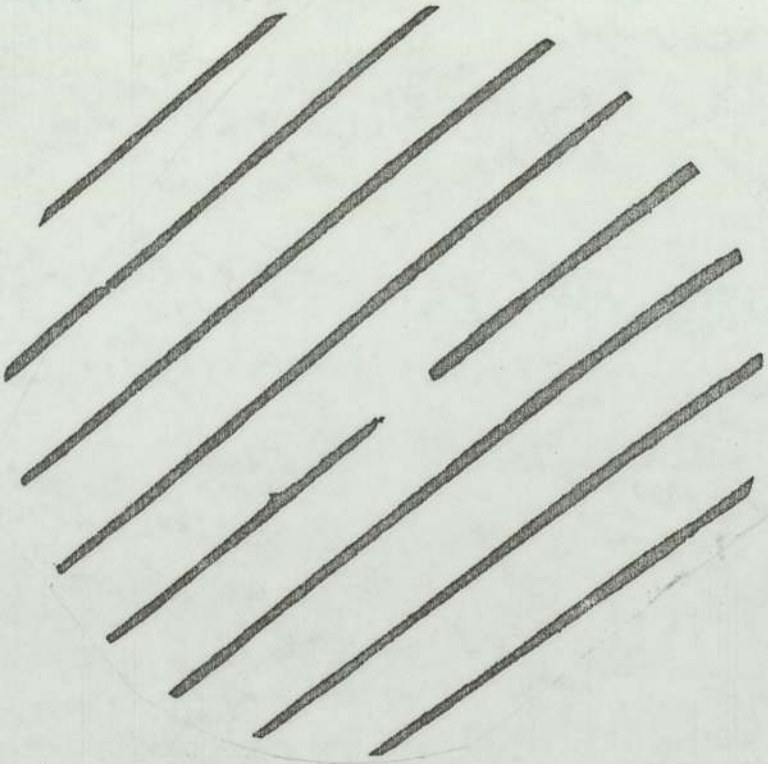

Figure (6.12b) A corrected image taken with the projection system. $NI/V_r^{\frac{1}{2}}(proj) = 13$; $NI/V_r^{\frac{1}{2}} = 24$; $\alpha_p = 22^\circ$; $\Delta\rho/\rho_{sp} < 2\%$.

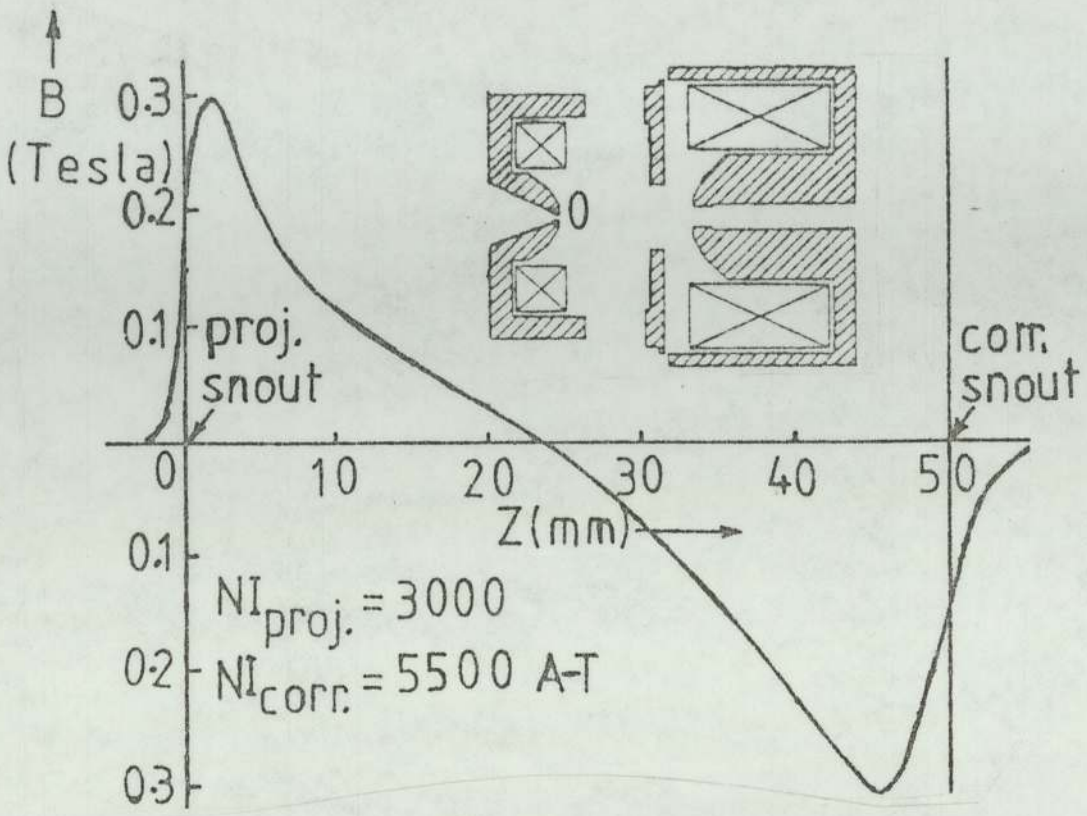

Figure (6.13) Combined field distribution of the projector ($NI/V_r^{\frac{1}{2}} = 13$) and the corrector ($NI/V_r^{\frac{1}{2}} = 24$).

At the operational excitations $f_p = 10$ mm., $f_{corr} = 32$ mm., $M_{corr} \simeq$ 3X and $\alpha_p = 22^\circ$.

(1) Q^*_{rad} (projector) = 1.02, i.e. the radial distortion from the projector lens is $\Delta\rho/\rho_{rad}$(projector) $\simeq$ 24%, i.e. pin-cushion distortion.

(2) Q^*_{sp}(projector) = 0.94, i.e. the spiral distortion from the projector lens is $\Delta\rho/\rho_{sp}$(projector) $\simeq$ 21%.

(3) Q_{rad}(corrector) = -9.79, the negative sign refers to barrel distortion. Thus the reduced Q_{rad} of the corrector lens at the final image will amount to

$$\frac{Q_{rad}(\text{corrector})\, f_p}{f_{corr}\, M_{corr}} \simeq 1.02$$

Hence the radial distortion from the corrector lens is $\Delta\rho/\rho_{rad}(\text{corrector}) \simeq -24\%$. This means that the two radial distortions (pin-cushion and barrel) will cancel each other.

(4) $Q_{sp}(\text{corrector}) = -9.02$. If this is referred to the final image we obtain

$$\frac{Q_{sp}(\text{corrector})\, f_p}{f_{corr}\, M_{corr}} \simeq -0.94$$

i.e. $\Delta\rho/\rho_{sp}(\text{corrector}) \simeq -21\%$. Similarly, the two spiral distortions of opposite sign will also cancel each other.

It is therefore clear that the corrector lens can compensate the spiral distortion produced by the projector lens as well as providing sufficient (barrel) radial distortion to compensate the (pin-cushion) radial distortion introduced by the projector.

CHAPTER 7

A WIDE-ANGLE PROJECTION SYSTEM (SEMI-ANGLE 30°)

7.1 THE REDESIGNED PROJECTOR LENS

These successful preliminary results described in Chapter (6) in the correction of spiral distortion with a projection semi-angle of 22° served as an incentive for designing an improved system capable of operating at an even larger semi-angle, possibly up to 35°. In this system, the design of the projector lens snout was altered considerably especially in the regions of the entrance and outlet of the electron beam in the light of the electron trajectory calculations. The re-shaped polepiece is shown schematically in figure (7.1a). The polepiece exit was also opened into a cone of 35° semi-angle. In reshaping the front part of the polepiece only the minimum amount of iron must be removed so as not to change the favourable field distribution in this critical region. Figure (7.1b) shows the detailed changes made in the new polepiece ($\alpha_p = 35^\circ$) compared with that in the old one ($\alpha_p = 22^\circ$).

The axial magnetic field density distribution of the redesigned projector lens, measured with a Hall probe is shown in figure (7.2). These experiments showed that the reshaping operations had not significantly altered the favourable flux density distribution B_z and no iron saturation effects occurred for excitations NI_{max} up to 8750 ampere-turns. Reshaping the projector lens polepiece caused some changes in the electron-optical constants of the lens. The half-width was increased from 7.6 mm. to 13.5 mm. and the maximum field B_{max} had decreased by 35%. These changes were

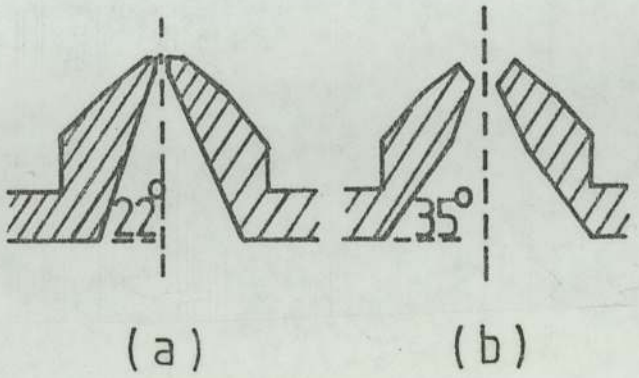

Figure (7.1a) Polepiece design for a wide-angle projector lens (a) $\alpha_p = 22^\circ$ (b) $\alpha_p = 35^\circ$.

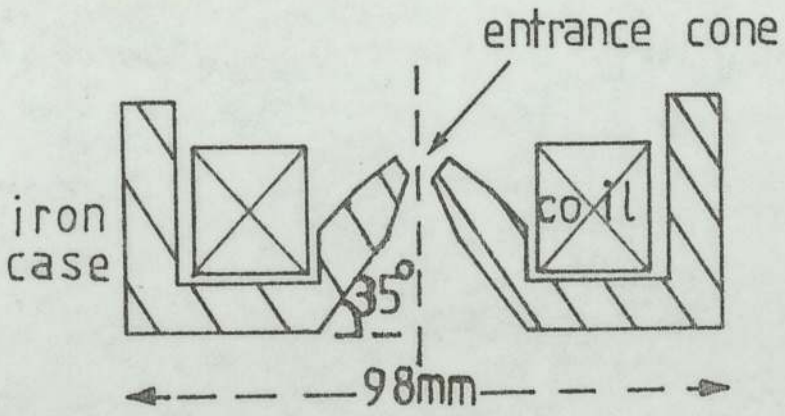

Figure (7.1b) Cross-section (brass lid removed) of the wide-angle single-polepiece projector lens ($\alpha_p = 35^\circ$). Note the entrance cone at the poleface.

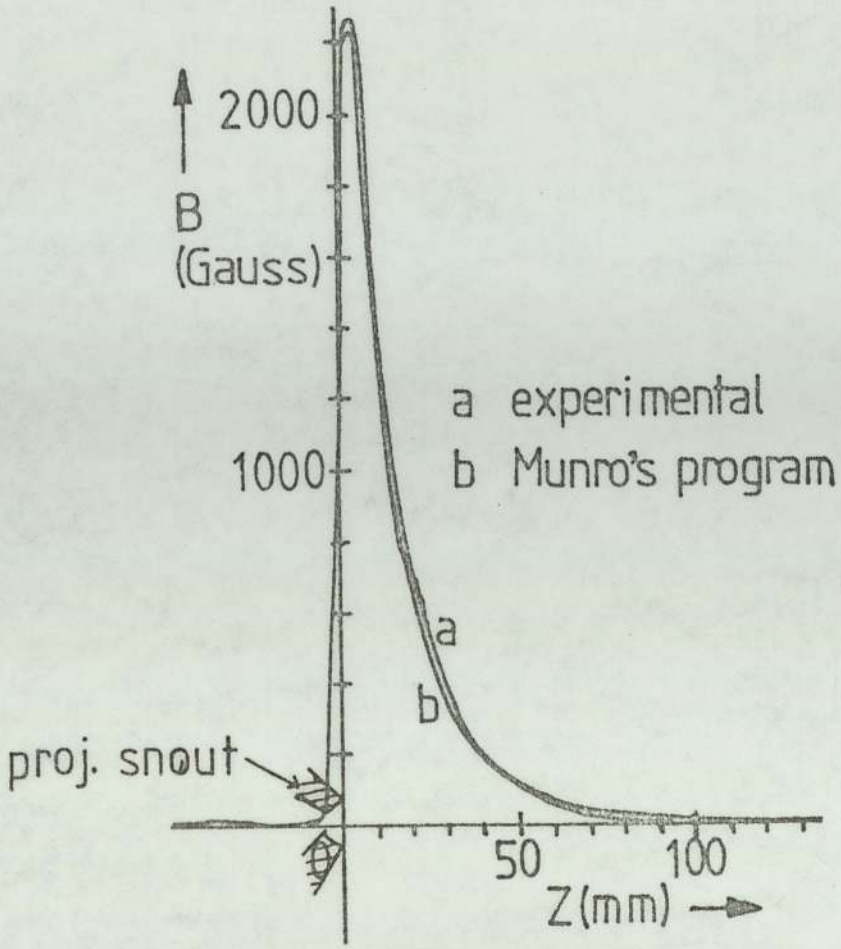

Figure (7.2) Axial magnetic field distribution of the redesigned projector lens (a) experimental (b) Munro's program.

also due to the lens bore diameter being widened from 2.5 mm. to 4 mm. The minimum focal length went from 8 mm. to 11.9 mm. at an excitation parameter $NI/V_r^{\frac{1}{2}}$ of about 14 rather than the 15 of the original design as described in Chapter (4). The focal length of the redesigned projector lens is shown in figure (7.3) as a function of the excitation parameter $NI/V_r^{\frac{1}{2}}$.

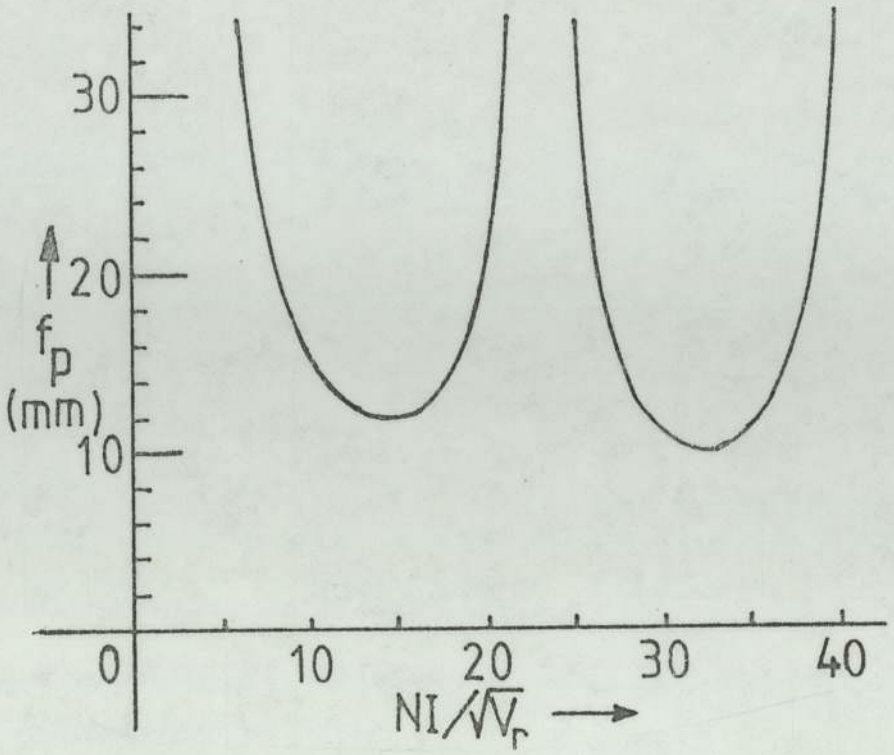

Figure (7.3) Increased focal length f_p of the redesigned projector lens as a function of the excitation parameter $NI/V_r^{\frac{1}{2}}$.

The distortion coefficients D_{rad} and D_{sp} and the quality factors Q_{rad} and Q_{sp} were also affected. The broadening of the half-width had increased both Q_{rad} and Q_{sp} by about 10%. The relevant distortion coefficients are shown in figure (7.4) as a function of the excitation parameter $NI/V_r^{\frac{1}{2}}$ while the corresponding quality factors are shown in figure (7.5).

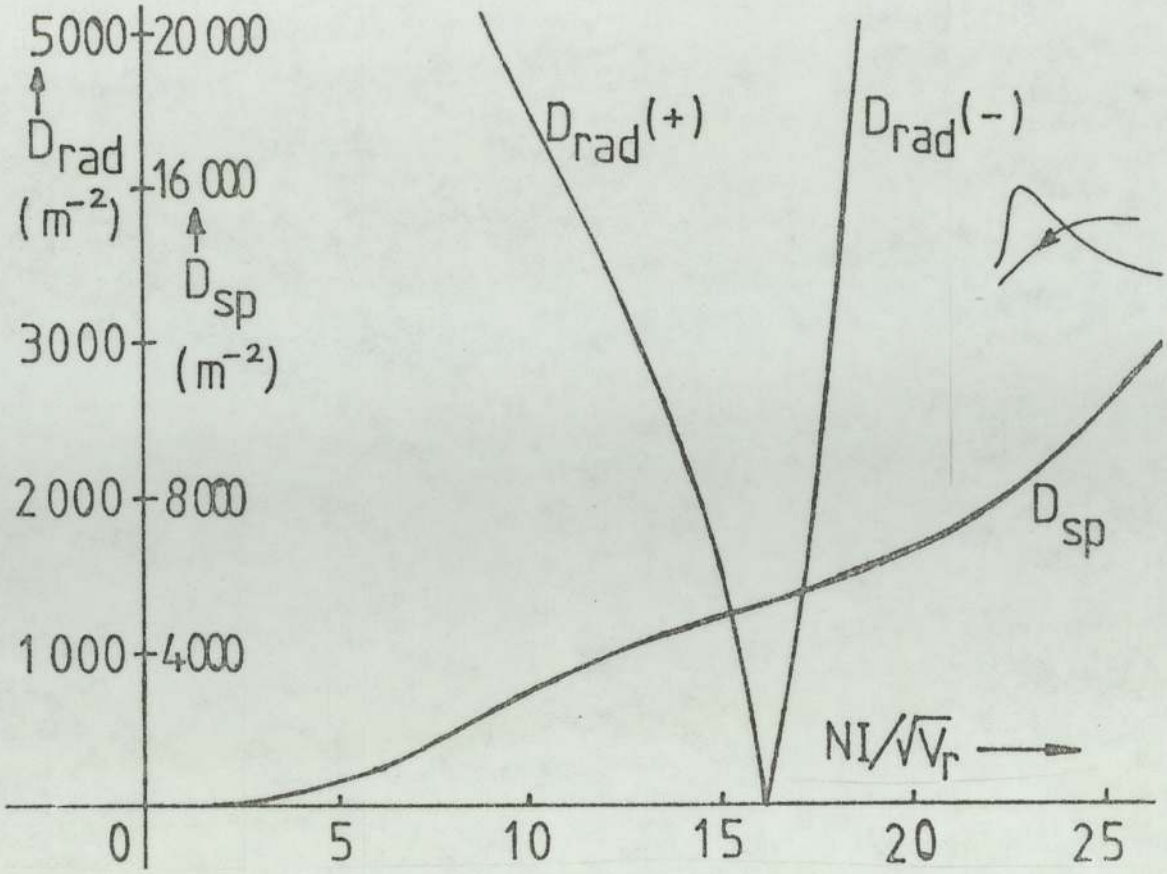

Figure (7.4) Increased distortion coefficients D_{rad} and D_{sp} of the redesigned projector lens versus the excitation parameter $NI/V_r^{\frac{1}{2}}$.

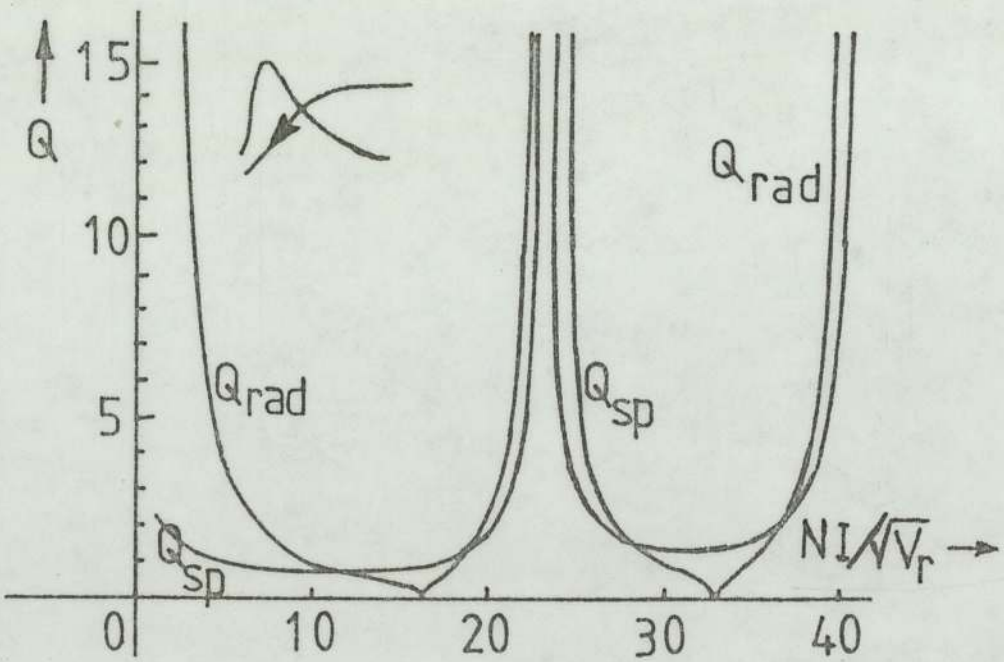

Figure (7.5) Increased quality factors Q_{rad} and Q_{sp} of the redesigned projector lens versus the excitation parameter $NI/V_r^{\frac{1}{2}}$.

7.2 THE COMPLETE WIDE-ANGLE PROJECTION SYSTEM

The final version of the corrector/projector system is shown in figure (7.6). It consists of the redesigned projector lens, the corrector lens described in Chapter (5) complete with an iron face plate between the two lenses. The separation between the polefaces of the two lenses was set at 52 mm., as this seemed to be a favourable compromise, bearing in mind the conflicting requirements discussed previously. The total axial height of the projection system from the top of the corrector lens to the transmission screen is about 21 cm. Figure (7.7) is a photograph showing the complete system. The wide-angle transmission screen is visible through the viewing window of the viewing chamber.

The field distribution of the complete corrector-projector system was computed. Figure (7.8) shows the 32 X 70 mesh distribution corresponding to the entire projection system. Here M_{corr} = 5590 A-T and $NI_{proj.}$ = 3000 A-T corresponding to the expected operational excitation parameters $NI/V_r^{\frac{1}{2}}$ of 24.4 (corrector) and 13(projector). The output from Munro's M13 program produced the axial magnetic field of the projection system shown in figure (7.9) together with an experimental measurement of the actual field distribution. There is good agreement between the computed and experimental results. The field distribution of the two-lens system was also computed for corrector excitations $NI/V_r^{\frac{1}{2}}$ of 15, 23, 29.5, and 33 with the projector excitation constant at $NI/V_r^{\frac{1}{2}}$ 13. These are shown in figure (7.10).

A more important investigation concerns the effect of the iron screening plate on the combined field distribution.

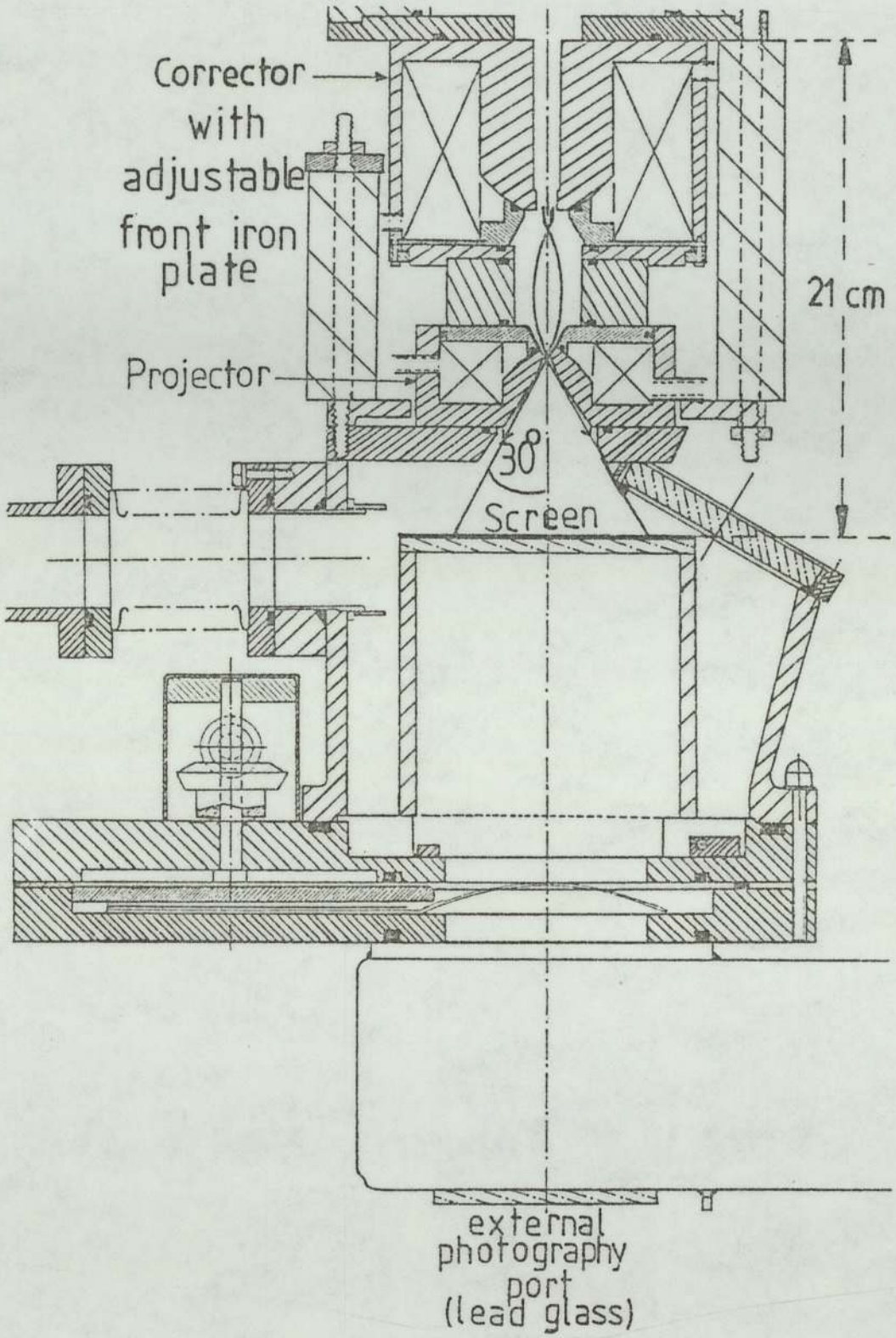

Figure (7.6) The redesigned projection system with a maximum projection semi-angle $\alpha_p = 35^\circ$. The calculated trajectories indicate a ray leaving at an angle $\alpha_p = 30^\circ$ when $NI/V_r^{\frac{1}{2}}$ (proj) 13 and $NI/V_r^{\frac{1}{2}}$(corr) = 24.4.

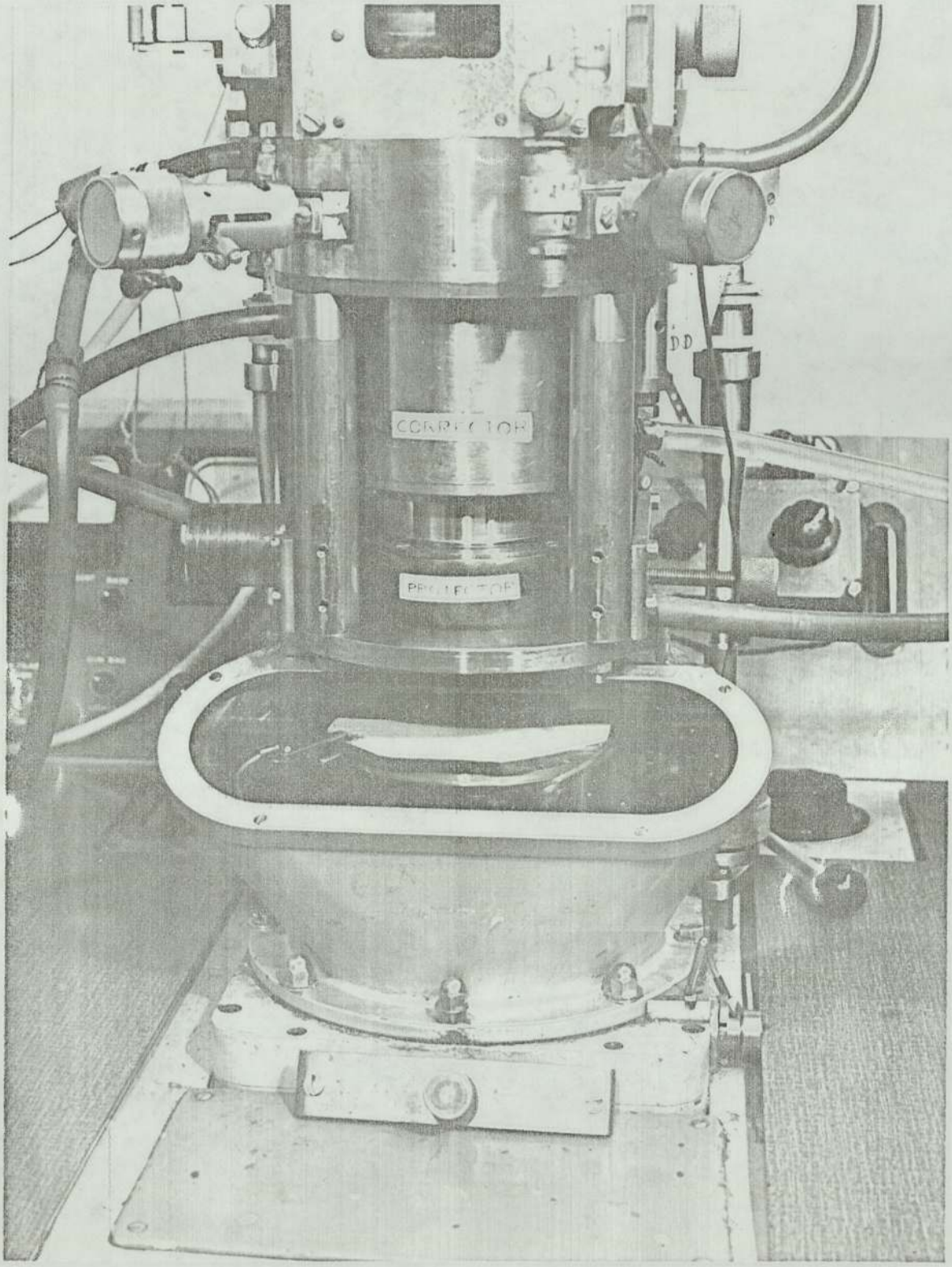

Figure (7.7) Photograph of the improved projection system mounted in the experimental microscope.

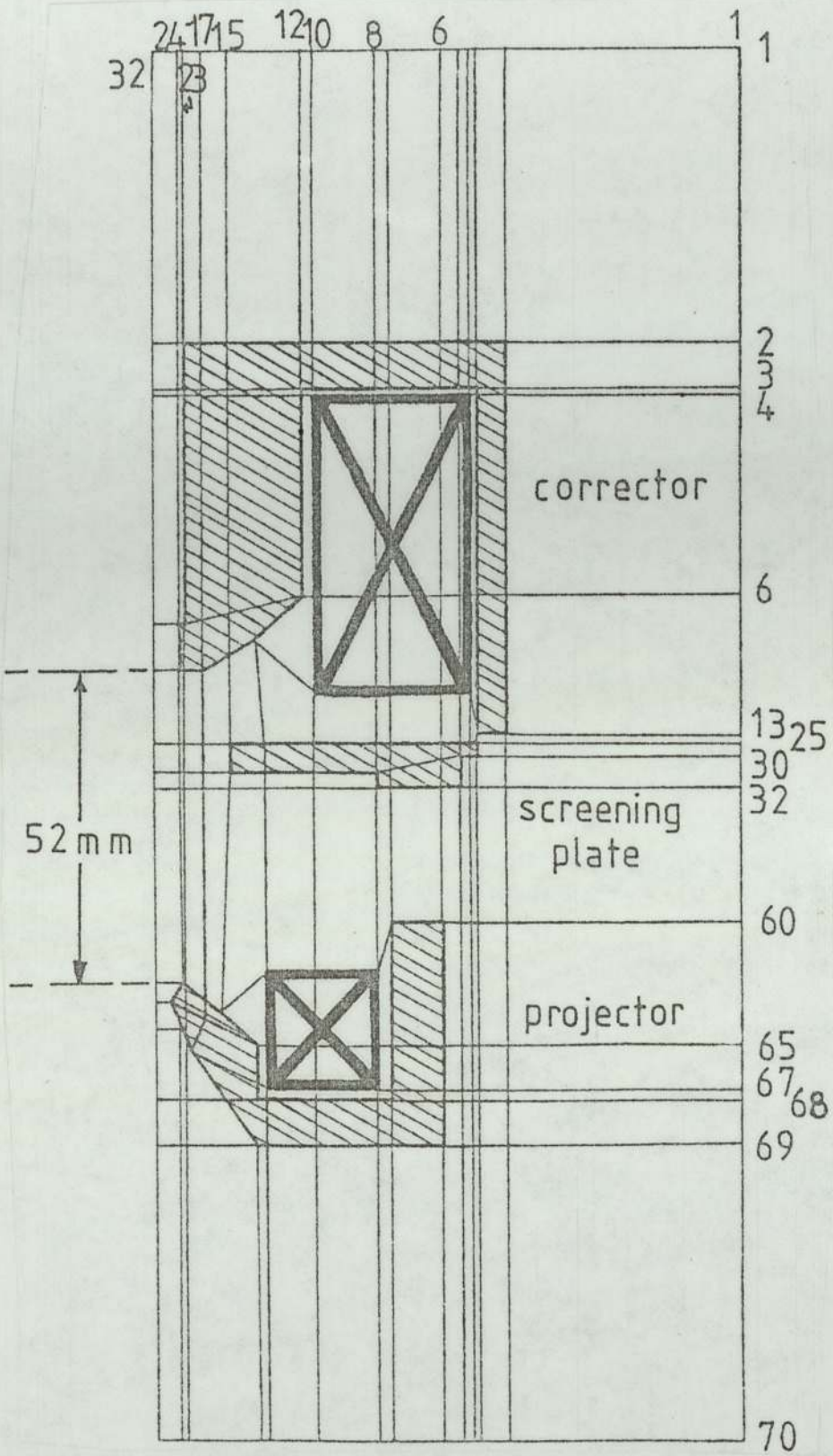

Figure (7.8) Mesh distribution of the redesigned projection system using Munro's program. The iron face plate is separated from the corrector and projector lenses by non-magnetic spacers as shown in figure (7.6).

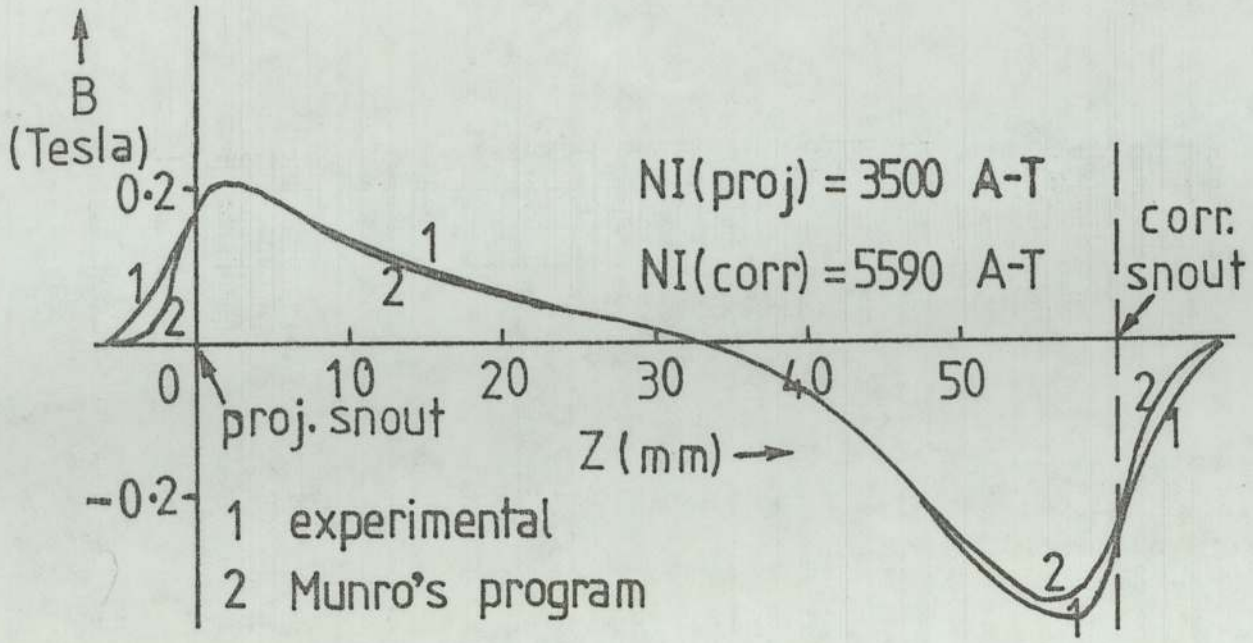

Figure (7.9) Axial magnetic field distribution of the improved projection system (1) experimental (2) calculated (using Munro's program).

This was carried out for various inside diameters of the plate as shown in figure (7.11) at a constant excitation parameter of 13 for the projector and 24.4 for the corrector. At these excitations the total ampere-turn cancellation of the combined field distribution was about 20% for each inside diameter of the face plate, as shown in figure (7.12). Figure (7.11) also shows the combined field distribution in the absence of the iron screening plate where the ampere-turn cancellation is exceptionally high (43%).

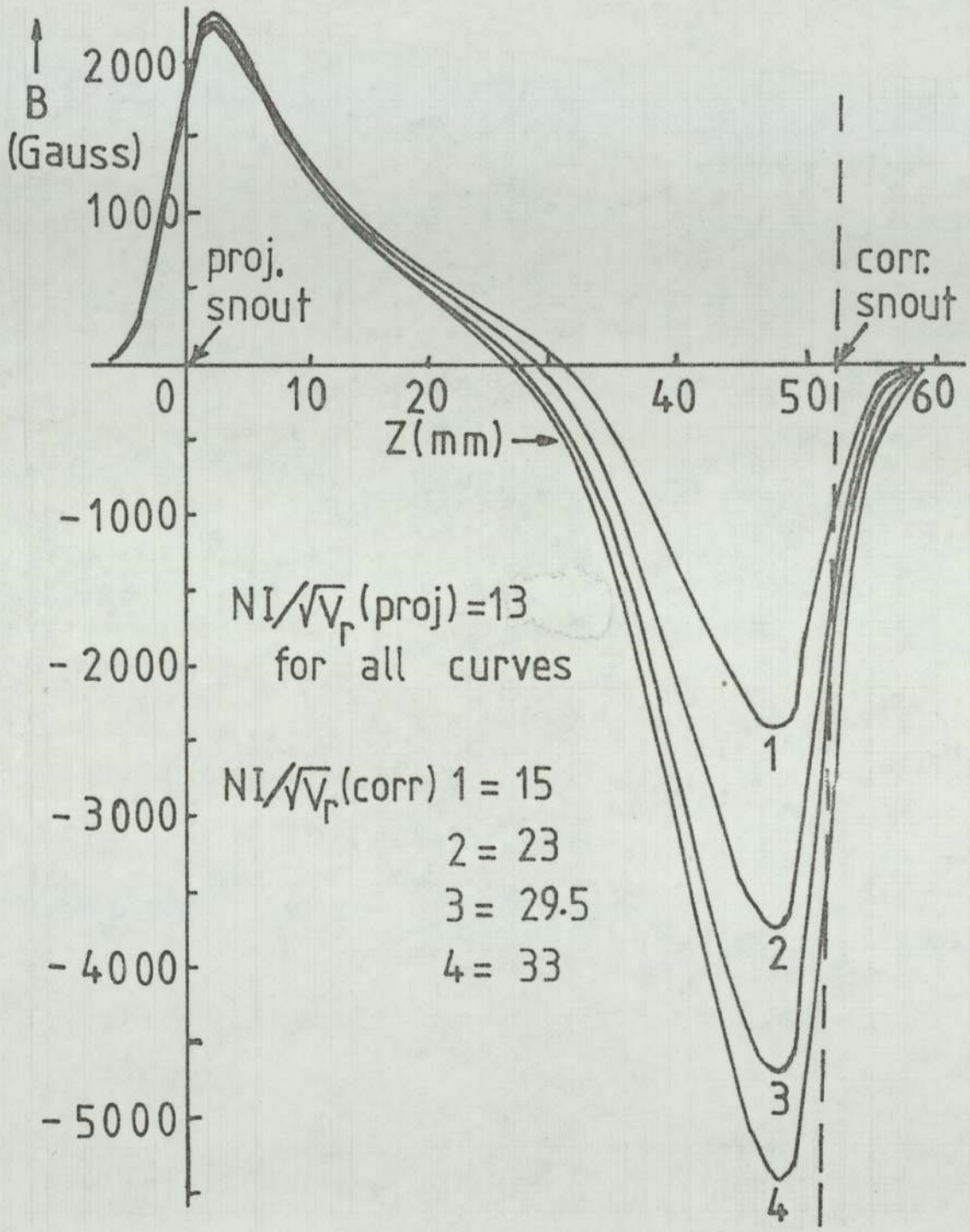

Figure (7.10) Effect of varying corrector excitation on combined field distribution.

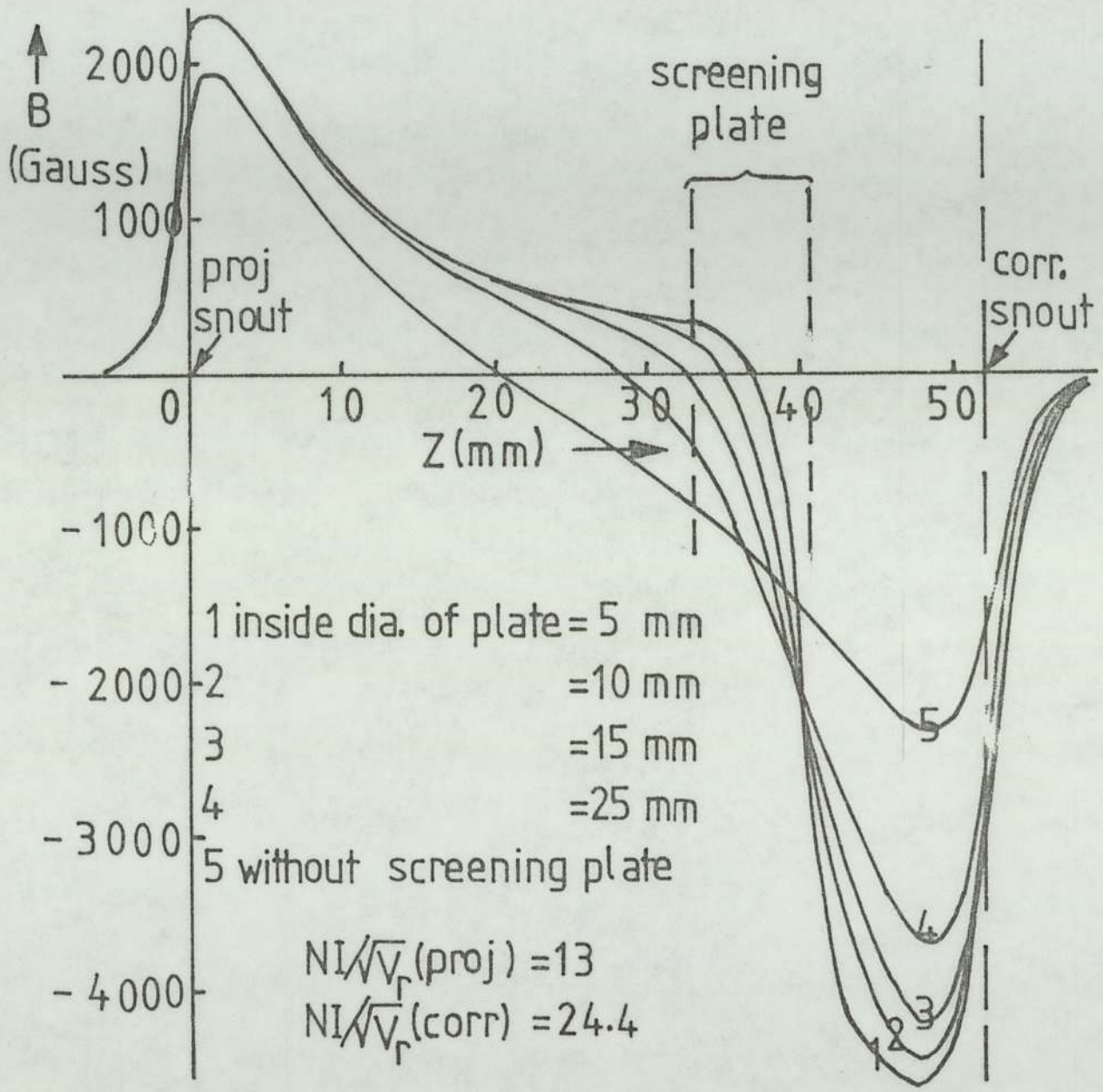

Figure (7.11) Effect of inside diameter of screening plate on the combined field distribution of the projection system.

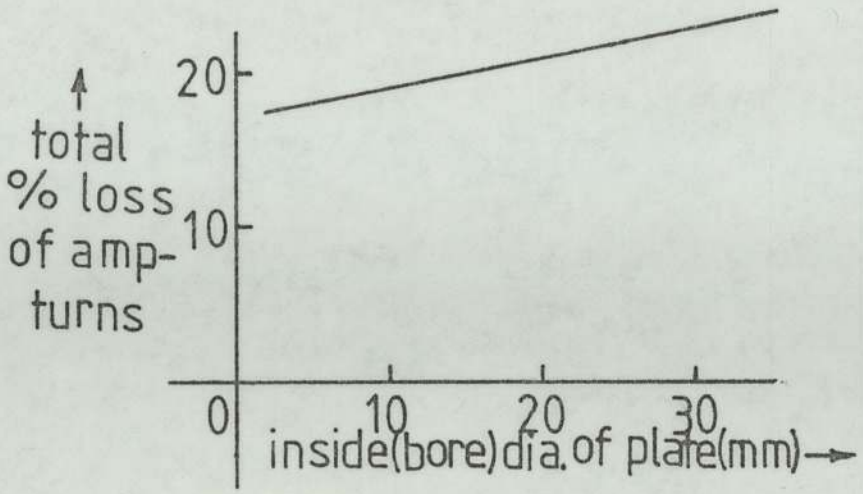

Figure (7.12) Effect of inside diameter of iron screening plate on ampere-turns percentage loss of combined field distribution of projection lenses.

The family of graphs of figure (7.10) is now further summarised in figure (7.13) since the most important parameters in any field distribution are the magnitudes of the maximum magnetic field and the half-width. These are drawn with respect to the inside diameter of the screening plate for the projector and corrector lenses respectively. Such curves are of great importance in designing projection systems where magnetic fields interact.

Futher analysis on the effect of the iron face plate was carried out in order to determine the best axial position relative to the polepieces. The results are shown in figures (7.14 a,b) for inside screening plate diameters of 5 and 25 mm. respectively at the standard projection excitation parameter

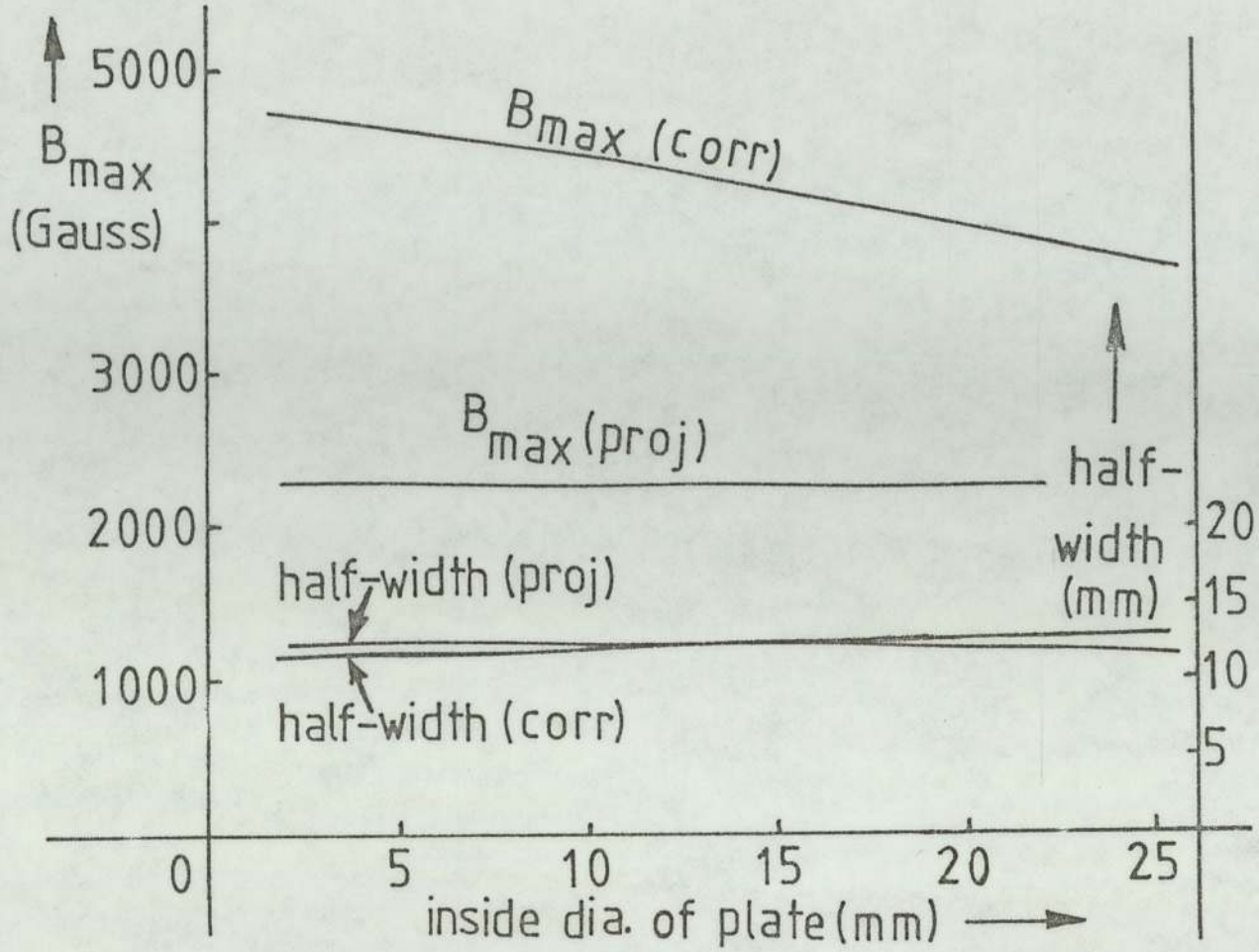

Figure (7.13) Effects of inside diameter of iron screening plate on B_{max} and half-width a of projector and corrector lenses.

$NI/V_r^{\frac{1}{2}}$ = 13 and the standard corrector excitation parameter $NI/V_r^{\frac{1}{2}}$ = 24.4. These experiments showed that given the requirement that the plate should not be placed too near the projection lens, its axial position and inside diameter did not critically affect the field cancellation, which amounted to some 20% in all positions.

The projection semi-angle α_p and the corresponding

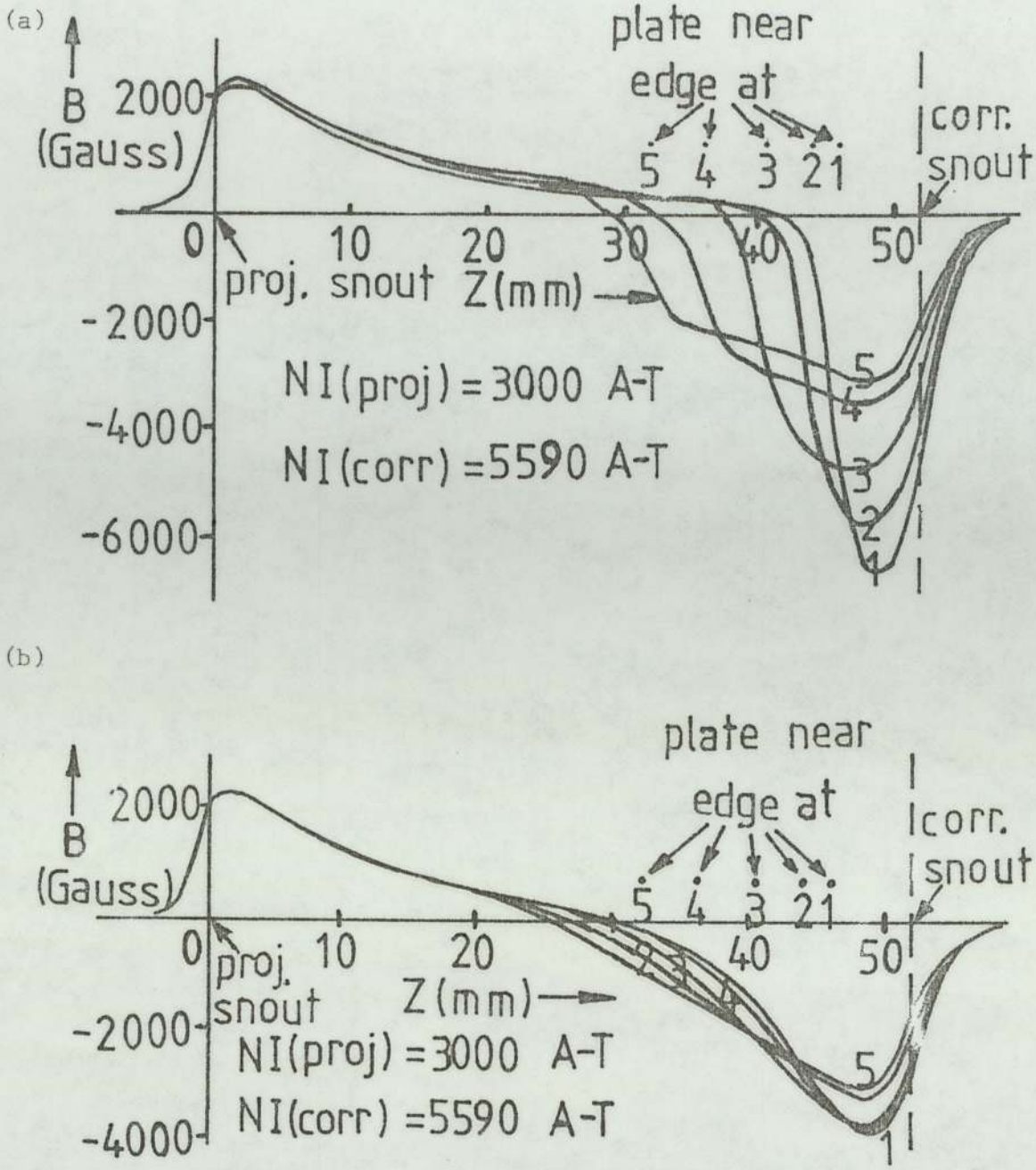

1. near edge of face plate at 6 mm. from corrector snout.
2. near edge of face plate at 8 mm. from corrector snout.
3. near edge of face plate at 11.5 mm. from corrector snout.
4. near edge of face plate at 16 mm. from corrector snout.
5. near edge of face plate at 20 mm. from corrector snout.

Figure (7.14) Effect of position of a screening plate on the combined field distribution (a)plate inside diameter 5 mm. (b) plate inside diameter 25 mm. Note: the screening plate exerts its main influence on the field distribution of the corrector.

magnification of the projector and corrector lenses were calculated (a) with the projector lens operated at $NI/V_r^{\frac{1}{2}} = 13$ and the corrector lens switched off, the results are shown in figure (7.15); (b) with the corrector lens operated at $NI/V_r^{\frac{1}{2}} = 24.4$ and the projector lens switched off, the results are shown in figure (7.16). In both cases the initial ray height was taken as 2 mm. at the corrector snout; the variation of the two parameters α_p $[\alpha_{p(m=o)}$ or $\alpha_{corr}]$ and M (M_2 or M_{corr}) are plotted against $NI/V_r^{\frac{1}{2}}$ for both lenses respectively. Finally, the relationship between α_p and the total magnification M_1 at the final screen for a projector excitation $NI/V_r^{\frac{1}{2}} = 13$ but with variable corrector excitation is shown in figure (7.17). The significance of these curves is that they show that a large variation of corrector lens excitation is possible without influencing the maximum projection semi-angle of 35^o set by the polepiece construction.

Finally, figures (7.18) and (7.19) show the effective quality factors Q_{rad} and Q_{sp} of the projector lens and the corrector lens referred to the final screen. These curves show that at a projector excitation of $NI/V_r^{\frac{1}{2}}$ 13 ($NI/NI_o = 0.76$), corresponding to the point at which full correction occurs, the quality factors are $Q_{rad} = 1.02$ and $Q_{sp} = 0.94$. At minimum projector focal length ($NI/NI_o = 1$) the quality factors are $Q_{rad} = 0.53$ and $Q_{sp} = 1$. The increase in the radial distortion of the projector at the lower excitation is necessary for the compensation of the high barrel distortion produced by the corrector lens, as discussed in the next section.

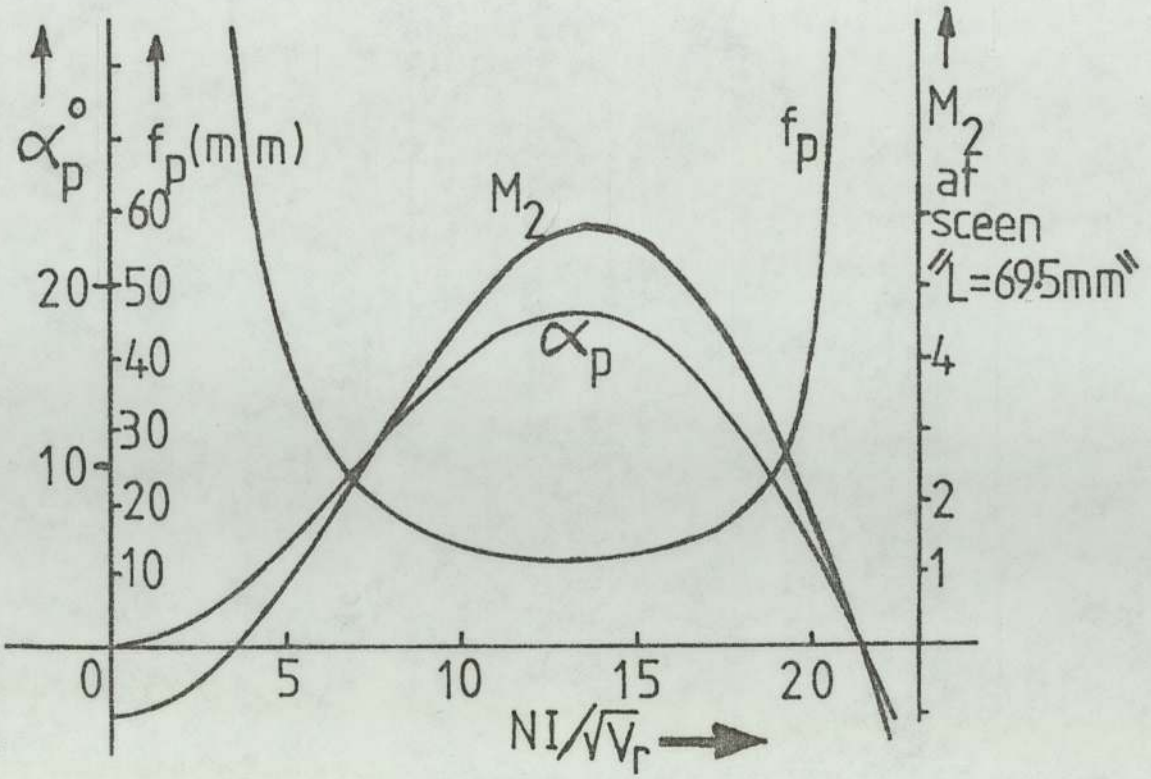

Figure (7.15) The projection semi-angle $\alpha_{p(m=o)}$ and the projector magnification M_2 of the redesigned projector lens against the excitation parameter $NI/V_r^{\frac{1}{2}}$(proj) with the corrector lens switched off.

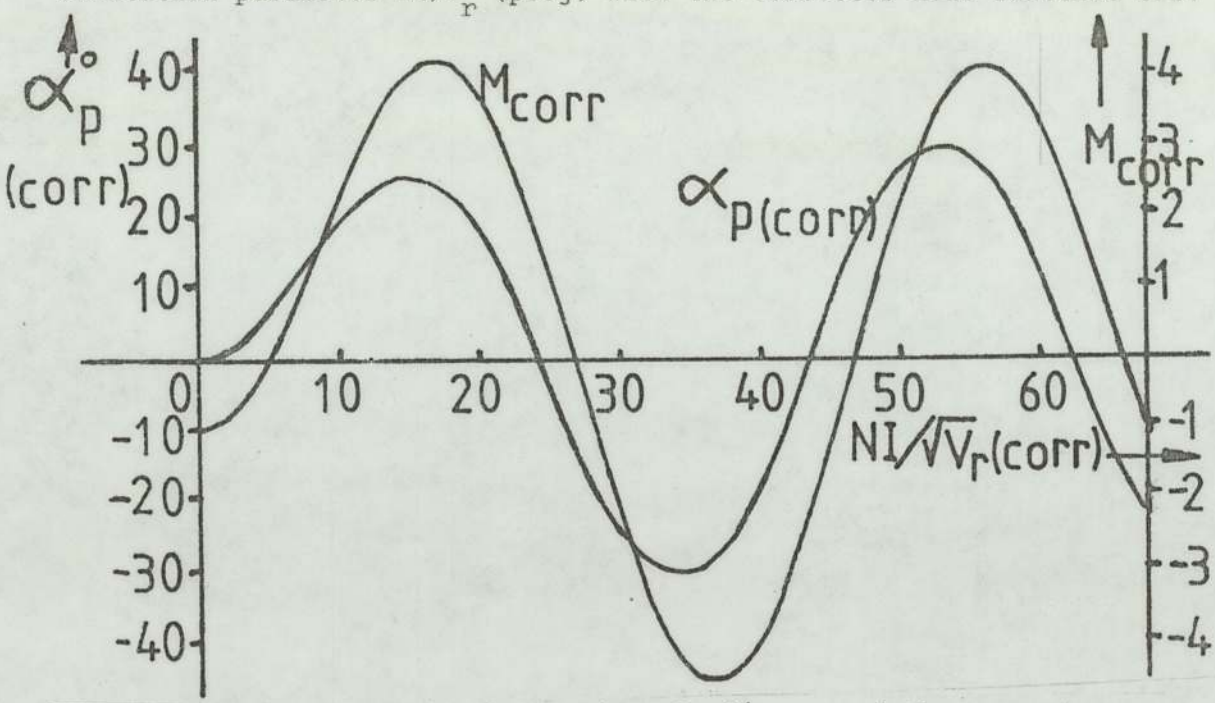

Figure (7.16) The projection semi-angle α_{corr} and the corrector magnification M_{corr} of the corrector lens against the excitation parameter $NI/V_r^{\frac{1}{2}}$(corr) with the projector lens switched off.

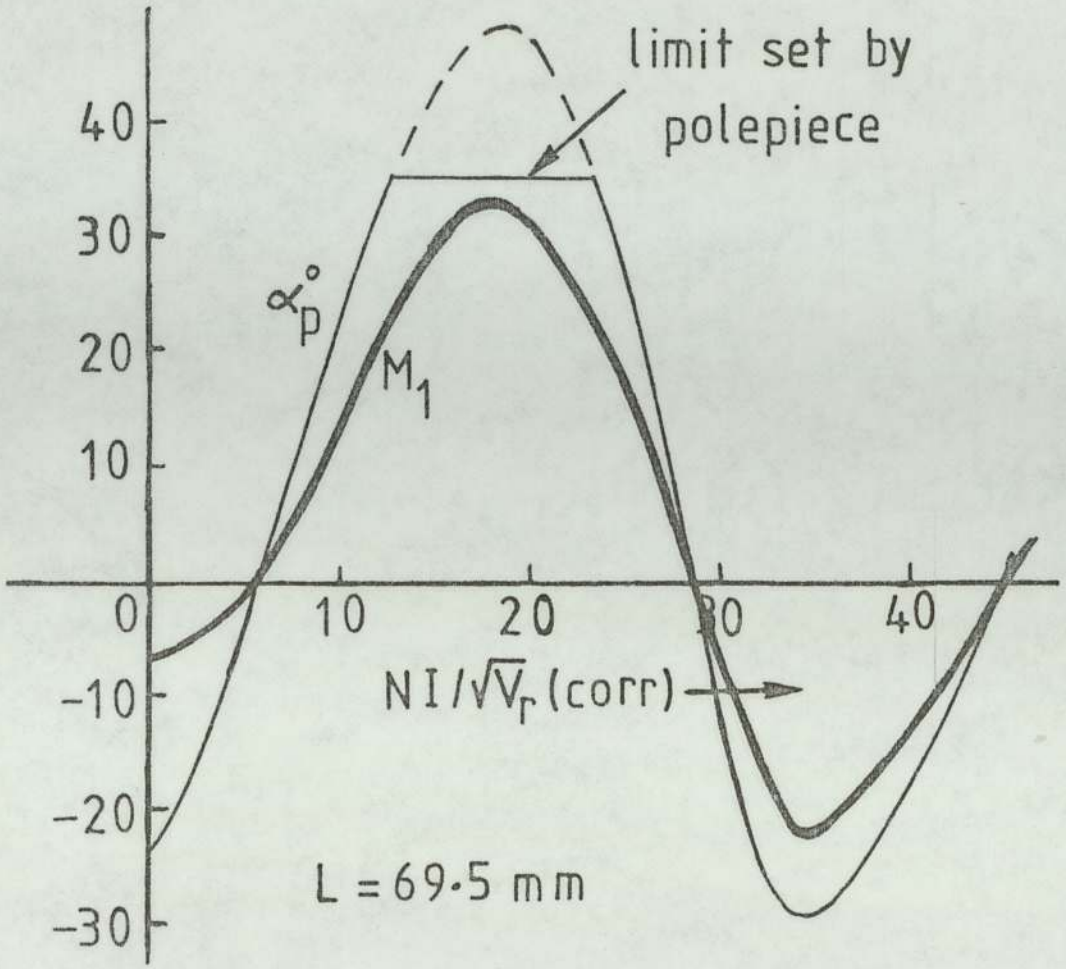

Figure (7.17) The projection semi-angle α_p and the total magnification M_1 of the improved projection system, for constant $NI/V_r^{\frac{1}{2}}(proj) = 13$, as a function of the excitation $NI/V_r^{\frac{1}{2}}(corr)$ of the corrector lens.

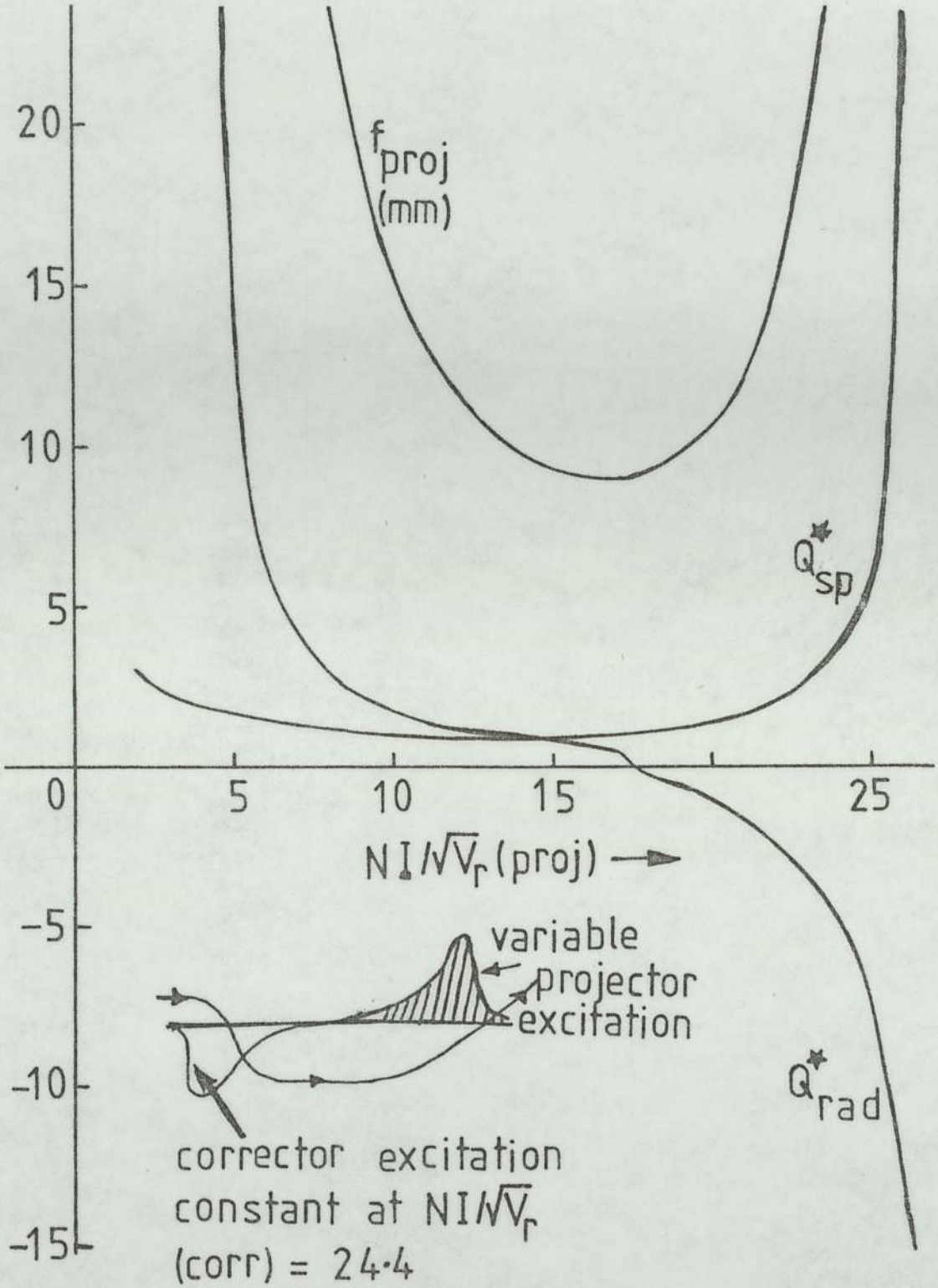

Figure (7.18) The effective quality factors Q_{rad} and Q_{sp}, referred to the final screen, and the focal length f_p of the contribution of the projector lens against $NI/V_r^{\frac{1}{2}}$(proj). The corrector excitation was fixed at $NI/V_r^{\frac{1}{2}}$(corr) = 24.4.

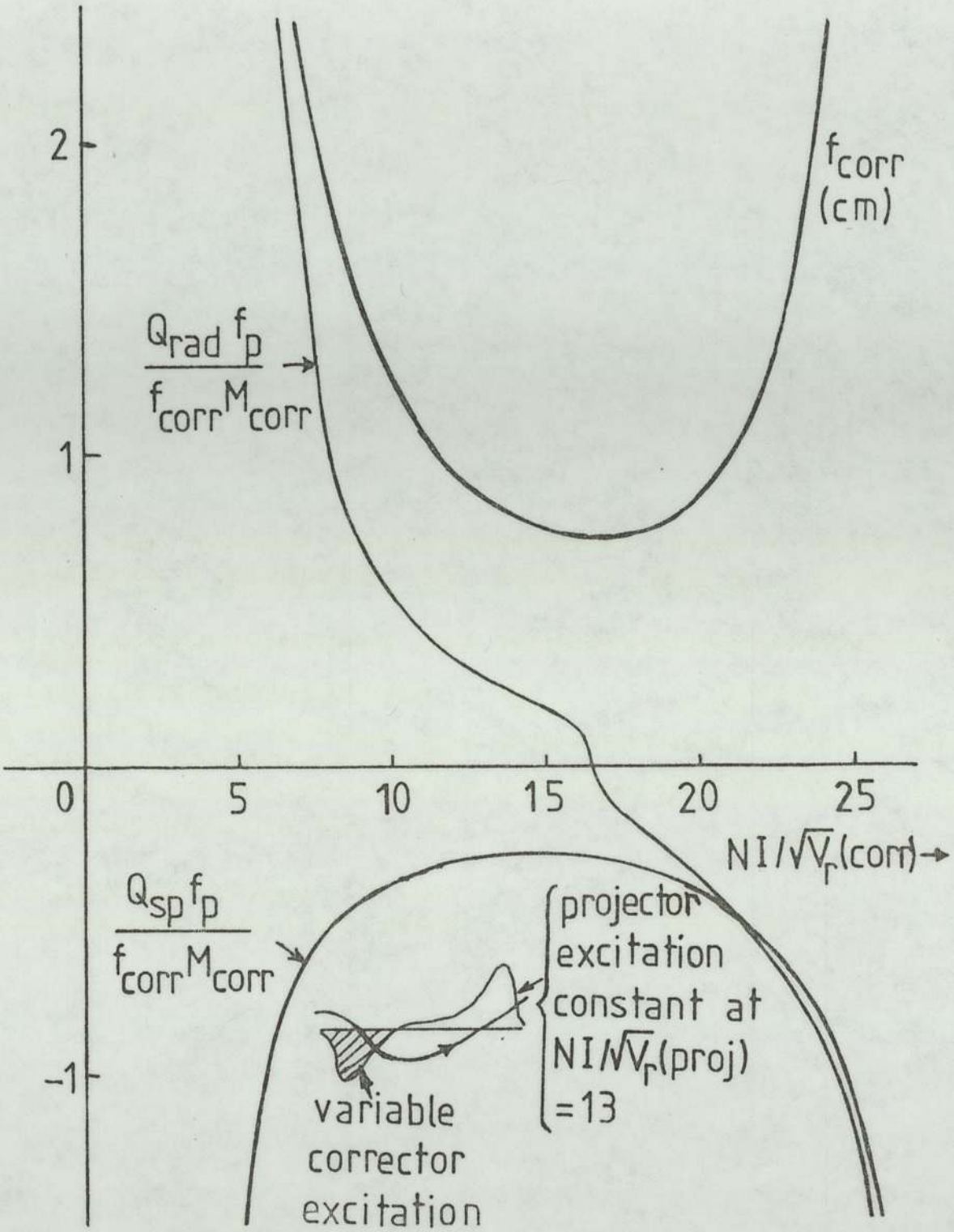

Figure (7.19) The effective quality factors Q_{rad} and Q_{sp}, referred to the final screen, and the focal length f_{corr} of the contribution of the corrector lens against $NI/V_r^{\frac{1}{2}}$(corr). The projector excitation was fixed at $NI/V_r^{\frac{1}{2}}$(proj) = 13.

7.3 ANALYSIS OF RESULTS

The preliminary results discussed in Chapter (6) established the insensitivity of the correcting system to poleface separation and the position of the iron face plate. In the final design the polepiece separation was set at 52 mm. as the best practical compromise. This final arrangement is shown in figure (7.20).

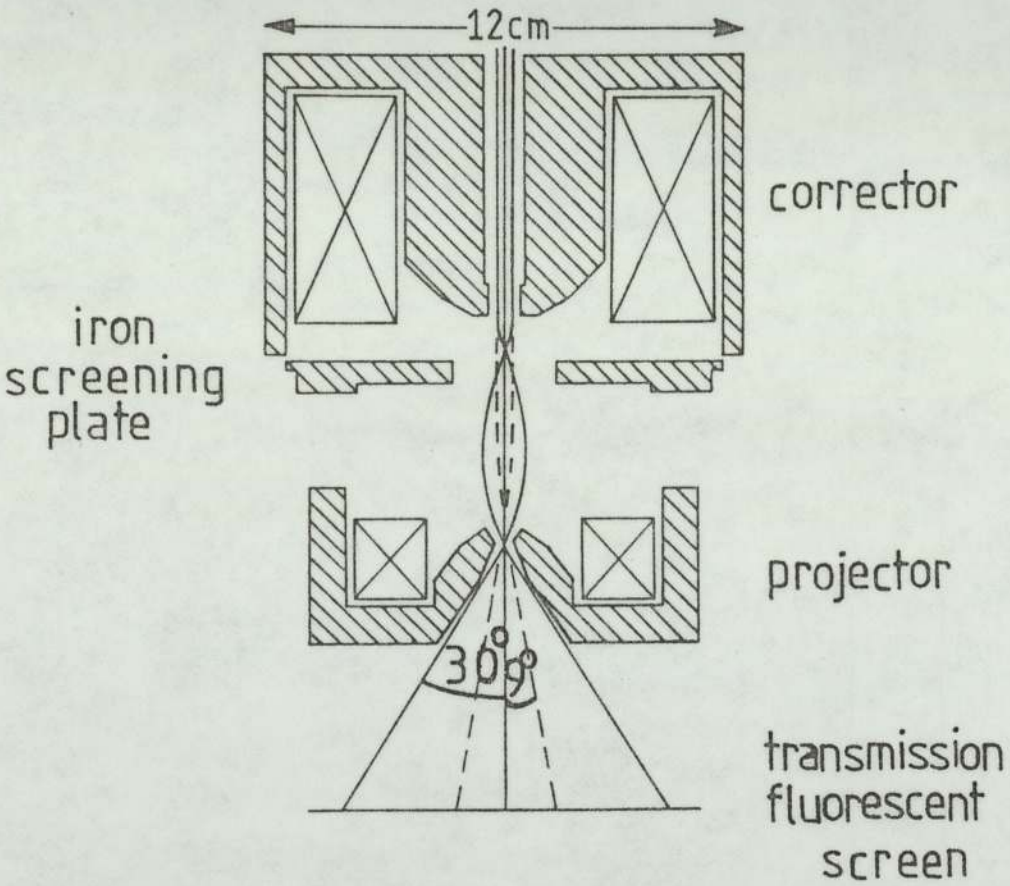

Figure (7.20) Electron ray trajectories (solid lines) through the wide-angle corrector system with projection semi-angle $\alpha_p = 30^\circ$. Electron trajectories (dashed lines) through the system when the corrector lens is not energised.

The figure shows the electron trajectories (solid lines) through the system with both lenses switched on ($\alpha_p = 30^\circ$), and with the corrector lens switched off ($\alpha_p = 9^\circ$, dashed lines). It should be noted that the maximum projection semi-angle of the system with the corrector lens switched off is some 25°, limited by the size of the corrector bore, as shown in figure (7.21). The achievement of a projection semi-angle of 30° is an important step towards shortening the projection distance and of observing large fields of view. For an image to fill a 14 cm. diameter screen at a projection semi-angle of 30° we require a projection distance of only 12.1 cm., i.e. four times shorter than that of a standard 100 KV electron microscope. Furthermore, an increase in α_p from 8° to 30° increases the image diameter by a factor 4.12 which in turn increases the field of view by 17 times. The inner circle marked on the image of figure (7.21) corresponds to $\alpha_p = 8^\circ$. The spiral distortion in this case is 1.2% compared with the 2% expected in a double-polepiece projector lens. This amount of spiral distortion is undetectable by eye.

The full image in figure (7.21) shows the nature of the distortion in an uncorrected wide-angle ($\alpha_p = 25^\circ$) projector lens operated at an excitation($NI/V_r^{\frac{1}{2}} = 13$) just below the point of maximum magnification ($NI/V_r^{\frac{1}{2}} = 15.5$). At the edge of the image pin-cusion distortion of about 23% is visible, accompanied by spiral distortion of about 19%. It should perhaps be mentioned that in this design variation of the projector lens excitation has very little effect on the spiral distortion [see, for example, figure (7.18)] but a big effect on radial distortion. This is an important feature of the present design since once the

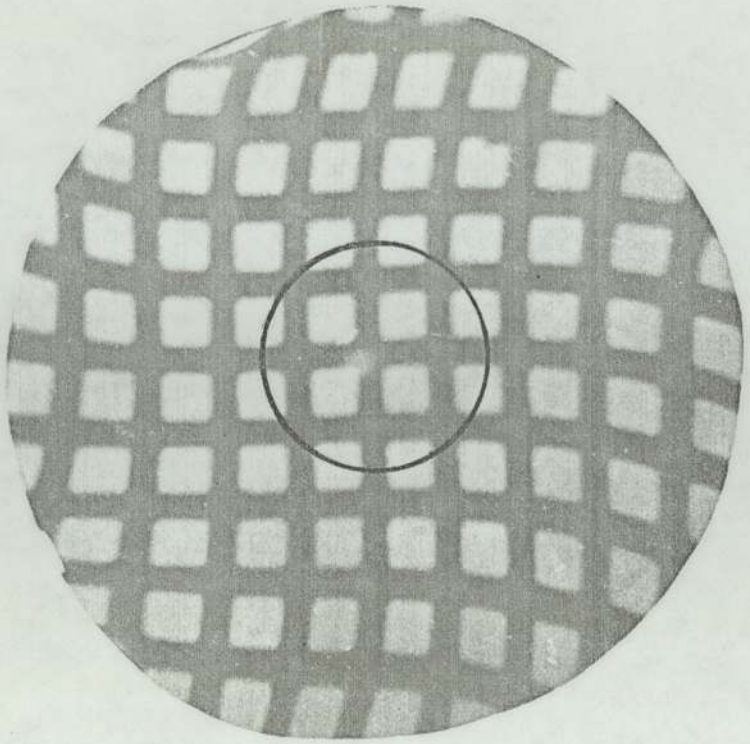

Figure (7.21) An uncorrected projection image of a 150 mesh grid taken with the redesigned projector lens ($NI/V_r^{\frac{1}{2}} = 13$) at a projection semi-angle of 25° (outer circle). The inner circle ($\alpha_p = 8^{\circ}$) corresponds to that of a double-polepiece conventional.

spiral distortion has been corrected by an appropriate setting of the corrector excitation the residual radial distortion can be corrected by a final adjustment of the projector excitation.

This situation is illustrated in figure (7.22a) which shows a corrected image ($\alpha_p = 30^{\circ}$). Figures (7.22a and b) compares the relative sizes of distortion-free images of (a) the present system (b) conventional double-polepiece and single-polepiece projector lenses respectively. A series of micrograph images produced by the present projection system were produced for varying corrector excitation parameter $NI/V_r^{\frac{1}{2}}$ 13. Measurements on the effective radial and spiral distortion were carried out from the

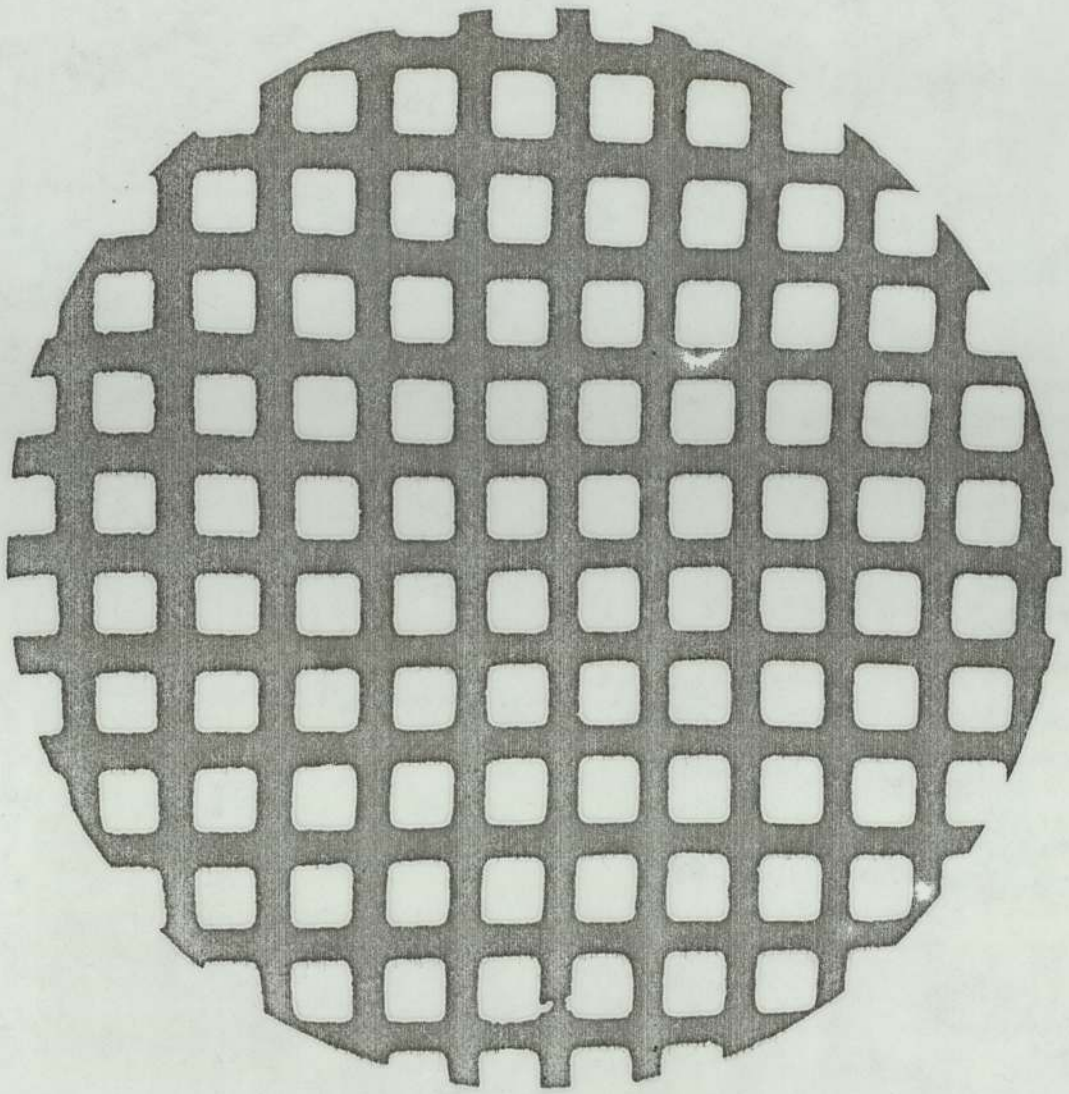

Figure (7.22a) A corrected image of a 400 mesh grid taken with the improved projection system. $NI/V_r^{\frac{1}{2}}$(projector) = 13; $NI/V_r^{\frac{1}{2}}$ (corrector) = 24.4; $\alpha_p = 30^\circ$.

(i)  (ii) 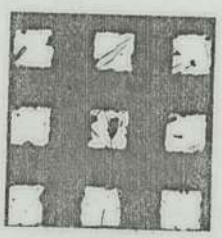

Figure (7.22b) Size of image, relative to that of figure (7.22a), taken with (i) a conventional double-polepiece lens, $\alpha_p = 8^\circ$ (ii) a single-polepiece lens, $\alpha_p = 12^\circ$.

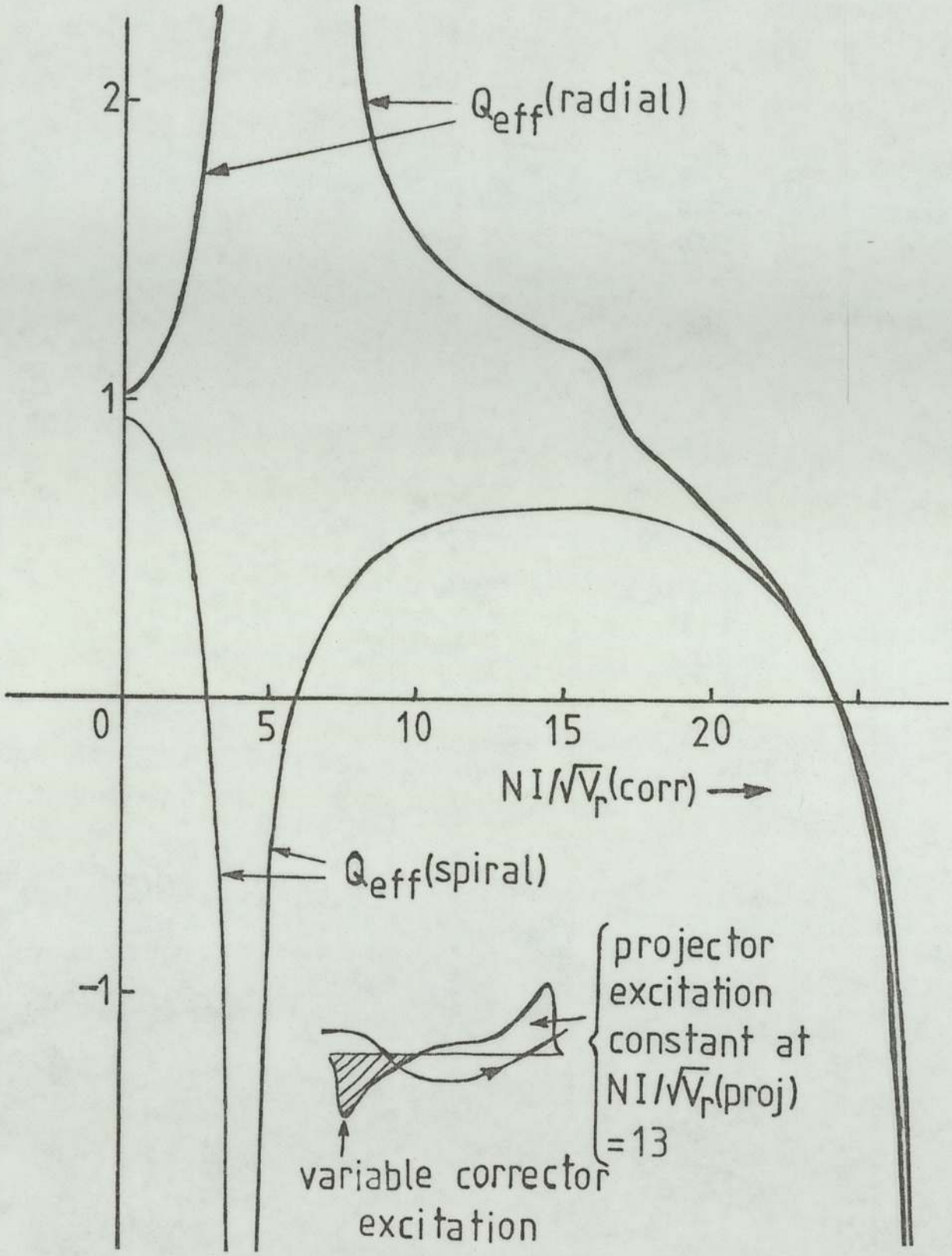

Figure (7.23) The effective quality factors and distortion of the projection system, referred to the final viewing screen, against the corrector excitation.

micrographs and their quality factors and percentage values $\Delta\varrho/\varrho$ are shown in figure (7.23). The correction of distortion occurred at a corrector excitation $NI/V_r^{\frac{1}{2}} = 24.4$. Here an introduction of 1% radial distortion is possible at a current setting accuracy of up to $\pm$ 3.3%, as shown in figure (7.23). Similarly, the acceptable limit of 2% spiral distortion can be reached if the corrector current setting is changed by $\pm$ 4.9%. These values, however, are of the same order of magnitude as when a projector lens is operated at the excitation of no radial distortion.

CHAPTER 8

CONCLUSIONS AND FUTURE DEVELOPMENTS

The present investigation has shown that the single-polepiece lens has marked advantages over a conventional twin-polepiece lens for use in the projection system of an electron microscope. Because of the asymmetrical nature of the magnetic field distribution one has the possibility of producing higher or lower image distortion than would be possible in a conventional lens merely by reversing the direction of the field distribution with respect to the incoming beam. This means, in practice, that the final projector lens will produce only about half as much distortion as that from a conventional lens, for a given semi-angle of projection.

On the other hand, when used as a corrector lens, a single-polepiece lens will produce a distortion higher than that from a conventional lens by a factor of about one-half, thereby permitting the corrector lens to work at a higher magnification than would otherwise be possible.

With the lens arrangement finally evolved in the course of the present investigation, it proved possible to achieve acceptable correction of the distortion up to a projection semi-angle of 30°. This compares very favourably with the typical semi-angle of 8° found in present day commercial instruments. There are good reasons to believe that this represents an upper limit for this type of design. Attempts to increase this semi-angle even to 35° revealed the sudden onset of higher order aberrations that cannot be compensated at present.

At a projection semi-angle of 30° the projection length to the photographic plate of 10 cm. diameter is only 8.66 cm. This means that a camera with a full-size photographic plate can be placed between the projector and the viewing screen. The size of the viewing screen is then a matter of convenience. Assuming that the least resolved distance of the phosphor is three times greater than that of the photographic plate, the corresponding projection distance would be some 26 cm. for the viewing screen whose diameter could be as large as 30 cm. if required. This would be quite straightforward to arrange in an instrument provided with a transmission fluorescent screen, but would call for careful design of the viewing chamber in a standard instrument.

It should be noted that in a wide-angle projection system, it is not possible to change the magnification. In the present design the magnification at the photographic plate (for L = 8.66 cm.) would be about 20X. This is sufficiently small to allow all the necessary change in magnification to be accomplished by the previous lenses. Since the trajectories in the wide-angle projection system are invariant, even with changes of accelerating voltage, the small bore of the final projector lens [see figure (7.1)] acts as a differential pumping aperture so that a good vacuum can be maintained in the upper column in spite of the more modest vacuum that may exist in the viewing chamber due to possible outgassing of photographic plates.

It should perhaps be mentioned here that the present correcting system only makes modest demands on electrical stability. At the point of zero distortion for the system, a change of 3% in the excitation of the corrector lens will introduce 1% of radial

distortion into the image, the increase in spiral distortion is approximately of the same order. Corresponding changes in the projector lens excitation will be less serious. Hence the stability of the lens currents for maintaining negligible distortion (3 parts in 100) is less serious than the short term stability required for maintaining constant magnification (1 part in 2000). However, it is of course desirable that the power supplies are reproducible at the 3% level on a day to day basis to avoid the need for frequent readjustment of the corrector system.

On the basis of the experimental system investigated, it is possible to put forward a design for an integrated design structure as shown in figure (8.1). Coil parameters and dimensions of the iron circuit were carried out according to the methods described in Appendix (4). Figure (8.1) also shows the computed electron trajectories through the complete system. The effective magnification is approximately 60X at a projection distance L = 20 cm. on a screen of diameter 23 cm. ($\alpha_p = 30^\circ$).

This projection system coupled with a suitable miniature objective lens of magnification 20X and axial depths of 12 cm. would give a total magnification of 1200X on the final viewing screen. Two additional intermediate projection lenses, each of 10cm. axial depth and 20X magnification, may be added to provide a wide range of distortion-free magnification and diffraction camera lengths. The overall magnification would amount to 480 000X. Adding two miniature condenser lenses of axial depth 10 cm. each and a specimen stage 10-15 cm. high, would bring the column length

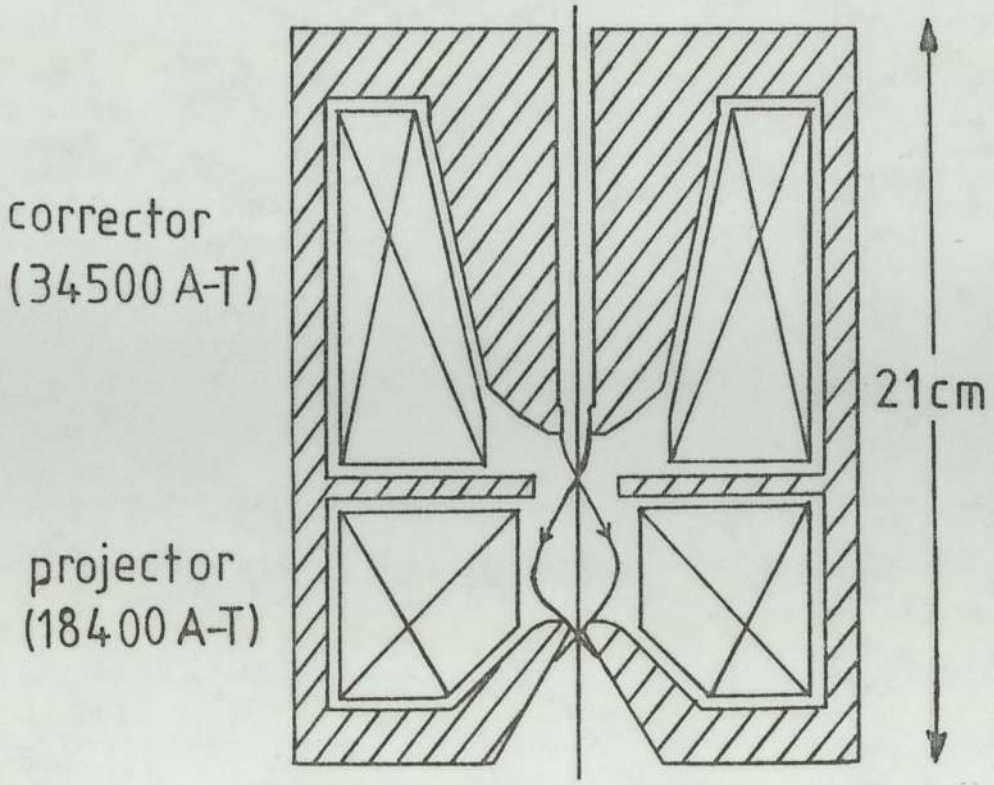

Figure (8.1) Integrated wide-angle projection system for a high voltage electron microscope. NI(proj) = 18400 A-T; NI(corr) = 34500 A-T.

up to about 1 metre from the top of the first condenser lens to the viewing screen; this is comparable to the 106 cm. of the Philips EM 200 100 KV TEM. It would therefore seem that future high voltage microscopes could have a column size comparable with those of present day 100 KV instruments.

REFERENCES

Alshwaikh, A. (1979). Ph.D. thesis. The University of Aston in Birmingham.

Alshwaikh, A. and Mulvey, T. (1977). The magnetised iron sphere, a realistic model for single-polepiece lenses. Developments in electron microscopy and analysis. ed. D.L. Misell. Inst. Phys. Conf. Ser. No. 36 (EMAG 77). pp. 25-8.

Cooke, C.J. and Duncumb, P. (1968). Performance analysis of a combined electron microscope and electron probe microanalyser "EMMA". Proc. 5th Int. Conf. x-ray optics and microanalysis. ed. G. Möllenstedt and K.H. Gaukler. Springer-Verlag. pp. 245-7.

Crewe, A.V. (1976). Design trends in the STEM. Proc 6th Euro. Congr. on electron microscopy. ed. D. G. Brandon. Tal international publishing company. pp. 65-6.

Durandeau, P. and Fert, C. (1957). Lentilles électroniques magnétiques. Rev. Opt. 36, pp. 205-34.

Elkamali, H.H. and Mulvey, T. (1977). Improved viewing arrangements in the TEM. Developments in electron microscopy and analysis. ed. D.L. Misell. Inst. Phys. Conf. Ser. No. 36 (EMAG 77). pp. 33-4.

Elkamali, H.H. and Mulvey, T. (1980). A double lens system for the correction of spiral distortion. Electron microscopy and analysis. ed. T. Mulvey. Inst. Phys. Conf. Ser. No. 52 (EMAG 79). pp. 63-4.

Elkamali, H.H. and Mulvey, T. (1980). A wide-angle TEM projection system. Proc. 7th Euro. Congr. on electron microscopy. ed. P. Brederoo and G. Boom. 7th Euro. Cong. on electron microscopy foundation, Leiden. 1, pp. 74-5.

Fert, C. and Durandeau, P. (1967). Chapter 2.3. Magnetic electron lenses. Focusing of charged particles. ed. A. Septier. Academic Press. 1, pp. 309-52.

Hillier, J. (1946). A study of distortion in electron microscope projection lens. J. Appl. Phys. 17, pp. 411-9.

Juma, S.M. (1975). Ph.D. thesis. The University of Aston in Birmingham.

Juma, S.M. and Mulvey, T. (1974). New rotation-free magnetic electron lenses. Electron microscopy. ed. J.V. Sanders and D.J. Goodchild. Canberra: Australian Academy of Sciences. 1, pp.134-5.

Juma, S.M. and Mulvey, T. (1975). A new experimental electron microscope with a rotation-free projector system. Developments in electron microscopy and analysis. ed. J.A. Venables. EMAG 75. New York: Academic press. pp. 45-8.

Juma, S.M. and Mulvey, T. (1978). Miniature rotation-free magnetic electron lenses for the electron microscope. J. Phys. E: Sci Instrum. 1, pp. 759-64.

Juma, S.M. and Mulvey, T. (1980). The axial field distribution of single-polepiece lenses. Electron microscopy and analysis. ed. T. Mulvey. Inst. Phys. Conf. Ser. No. 52 (EMAG 79). pp. 59-60.

Klemperer, O. and Barnett, M.E. (1971) . Electron optics. Third edition. Cambridge University Press.

Lambrakis, E., Marai, F.Z. and Mulvey, T. Correction of spiral disortion in the transmission electron microscope. Developments in electron microscopy and analysis. ed. D.L. Misell. Inst. Phys. Conf. Ser. No. 36 (EMAG 77). pp. 35-8.

Le Poole, J.B. (1964). A miniature magnetic electron lens. Proc. 3rd. Euro. Conf. on electron microscopy. ed. M. Titlbach. Prague. Czech. Acad. Sci. Supplementary pages.

Liebmann, G. (1951). Magnetic electron microscope projector lenses. Proc. Phys. Soc., B65, pp. 94-108.

Marai, F.Z.A. (1977). Ph.D. thesis. The University of Aston in Birmingham.

Marai, F.Z.A. and Mulvey, T. (1977). Scherzer's formula and the correction of spiral distortion in the electron microscope. Ultramicroscopy. 2, pp. 187-92.

Mulvey, T. (1953). The magnetic circuit in electron microscope lenses. Proc. Phys. Soc. B66, pp. 441-7.

Mulvey, T. (1976). Design trends in TEM, STEM and SEM electron microscopy. Proc. 6th Euro. Congr. on electron microscopy. ed. D.G. Brandon. Tal international publishing company. 1, pp. 59-64.

Mulvey, T. (1980). Electron guns and instrumentation. Proc. 7th Euro. Congr. on electron microscopy. ed. P. Brederoo and G. Boom. 7th Euro. Cong. on electron microscopy foundation, Leiden. 1, pp. 46-53.

Mulvey, T. and Newman, C.D. (1972). Versatile miniature electron lenses. Proc. 5th Euro. Cong. on electron microscopy. Manchester 1972. Inst. Phys. pp. 116-7.

Munro, E. (1975). Report CUED/B - Elect./TR. 45. The University of Cambridge.

Nasr, H. (1978). M.Sc. thesis. The University of Aston in Birmingham.

Newman, C.D. (1976) Ph.D. thesis. The University of Aston in Birmingham.

Ozasa, S., Sakitani, Y., Katagini, S., Kimura, H., Sugata, E., Fukai, K., Fujita, E., Fujita, H. and Ura, K. (1970). Development of 3 MeV electron microscope column. Microscopie electronique. ed. P. Favard. Societe Francaise de microscopie electronique. 1, pp. 123-4.

Parker, N.W. Utlaut, M. and Crewe, A.V. (1976). Evaporative cooling of high current density mini-lenses. Proc. 34th Annual EMSA Meeting. pp. 536-7.

Scherzer, O. (1936). Uber einiger Fehler von Elektronenlinsen. Z. Physik. 101, pp. 593-603.

APPENDIX 1

IMPROVED VIEWING ARRANGEMENTS IN THE TEM

(A paper published by the Institute of Physics for EMAG 77, Glasgow 1977).

IMPROVED VIEWING ARRANGEMENTS IN THE TEM

H H Elkamali and T Mulvey

Department of Physics, The University of Aston in Birmingham
Birmingham B4 7ET (UK)

1. Introduction

An experimental system has been described for the correction of spiral distortion in electron lenses (Lambrakis et al 1977). The present investigation was concerned with the performance of such a system in a TEM. Correction systems should only be applied to the best available lenses and so care was taken to find the best lens. This investigation could be relevant to a wide range of TEMs, especially those operating at high accelerating voltages, since it is in this area that the excessive volume and size of the viewing chamber causes difficulties in viewing the screen and in optimising the x-ray protection. The viewing chamber and projection system of an EM6 electron microscope were drastically modified as shown in Figure 1. First, the height of the viewing chamber was reduced from 23.5 to 14.9cm. The final projector lens was removed and replaced by a single-polepiece mini-projector lens of 10mm focal length capable of operating up to an accelerating voltage of one million. The intermediate lens was replaced by a wide bore (15mm) single-polepiece intermediate lens to act as a corrector lens for spiral distortion. The separation of these lenses could be altered by means of fixed spacers. These changes led to a reduction of the projection distance L (from focal point of the projector to the photographic plate) from 36cm to 24.5cm. The large semi-angle (22^{o}) of the conical back bore permits an unusually large image to be projected through the lens. This is more than sufficient to fill the maximum diameter of the viewing chamber (15cm); an extended fluorescent screen was therefore fitted for visual observation of image distortion. Calculations showed that an image of standard radius (5cm) on the photographic plate would be free from radial distortion but would suffer from just less than 3% of spiral distortion, i.e. an amount quite difficult to detect in normal images. On the other hand, a wide-angle image on the fluorescent screen should show about 6.8% spiral distortion at the edge of a 15cm diameter screen. It was felt that this would offer a ready means for checking the action of the correcting lens.

2. Results

The excellent performance of the single-polepiece projector can be seen from the micrograph in Figure 2, taken at a projection distance of 24.5cm. Spiral distortion, although present, is not easy to detect, as it is just below the 3% level. In order to reduce this below 2% the projection distance would have to be extended to 29cm in excellent agreement with the calculated results for this lens. It should perhaps be pointed out that for a lens of 10mm focal length an object of diameter 8mm is needed to fill the exit cone. Since the focal point is close to the apex of this cone at high magnification, the small lens bore (2mm) does not restrict the field of view, but acts as a differential pumping system separating the vacuum in the viewing chamber from that of the more critical part of the electron-

optical column.

3. Correction of spiral distortion

The correcting lens was a general purpose lens, readily available and not specially designed for correcting spiral distortion. In particular its maximum excitation parameter $NI/V_r^{\frac{1}{2}}$ lies in the region of 16, so that it can operate only in the first focal zone. Preliminary experiments have indicated that although partial correction of spiral distortion can be obtained with such a lens, it is highly desirable to operate the correcting lens in the second focal zone ($NI/V_r^{\frac{1}{2}} \approx 30$) corresponding to an excitation of 10,000 A-t at 100kV. Further experiments with such a lens are needed before a full assessment of the method can be made. Nevertheless, the investigation has already shown that, even without a corrector, appreciable improvements are possible in the design of the projection system of the TEM.

Fig.1. Experimental compact viewing system for the electron microscope with 1000 KV mini-projector (98mm dia.) and single-polepiece corrector lens mounted above.

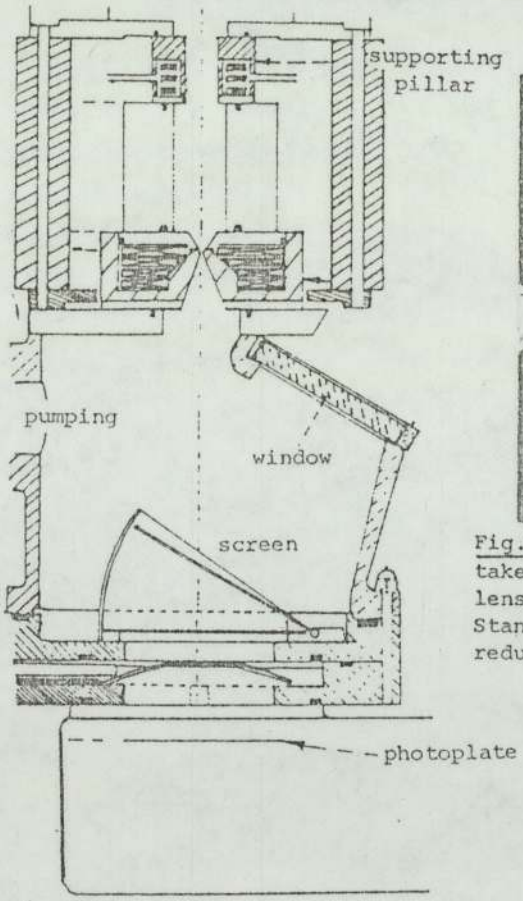

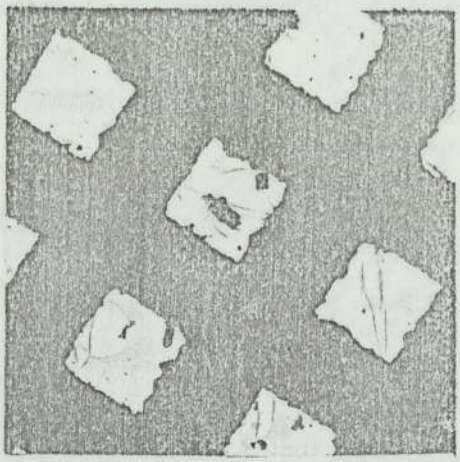

Fig.2.(above).Electron micrograph taken with a single-pole projector lens in the low-distortion mode. Standard image size (ρ=5cm) but reduced projection distance(L=24.5cm)

4. References

Lambrakis E, Marai F Z and Mulvey T 1977 These proceedings.

APPENDIX 2

A DOUBLE LENS SYSTEM FOR THE CORRECTION OF SPIRAL DISTORTION

(A paper published by the Institute of Physics for EMAG 79, Brighton 1979).

A DOUBLE LENS SYSTEM FOR THE CORRECTION OF SPIRAL DISTORTION

H H Elkamali and T Mulvey

Department of Physics, The University of Aston in Birmingham, Birmingham B4 7ET (UK)

1. Introduction

The distortion $\Delta\rho/\rho$ in the final image of an electron microscope, limited essentially by spiral distortion, is equal to $Q^2\alpha_p^2$ (Lambrakis et al. 1977) where Q^2 is the product of the square of the projector focal length f_p and of the spiral distortion coefficient D_{sp}, and α_p is the semi-angle subtended by the image at the focal point of the projector lens. For conventional lenses $Q^2 = 1$ (Marai and Mulvey 1977) so that α_p must be restricted to a value of some 8^o for a tolerable amount (2%) of image distortion. For a single-polepiece projector lens the semi-angle can be usefully increased to 10^o. Further increase, to $\alpha_p = 22^o$, can be obtained by using a single-pole-piece corrector lens having a large spiral distortion in the opposite sense to that of the projector (Lambrakis et al. 1977). In this method the corrector lens is operated at its minimum focal length in order to minimise radial distortion. This necessitated operation in the second focal zone at high excitation, $NI/V_r^{\frac{1}{2}} = 34$ compared with $NI/V_r^{\frac{1}{2}} = 16$ in the projector. Here NI is the lens excitation and V_r is the relativistically corrected accelerating voltage. In order to investigate the possibility of more favourable operating conditions the modified 100kV EM6 electron microscope previously described (El Kamali and Mulvey 1977) was further modified as shown in Figure 1. A transmission fluorescent screen was fitted just below the projector lens capable of registering an image of semi-angle $\alpha_p = 25^o$, corresponding to 12% of spiral distortion for the uncorrected projector lens. This image could be photographed by an external camera, through a glass port in the base of the normal EM6 plate camera.

2. The corrector system

The polepieces of the corrector and the projector, magnetised with opposite polarity face each other (Fig.1). This arrangement leads to the desired high spiral distortion in the corrector and low spiral distortion in the projector. The corrector lens contributes a magnification factor $M_1 = 3$ to the total image magnification. The choice of M_1 is important; if M_1 is too small, the finite conjugates of the projector lens lead to an undue increase in its aberrations. If M_1 is too large the distortion produced by the corrector will be insufficient since its aberrations, when referred to the final image, are reduced by a factor of M_1^2. Typical electron trajectories are shown in Figure 2. The corrector is operating at an excitation $NI/V_r^{\frac{1}{2}} = 24$ in the first focal zone. The shape of the projector polepiece is important if the outer rays are not to be obstructed. The corrector lens produces a considerable amount of barrel distortion. Its effect on the final image will, however, be reduced by the factor M_1^2. Taking an extreme case, a barrel distortion of 45% in the corrector will appear as 5% in the final image. This is readily compensated by a slight reduction of the excitation of the projector. The settings of the corrector and projector lenses to achieve this are not critical.

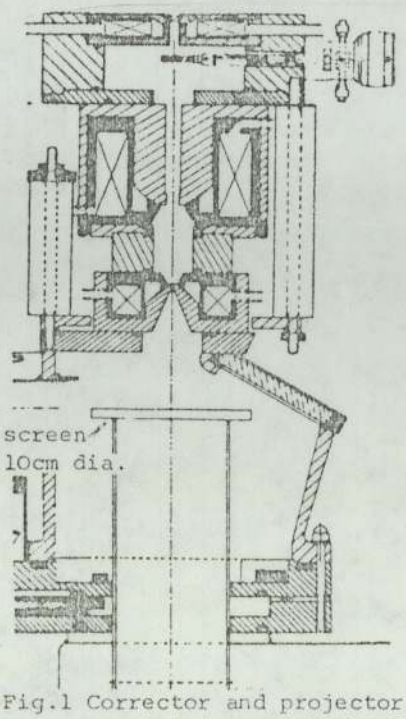

Fig.1 Corrector and projector mounted in modified EM6 electron microscope

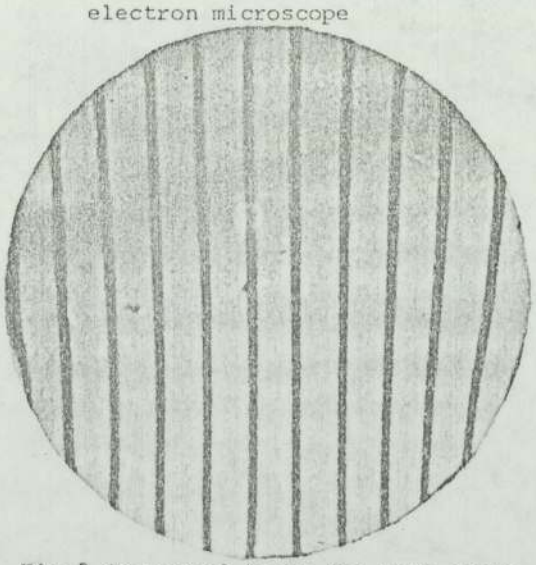

Fig.3 Corrected image for semi-angle $\alpha_p = 22^o$, equivalent to screen of 40cm diameter at 50cm projection distance.

3. Results

Figure 3 shows a corrected image for a semi-angle $\alpha_p = 22^o$. The specimen is a grid of parallel bars imaged under the conditions of Figure 2. Distortion with the corrector off was 10%. It should perhaps be mentioned that this image corresponds to a standard image (2p = 100mm) taken at a projection distance of 125mm. The design of the corrector system described here is suitable for high voltage electron microscopes, but it could also find application in instruments employing transmission viewing screens.

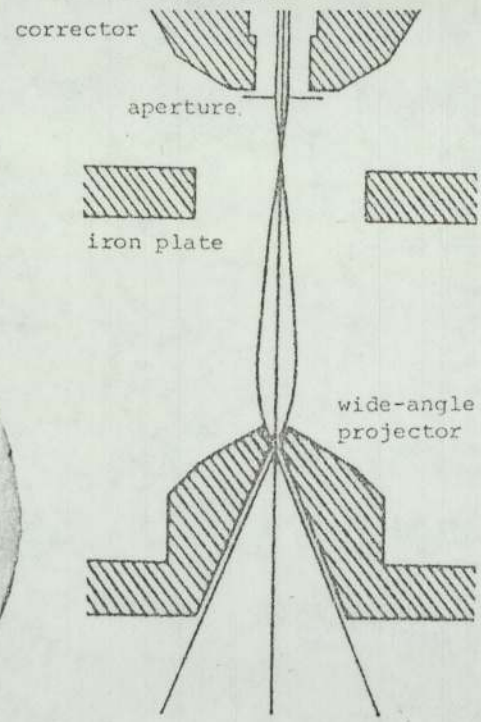

Fig.2 Electron trajectories in corrector lens and wide-angle projector. Polepiece separation 50mm.

4. References

El Kamali H H and Mulvey T 1977 Inst.Phys.Conf.Ser. No.36 33-34.
Lambrakis E, Marai F Z and Mulvey T Ibid. 35-38.
Marai F Z and Mulvey T 1977 Ultramicroscopy 2 187-192

APPENDIX 3

A WIDE-ANGLE TEM PROJECTION SYSTEM

(A paper published by the 7th EUREM 80 on Electron Microscopy. The Hague. The Netherlands 1980).

A WIDE-ANGLE TEM PROJECTION SYSTEM

H.H.Elkamali and T.Mulvey

Department of Physics, The University of Aston in Birmingham B4 7ET (UK)

It is important that an electron microscope image should be free from noticeable distortion. In general, one can tolerate about 1% of radial distortion and 2% of spiral distortion. The aberration of distortion is produced mainly by the final projector lens. Fortunately, in the region of maximum magnification, radial distortion can be made negligible by the correct choice of lens excitation so that only spiral distortion need to be considered[1]. The distortion $\Delta\rho/\rho$ in the image is equal to $Q^2\tan^2\alpha_p$ where α_p is the semi-angle of projection of the outermost image ray and Q is a dimensionless image quality factor equal to unity for conventional symmetrical magnetic lenses and 0.75 for the best single-polepiece lenses[2]. In commercial electron microscopes, image distortion is kept within acceptable limits by restricting the projection semi-angle to about 8^o. This places severe restrictions on the design of the viewing and recording system. In a previous paper[3] a twin single-polepiece correcting system was described which enabled the semi-angle α_p to be increased from 8^o to 22^o. The present paper describes a further improved projector lens unit in which this projection angle has been increased to 30^o.

Figure 1 shows the calculated electron trajectories through the system. The final projector lens is a single pole lens with a shaped polepiece (fig.1) allowing the passage of a cone of rays making an angle of 35^o with the axis whilst still retaining favourable electron optical properties. Its excitation at 100kV is about 5000 A-t. The corrector lens, mounted above the projector lens, is also a single-polepiece lens with its polepiece oriented so as to produce a large amount of spiral distortion. Between the two lenses, whose polepieces are operated with opposite polarities, is an iron plate with an axial hole. Its function is to minimise magnetic field cancellation effects whilst retaining the desired asymmetrical axial field distribution. The corrector lens operates in the first focal zone but at a fairly high excitation, typically $NI/V_r^{\frac{1}{2}} = 24.4$, corresponding to about 8000 A-t at 100kV. This produces a magnified (3x) image with sufficient negative spiral distortion (80%) to cancel the 20% of spiral distortion of the projector lens. This high excitation inevitably produces some barrel distortion in the final image. This is easily removed by operating the final projector at an excitation slightly below that needed for minimum focal length. This in turn reduces the spiral distortion that is to be corrected. Both calculation and experiment indicate that this method is economical in lens excitation and insensitive to the lens separation and the position of the iron screening plate. The combined focal length of the unit is 3.5mm. The distance between the upper surface of the corrector lens and the photographic recording plane for a standard image of 10cm in diameter is only 21cm. The corresponding magnification is 25x. Figure 2a shows a wide angle ($\alpha_p = 30^o$) image obtained in a modified EM6 electron microscope (see Ref.3) and Figure 2b shows a computer-simulated image for a conventional projector lens (Q=1) operated under the same conditions giving a spiral distortion of 33%. The inner circle indicates the maximum tolerable image size for 2% spiral distortion. It should perhaps be pointed out that at the standard projection distance (L = 40cm) the corrected image of Figure 2a would be about 46cm in diameter, an increase of distortion-free area by a factor of seventeen. Alternatively, the screen area may be kept the same and the projection distance L reduced by a factor of four. Either measure could lead to a noticeable improvement in the image viewing system of the microscope.

1. E.Lambrakis, F.Z.Marai and T.Mulvey, Inst. Phys. Conf. Ser.No.36, 35-38, 1977.
2. F.Z.Marai and T.Mulvey, Ultramicroscopy 2, 187-192, 1977.
3. H.H.Elkamali and T.Mulvey, Inst. Phys. Conf. Ser.No.52, 63-64, 1980.

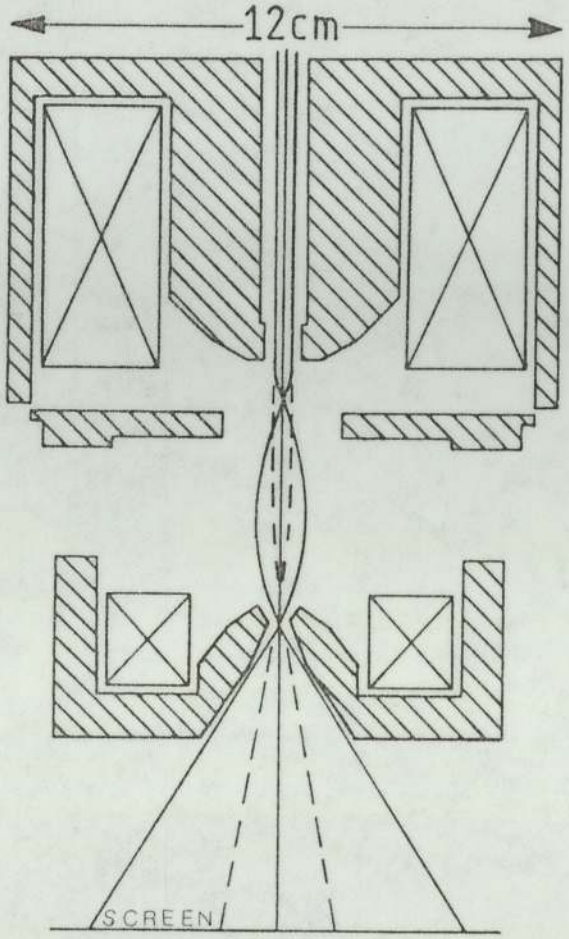

Fig.1: Electron trajectories through the wide-angle projection system. Full line, corrector lens on. Dashed line, corrector lens off.

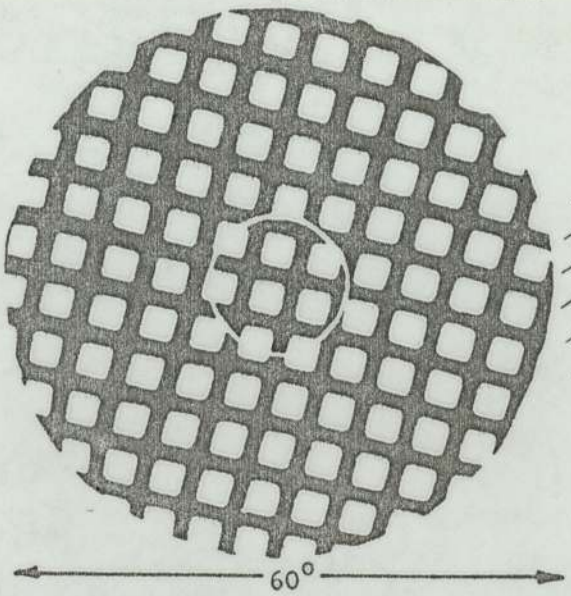

Fig.2a : Wide-angle ($2\alpha_p=60^\circ$) single-polepiece projection image in a modified EM6 electron microscope.

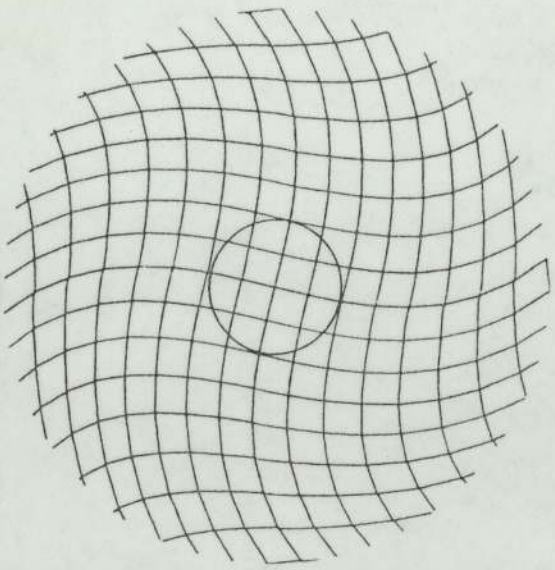

Fig.2b: Computer simulated wide-angle image ($2\alpha_p=60^\circ$) for a conventional projector lens. Distortion at edge of image 33 %. Inner circle indicates standard viewing angle ($2\alpha_p=16^\circ$)

APPENDIX 4

DESIGN OF LENS COILS AND IRON CIRCUITS FOR HIGH EXCITATION

A4.1 POWER REQUIRMENTS

Every lens requires a certain maximum number of ampere-turns (NI); this depends on the range of the excitation parameter $(NI/V_r^{\frac{1}{2}})$.

Figure (A4.1)

Coil of rectangular cross-section

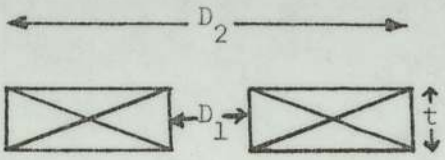

Consider a coil excited by a current I. The cross-sectional area A_c, figure (A4.1) is given by

$$A_c = \frac{t}{2}(D_2 - D_1)$$

where t is the axial depth of the coil and D_1 and D_2 are the inner and outer diameters of the coil respectively. The volume of the coil is given by

$$V_{vol} = \frac{\pi}{2}(D_2 - D_1) A_c$$

$$\text{Input power} = P = \rho_e \sigma^2 V_{vol} \quad \ldots\ldots\ldots\ldots (A4.1)$$

where ρ_e is the resistivity and σ is the current density given by

$$\sigma = I/A_w \quad \ldots\ldots\ldots\ldots\ldots\ldots\ldots\ldots\ldots\ldots (A4.2)$$

where A_w is the cross-sectional area of the wire.

$$\text{But } (NI)_{max} = N \frac{\sigma A_c}{N} \sigma_{max} A_c \quad \ldots\ldots\ldots (A4.3)$$

$$P = \pi \rho_e (NI)^2_{max}/t \quad \ldots\ldots\ldots\ldots\ldots\ldots\ldots (A4.4)$$

It may then be concluded from equation (A4.4) that miniature lenses need high input power due to their small axial depth (t). Such a situation necessitates an efficient method of cooling. It is also apparent from equation (A4.3) that the maximum ampere-turns is independent of the number of turns but directly proportional to the current and the rectangular cross-section of the coil and inversely proportional to the cross-sectional area of the wire A.

The mean diameter D_m and resistance R of the coil are expressed as

$$D_m = (D_2 + D_1)/2 \quad \text{.....(A4.5)}$$

$$R = \rho_e \, l/A_w \quad \text{.....(A4.6)}$$

where l is the length of the wire forming the coil and given by

$$l = \pi D_m N \quad \text{.....(A4.7)}$$

Thus the input power can also be expressed as

$$P = I^2 R \quad \text{.....(A4.8)}$$

$$= \pi \rho_e D_m N I^2 / A_w \quad \text{.....(A4.9)}$$

$$= \pi \rho_e \sigma D_m N I \quad \text{.....(A4.10)}$$

A4.2 APPROPRIATE MATCHING OF COIL TO POWER SUPPLY

If a power supply provides a maximum voltage V_{max} and a maximum current I_{max}, then the coil in question should have a resistance of

$$R_T = V_{max}/I_{max} \quad \text{.....(A4.11)}$$

Ideally this should be the maximum resistance of the coil and not its resistance at room temperature R_o.

But $$R_T = R_o (1 + \alpha T) \quad \text{.....(A4.12)}$$

or alternatively

$$T = \frac{R_T - R_o}{R_o} \times \frac{10^3}{4} \quad \text{.....(A4.13)}$$

where $$T = T_s - T_w \quad \text{.....(A4.14)}$$

and that T_s is the surface temperature of the coil and T_w is the temperature of the water. Equation (A4.13) is based on the fact that when the resistance of a copper wire is increased by 40% the temperature increase ΔT will be $100^{o}C$. Once the value of the resistance is determined we can then calculate all other parameters like area of coil, length and type of wire, etc. All copper wire and tape manufacturers provide characteristic tables displaying diameter, resistance, length per mass, current rating per area of coil, and number of turns per unit area of coil; table (A4.1). However, these tables are made for machine windings whereas most of our designed coils are loosely wound, for cooling purposes. Thus in order to make use of the data available in any of these tables we have to reduce the calculated number of turns by about 30%.

SWG	Diameter (inches)	Resistance (ohms per 1000 yeards)	Turns (enamel) per square inch
16	0.064	7.463	219
18	0.048	13.270	388
20	0.036	23.590	676
22	0.028	38.990	1089
24	0.022	63.160	1731
26	0.018	94.400	2520

TABLE (A4.1) Table of copper wires.

A4.3 COIL WINDING

In practice, coils are wound outside the lens structure. A separate former is needed for this purpose. During the process of winding it is found necessary to clear the wire with soap water so as to get rid all the dirt and dust that might help to develop air pockets in the presence of the coolant, water. The coil leads must be correctly orientated to fit into the lens and the outlet pipe since too much bending of the wire may lift off the wire enamel. Furthermore, the leads must be securely clamped and not rubbing against the case or each other. The coil is then wrapped with a piece of the cotton cloth so that capillary action can take place in the event of the water level being dropped, reduced or switched off. However, enough water will be available since the water inlet is at the bottom and outlet at the top of the lens.

Sometimes we get pinholes in the insulation of the wire which permit a leakage current, short circuit,to be drawn from one pinhole to another either directly through the water or indirectly via the iron case. To avoid the latter possibility it is advisable to insulate the inside of the iron case by either silicone rubber or araldite; or better still to provide a perspex box to contain the coil. Great care is needed in making and handling of coils in order to avoid the formation of cracks in the insulation.

A4.4 ELECTRIC-RESISTANCE COOLING PARAMETERS

Copper wire coils are capable of attaining high temperatures (180°C). To prevent the wire from burning out, the coolant should be capable of receiving the heat at a sufficiently rapid rate. The energy flux in watts per square centimetre of surface is given by

$$q = P/A_{sc} \quad \text{.....(A4.15)}$$

where A_{sc} is the surface area of the coil.

The temperature difference between the coil and the coolant can be evaluated from equation (A4.13) or from the volatage difference of the coil as follows,

$$T = T_s - T_w = \frac{V_2 - V_1}{V_1} \times \frac{10^3}{4} \quad \text{.....(A4.16)}$$

The power transferred from the coil to the coolant is then given by

$$P = hA_{sc}(T_s - T_w) \quad \text{.....(A4.17)}$$

where h is the heat transfer coefficient.

In a process of this kind the heat transfer, heat conduction and thermal conductivity are contributed by both the copper wire and its insulation. The maximum amount of heat that can be removed by the coolant depends on the maximum temperature induced in the coil as well as the boiling temperature and latent heat of the coolant.

A4.5 WATER COOLING

It is generally accepted that water cooling is the cheapest, efficient and most readily available. In all the lenses described in this thesis cooling is by flowing water.

Two more methods of water cooling are currently under investigation by T. Mulvey (1980) and A.V. Crewe (1976) and N.W. Parker et.al.(1976). The former is dealing with cooling by boiling and evaporation while the latter is only studying evaporation. In an evaporative cooling system the coil is placed inside the vessel with inlet and outlet tubes leading to and from a water reservoir and a water-cooled heat exchange. The entire system is pumped down to about 20 torr. However, cooling is achieved by partially wrapping the coil with a wick (of cotton) so that cooling may only be applied to the bottom of the coil and that the capillary action of the wick will cool the coil. Here the bubble formation is due to surface evaporation and nucleate boiling.

On the other hand, cooling by boiling may have the advantage that once boiling is achieved the temperature rise stays constant regardless of any increase in coil power, i.e. current,

because the generated steam carries away the resulting excess heat. In either case the temperature of the boiling coolant can be reduced to room temperature by reducing the pressure to about 20 torr.

A4.6 EXPERIMENTAL INVESTIGATIONS ON COOLING BY FLOWING WATER

Now our aim is to run the experiment under the actual circumstances in which cooling takes place when the coil is inside the lens structure. The coil was made of SWG 18 enamelled copper wire whose geometrical and physical parameters are shown in table (A4.2).

Parameter	Numerical Value	Parameter	Numerical Value	Parameter	Numerical Value
D_1(cm)	10.0	NI_{max}(AT)	11875	l(metres)	118
D_2(cm)	5.8	A_c(cm^2)	13.42	R(Ω)	1.71
D_m(cm)	7.9	A_{sc}(cm^2)	627.06	P_{max}(watts)	1068.75
N(turns)	475.0	A_s(cm^2)	4519.67	t(cm)	6.4

Table (A4.2) Properties and characteristic parameters of coil used for experiments in cooling.

A_l is the rectangular cross-sectional area of the coil as explained in figure (1); A_{sc} is the surface area of the coil; and A_s is the surface area of the wire. t is the axial depth of the coil.

The significance of area A_c is design purposes where copper wire tables give an estimate of the average number of machine winding turns per area (A_c). The length of the coil wire (l) is obtained from the product of the number of turns (N), the mean diameter of coil (D_m) and the constant π,

$$l = \pi D_m N$$

and so the coil resistance can be calculated.

The loosely wound coil is mounted on a perspex former glued to another perspex cylindrical tube making a closed perspex box. The perspex box is now watertight and water flows through it by the inlet pipe connected to the cylindrical tube. The whole arrangement is then put inside the iron body of the magnetic lens as shown in figure (A4.2). The top of the perspex box near the water outlet is make like a bottle neck to prevent the trapping of bubbles.

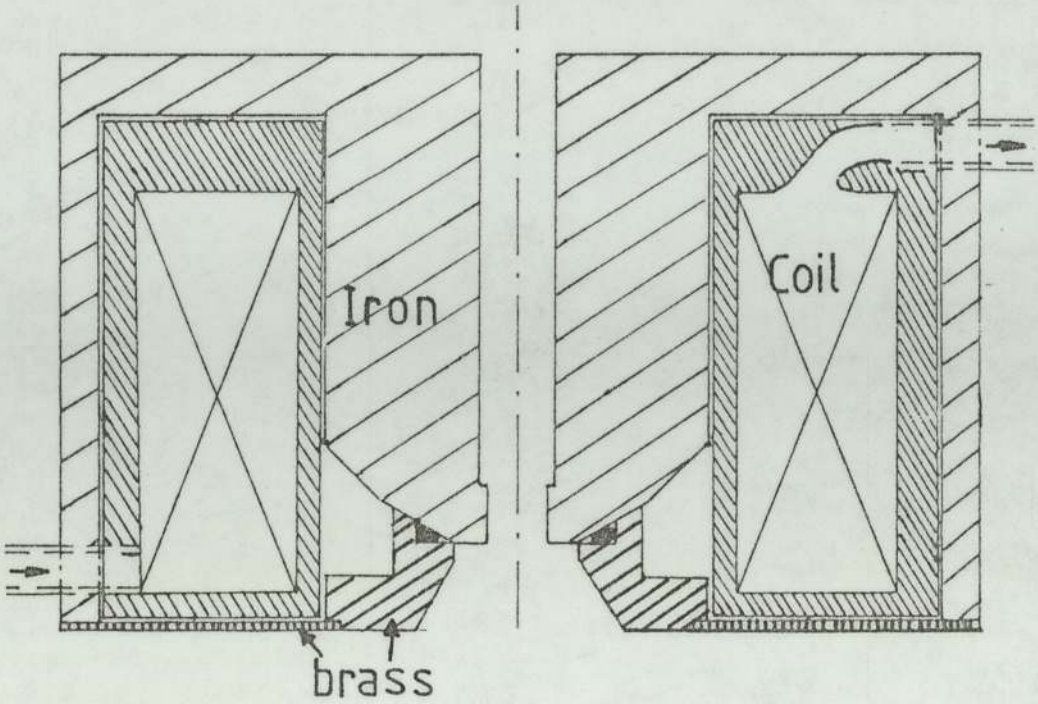

Figure (A4.2) Coil for cooling experiments inside the magentic lens structure.

Equation (4.12) shows that resistivity is temperature dependent. Figure (A4.3) shows the lagging behaviour of the voltage and current of the test coil under examination for different rates of flow of water. The resulting temperature difference between the coil surface and water is approximately proportional to the square of the current, figure (A4.4). However, the thermal time constant is only a fraction of a second. The temperature rise can be calcualted from equation (A4.16) using the rise in potential difference across the coil. The cooling water plays a major part in reducing the magnitude of the temperature rise. Its efficiency in removing the heat is determined by the rate of flow and hence the velocity, figure (A4.5). The rate of flow was measured directly from the outflowing water as the number of litres collected per minute.

The velocity is calculated as follows:

$$\text{Velocity} = \text{height of water in lens} \div \text{time taken}$$

$$= \frac{\text{volume of water in lens}}{\text{base area of lens}} \div \frac{\text{volume of water in lens}}{\text{rate of flow in water}}$$

and figure (A4.6) gives the relation between the rate of flow of water and its velocity.

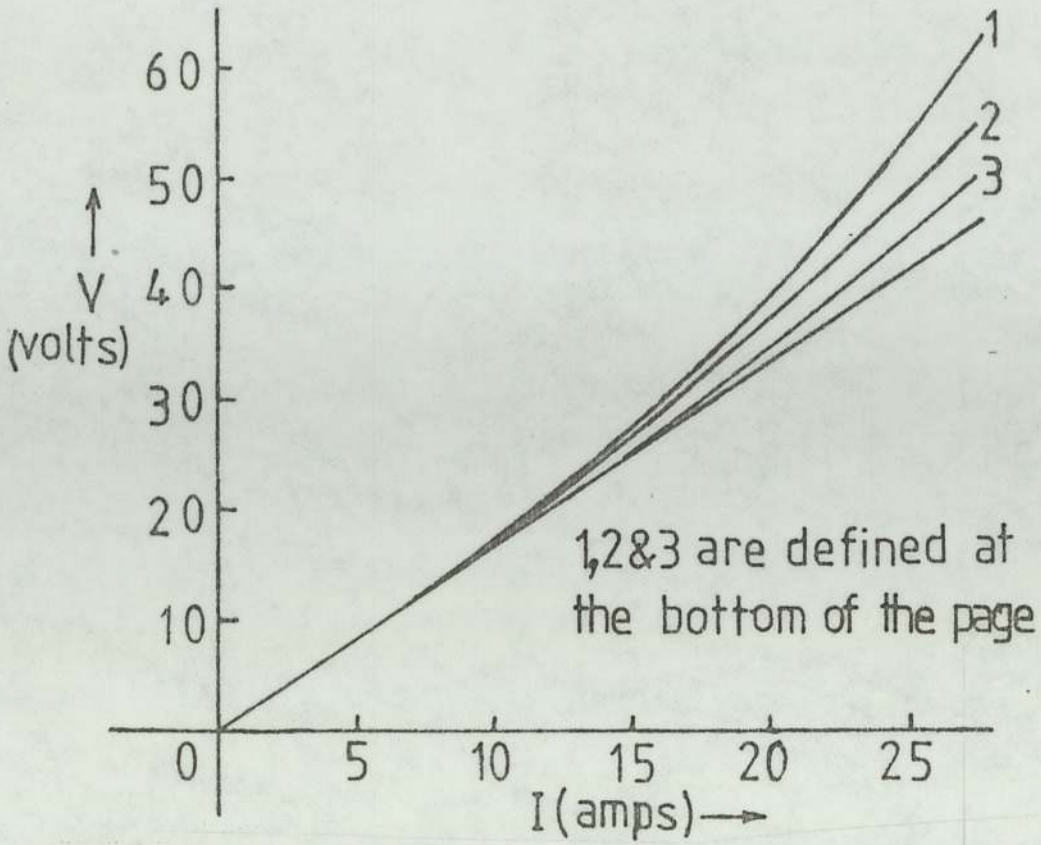

Figure (4.3) The Variation of voltage against current in the cooling test coil at various flow rates.

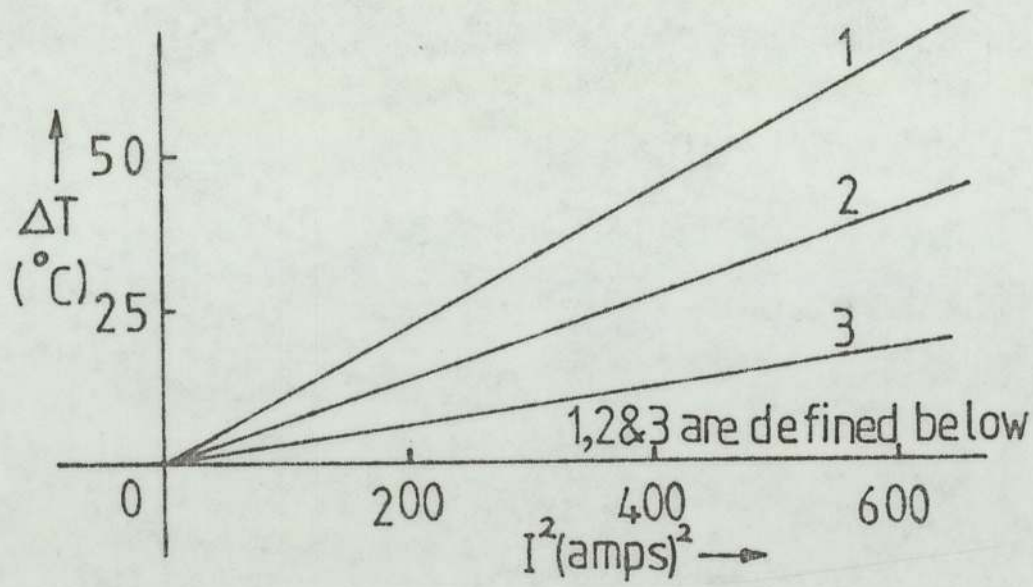

Figure (A4.4) The dependence of the temperature rise in cooling test coil on the square of the electric current at different rates of flow.

1. Rate of flow of water = 0.9 litres/min.

2. Rate of flow of water = 1.9 litres/min.

3. Rate of flow of water = 3.7 litres/min.

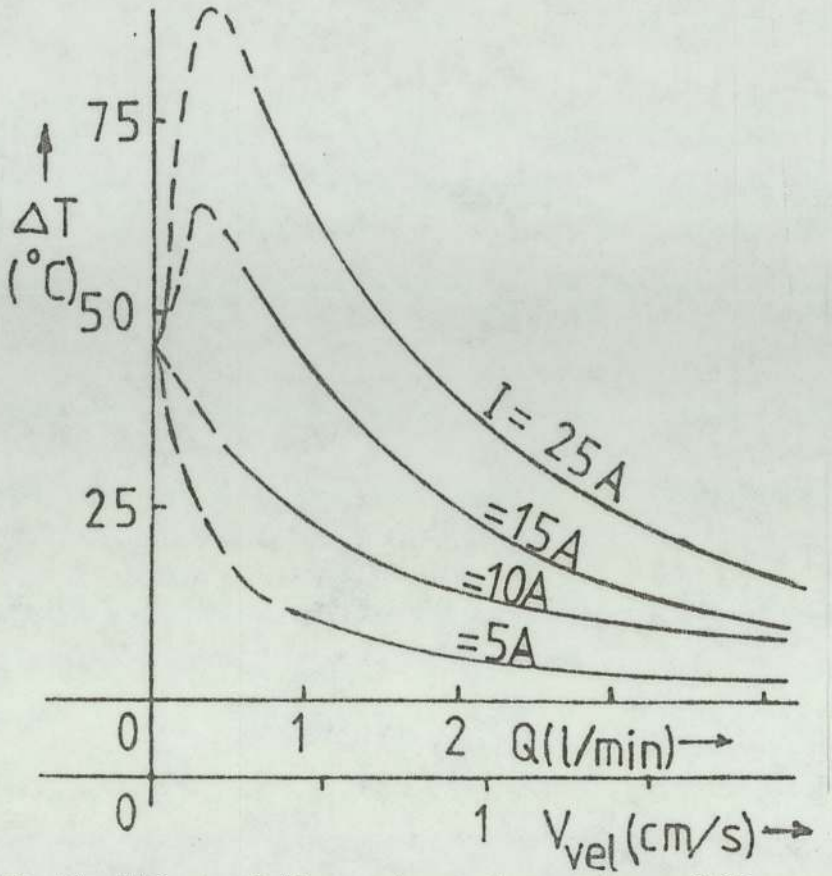

Figure(A4.5) Effect of flow rate on temperature difference between coil surface and water.

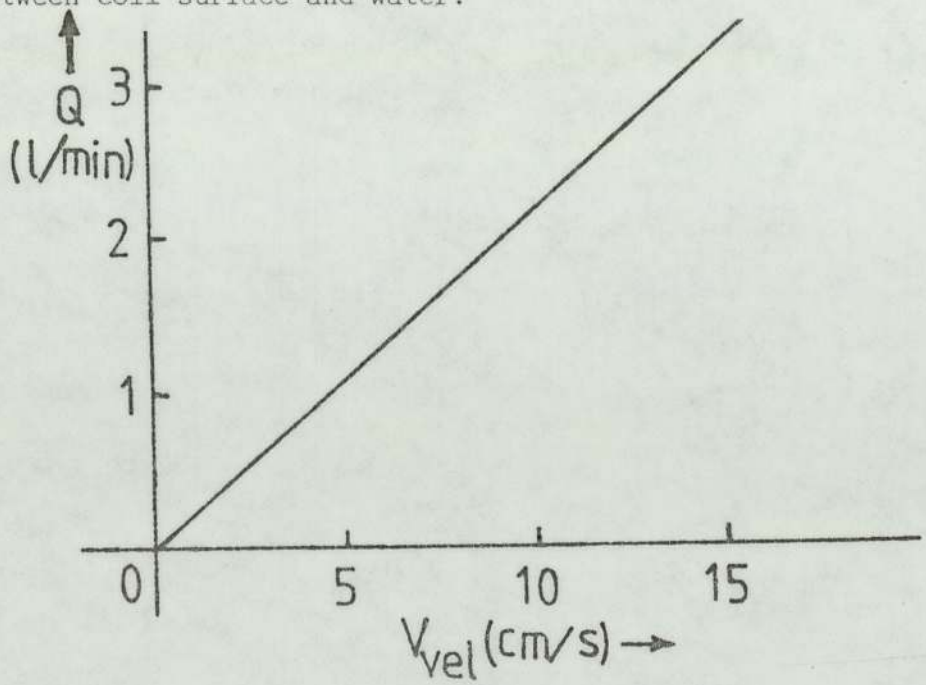

Figure (A4.6) The relation between the rate of flow of water and its velocity.

When the surface temperature of the wire (or tape) coil exceeds the boiling point of the water, vapour bubbles nucleate on the wire surface. The bubbles grow rapidly in the superheated water layer next to the wire surface until they eventually depart and escape, enabling sufficient heat transfer to take place.

Again the coolant is an important factor of heat transfer. It is noticed in figure (A4.7) that h has a specific value when the velocity is zero i.e. stationary water. This eventually favours cooling by boiling, first suggested by T. Mulvey. At such a high value for h and so long as there is some water in the lens however little, it will be enough for heat to be removed because the resulting water vapour from the steam cools the dry top part of the coil. In this experimental investigation we found that the temperature rise at stationary water is 45^{o}, using the voltage difference method of equation (A4.16).

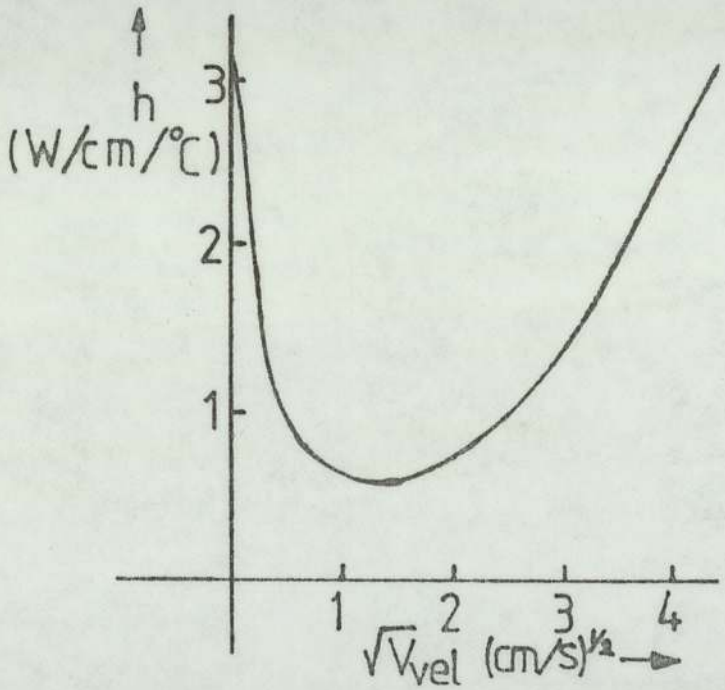

Figure (A4.7)

The heat transfer coefficient as a function of velocity of water.

A4.7 DESIGN OF THE IRON CIRCUIT OF A MAGNETIC LENS

Iron circuits, in magnetic lenses, should be designed in such a way that the magentic lines of force follow a continuous path falling entirely inside the iron circuit before they finally emerge at the air gap, or the outer wall of the lens structure as in the case of the single-polepiece lens, to complete the overall circuit. The leakage flux usually occurs when the lines of force enter into a cross-sectional area which is too small to allow all the lines of force to pass through it. For this reason special attention should be given wherever there is a change of cross-section i.e. at the corners of the iron body of the lens. These design considerations may be implemented by applying equation (A4.18) and figure (A4.8).

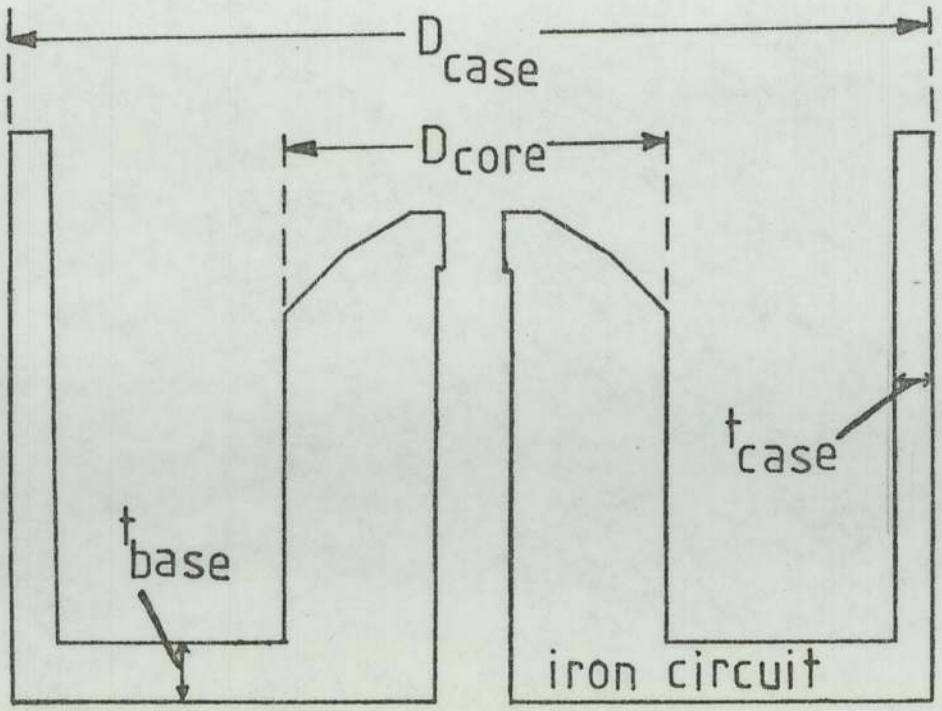

Figure (A4.8) The iron circuit of a single-polepiece magnetic lens showing the lines of force.

$$\pi(D_{core}/4) \leqslant (\pi D_{core})\, t_{base} \leqslant (\pi D_{case})\, t_{case} \quad \ldots(A4.18)$$

where D_{core} and D_{base} are the diameters of the core and the lens itself respectively and t_{base} and t_{case} are the thicknesses of the base and outer walls of the iron lens respectively.

APPENDIX 5

DERIVATION OF EXPRESSIONS FOR THE MAGNIFICATION AND EFFECTIVE FOCAL LENGTH IN A THREE-THIN-LENS SYSTEM AND ITS APPLICATION TO THE PRESENT AND LAMBRAKIS et.al. MAGNETIC PROJECTION SYSTEMS

The magnetic corrector lens in the present system and in that of Lambrakis et.al.(1977) will now be represented by two thin lenses. The magnetic projector lens, in both systems, will be represented by one thin lens since in the present investigation, the projector lens is operated at an excitation well below that of its minimum focal length and so the "weak lens" approximation is valid for present purposes. The three thin lenses will now be referred to as first, second and third lenses respectively whose focal lengths are f_1, f_2 and f_p respectively .

Consider a ray trajectory in each of the two systems, as shown in figure (A5.1), entering the first lens parallel to the principal axis at a radial height r_1, crossing the second and third lenses at heights r_2 and r_3 respectively, and striking the screen at an off-axis distance ρ_t. The magnification M_1 of the system is (ρ_t/r_1), as illustrated in figure (A5.1), and may be written as

$$M_1 = \frac{\rho_t}{r_3} \cdot \frac{r_3}{r_2} \cdot \frac{r_2}{r_1}$$

$$= \frac{\ell_p - v}{v} \cdot \frac{u}{v_2} \cdot \frac{u_2}{f_1} \qquad \text{.....(A5.1)}$$

where ℓ_p is the projection distance between the third lens and the screen. Here u and v are the object and image distances of the third lens respectively, and u_2 and v_2 are the object and image distances of the second lens respectively. From the thin lens equation, we get

$$v_2 = \frac{u_2 f_2}{u_2 - f_2} \qquad \text{.....(A5.2)}$$

and from figure (5.1)

$$u_2 = \ell_1 - f_1 \qquad \text{.....(A5.3)}$$

where ℓ_1 is the separation between the first and second lenses whose effective focal length f_{corr} is given by

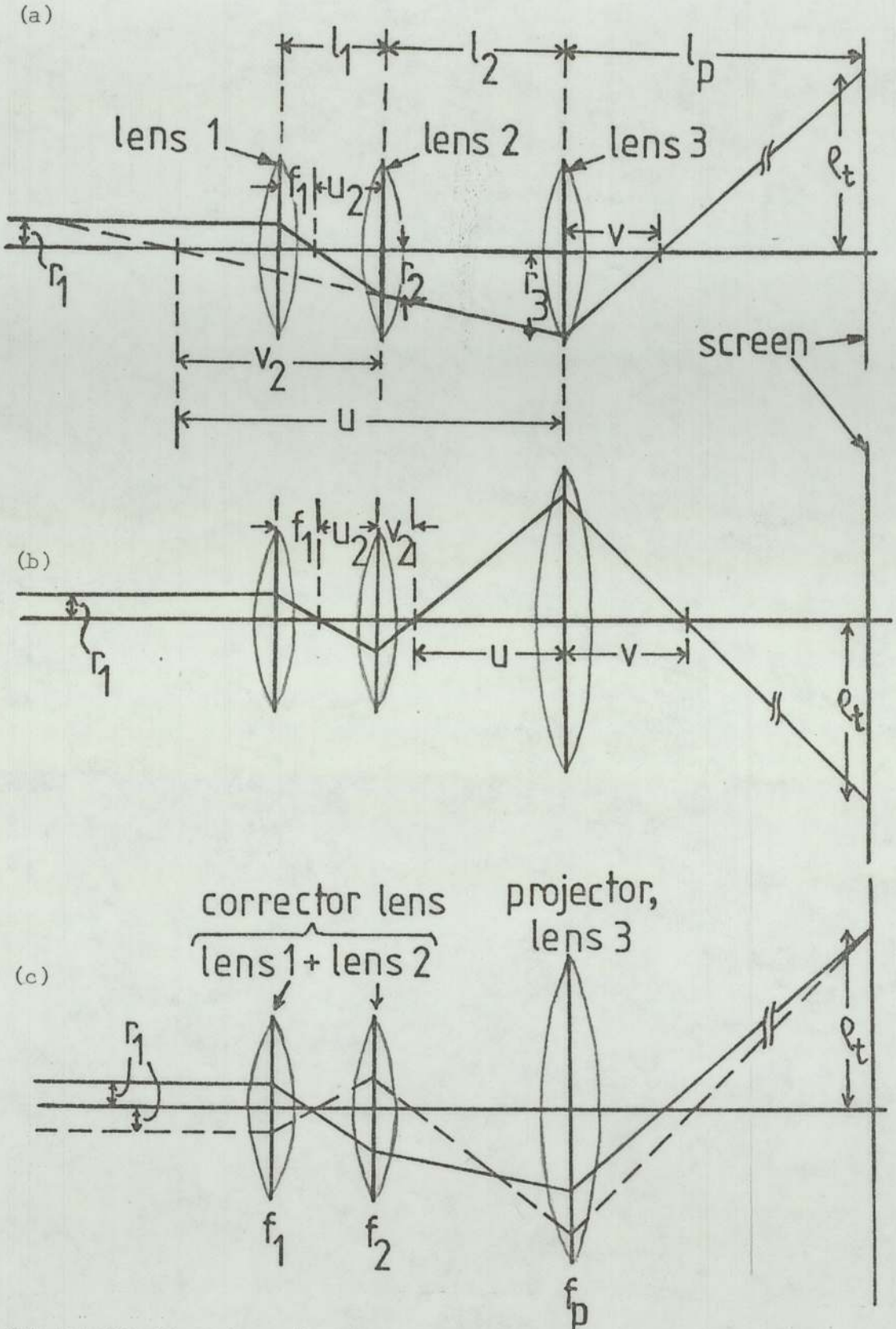

Figure (A5.1) Schematic diagrams of ray trajectories through three thin lenses representing (a) present system (b) Lambrakis et.al. system (c) present and Lambrakis et.al. systems. The two systems have the same r_1 and ρ_t.

$$\frac{1}{f_{corr}} = \frac{1}{f_1} + \frac{1}{f_2} - \frac{l_1}{f_1 f_2} \quad \text{.....(A5.4)}$$

Inserting equations (A5.2), (A5.3) and (A5.4) into equation (A5.1) we obtain,

$$M_1 = -\left(\frac{l_p - v}{v}\right)\left(\frac{u}{f_{corr}}\right) \quad \text{.....(A5.5)}$$

The thin lens equation also gives

$$v = \frac{uf_p}{u - f_p} \quad \text{.....(A5.6)}$$

thus equation (A5.5) becomes

$$M_1 = -\left(\frac{l_p - f_p}{f_p}\right)\frac{u}{f_{corr}} + \frac{l_p}{f_{corr}} \quad \text{.....(A5.7)}$$

From figure (A5.1)

$$u = l_2 - v_2 \quad \text{.....(A5.8)}$$

where l_2 is the separation between the second and third lenses. Substituting for v_2 from equations (A5.2), (A5.3) and (A5.4), we get

$$u = l_2 - f_{corr} + \frac{l_1 f_{corr}}{f_1} \quad \text{.....(A5.9)}$$

Therefore equation (A5.7) becomes

$$M_1 = -\left(\frac{l_p - f_p}{f_p}\right)\left(\frac{l_2}{f_{corr}} + \frac{l_1}{f_1} - 1\right) + \frac{l_p}{f_{corr}} \quad \text{..(A5.10)}$$

Equation (A5.10) gives the overall magnification M_1 of the three-thin-lens system at the final screen; M_1 is expressed in terms of the focal lengths and the lens separations.

The magnification M_2 of the third lens at the final screen may be obtained with the help of figure (A5.2) and is given by

$$M_2 = \frac{\rho_p}{r_1} = \frac{l_p - f_p}{f_p} \quad \text{.....(A5.11)}$$

where ρ_p is the off-axis distance on the final screen when the third lens alone is considered.

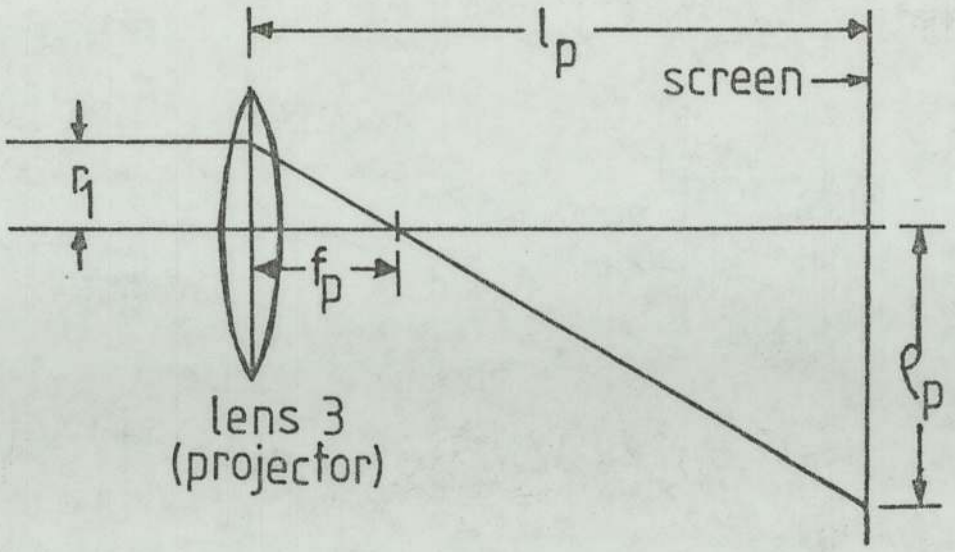

Figure (A5.2) Schematic diagram of a parallel beam of height r_1 passing through the third (final projector) lens and strikes the screen at an off-axis distance ρ_p. ($M_2 = \rho_p/r_1$).

Hence the magnification M_{corr} of the first two lenses is M_1/M_2. It therefore follows from equations (A5.10) and (A5.11) that

$$M_{corr} = -\left[\frac{l_2}{f_{corr}} + \frac{l_1}{f_1} - 1\right] + \frac{l_p f_p}{f_{corr}(l_p - f_p)} \quad \ldots (A5.12)$$

The effective focal length F of the three-thin-lens system may be calculated as follows. With the aid of figure (A5.3),

$$\tan \alpha_p = \frac{r_1}{F} = \frac{r_3}{v}$$

where α_p is the projection semi-angle. Hence the refractive power $1/F$ of the system is given by

$$\frac{1}{F} = \frac{r_3}{r_1 v} \quad \ldots\ldots\ldots\ldots\ldots\ldots\ldots\ldots (A5.13)$$

Since, from figure (A5.1),

$$r_3 = \frac{ur_2}{v_2} \quad \text{and} \quad r_2 = \frac{u_2 r_1}{f_1}$$

$$\frac{1}{F} = \frac{u\,u_2}{v\,v_2 f_1} \qquad \text{.....(A5.14)}$$

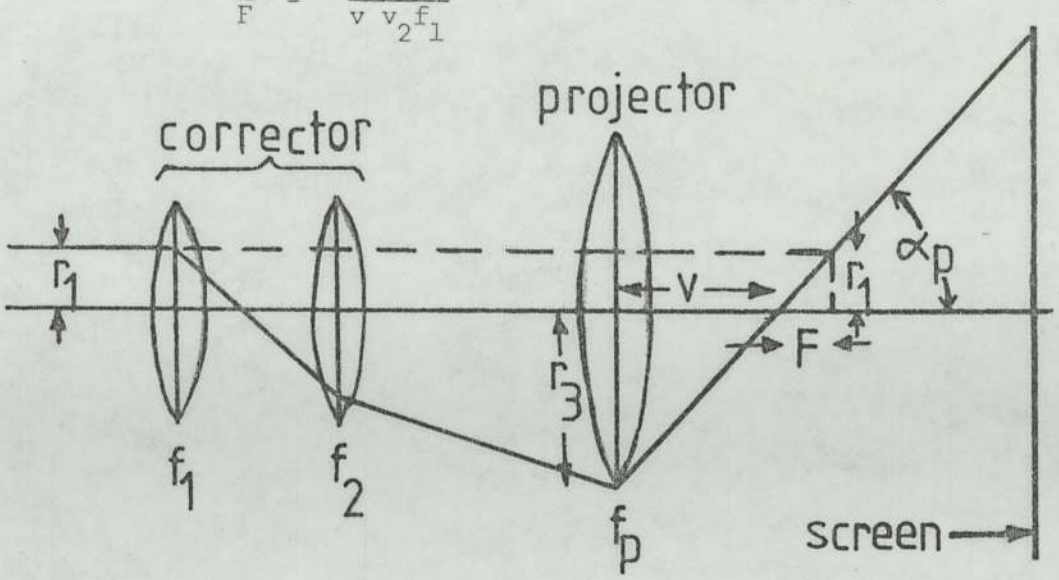

Figure (A5.3) Schematic diagram showing the effective focal length F of a three-thin-lens system.

Substituting for the values of v_2, u_2, v and u from equations (A5.2), (A5.3), (A5.6) and (A5.9) respectively into equation (A5.14) and rearranging we get

$$\frac{1}{F} = \frac{1}{f_p} + \frac{1}{f_{corr}} - \frac{1}{f_p}\left[\frac{l_2}{f_{corr}} + \frac{l_1}{f_1}\right] \qquad \text{.....(A5.15)}$$

The performance of the present system and that of Lambrakis et.al. may now be tested under comparable conditions. A realistic comparison dictates that the two systems should produce the same magnifications M_1 and M_{corr} at the final screen. This requirement, however, imposes certain different values of f_1 and f_2 in each system. The lens separations l_1 = 17 mm. and l_2 = 30 mm. were deduced from electron trajectories calculated for the experimental system. The same separations were also applied to Lambrakis et.al. system. The focal length f_p = 10 mm. of the third thin (final projector) lens was kept the same in both systems; the projection distance l_p = 400 mm. was also kept the same since this is a typical image throw in most commercial instruments. The full comparison between the two systems is tabulated in table (A5.1). In this table the numerical values of r_2, r_3, M_1, M_2, M_{corr} and α_p are based on an initial ray height r_1 = 1 mm.

	Present system	Lambrakis et.al. (1977) system
f_1(mm)	4.9	6.8
f_2(mm)	14.0	4.0
f_{corr}(mm)	36.1	-4.4
u_2(mm)	12.1	10.2
v_2(mm)	-89.2	6.6
u(mm)	-119.2	23.4
v(mm)	10.9	17.5
r_2(mm)	-2.5	-1.5
r_3(mm)	-3.3	5.3
m	0.09	0.75
D^*/D	1.13	2.75
M_1	-117	117
M_2	39	39
M_{corr}	-3	3
α_p^o	16.7	17
F	-3.31	3.27

Table (A5.1) A tabulated comparison between the geometrical and physical properties of the present and Lambrakis et.al.(1977) systems using the thin-lens model.

APPENDIX 6

COMPUTATION AND ANALYTICAL CALCULATION OF DISTORTION IN THE IMAGE

A6.1 A PROGRAM FOR SIMULATING IMAGES OBSERVED ON THE FINAL VIEWING SCREEN

This program simulate electron micrograph images as observed on the final viewing screen. It is based on the analytical solution of nature of distortion that is formulated and presented in the next section. The analysis assumes the knowledge of the object point coordinates. The object is taken to be a rectangular mesh grid, x and y axes. After experiencing distortion, the coordinates of an image point become X and Y. X and Y are then functions of x, y, M, k_1 and k_2. The object is a square grid, and x and y have equal intervals of 10 mm. M is the magnification whereas k_1 and k_2 are given by

$$k_1 = (Q_{rad}/L)^2 \quad \text{.....(A6.1)}$$

and

$$k_2 = (Q_{sp}/L)^2 \quad \text{.....(A6.2)}$$

where k_1 and k_2 are the linear radial and spiral distortion coeffiencents respectively; and so the distortion can be expressed as

$$(\Delta\rho_1/\rho) = k_1 \rho^2 \quad \text{.....(A6.3a)}$$

and

$$(\Delta\rho_2/\rho) = k_2 \rho^2 \quad \text{.....(A6.3b)}$$

$\Delta\rho_1$ and $\Delta\rho_2$ are radial and spiral displacements, L is the projection distance. Q_{rad} and Q_{sp} are computed from the distortion program of Marai (1977). Since Q varies with excitation then k_1 and k_2 are also excitation dependent.

The program essentially computes the coordinates of displaced image points according to the formulae [equation (A6.6) and (A6.7)] of the next section. The computation of the new coordinates is then followed by the graph plotter routine. The connection of image points is carried out by the method of cubic spline fits. The flow diagram of the program is shown in figure (A6.1) and an example of the output is given in figure (A6.2) The program is shown in this appendix where U and V stand for image coordinates X and Y respectively. A similar program was written by Nasr (1978), at a later stage, using a mini computer (WANG 2000).

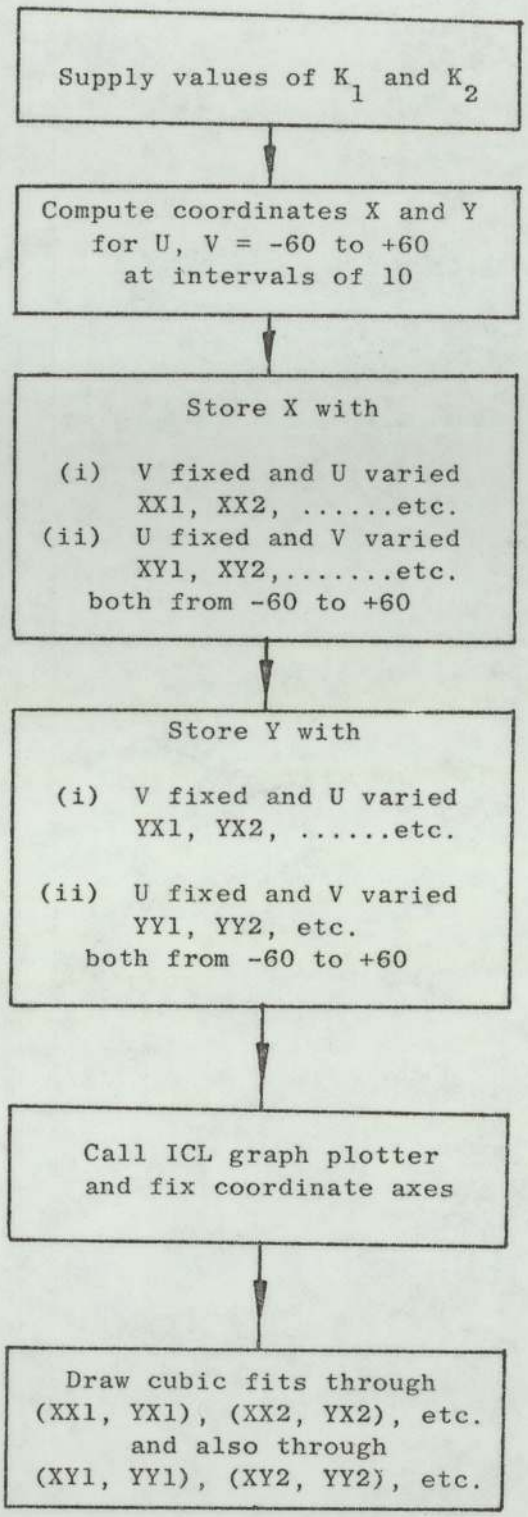

Figure (A6.1) Flow diagram of the computation of image simulation.

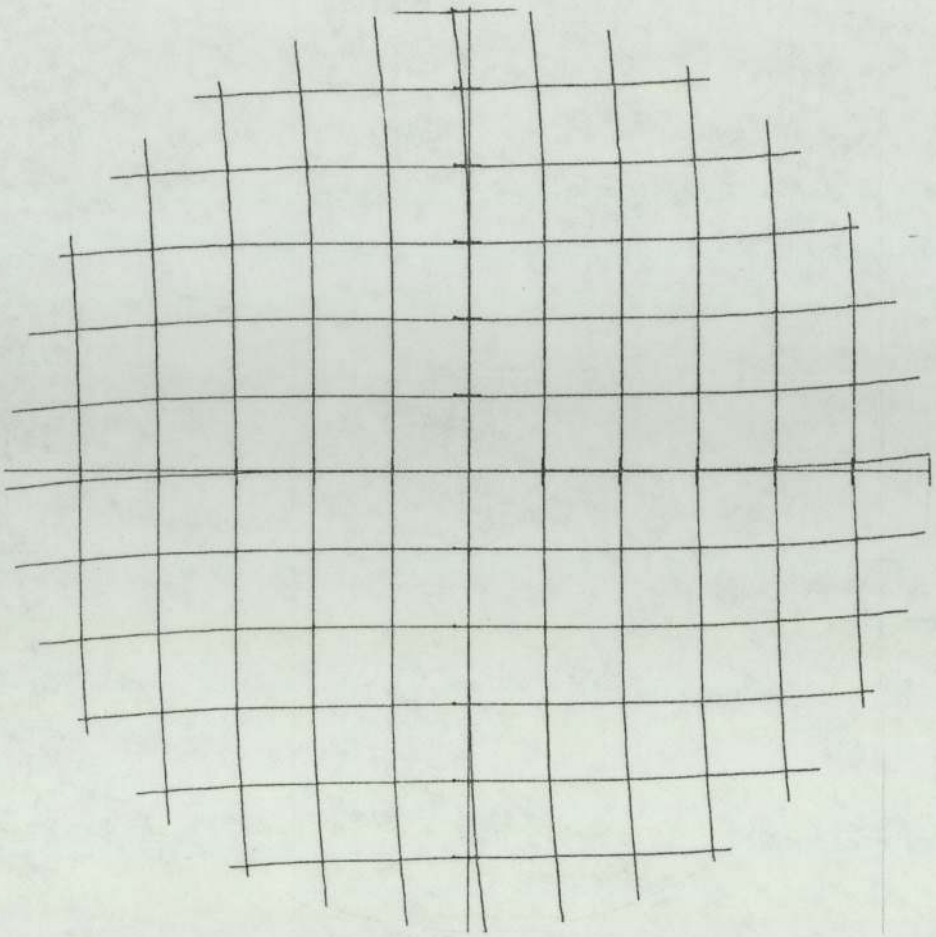

Figure (A6.2) Simulation of an electron micrograph image produced by the single-polepiece projector lens, described in Chapter 4, as observed on the final viewing screen. Pure spiral distortion. Spiral distortion at the edge, ρ = 6 cm., is 3.86%. (For a conventional double-polepiece lens this would be 6%) $\alpha_p = 13.8^{\circ}$.

A6.2 ANALYTICAL CALCULATION OF DISTORTION IN THE IMAGE

In this section we shall show the rotational effect of the spiral distortion and the path an image point will take from the aberration - free Gaussian point to its displaced point as the amount of distortion is increased. The two suggestions pointed out in the literature are paths perpendicular to radial direction and those that act along arcs or segments of circles. We investigated the two possibilities and found that the spiral distortion causes the image points to trace out circular paths. Together with this we shall include the presence of radial distortion. The analytical formulae will then be fed into the computer to simulate the shape of an image suffering from both types of distortion. The results of which will be compared

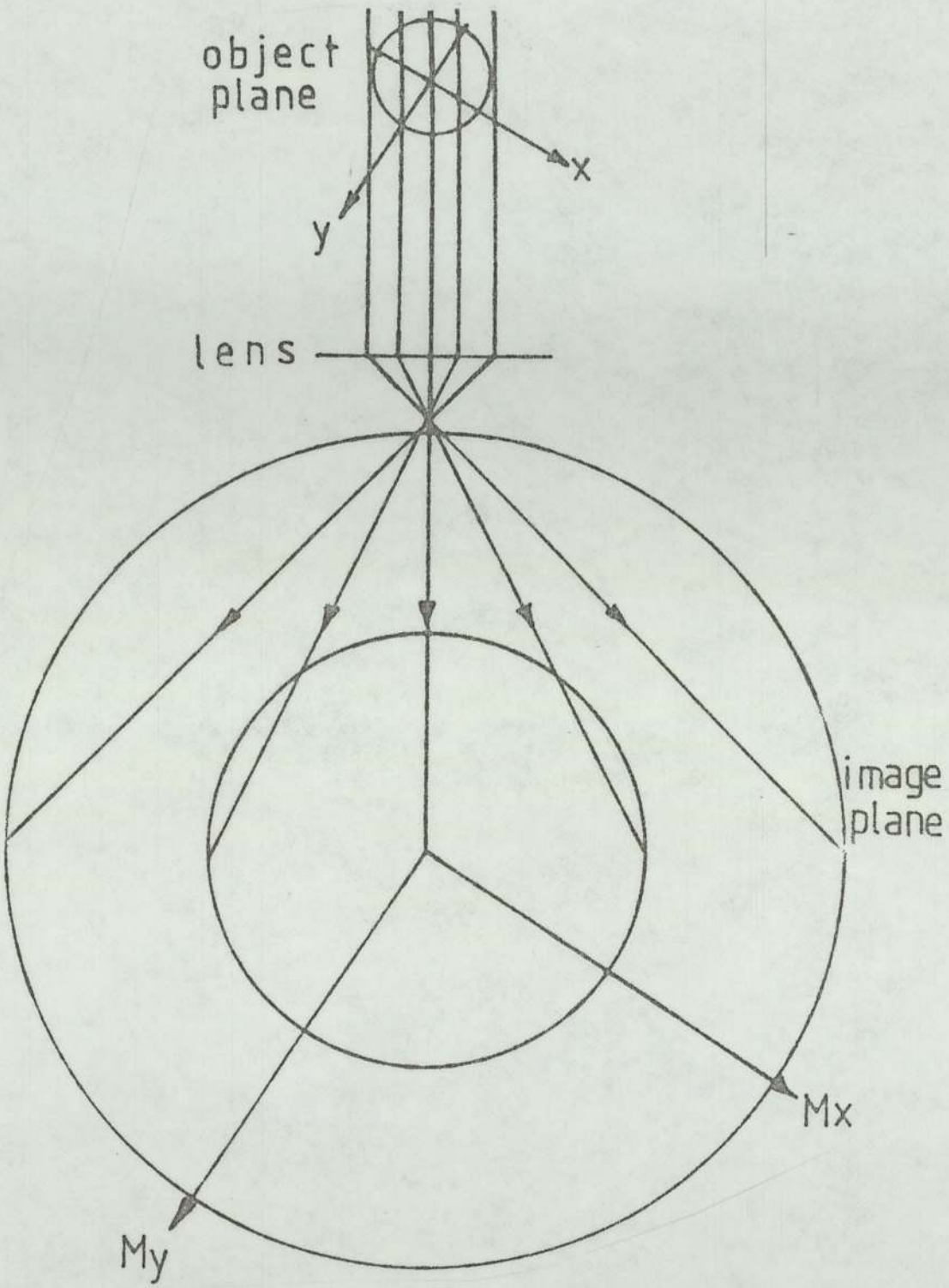

Figure (A6.3a) Object and image planes. Gaussian image and no rotation.

with experimental results. To avoid repetitive work done by other authors we are not going to consider each type of distortion separately but rather the combined effect on the displaced image point. However, we are not going to deal with the rotation of the image with respect to the object (θ) but only the increase in rotation($\delta\theta$).

Suppose that an object point has the coordinates x and y. If the magnification is M then the corresponding image point will have the coordinate Mx and My. This image point is suffering from distortion and we shall call the Gaussian image point (A), figure (A6.4). The radial (pin-cushion) distortion displaces point A to a new position B whilst the spiral distortion shifts point A to C. When the two types of distortion acts together

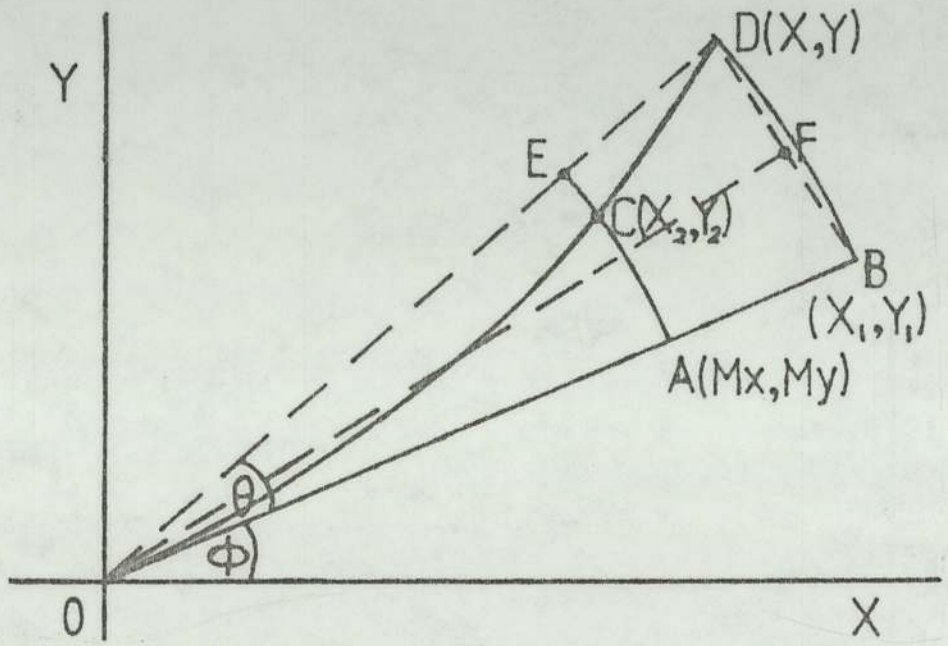

Figure (A6.4) Displacement of the Gaussian image point A by radial and spiral distortion.

the new position of the displaced image point A will be at point D. From equation (A6.3) we have

$$(\Delta\rho_1) = k_1 \rho^3 \quad \text{.....(A6.4)}$$

and

$$(\Delta\rho_2) = k_2 \rho^3 \quad \text{.....(A6.5)}$$

where $(\Delta\rho_1)$ is the radial shift AB and $(\Delta\rho_2)$ is the spiral (circumferential) shift AC. ρ is the Gaussian height of the image point = OA. It follows from figure (A6.4) that

$$\text{ARC AE} = \frac{r}{r + k_1 r^3} \quad \text{ARC BD}$$

$$\theta = \frac{\text{ARC AE}}{r} = k_2 r^2 (1 + k_1 r^2)$$

where $r^2 = M^2(x^2 + y^2)$

$$X = \left[1 + k_1 M^2 (x^2 + y^2)\right] \left\{ Mx \cos \left[k^2 M^2 (x^2 + y^2)\left(1 + k_1 M^2 (x^2 + y^2)\right)^2 \right.\right.$$

$$\left.\left. - My \sin \left[k^2 M^2 (x^2 + Y^2)\left(1 + k_1 M^2 (x^2 + y^2)\right)^2\right\}\right. \quad \text{.....(A6.6)}$$

and similarly

$$Y = \left[1 + kM^2 (x^2 + y^2)\right] \left\{ My \cos \left[k_2 M^2 (x^2 + y^2)\left(1 + k M^2 (x^2 + y^2)\right)^2 \right.\right.$$

$$\left.\left. + Mx \sin \left[k^2 M^2 (x^2 + y^2)\left(1 + k_1 M^2 (x^2 + y^2)\right)^2\right\}\right. \quad \text{.....(A6.7)}$$

The total distortion is

$$\frac{AD}{r} = \left\{ k_1^2 M^4 (x^2 + y^2)^2 + 2\left[1 + k_1 M^2 (x^2 + y^2)\right]\left[1 - \cos\left(k_2 M^2 (x^2 + y^2)\right)\right. \right.$$

$$\left.\left. \left(1 + k_1 M^2 (x^2 + y^2)\right)^2 \right\}^{\frac{1}{2}} \quad \text{.....(A6.8)}\right.$$

```
TRACE 2
MASTER DGPH
DIMENSION X(13,13),Y(13,13),XX1(13),XX2(13),XX3(13)
DIMENSION XX4(13),XX5(13),XX6(13),XX7(13),XX8(13)
DIMENSION XX9(13),XX10(13),XX11(13),XX12(13),YY1(13)
DIMENSION YY2(13),YY3(13),YY4(13),YY5(13),YY6(13)
DIMENSION YY7(13),YY8(13),YY9(13),YY10(13),YY11(13)
DIMENSION YY12(13),YY13(13),B(1),C(1),XY1(13),XY2(13)
DIMENSION XY3(13),XY4(13),XY5(13),XY6(13),XY7(13)
DIMENSION XY8(13),XY9(13),XY10(13),XY11(13),XY12(13)
DIMENSION XY13(13),YX1(13),YX2(13),YX3(13),YX4(13)
DIMENSION YX5(13),YX6(13),YX7(13),YX8(13),YX9(13)
DIMENSION YX10(13),YX11(13),YX12(13),YX13(13)
DATA B(1),C(1)/8HX-AXIS ,8HX-AXIS  /
AK1=0.156*0.254*0.254
AK2=0.1312*0.254*0.254
```

```
      DO 10 I=1,13
      DO 10 J=1,13
      U=-70+10*I
      V=-70+10*J
      U=U/25.4
      V=V/25.4
      X(I,J)=(1+AK1*(U*U+V*V))*(U*COS(AK2*(U*U+V*V)*(1+AK1*(U*
     +U+V*V))**2)-V*SIN(AK2*(U*U+V*V)*(1+AK1*(U*U+V*V))**2))
      Y(I,J)=(1+AK1*(U*U+V*V))*(V*COS(AK2*(U*U+V*V)*(1+AK1*(U*
     +U+V*V))**2)+U*SIN(AK2*(U*U+V*V)*(1+AK1*(U*U+V*V))**2))
      DO 30 I=1,13
       XX1(I)=X(1,I)
       XX2(I)=X(2,I)
       XX3(I)=X(3,I)
       XX4(I)=X(4,I)
       XX5(I)=X(5,I)
       XX6(I)=X(6,I)
       XX7(I)=X(7,I)
       XX8(I)=X(8,I)
       XX9(I)=X(9,I)
       XX10(I)=X(10,I)
       XX11(I)=X(11,I)
       XX12(I)=X(12,I)
30    XX13(I)=X(13,I)
      DO 40 I=1,13
       YX1(I)=Y(1,I)
       YX2(I)=Y(2,I)
       YX3(I)=Y(3,I)
       YX4(I)=Y(4,I)
       YX5(I)=Y(5,I)
       YX6(I)=Y(6,I)
       YX7(I)=Y(7,I)
       YX8(I)=Y(8,I)
       YX9(I)=Y(9,I)
       YX10(I)=Y(10,I)
       YX11(I)=Y(11,I)
       YX12(I)=Y(12,I)
40    YX13(I)=Y(13,I)
      DO 50 I=1,13
       XY1(I)=X(I,1)
       XY2(I)=X(I,2)
       XY3(I)=X(I,3)
       XY4(I)=X(I,4)
       XY5(I)=X(I,5)
       XY6(I)=X(I,6)
       XY7(I)=X(I,7)
       XY8(I)=X(I,8)
       XY9(I)=X(I,9)
       XY10(I)=X(I,10)
       XY11(I)=X(I,11)
       XY12(I)=X(I,12)
50    XY13(I)=X(I,13)
```

```
      DO 60 I=1,13
       YY1(I)=Y(I,1)
       YY2(I)=Y(I,2)
       YY3(I)=Y(I,3)
       YY4(I)=Y(I,4)
       YY5(I)=Y(I,5)
       YY6(I)=Y(I,6)
       YY7(I)=Y(I,7)
       YY8(I)=Y(I,8)
       YY9(I)=Y(I,9)
       YY10(I)=Y(I,10)
       YY11(I)=Y(I,11)
       YY12(I)=Y(I,12)
   60 YY13(I)=Y(I,13)
      CALL OPENPLOT
      CALL HGPLOT(-10.0,10.0,0,4)
      CALL HGPAXIS(-5.905,0.0,8(1),-8,11.81,0.0,-1500.0,100.0)
      CALL HGPAXIS(0.0,-5.905,C(1),8,11.81,90.0,-1500.0,100.0)
      CALL HGPSCURVE(XX1,YX1,13,0,0,0,)
      CALL HGPSCURVE(XX2,YX2,13,0,0,0)
      CALL HGPSCURVE(XX3,YX3,13,0,0,0)
      CALL HGPSCURVE(XX4,YX4,13,0,0,0)
      CALL HGPSCURVE(XX5,YX5,13,0,0,0)
      CALL HGPSCURVE(XX6,YX6,13,0,0,0)
      CALL HGPSCURVE(XX7,YX7,13,0,0,0)
      CALL HGPSCURVE(XX8,YX8,13,0,0,0)
      CALL HGPSCURVE(XX9,YX9,13,0,0,0)
      CALL HGPSCURVE(XX10,YX10,13,0,0,0)
      CALL HGPSCURVE(XX11,YX11,13,0,0,0)
      CALL HGPSCURVE(XX12,YX12,13,0,0,0)
      CALL HGPSCURVE(XX13,YX13,13,0,0,0)
      CALL HGPSCURVE(XY1,YY1,13,0,0,0)
      CALL HGPSCURVE(XY2,YY2,13,0,0,0)
      CALL HGPSCURVE(XY3,YY3,13,0,0,0)
      CALL HGPSCURVE(XY4,YY4,13,0,0,0)
      CALL HGPSCURVE(XY5,YY5,13,0,0,0)
      CALL HGPSCURVE(XY6,YY6,13,0,0,0)
      CALL HGPSCURVE(XY7,YY7,13,0,0,0)
      CALL HGPSCURVE(XY8,YY8,13,0,0,0)
      CALL HGPSCURVE(XY9,YY9,13,0,0,0)
      CALL HGPSCURVE(XY10,YY10,13,0,0,0)
      CALL HGPSCURVE(XY11,YY11,13,0,0,0)
      CALL HGPSCURVE(XY12,YY12,13,0,0,0)
      CALL HGPSCURVE(XY13,YY13,13,0,0,0)
      CALL CLOSEPLOT
      STOP
      END
****
```

APPENDIX 7

DERIVATION OF THE RELATIVE SENSITIVITY (IMAGE DEFLECTION) PRODUCED BY STRAY A.C. MAGNETIC FIELDS

When an electron passing along the optical axis experiences a magnetic force from a uniform magnetic field it is deflected, as shown in figure (A7.1). The deflection y on the final viewing screen is given by

$$y = L^2/2\ R_{arc} \quad \ldots\ldots\ldots\ldots\ldots\ldots\ldots\ldots (A7.1)$$

where L is the projection distance and R_{arc} is the radius of curvature traced out by the electron due to the presence of the uniform magnetic field (B). This arises since the force F on

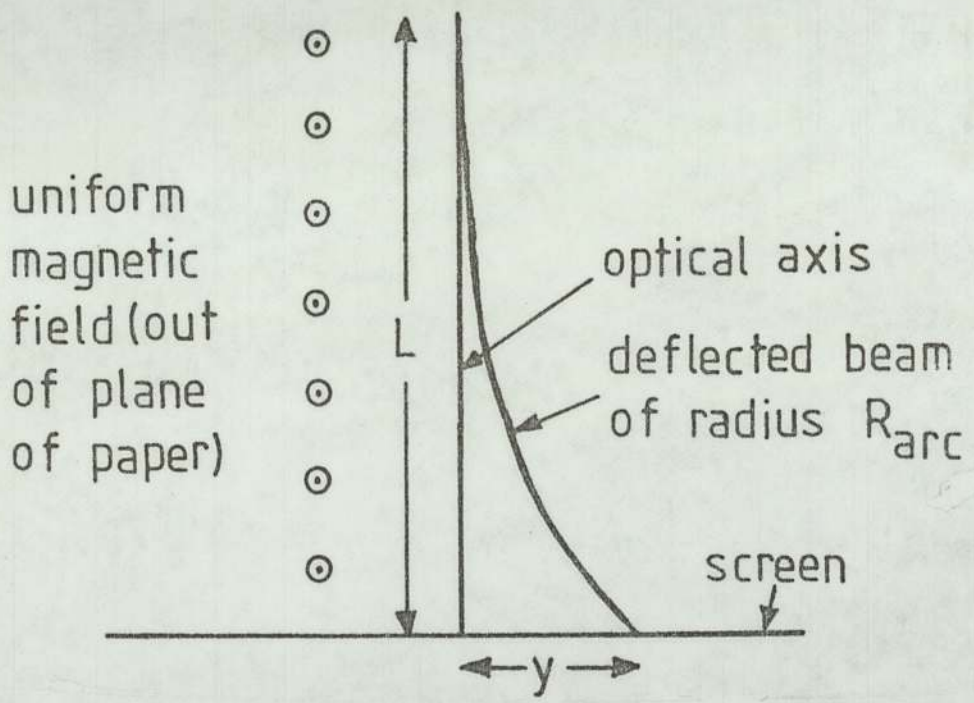

Figure (A7.1) Deflection of the final image by a magnetic field.

the electron is given by

$$F = m(v_{vel})^2/R_{arc} = evB \quad \ldots\ldots\ldots\ldots\ldots (A7.2)$$

where v_{vel} is the velocity of the electron given by

$$v_{vel} = (2eV_r/m)^{\frac{1}{2}} \quad \text{.....(A7.3)}$$

e/m is the ratio of charge to mass of the electron, B is the uniform magnetic field, and V_r is the relativistically corrected accelerating voltage. From equations (A7.2) and (A7.3), we obtain

$$R_{arc} = (2mV_r/e)^{\frac{1}{2}}/B \quad \text{.....(A7.4)}$$

and hence

$$y = L^2B\,(e/8mV_r)^{\frac{1}{2}}$$

$$= 1.483 \times 10^5\, L^2B/V_r^{\frac{1}{2}} \quad \text{.....(A7.5)}$$

y is expressed in S.I. units, i.e. L, B , and V_r are measured in metres, Testa and volts respectively. From equation (A7.5) we realise that the relative sensitivity y is proportional to the magnetic field B , producing it and to the square of the projection distance L; and inversely proportional to the square root of the relativistic applied voltage V_r. However, the scaling factor n referred to in Chapter 1 is proportional to $V_r^{\frac{1}{2}}$; hence L^2 is proportional to V_r. Therefore for a projector lens of a given magnification, y is proportional to $(B\,V_r^{\frac{1}{2}})$. This means that under these circumstances, the projector system becomes more sensitive to stray magnetic fields as the accelerating voltage increases.